# Histological Validation of Diffusion MRI

By

Kurt Schilling

Dissertation

Submitted to the Faculty of the

Graduate School of Vanderbilt University

in partial fulfillment of the requirements

for the degree of

DOCTOR OF PHILOSOPHY

In

Biomedical Engineering

December 16, 2017

Nashville, Tennessee

Approved:

Adam W. Anderson, Ph.D.

Mark D. Does, Ph.D.

Bennett A. Landman, Ph.D.

Iwona Stepniewska, Ph.D.

John C. Gore, Ph.D.

# ACKNOWLEDGEMENTS

My time as a graduate student has been extremely gratifying, both personally and academically. First and foremost, I would like to thank my wife, Emma. I am tremendously grateful for your patience, support, and understanding. I don’t know where I would be without your constant encouragement and the many sacrifices you’ve made that allow me to continue to pursue my degree.

At Vanderbilt, I am grateful for the leadership and encouragement provided by my thesis advisor, Dr. Adam Anderson. The door to your office was always open whenever I had questions, and you consistently allowed me to explore research and projects I was enthusiastic about, while steering me in the right direction when needed. I would also like to thank my committee members Dr. Mark Does, Dr. Bennett Landman, Dr. Iwona Stepniewska, and Dr. John Gore for their direction, dedication, and invaluable advice along this project.

Finally, I would not be where I am today without the support and love of learning instilled by my family. To my parents, Barb and Greg, thank you for always encouraging me to follow my interests, both in and out of the classroom. To my younger brother, Clay, I’d like to think that our intense competitive nature pushed me to always give my all – thanks for always “letting” me win in both academics and athletics.

# ABSTRACT

The ability of diffusion magnetic resonance imaging (dMRI) fiber tractography to non-invasively map the three-dimensional (3D) network of the human brain has proven to be a valuable neuroimaging tool, improving our understanding of both normal development and complex brain disorders. However, the process from data acquisition to generation of a 3D map of reconstructed fibers is a multi-step procedure with numerous assumptions and uncertainties that can ultimately affect the ability of this technique to faithfully represent the true axonal connections of the brain. Because of this, validating dMRI tractography is required on many levels. It is necessary not only to measure the ability of these techniques to track white matter fibers from voxel to voxel, but also to quantify the ability of dMRI to assess the underlying fiber orientation distribution (FOD) within each voxel. To do this, we propose to compare diffusion data directly to histology data on both the microstructural scale of tissues and the macrostructural scale of brain connectivity. These experiments will lead to a better understanding of the limitations and pitfalls of dMRI experiments, and provide a quantitative assessment of the reliability of these techniques.

# TABLE OF CONTENTS

Page

# LIST OF TABLES

# LIST OF FIGURES

FIGURE PAGE

# CHAPTER 1: INTRODUCTION

## 1.1 Connectivity

A major goal in neuroscience research is to build a comprehensive map of the neuronal connections in the brain. This has been named the “connectome” in direct analogy to an organism’s full complement of genetic information, the genome. The connectome could serve as a fundamental research tool for understanding how the brain works as a complex system, offering insight into normal brain function and dysfunction, normal brain changes (e.g. aging and development), disease, and injury of specific white matter pathways.

For centuries, mapping the structural connectivity of the brain was limited to using anatomical dissection techniques in cadavers [1, 2] or invasive chemical tracer studies in animal models. In the late 1980’s an MRI technique sensitive to the diffusion of water molecules in biological tissues was introduced [3]. Scientists soon realized that this technique, called diffusion MRI (dMRI), offered the ability to probe tissue microstructure and map out white matter connections both in vivo and non-invasively in a process termed “fiber tractography” (see [4] for a review). The potential of dMRI to non-invasively describe the connectivity between brain regions led to a renewed interest in constructing the human connectome, and opened the door to a new level of understanding of the living brain.

Now, 25 years after its introduction, there is a plethora of dMRI methods for image acquisition [5], image analysis [6], and fiber tractography [7] - all of which are based on an attenuation of the MR signal caused by diffusion of water molecules. These tractographic reconstructions provide us with beautiful images of the neuronal connections in the brain, many of which qualitatively appear to be valid and in-line with existing anatomical knowledge. However, the process from data acquisition to generation of a 3D map of reconstructed fibers is a multi-step procedure with numerous assumptions and uncertainties that can ultimately affect the ability of this technique to faithfully represent the true axonal connections of the brain.

The first source of error is in the inference of fiber orientation in each MRI voxel. The challenge here lies in the fact that axons have diameters in the micron range, while a typical MRI voxel can be on the order of millimeters and contain hundreds of thousands of axons, with a wide range of possible configurations. This discrepancy in spatial scales leads to uncertainty in the estimated underlying distribution of fiber orientations in a voxel, which is what we would ideally like to be able to input into the various fiber tracking algorithms. The second source of error lies in tracking a continuous fiber trajectory from discrete, voxel-by-voxel estimates of fiber orientation. The success of fiber tracking is dependent upon imaging conditions (including signal-to-noise ratio, resolution, diffusion weighting), the tracking parameters (e.g. seeding and stopping criteria), and the tracking algorithm itself [8]. Because uncertainty in either of these steps can easily lead to misleading connectivity results, it is necessary to (A) validate the ability of diffusion MRI to assess fiber orientation within each voxel and (B) to validate the ability of diffusion tractography to track fibers from voxel to voxel.

## 1.2 Outline of thesis

This thesis begins with a series of chapters that provide the background and motivation for the research chapters that follow. The focus of Chapter 2 is how MRI can be used to non-invasively probe the tissue microstructure of the brain, with a focus on a technique called diffusion MRI, or diffusion weighted imaging. The acquisition, biophysics, and modeling of diffusion MRI are explored in depth. This is followed by a review of diffusion fiber tractography. Here, we discuss the assumptions inherent in this process, existing approaches to map connectivity, and applications of in vivo fiber tractography. This chapter concludes with a brief description of classical neuroanatomy relevant to brain connectivity and fiber tractography. Chapter 3 wraps up the introductory chapters by summarizing the current state of diffusion MRI validation. This chapter begins by motivating the need for validation (specifically histological validation), followed by a literature review of validation studies and the known pitfalls and limitations of the tractography process.

The creation of a digital atlas of the squirrel monkey brain is described in Chapter 4. Non-human primates (NHPs) serve as a valuable model for validation studies of the brain. This atlas contains data from multiple monkeys, with multiple imaging modalities, and will facilitate comparisons of MRI and microscopy utilized in Chapter 6 and 7. In addition, the image registration and image processing techniques used in atlas creation are employed in Chapters 5 and 8, which use the macaque brain for validation.

Chapter 5 is the first of four research-based chapters. Before stepping directly into validation studies, we ask whether technical and hardware advancements in MRI can mitigate some of the limitations inherent in diffusion imaging techniques by increasing spatial resolution. Specifically, an (in)famous problem in the dMRI community is the “crossing fiber” problem, which describes the situation where an imaging voxel contains multiple white matter fiber populations, introducing uncertainty in the inverse problem of estimating the voxel-wise fiber geometry from the diffusion signal. Finding that this problem exists at imaging resolutions currently unachievable even on pre-clinical scanners, and will always exist in diffusion datasets, further motivates the endeavor to fully validate the methods developed to solve this problem by fully characterizing the white matter configurations in each voxel.

Chapters 6 and 7 address the first aim of the thesis, to verify the accuracy of dMRI in assessing fiber orientation information. The challenge lies in characterizing the complex distribution of neuronal fibers using histology and making direct comparisons to the dMRI orientation distribution estimates. Chapter 6 begins by describing the approaches used to extract the fiber orientation distribution from 3D confocal data of ex vivo tissue, as well as the spatial registration of dMRI data to the confocal z-stacks to facilitate comparisons of the same tissue volumes. Chapter 7 then utilizes this methodology to focus on determining how well existing diffusion models predict the histological fiber distributions. The results of this study provide quantitative measures of the reliability and limitations of dMRI reconstruction methods, identify relative advantages of competing approaches, and suggest potential strategies for improving accuracy.

The next aim is addressed in Chapter 8. Aim two of the thesis is to validate the anatomical accuracy of dMRI tractography methods, and to determine sources of error in dMRI connectivity estimates. There is growing concern in the dMRI field over an anatomically-correlated bias in tractography findings. In this chapter, we demonstrate that there is a bias for fiber tracking algorithms to terminate preferentially on gyral crowns, rather than sulcal banks. We compare tractography estimates of white matter pathways to histological measurements on a voxel-by-voxel basis in order to better understand and quantify potential sources of this bias. This work sheds light on a significant limitation of diffusion tractography and may help to prioritize development of more sophisticated or anatomically-informed methods.

To conclude, Chapter 9 presents general discussion and conclusions. This chapter summarizes the contributions to the field of diffusion MRI reported in the thesis, proposes potential future directions for this work, and discusses the implications of the present work regarding characterizing the tissue microstructure and brain macrostructure utilizing diffusion MRI.

# CHAPTER 2: DIFFUSION MRI

Conventional MRI contrasts obtained from T1, T2, and T2* relaxation processes provide indispensable insight into the molecular environment of the brain in both health and disease. However, these contrasts provide little information on the geometric microarchitecture of the brain. However, diffusion MRI, which measures the random motion of water molecules in tissues, allows non-invasive investigation of the organization of the brain, including dimensions and arrangements of neurons and other cells that make up both white and gray matter tissue. Since its introduction in the mid-1980's, dMRI has become a pillar of neuroimaging in both clinical and research domains.

Clinically, the primary application of diffusion MRI has been for early detection and characterization of cerebral ischemia. Diffusion weighted images (DWIs) clearly show a bright signal in regions under ischemic attack, easily discernable from the normal brain tissue, with a contrast not easily seen (acutely) in conventional T1 or T2-weighted images. Because of this, dMRI has become the primary modality for management of stroke patients, including selecting therapeutic approaches [9], monitoring patient progress [10], and predicting clinical outcome [10, 11]. Diffusion MRI is also being increasingly used to manage cancer patients. Water diffusion slows when tumor cellularity increases [12], with decreased diffusion associated with a high degree of malignancy [13], and high diffusion a potential predictor of poor therapeutic response [14]. In the research domain, diffusion MRI is best known for mapping the white matter fibers of the brain. As the only available technique to infer anatomical connections between brain regions in vivo, diffusion MRI has provided tremendous insight into how brain connections underlie function and opened up new investigations into cognitive neuroscience and brain dysfunction in aging, addiction, mental health disorders, and neurological disease [15]. Another branch of diffusion MRI is microstructure imaging. It aims to provide quantitative, physically and physiologically meaningful microstructural tissue parameters, with the potential to someday provide a virtual biopsy of brain tissue.

This chapter describes the physics and MRI background needed to understand the work in this thesis. The various models of diffusion in the brain are presented, with a focus on those that attempt to recover the underlying neuronal geometry or fiber orientations, as well as a recent multi-compartment model. Here, we also briefly introduce a common confound in diffusion MRI, the “crossing fiber” problem, which has spurred the development of many of these models and algorithms. Finally, the basic principles of fiber tractography are introduced and different algorithms are discussed.

## 2.1 Physics of Diffusion

Diffusion is the random translational motion of molecules driven by internal thermal energy. In 1855, Adolf Fick derived two differential equations to describe the diffusion of molecules through thin membranes [16]. According to Fick’s first law of diffusion, the number of particles that moves through a 2D plane per unit time (i.e. the flux, **J**), at a spatial position **r** and time t, is proportional to the concentration gradient $\nabla c$ according to:

$$\mathbf{J}(\mathbf{r},\mathrm{t}) = -\mathrm{D}\nabla\mathrm{c}(\mathbf{r},\mathrm{t}) \tag{1}$$

where D is the diffusion coefficient and c(**r**,t) is the concentration of particles. Combining this with conservation of mass, expressed by the equation of continuity:

$$\frac{\partial\mathrm{c}(\mathbf{r},\mathrm{t})}{\partial\mathrm{t}} = -\nabla\cdot\mathbf{J}(\mathbf{r},\mathrm{t}) \tag{2}$$

leads to Fick’s second law of diffusion:

$$\frac{\partial\mathrm{c}(\mathbf{r},\mathrm{t})}{\partial\mathrm{t}} = \mathrm{D}\nabla^2\mathrm{c}(\mathbf{r},\mathrm{t}) \tag{3}$$

Up to this point, derivations have assumed a net flux by diffusion over a concentration gradient. To describe the diffusion in the absence of internal concentration gradients, for example diffusion in pure water, it is convenient to introduce the diffusion propagator, or probability function, $P(\mathbf{r}_0|\mathbf{r},t)$, which gives the probability of a particle having moved from position $r_0$ to position r over time t. For isotropic diffusion, the propagator obeys Fick’s second law of diffusion:

$$\frac{\partial\mathrm{P}(\mathbf{r}_0|\mathbf{r},\mathrm{t})}{\partial\mathrm{t}} = \mathrm{D}\nabla^2\mathrm{P}(\mathbf{r}_0|\mathbf{r},\mathrm{t}) \tag{4}$$

Given the starting condition $P(\mathbf{r}_0|\mathbf{r},0) = \delta(\mathbf{r}_0-\mathbf{r})$, and boundary condition $P(\mathbf{r}_0|\mathbf{r},0) \rightarrow 0$ for $r \rightarrow \infty$, the solution to this equation for unbounded isotropic diffusion yields a Gaussian displacement function:

$$\mathrm{P}(\mathbf{r}_0|\mathbf{r},\mathrm{t})) = (4\pi\mathrm{Dt})^{-3/2}\exp\left[-(\mathbf{r}-\mathbf{r}_0)^2/4\mathrm{Dt}\right] \tag{5}$$

Since diffusion is a random process with displacements equally probable in all directions, the net (mean) displacement $\langle(\mathbf{r}-\mathbf{r}_0)\rangle$ is zero (here $\langle\ldots\rangle$ indicates averaging over all particles). Thus, the molecular displacement with 3D diffusion is described with the mean-squared displacement derived by Albert Einstein [17]:

$$\lambda = \langle(\mathbf{r}-\mathbf{r_0})^2\rangle = 6\mathrm{Dt} \tag{6}$$

This relationship states that the squared displacement of molecules from their starting point, averaged over all molecules in the sample, is directly proportional to the observation time, t, with the constant of proportionality being the self-diffusion coefficient, D. However, for water diffusion in biological tissue, equations (5) and (6), in general, do not hold true [18]. If diffusing water molecules encounter any barriers along their random walk, such as from cell membranes and macromolecules, the mean squared displacement will be lower than that of free water. If Einstein's equation were applied to calculate the diffusion coefficient, it would be lower than expected. Thus, diffusion may act as a sensitive probe for tissue microstructure.

## 2.2 Diffusion MRI

Early in the history of NMR it was recognized that the signal is influenced by spin diffusion in the presence of magnetic field gradients (for a full review of the history of Diffusion MRI, see Addendum 1). In the classic 1950 paper on spin-echoes, Hahn [19] outlined the measurement of diffusion in the presence of a constant background gradient, which was subsequently modified and further developed by Carr and Purcell in 1954 [20], who deliberately sensitized the MR signal to diffusion. The mathematical formalism describing the effects of diffusion in the presence of time varying magnetic field gradients was outlined by Torrey [21], who adapted the Bloch equations to account for diffusion. The Bloch-Torrey equation is:

$$\frac{\partial\mathbf{M}}{\partial\mathrm{t}} = \gamma\mathbf{M}\times\mathbf{B} - \frac{\mathbf{M}_\mathrm{x}\hat{\mathrm{x}} + \mathbf{M}_\mathrm{y}\hat{\mathrm{y}}}{\mathrm{T}_2} - \frac{(\mathbf{M}_\mathrm{z}-\mathbf{M}_0)\hat{\mathrm{z}}}{\mathrm{T}_1} + \nabla\cdot\mathbf{D}\nabla\mathbf{M} \tag{7}$$

where the macroscopic magnetization **M** is the vector sum of $M_x$, $M_y$, and $M_z$, along the unit axes $\hat{x}$, $\hat{y}$, and $\hat{z}$, respectively. The first three terms on the right-hand side are the classic Bloch equations, while the last term describes diffusion, and shows similarities to Fick's second law of diffusion from equation (3). The Bloch-Torrey equation has the solution for transverse magnetization, $\mathbf{M}_{xy}$:

$$\mathbf{M}_{\mathrm{xy}} = \mathbf{M}_0 \mathrm{e}^{-\frac{\mathrm{t}}{\mathrm{T}_2}} \mathrm{e}^{-\mathrm{bD}} \tag{8}$$

where $\mathbf{M}_0$ is the magnetization after excitation, and *b* defines the so-called “b-value” that describes the diffusion-weighting, or sensitivity, introduced by the magnetic field gradients:

$$\mathrm{b} = \gamma^2 \int_0^{TE} \left( \int_0^t G(t')dt' \right)^2 dt \tag{9}$$

The diffusion pulse sequence most widely used today is the pulsed gradient spin echo (PGSE) proposed by Stejskal and Tanner in 1965 [22].

### 2.2.1 The Pulsed Gradient Spin Echo

As previously described, diffusion measurements in an MRI experiment rely on the principle of signal loss through diffusion dependent phase dispersal. Strong magnetic field gradients can be applied to enhance diffusion sensitivity. In the PGSE sequence (Figure 2.1), the standard spin echo sequence is complemented with two diffusion gradient pulses, with strength **G** and duration $\delta$, on either side of the refocusing pulse. After excitation, the first gradient pulse imposes a phase on protons, $\phi_1$, that varies with spatial location in the direction in which the gradient is applied ($\phi_1 = \gamma \mathrm{r} \mathbf{G} \delta$). The refocusing pulse then reverses spin phase. A second gradient pulse of equal duration and amplitude, applied following a delay (the diffusion time, $\Delta$), induces a position dependent phase $\phi_2$. If all spins are stationary, $\phi_1 = \phi_2$, and at the time of data acquisition all spins have zero phase. However, if protons diffuse through the tissue, changing spatial position during the delay, $\Delta$, the phase induced by the second magnetic field gradient no longer cancels the phase induced by the first. Therefore, application of gradients in the presence of diffusion leads to phase dispersal across the sample, resulting in signal loss. The difference in phase is proportional to the distance the proton has moved in the direction of the diffusion gradient. This relation is only strictly valid if the pulse duration is short compared to the gradient separation, $\delta \ll \Delta$, an assumption known as the narrow pulse approximation.

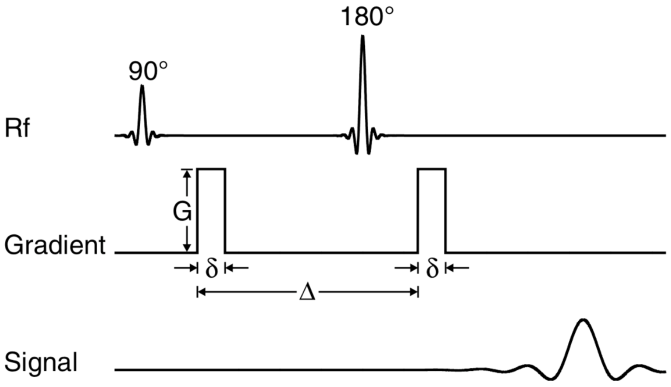

Figure 2.1: Pulsed Gradient Spin Echo Sequence. Spins are excited by a 90-degree pulse, refocused by a 180-degree pulse, resulting in a spin echo. Diffusion weighting gradients are applied on both sides of the 180-degre pulse, with amplitude G, duration δ, and separated by diffusion time Δ.

While the exact functional form the for diffusion dependent signal loss is given below, it is straightforward to see that the function will be dependent on the diffusion coefficient (D), the area of the magnetic field gradient (i.e. the amplitude and duration), as well as the separation between magnetic field gradients. For example, increasing the diffusion time allows more time for protons to diffuse and an increased mean square displacement. As the spins move farther in the direction of the gradient, the dephasing of the system will be larger, and more signal loss will occur. Specifically, for a PGSE sequence, the diffusion weighting imposed by the gradient pulses is determined by the gradient amplitude (**G**), duration (δ), and separation (Δ), with a b-value given by:

$$\mathrm{b} = \gamma^2\delta^2\boldsymbol{G}^2(\Delta - \frac{\delta}{3}) \tag{10}$$

The diffusion weighted MR signal is then related to the diffusion coefficient D and the b-value by:

$$\mathrm{S} = S_0 e^{-bD} \tag{11}$$

where $S_0$ is the signal in the absence of diffusion gradient pulses. The PGSE sequence has been used extensively in the diffusion MRI community to probe diffusivity in a particular direction, and is the diffusion weighting module employed in all chapters of this thesis.

### 2.2.2 Q-space Imaging

Previously, the diffusion propagator was introduced in Equation 5 as a general description of the probability of proton displacements as a function of diffusion time. In effect, the PGSE experiment allows us to sample the voxel-wise diffusion propagator after a given diffusion time, and the b-value is derived as a convenient way to express the MR signal as a simple exponential decay in the presence of Gaussian diffusion. As described below, protons can be highly hindered, or even restricted, in different tissue compartments, causing deviations from Gaussian diffusion. As an alternative, it may be convenient to describe the “diffusion weighting” of the experiment using the “q-space” formalism [23]. If the diffusion gradient pulse is short (again, the narrow pulse approximation), the MR signal can be related to the diffusion propagator by the Fourier relation:

$$\frac{\mathrm{S}(\mathbf{q})}{S_0} = \int p(\boldsymbol{r}, \Delta) e^{i\boldsymbol{qr}} d\boldsymbol{r} \tag{12}$$

with the wave-vector, or q-vector

$$\mathbf{q} = \frac{\gamma\delta\boldsymbol{G}}{2\pi} \tag{13}$$

where the displacement vector, **r**, forms a Fourier pair with the wave-vector for a fixed diffusion time. In a direct analogy to MRI “k-space” sampling during MR measurements - which describes the Fourier transform of the MR image - the voxel-wise sampling of 3D proton displacements is described by parameter **q**, in “q-space”. Note that the b-value is directly proportional to the square of the q-value.

It is feasible to sample a Cartesian grid in q-space, and perform a simple Fourier transform of the data to calculate the diffusion propagator. This technique has been termed Diffusion Spectrum Imaging (DSI) [24]. The range of q-space sampled determines the resolution at which the diffusion propagator can be reconstructed. This means that for characterizing small displacements, or small diffusion restrictions, high q-values (and consequently high b-values) are required. In addition to capturing smaller displacements, higher diffusion weightings (i.e. higher b-values) lead to larger deviations from Gaussian behavior, and can be advantageous to improve angular contrast, for example accentuating directions of maximum diffusivity which can be used to broadly reflect the orientation of axons in a voxel (see Section 2.3 Biophysics of Diffusion in the Brain). The density of q-space sampling ($1/\Delta\mathbf{q}$) then determines the field of view of diffusion displacements, or the range of displacement distances included in the measurements.

### 2.2.3 High Angular Resolution Diffusion Imaging

Although the DSI q-space acquisition provides the most complete characterization of diffusion in each MR voxel, the large number of DWIs required (often >500) leads to long scan times, making it impractical for routine use. Further, the large q-values required can only be achieved using long echo times, resulting in compromises in SNR and image resolution. For these reasons, a majority of the methods proposed to characterize brain tissue geometry (particularly those that estimate the orientation distribution of fibers in a voxel for subsequent tractography) are designed to operate using a sparser acquisition strategy. For example, it is common to acquire a large number of DWIs at only a single $|\vec{q}|$-value (or b-value), acquiring a single spherical “shell” in q-space, in a strategy often referred to as a High Angular Resolution Diffusion Imaging (HARDI) acquisition. Although HARDI acquisitions provide little information about the radial distribution of displacements, **r**, they do provide a concise characterization of the angular dependence of the diffusion signal over a sphere, which is critical for resolving the geometric orientation of white matter in a voxel. The advantage of this approach is the reduced acquisition times, since q-space coverage is reduced from a 3D volume to a 2D spherical shell in q-space.

A major focus of this thesis is on models and techniques that utilize single-shell HARDI spherical acquisition strategies which have become common in both research and clinical domains. Specifically, we validate the ability of different methods to both assess fiber orientation information and to accurately reflect the white matter anatomy using fiber tractography. A full description of many of the validated models and techniques is given in Section 2.4 Models of Diffusion in the Brain, in addition to a brief description of the “crossing fiber problem”, which has provided motivation for development and advancement of diffusion MRI acquisition and reconstruction strategies.

## 2.3 Biophysics of Diffusion in the Brain

The self-diffusion coefficient of free water is around $3.0 \times 10^{-9}$ $m^2/s$ at 37° C [25]. Using Einstein's equation (Equation 6), this translates to a mean squared displacement of 17um during 50 milliseconds. Einstein's equation assumes a "free" diffusion, much like an ink drop diffusing through a large glass of water, where the distribution of molecular displacements obeys a Gaussian law. In biological tissue of the brain, however, diffusion is not free but is hindered by physical barriers such as cell membranes, fibers, or macromolecules, causing the molecular displacements to deviate from a Gaussian distribution. Consequently, the diffusion coefficient derived from DWIs is no longer the free diffusion coefficient of water, but an *apparent* diffusion coefficient (ADC). The actual diffusion distance is reduced to a few micrometers, a fortuitous scale that is perfectly suited to explore brain tissue structure, where axons are typically on the order of ~1um and cell bodies on the order of ~1-100um.

The brain parenchyma relevant to diffusion MRI can roughly be divided into extracellular and intracellular space. The extracellular space accounts for approximately 20% of the volume fraction of the parenchyma. Macromolecules of the extracellular matrix hinder diffusion of the interstitial fluid. In combination with the tortuous geometry of cellular barriers, the diffusion in this continuous space is typically considered "hindered" diffusion [26] – lower than free diffusion, but reasonably approximated by a Gaussian diffusion propagator (Figure 2.2, left). In contrast, the remaining 80% of the volume occupied by cells, the intracellular space, is often said to be "restricted". In addition to diffusion hindrance due to cytoskeletal filaments and intracellular organelles [27], cellular membranes act as impermeable barriers (on typical time scales of diffusion MRI experiments), confining protons within the cell and limiting displacements to the size of the cell's dimensions. There is significant interest in characterizing these restrictions to investigate the size and geometry of these compartments.

A remarkable feature of diffusion in brain tissue is that the distance a molecule diffuses in one direction in space may or may not be the same as in other directions. In a sample with no hindrances to diffusion, or where barriers are not coherently oriented, diffusion is the same in all directions and is termed *isotropic* diffusion. However, if diffusion depends on direction, for example due to an orientational preference of barriers, it is termed *anisotropic* diffusion. It was recognized early on that diffusion in brain white matter is anisotropic [28]. This was hypothesized to be caused by the fact that neurons are elongated cylindrical processes typically structured into organized bundles or sheets. Researchers found that diffusion was typically fast in the direction of these neuronal "fibers", and slower perpendicular to them (Figure 2.2, right), influenced largely by hindrance of diffusion by the myelin sheath and axon membranes [18]. After this discovery, it was soon suggested that this feature of diffusion directional specificity could be used to determine and map the orientation of white matter fibers in the brain, assuming that the direction of the fibers was parallel to the direction with the fastest diffusion. Mapping and modeling the geometric fiber configurations in each voxel from a set of diffusion measurements has become a major goal of the diffusion MRI community.

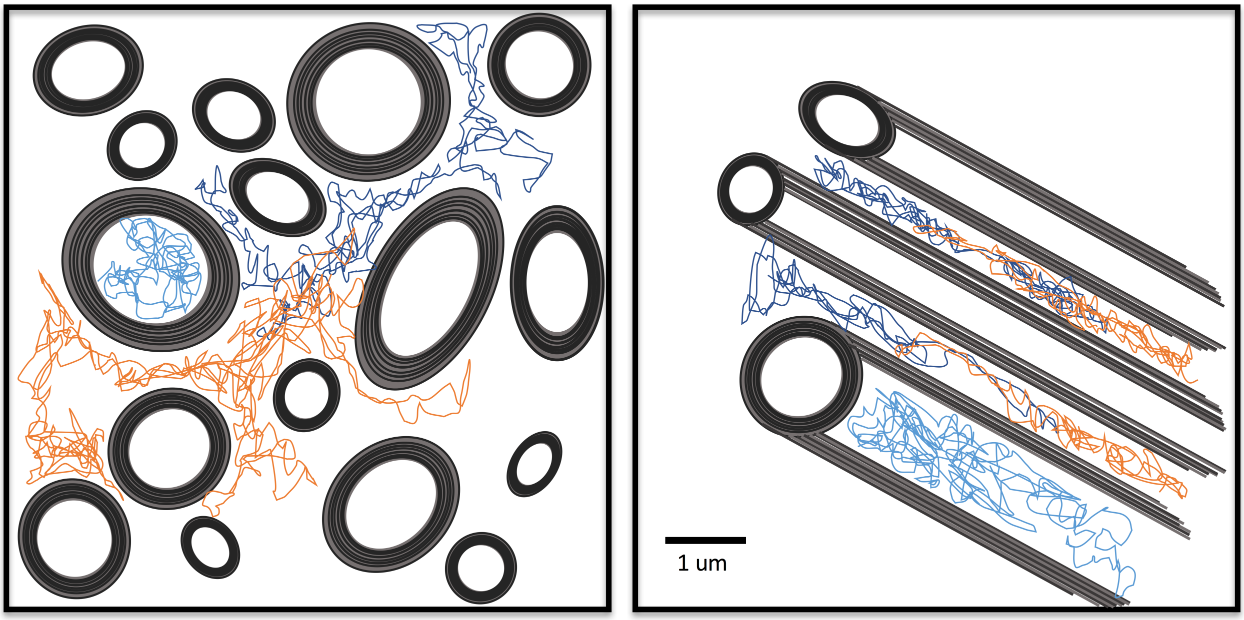

Figure 2.2 Diffusion in the Brain. Cartoon representation of myelinated axons with displacement trajectories of three protons shown in intracellular and extracellular space (left) and anisotropic diffusion along axons (right).

## 2.4 Models of Diffusion in the Brain

As previously described, the PGSE experiment can be used to probe diffusivity in a particular direction. In many applications, it is beneficial to be able to obtain a full characterization of the diffusion processes via the diffusion propagator, from which measures of restriction, compartment volume fractions, and diffusivities can be inferred. When investigating structural connectivity via diffusion fiber tractography, the features of interest that we would like to obtain are the orientations of neuronal fibers in each voxel. Thus, many

HARDI techniques use the PGSE experiment to sample the diffusion propagator in multiple directions, with the aim of relating diffusion measurements to orientation features of the propagator, or directly to biophysical features of the brain tissue itself. Towards this end, a number of algorithms have been developed to estimate fiber orientations. In this chapter, a number of the algorithms implemented in this thesis are classified according to how they encode fiber orientation information.

Many q-space methods aim to provide an estimate of a spherical function called the diffusion orientation distribution function (dODF). The dODF is the radial integration of the diffusion propagator:

$$\mathrm{ODF}(\hat{\boldsymbol{x}}) = \int_0^\infty P(r, \hat{\boldsymbol{x}}) f(r) dr \tag{14}$$

where $\hat{\boldsymbol{x}}$ is a unit vector in the direction of **x**, r is the radial distance from the origin, and the function *f* weights the contribution to the integration along different radii. The dODF then reflects the relative number of spins that have diffused in a given direction, **x**. One can look for peaks, or local maxima, of the dODF over a sphere, which represent the directions of maximum diffusion. Fiber orientations are then typically assumed to coincide with these discrete peaks in the ODF, and tractography can be performed using these orientations [29].

While the dODF characterizes features of the diffusion process itself, it may be more relevant to directly estimate the fraction of fibers in each voxel that point in each direction. This object is referred to as the fiber orientation distribution (FOD), and is ideally what we would like use as input to fiber tractography algorithms. A large class of methods estimate this function directly, and have theoretical advantages over functions based on features of the propagator (for example the ODF) which may reflect the FOD only in an obscure way. Both the FOD and ODF are functions defined over a sphere, and are commonly used as input to subsequent tractography algorithms.

In this section, we give a brief description of the reconstruction methods implemented in this study. Again, the focus is on those that attempt to describe the underlying geometry of neuronal fibers, whether by the ODF, FOD, or some other function which parameterizes orientation features. Because of the large number of these techniques proposed in the literature, the assessment presented in this work is not exhaustive, yet comprises some of the more commonly implemented reconstruction techniques.

### 2.4.1 Diffusion Tensor

Diffusion Tensor Imaging (DTI) [30, 31] was one of the first and certainly remains the most commonly implemented of the algorithms to model anisotropic diffusion. DTI models the diffusion propagator as a zero-mean Gaussian distribution in three dimensions using a rank-2 symmetric positive definite tensor (or matrix) **D**:

$$\mathbf{D} = \begin{bmatrix} D_{xx} & D_{xy} & D_{xz} \\ D_{xy} & D_{yy} & D_{yz} \\ D_{xz} & D_{yz} & D_{zz} \end{bmatrix} \tag{15}$$

which replaces the 1D diffusion coefficient D in Equation 11 as:

$$\mathrm{S} = S_0 e^{-\boldsymbol{b}:\boldsymbol{D}} \tag{16}$$

and can be rewritten as

$$\ln\left(\frac{S}{S_0}\right) = -\sum_{i=1}^{3}\sum_{i=1}^{3} b_{ij} D_{ij} \tag{17}$$

where $b_{ij}$ are the components of the b-matrix (which can be calculated based on Equation 9), and $D_{ij}$ are the components of the tensor. The diagonal elements ($D_{ii} > 0$) are the displacement variances along the scanner's x, y and z axes, and the off-diagonal elements are the covariance terms and are symmetric about the diagonal ($D_{ij} = D_{ji}$). Diagonalization of the diffusion tensor yields the eigenvalues ($\lambda_1$, $\lambda$, $\lambda_3$) and corresponding eigenvectors ($\boldsymbol{v}_1$, $\boldsymbol{v}_2$, $\boldsymbol{v}_3$), which describe the directions and apparent diffusivities along the axes of principal diffusion. The diffusion tensor may be visualized using an ellipsoid with the eigenvectors defining the directions of the principal axes and the lengths of the semi-major axes defined by the eigenvalues (Figure 2.3, A).

From the tensor, measures of ellipsoid size and shape can be calculated which allows a geometric representation of the apparent diffusion in 3 dimensions. The most commonly implemented metrics of the tensor are the mean diffusivity (MD), defined as the mean of the eigenvalues, and the fractional anisotropy (FA), a dimensionless value that ranges from 0 to 1 and describes the anisotropy of the DTI ellipsoid (0 for perfectly isotropic and 1 for purely one-dimensional diffusion). These metrics have become invaluable as biomarkers for tissue states. The MD is sensitive to the overall density of structural boundaries. This makes MD an excellent biomarker for pathologies that affect membrane spacing, such as edema, necrosis, and overall cellularity. Major applications of MD are in evaluating stroke and tumor cellularity. The FA has historically been interpreted (and often misinterpreted [32]) as a measure of axonal integrity. FA is highly sensitive to microstructural changes including fiber density, fiber diameter, myelination, and fiber geometries, however FA lacks specificity for the sources of anisotropy.

DTI also provides orientation information given by the principal axis of the tensor, $\mathbf{v}_1$. It was proposed that in ordered tissue, the eigenvector associated with the largest eigenvalue within a voxel lies parallel to the local fiber direction [31]. This became the basis of several of the earliest strategies for fiber tractography. Due to its overwhelming popularity, many flavors of tractography today are still referred to as DTI tractography, even if DTI is not the technique used to model diffusion processes. Although limitations and pitfalls of DTI are well known (see section 2.4.2 The Crossing Fiber Problem), the tensor is included in this manuscript due to its prevalence in the imaging community, and as a baseline from which more advanced models can be compared.

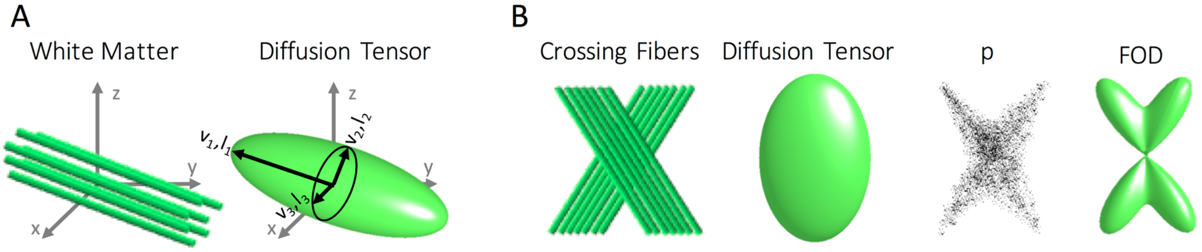

Figure 2.3 Axon configurations and the estimated diffusion tensor. The tensor model provides adequate characterization of fiber orientations when only a single fiber bundle is present within a voxel (A), but may fail to properly reflect the true fiber geometry in crossing fiber regions (B). Here, alternative modeling of the diffusion propagator, or direct estimation of the FOD, may better reflect axonal geometries.

### 2.4.2 The Crossing Fiber Problem

Although DTI has proven to be extremely useful in both mapping microstructural properties and mapping structural connectivity, this model is inadequate in voxels that contain complex fiber configurations, an issue known as the “crossing fiber problem”. This problem typically refers to the situation where there are two or more differently oriented white matter bundles in the same MR voxel, with both fibers contributing to the diffusion MRI signal, in effect causing a partial volume effect. In general, this partial volume effect occurs anytime axons within a voxel do not all run parallel to each other, including not only crossing, but also bending, fanning, and so-called “kissing” geometries. Because DTI allows an estimate of only a single fiber direction per voxel, in these situations DTI can lead to incorrect estimates of fiber orientation, for example showing a single peak *in between* the actual fiber directions (Figure 2.3, B). These crossing fiber regions have been shown not only to lead to ambiguous microstructural indices, for example FA, but also to result in anatomically inaccurate tractography [33, 34]. Ideally, the scatter pattern of molecules (i.e., the propagator), or some estimate of the FOD itself, should allow a proper characterization of the fiber geometry in each voxel (Figure 2.3, B). Because of this, a large number of methods have been introduced to resolve crossing fibers for tractography, most often based on some feature of the propagator (i.e., the ODF) or a direct estimate of the FOD from the diffusion signal. The following section lists the diffusion reconstruction methods relevant in this dissertation, as well as a very brief description of each.

### 2.4.3 HARDI models

Diffusion Spectrum Imaging (DSI): DSI uses the q-space imaging method described above (Section 2.2.2 Q-space Imaging) to obtain the diffusion propagator by acquiring data on a rectilinear grid in q-space [24] and performing a Fourier transform of the data. The dODF is then calculated as the radial projection of the propagator as in Equation 14.

Q-ball Imaging, with regularization (QBIr): QBIr samples measurements only on a single shell in q-space (single b-value) - as do all the following HARDI models. Because a Fourier transform is no longer possible, QBI approximates the dODF using the Funk Radon transform of the diffusion attenuation on a shell in q-space [35]. A Radon transform finds the projection of an object over a number of angles. The Funk-Radon transform is the spherical analogue of the Radon transform, where each radial projection is obtained by integrating the signal over the equator that is normal to the projection. QBIr was one of the first methods proposed to resolve crossing fibers, and uses $f(\alpha)=1$ from Equation 14. Finally, QBIr incorporates Laplace-Beltrami regularization when solving for the “Q-ball” in order to better denoise the dODF [36].

Q-ball Imaging, constant solid angle (QBIcsa): While related to QBIr, this function computes the mathematically correct formulation of the marginal probability of diffusion in a given direction (i.e. the dODF) by increasing the weighting of high-frequency information with a quadratic weighting function $f(\alpha)=\alpha^2$, compared to the linear formulation of QBIr [37]. This function generally provides sharper peaks than QBIr.

Diffusion Orientation Transform (DOT): Using a slightly different function over a sphere, DOT approximates a single contour of the diffusion propagator at a fixed displacement radius [38]. This function differs slightly from the dODF in that it is not a radial projection of the propagator (i.e., the sum of all contours), but is still a function of the propagator.

Diffusion orientation transform, revisited (DOTr1): DOTr1 uses the DOT formalism and a linear first-order radial projection ($f(\alpha)=\alpha$), of the diffusion propagator to estimate the ODF [39].

Persistent Angular Structure (PAS): Using another function on the unit sphere, PAS MRI attempts to capture the angular structure of the diffusion propagator that persists over the most important range of diffusion displacements, and it is intended to reflect the angular structure of the FOD [40]. Thus, it is intended to have much sharper peaks in regions of crossing fibers.

Spherical Deconvolution: Spherical deconvolution is based on the assumption that the diffusion signal from a single voxel can be modelled as a convolution between the FOD and the fiber response function that describes the signal profile due to a single coherently oriented fiber population [41-43], thus this method estimates the physical FOD directly. The key idea here is to consider the set of diffusion-weighted signal attenuation measurements as the sum of measurements we would get from a fiber population with each orientation weighted by the fraction of fibers in that orientation. Mathematically, the signal $S(\theta,\varphi)$ is then a convolution of the response function for a single fiber population, $R(\theta)$, with the FOD:

$$S(\theta, \varphi) = F(\theta, \varphi) \otimes R(\theta) \tag{18}$$

The fraction of fibers aligned in each direction (i.e. the FOD) can then be obtained by a deconvolution of $R(\theta)$ from $S(\theta,\varphi)$. The fiber response function, R, is typically estimated from the data by considering only voxels with the highest anisotropy as in [43], which should contain only single fiber voxels. Alternatively, the response function can be modelled as a diffusion tensor with fixed eigenvalues [41]. Often, both the signal and the fiber response function are represented as spherical harmonic (SH) coefficients, a set of orthogonal functions used to represent functions defined on the surface of the sphere (just as sines and cosines are used to represents functions on a circle via the Fourier Series). In this way, the deconvolution turns into a simple matrix inversion that yields the FOD, also represented as SH coefficients (note that all functions of a sphere in this manuscript are represented as SH series, including the output to all HARDI methods described).

Because this inversion is ill-posed, filtering and regularization are necessary to prevent spurious results. Thus, we implement two variations of spherical deconvolution. First, constrained spherical deconvolution, with Richardson-Lucy regularization (CSDlrd) utilizes a damped Richardson-Lucy algorithm to condition the inverse problem [44]. Second, super-resolved constrained spherical deconvolution (sCSD) implements a non-negativity constraint on an iterative deconvolution process, which allows an FOD estimate that preserves angular resolution while remaining robust to noise [45].

### 2.4.4 Biophysical models

Rather than extracting orientation information only, it is often desirable to relate the diffusion process to specific features of the microstructural environment. Biophysical models aim to describe this environment by separating the tissue of interest into multiple compartments, each affecting the diffusion signal in a different way. Two compartments most commonly included in most models are the intracellular and extracellular spaces. For example, the first multi-compartment model was introduced in 1995 by Szafer et al. [46, 47] and modeled intracellular and extracellular diffusion coefficients in a periodic array of boxes (cells) surrounded by partially permeable membranes. Today, white matter is often modelled as stacks of cylinders, with the space inside and outside the cylinders representing intra- and extra-axonal compartments. Various other geometries have been employed in the literature, ranging from sticks, balls, zeppelins, dots, and astrosticks - all designed to capture diffusion in various compartments that may exist in the brain. From these, geometrical parameters in the model can be varied to include measures of axon diameters, fiber densities, and myelin thickness, among others [48-53].

The model most relevant to this dissertation is the neurite orientation dispersion and density imaging (NODDI) method, proposed by Zhang et al. [54]. NODDI models intra-cellular, extra-cellular, and CSF components as sticks, an anisotropic tensor, and an isotropic compartment, respectively. The intracellular volume fraction provides information on axon and dendrite density, while the sticks provide orientation information. One particularly interesting feature of the intracellular compartment is that it models the dispersion in orientations of the sticks, capturing an orientation dispersion index (ODI) that describes the overall dispersion, or spread, of the underlying FOD. The ODI has several promising applications, including quantifying bending and fanning of axons potentially providing informative priors for mapping connectivity, as well as the ability to identify crossing fiber regions. In gray matter, the index can quantify the pattern of sprawling dendritic processes, which may be a marker for gray matter complexity or integrity. To date, there has been no histological validation of the estimated orientation dispersion in the brain using this model. Because this index may provide specificity towards different fiber configurations, fiber complexities, and potentially different pathologies, validation of the ability to model dispersion using NODDI is an important step towards its implementation as a useful biomedical tool.

## 2.5 Tractography

The connections between brain regions are mainly contained within the brains white matter, which is composed of myelinated bundles of axons. These connections form the substrate for information transfer between brain regions, and are central to our understanding of brain structure and function in both the normal and diseased brain. Until recently, studying connectivity was limited to anatomical dissection techniques in cadavers and invasive chemical tracer studies in animals. However, the axonal orientation information provided by diffusion MRI may be used to reconstruct estimates of white matter pathways in the living brain non-invasively. The methods for doing this are called white matter *fiber tractography*. The non-invasive nature of fiber tractography techniques, as well as ease of measurements, makes diffusion tractography potentially valuable in both basic neuroscience and clinical research.

The two main components of any tractography process are (1) discrete, voxel-wise measures of fiber orientation, and (2) an algorithm to reconstruct continuous pathways (fiber tracts) from these discrete measurements. Regarding component (1), all tractography techniques rely on the assumption that the diffusion of water molecules will be hindered to a greater extent across axons than along them. This assumption is investigated in detail in Aim 1 of this thesis, and methods to extract measurements of fiber orientation are described in Section 2.4.3 HARDI models. The strategies employed to find continuous paths through the data field vary greatly from algorithm to algorithm. Here, we describe the basic principles of two broad classes of algorithms designed to approximate continuous white matter pathways: deterministic tractography and probabilistic tractography.

### 2.5.1 Deterministic Tractography

A streamline through a vector field is any curve whose tangent is always parallel to the vector field. Making these streamlines is an intuitive method for performing tractography – by starting at a *seed* point and following the local vector information step-by-step, a representation of a white matter pathway is created by effectively “joining the arrows”. If these orientations are discrete estimates of the underlying fiber orientations (for example the primary eigenvector of the diffusion tensor, or a “peak” of the FOD), this creation of 3D streamlines is considered *deterministic* tractography (Figure 2.4, top).

The first attempt at tractography was a deterministic method introduced in 1999 by Mori et al. [55]. This method, called Fiber Assignment by Continuous Tracking (FACT) simply followed the primary eigenvector of the diffusion tensor over the entire voxel. This basic tracking still serves as the framework for all present-day deterministic algorithms, with only minor variations in streamline propagation. For example, interpolation can be performed between voxels in order to estimate the local path direction (i.e. a Runge-Kutta or Euler integration [56]rather than nearest neighbor interpolation of FACT). In addition, neighboring information can be used in combination with the direction of the incoming streamline to make informed decisions when tracking through areas associated with low anisotropy [57]. With the realization that DTI cannot adequately represent crossing fibers (see Section 2.4.2 The Crossing Fiber Problem), many deterministic algorithms were tailored towards use with HARDI models by allowing more than one fiber orientation per voxel. The peaks from any ODF or FOD can be used as inputs to these algorithms, with streamline propagation typically following the peak that is closest to the incoming tracking direction. The use of HARDI models has been shown to be able to track through crossing fiber regions [29, 58], and reduce both false positive and false negative connections.

Two critical criteria that significantly affect the resulting tractography are where to start and terminate streamlines. It is important to stop streamline propagation when tracts either leave the region of interest, or become unreliable. Often, one wants to track only white matter, thus stopping should occur in gray matter. Because FA is low in gray matter, it is convenient to stop when entering a region of low FA. This has the added benefit of stopping when the estimate of the major eigenvector has a large variance, meaning it is less well defined. Further, assuming that most pathways do not bend sharply in the brain, most algorithms will stop tracking when the trajectory bends more than a prescribed angle over a certain distance in order to avoid back-tracking and jumping to a crossing fiber.

Tractography is initiated at so-called seed points. There are two main strategies for seed placement. The traditional approach is to select a voxel or region of voxels (a region of interest) where tractograms will be initiated. A second approach is to select seeds over the entire brain, termed “whole brain seeding”. In both cases, multiple seeds can be placed in a voxel with sub-voxel locations to generate multiple tract solutions (because with deterministic tractography, the same seed will always result in the same tract given a certain algorithm). Whole-brain seeding generates nearly all possible pathways, while regional seeds are often used when trying to extract a specific pathway or mapping tracts from a specific region.

After tractograms have been generated, regional constraints are often imposed to extract pathways that meet specific criteria. Most often, rules based on Boolean logic are developed in order to select specific pathways using inclusive waypoints, or in order to minimize unintended tracts using exclusive waypoints. This use of prior anatomical knowledge of white matter trajectories to apply region of interest constraints parallels the fiber dissection approaches taken by early anatomists to segment white matter into functionally distinct pathways. Thus, these approaches are often referred to as *in vivo* dissection. Streamlines are often rendered as lines, or tubes, for visualization (Figure 2.4, top).

### 2.5.2 Probabilistic Tractography

The data and modeling that tractography rely on are subject to errors, and these errors propagate through the tractography process, potentially leading to erroneous connectivity estimates. While deterministic tractography generates tracks through the data on the basis of a best estimate of the underlying fiber orientation, a different set of techniques, known as *probabilistic tractography*, takes into account sources of uncertainty in these orientation estimates in order to provide an indication of the probability that a particular voxel in the brain is connected to another given the diffusion data. Probabilistic tractography gives an assessment of confidence with which a connection can be observed, and aims to allow the researcher to make the statement: “with these data, and a given reconstruction model, I have X% confidence that the path of least hindrance to diffusion from seed point A passes through region B.” To do this, a streamline experiment is repeated many times while incorporating the uncertainty associated with the fiber orientation estimate into the propagation procedure (Figure 2.4, bottom). The connection “probability” for a given voxel is obtained by counting the number of streamlines that traverse that voxel.

The key step in any probabilistic tractography technique is to build a function that characterizes the uncertainty in the fiber orientation estimates. As an intuitive example, instead of selecting the peak of the FOD, a random sample can be drawn from the orientation distribution in order to select the tracking direction for the next step of the tracking process. Thus, at any point on the trajectory, a different direction is likely to be taken for every repetition of the tracking process. Over many repetitions, the pathways visited most often will have a higher probability index, often visualized as a hot-cold colormap (Figure 2.4, bottom). Other approaches to characterizing uncertainty include bootstrapping from multiple repetitions or multiple combinations of the data [59, 60], or Bayesian approaches [61, 62] to infer uncertainties from the given parametric model.

When compared to deterministic methods, probabilistic tractography offers the benefit of an assessment of confidence in the observed connections. This allows researchers to make judgements on the reliability of their observations, as well as confidence in the existence of tracks existing in the data. A second benefit is that these methods may be better able to cope with axonal branching and crossing patterns, rather than following a single orientation throughout a voxel. However, these connection indices are still not a true quantitative assessment of anatomical connectivity, but rather the probability of a connection through the diffusion data based on the chosen model of the diffusion signal and on the assumptions of the tracking process itself.

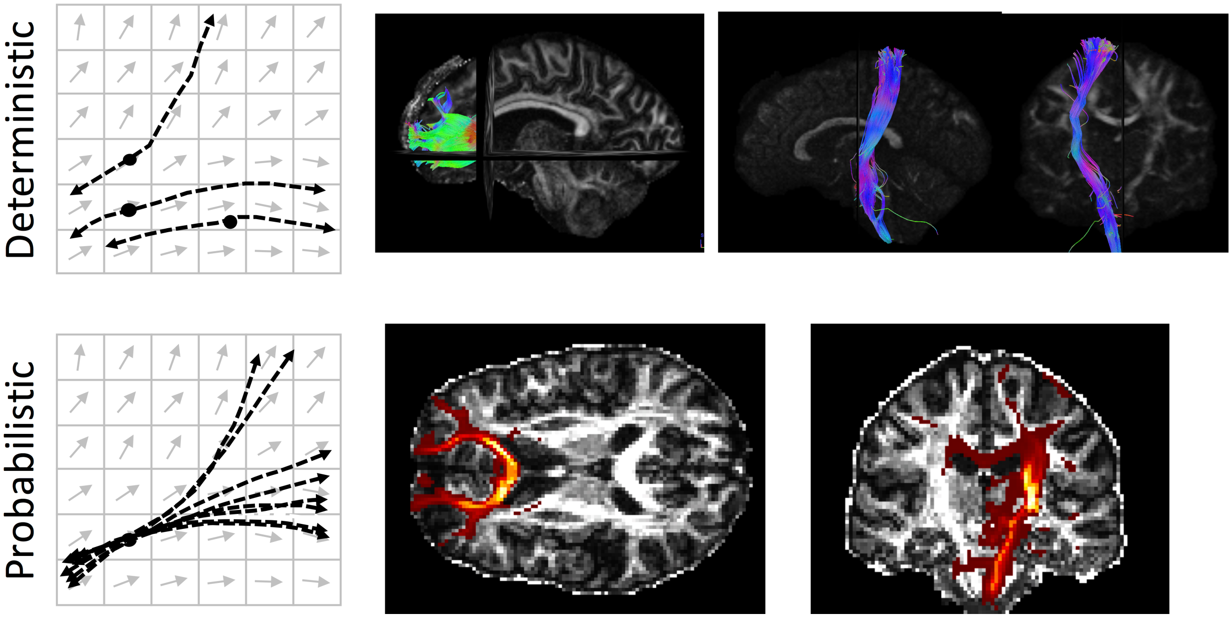

Figure 2.4 Deterministic and probabilistic Tractography. Streamlines for deterministic (top) and probabilistic (bottom) tractography are shown schematically, along with in vivo tracking of the frontal projections of the corpus callosum (forceps minor) and the corticospinal tract.

### 2.5.3 Applications of Tractography

Since its introduction in 1999 [55], diffusion fiber tractography has become an extremely useful tool to study the central nervous system, with a wide range of applications in both clinical and basic neuroscience. Most analysis of MR-tractography can typically be classified into three main techniques. First, tractography can be used to segment white matter into specific pathways in order to examine some quantitative imaging measure along the course of the selected pathway, for example a comparison of a specific pathway in healthy and diseased subjects. Second, tractography has been used to identify new white matter pathways, or characterize the presence, absence, or changes in specific tracts. Third, tractography has been used to gain insights into normal brain anatomy, which adds to our understanding of structural connectivity and the consequences of localized pathologies, and can guide interventions.

The first application of fiber tractography is to improve models of normal human white matter anatomy. Understanding the patterns of cognitive, motor, and sensory impairments resulting from brain damage depends on good models of functional and structural anatomy. For example, much is known about the anatomy of the language network from animal studies. The anatomy of this network has been extrapolated from animals to in vivo humans and has been a subject of a number of tractography studies that localize pathways involving Broca's and Wernicke's areas in healthy human brains [63, 64]. Understanding the basic language processing routes provides a framework for understanding deficits that may arise from white matter damage to these areas. Recently, there has been a large effort to map the human "connectome", a comprehensive map of the neural connections of the brain [65, 66]. Studying the brain as a network, rather than individual white matter structures could shed light on relationships between structural and functional connectivity, and aid in deciphering the networks that generate cognition, emotion, and behavior.

Tractography has also been applied to segmentation of the brain into functionally and structurally distinct subareas, for example, segmenting the thalamus according to its cortical connectivity [67, 68]. Likewise, segmentation of gray matter regions may be defined based on patterns, an example being defining the functional boundary between supplemental and pre-supplemental motor cortex of the medial frontal cortex [69].

A number of developmental brain disorders and abnormalities have been described using tractography. Tractography has demonstrated incomplete development of tracts in disorders such as lissencephaly [70], or smaller/absent white matter pathways in holoprosencephalies [71, 72]. DTI tractography has demonstrated both widespread as well as tract specific changes in anisotropy and diffusivities in premature newborns, and allows monitoring and assessment of development during the first few months of life [73, 74].

Mild decreases in anisotropy have been observed in healthy subjects as a result of aging. However, tractography has shown additional changes in patients with several types of neurodegenerative diseases and dementia. A common theme with these diseases is a decreased anisotropy (and often an increased diffusivity) in one or more pathways identified using tractography. For example, patients with Parkinson disease show decreased anisotropy in the substantia nigra [75], while the corpus callosum (in addition to frontal, temporal, and parietal white matter pathways) demonstrated decreased anisotropy in both Huntington's [76] and Alzheimer's disease [77, 78]. The disruption of these callosal pathways has been correlated to disturbances of motor or cognitive processing that characterize these diseases. Finally, decreased anisotropy in the corticospinal tract in amyotrophic lateral sclerosis has been correlated with both disease progression and slower nerve conduction time [79, 80].

Similar studies of tractography have been applied to psychiatric diseases, again typically using tractography to examine some quantitative index along a tractography-defined pathway. Decreased anisotropy (often interpreted as decreased white matter integrity) has been observed in prefrontal white matter of patients with bipolar disorder [81], in the superior frontal gyrus of patients with depression [82], and in a number of white matter regions in children with autism [83], obsessive-compulsive disorder [84, 85], and attention deficit disorder [86, 87]. Because schizophrenia may involve disordered brain activity, many investigators have used tractography to demonstrate a variety of white matter abnormalities, often correlated with performance on cognitive tests. These findings included decreased anisotropy in frontal and temporal regions, as well as altered structural connectivity of the thalamus, frontal, temporal, and parietal cortices [88-91].

Because diffusion is exquisitely sensitive to both myelin loss, axonal damage, and edema, tractography has been particularly useful for demyelinating diseases, particularly multiple sclerosis. An increased diffusivity has been observed in many tracts in patients with motor symptoms, as well as specific white matter changes in a variety of white matter tracks [92-94]. In addition, a network analysis using graph theoretical measures indicates decreased network efficiencies in multiple sclerosis patients, particularly in sensorimotor, visual, and default-mode areas [95]. Related, patients presenting with optic neuritis show reduced connection strengths along the optic radiations.

Finally, diffusion tractography is emerging as an important part of preoperative neurosurgical planning. When a surgeon aims to remove tumors, tractography could provide information on the location of critical structures to avoid, for example the corticospinal tract [96]. By seeding from areas defined by functional imaging, tractography allows the tracing of these pathways displaced by tumors [97], informing tumor removal approaches [98], and delineating tumor margins [99, 100]. Neurosurgical uses have not been limited to oncology, but have also been used in surgical planning for epilepsy. Again, tractography has been used to determine whether seizure foci involve visual radiations, or to predict visual field impairments after temporal lobe resections [101-103].

# Addendum 1: History of Diffusion, Diffusion MRI, and Fiber Tracking

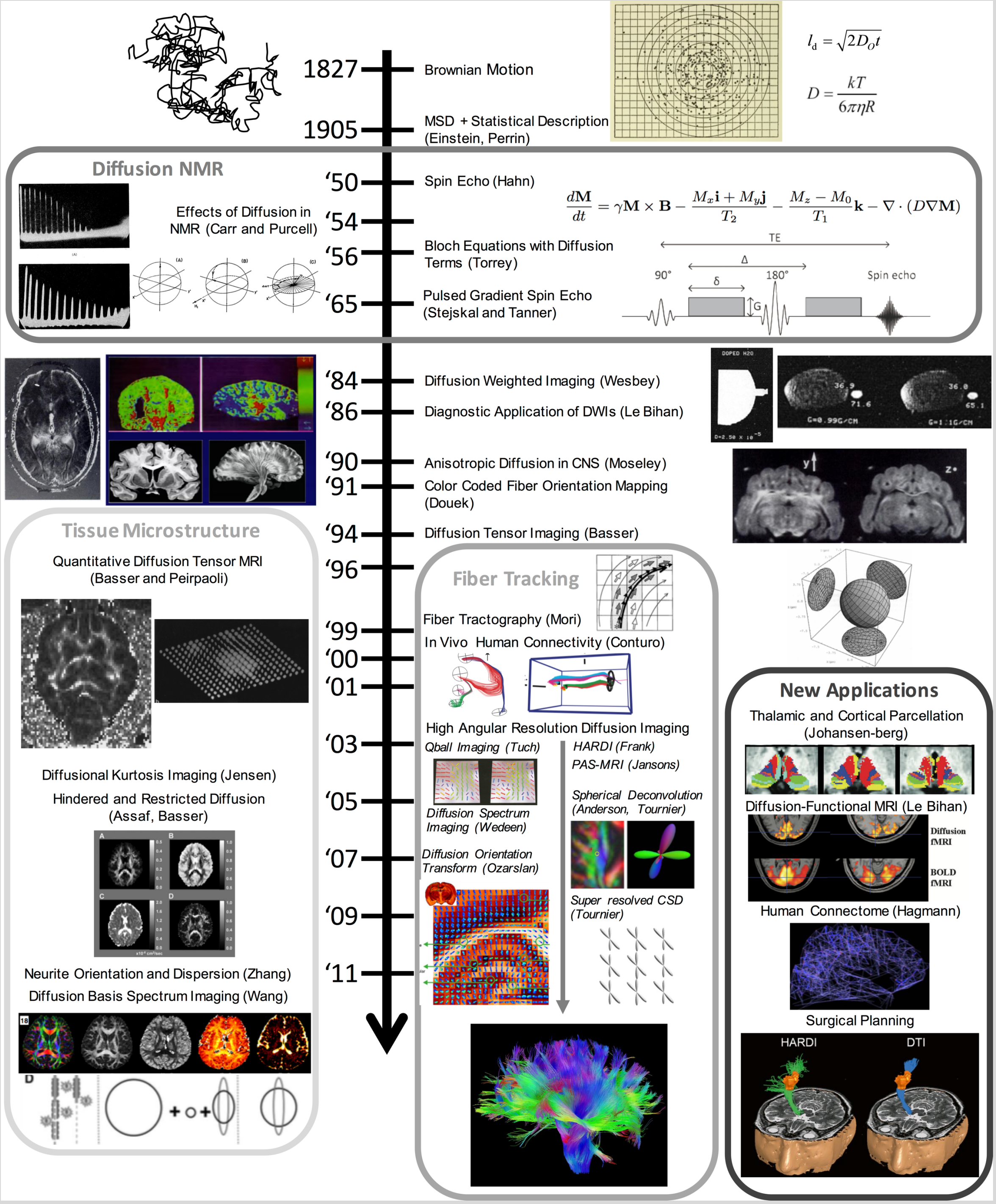

## Diffusion

Diffusion is the process by which matter is transported from one part of a system to another as a result of random molecular motion, also called Brownian motion. This random motion was described as early as 60 BC, where the Roman Lucretius described dust particles mingling and tumbling through sunbeams in a poem titled “On the Nature of Things”. He used this as proof of the existence of what we now know as atoms and molecules. Similarly, the Dutch physiologist Jan Ingenhousz described the irregular motion of coal dust particles on the surface of alcohols in 1785. However, the discovery of this random molecular walk of thermal origin is traditionally credited to the botanist Robert Brown in 1827 (which subsequently was named after him, “Brownian motion”), who described the jittering of pollen grains, in addition to inorganic material, under a microscope. It wasn’t until 1905 that Albert Einstein explained in mathematical detail the motion of individual water molecules observed by Brown. Here, he formulated diffusion equations relating the diffusion coefficient to the mean squared displacement of particles, in addition to relating the diffusion coefficient to measurable physical quantities of the particle and medium. In doing so, he indirectly confirmed the existence of atoms and molecules. Shortly after, in 1908 the French physicist Jean Perrin confirmed Einstein’s relations experimentally and confirmed the molecular kinetic theory (in addition to determining Avogadro’s number).

### Diffusion NMR

Half a century later, Erwin Hahn showed that spin echoes in nuclear magnetic resonance (NMR) offer a way to measure translational motion of molecules, or the self-diffusion coefficient [Hahn, Phys Rev 1950]. In his experiments, spin echoes occur because spins were immersed in an inhomogeneous field. This results in a distribution of Larmor frequencies, causing dephasing and a decay of the signal. With the phase reversal from a second RF pulse, the effect of the inhomogeneous field was to cause spin phases to converge and result in an echo. Hahn realized that the formation of this echo is dependent on the molecules remaining in the same field, and that any translational motion would disturb the refocusing and result in an attenuation of the spin echo amplitude.

The original Hahn experiment utilized two 90° pulses. The spin echo was further developed in 1954 by Herman Carr and Edward Purcell who not only showed that echoes could be repeated successively with a 90° pulse followed by a train of 180° pulses, but also showed that this technique permitted a direct measurement of the molecular self-diffusion constant in fluids – the first quantitative measurement of diffusion using MR [Carr and Purcell, Phys Rev 1954]. Just two years later, Henry Torrey revised and generalized the NMR Bloch equations by including an additional term that accounted for both self-diffusion and flow [Torrey, Phys Rev 1956], and was represented as a form of “transport of magnetization”. The new form of this equation is now referred to as the Bloch-Torrey equation. It was soon suggested that diffusion gradients may be more usefully applied in the form of rectangular pulses before and after the refocusing pulses, but turned off during RF pulse transmission and signal detection. The pulsed-gradient spin echo (PGSE) was first demonstrated by Tanner and Stejskal [Stejskal and Tanner, Phys Rev 1965], who also provided the mathematical analysis of the PGSE diffusion weighted sequence. This new acquisition allowed a precise measure of diffusion time, and eliminated difficulties associated with using diffusion gradients during the refocusing pulse. The PGSE is now the most common form of diffusion weighting today.

### Diffusion MRI

The first diffusion weighted *images* were acquired in 1984 using the methods proposed by Stejskal and Tanner, now with the addition of linear gradients to create a 2D image. For example, George Wesbey suggested diffusion could be imaged by using regular MR imaging sequences and varying the slice selection gradient pulses – and performed subsequent experiments in both water phantoms and in canine myocardium [Wesbey et al., Invest Radiol 1984]. The first diffusion images of the brain were made in 1985 and presented at the Society of Magnetic Resonance in Medicine (SMRM) meeting in London. Here, Dieter Merboldt and Denis Le Bihan were two of only three abstracts at that meeting on diffusion imaging (the third was a poster by Taylor and Bushel showing diffusion measurements in a chicken egg). For the first time *in vivo*, in addition to measuring T1, T2, PD, velocity, and susceptibility, molecular self-diffusion coefficients are now on the list of biophysical parameters capable of being measured by MRI for characterizing biological systems. The tremendous clinical potential of DWI was soon realized. In 1986, Le Bihan introduced the first application of DWI towards medical use by measuring what is now commonly referred to as intra-voxel incoherent motion (IVIM), a measure which includes both diffusion and microcirculation of blood in capillary networks [Le Bihan et al., Radiology 1986]. Here, ADC and IVIM differences were found between normal and pathological tissue, extending the capabilities of diffusion MRI into diagnostic imaging.

Shortly after, it was recognized that diffusion in the central nervous system was not the same in all directions (i.e. diffusion is anisotropic). Michael Moseley showed that diffusion in the cat CNS depends on orientation, particularly in the white matter and the spinal cord [Moseley et al., Radiology 1990], suggesting that diffusion anisotropy could be used to identify white matter orientation. This immediately suggested the use of diffusion to characterize pathologies such as demyelination, however the recognition that water diffusion is lower perpendicular to axons opened the door to tracking fiber orientation throughout the brain. In 1990, the first color-coded orientation maps [Douek et al., JACT 1991] were rendered, reflecting the fiber direction, and producing the stunning visualization that diffusion MRI is known for. In 1994, Peter Basser introduced diffusion tensor imaging (DTI) [Basser et al., Biophys J 1994]. DTI models the diffusion process as a 3D Gaussian function by describing it with a tensor formalism. Now, it was possible to model not only fiber orientation, but also quantitative indices of microstructure and anatomy. For the first time, instead of a diffusion coefficient, DTI allows calculation of invariants of the tensor and its eigensystem to produce a variety of useful maps and information that had previously not existed in the MRI community. For example, some of the first quantitative metrics of diffusion (other than simple ADC) were introduced [Basser and Pierpaoli, JMR 1996], one of them being the commonly used fractional anisotropy. These metrics offered sensitivity to microstructure of the brain, allowing monitoring of structural changes in development, aging, and disease. These microstructural measures are still a major topic of research today.

### Fiber Tracking

In 1999, Susumu Mori proposed a way to use the estimated axon orientation provided by DTI in order to reconstruct the neuronal projections of the brain in a process known as fiber tracking [Mori et al., Ann Neurol. 1999]. Here, he used a simple method of linking the vector field of orientations in a process named fiber assignment by continuous tracking (FACT) to noninvasively create streamlines of the rat brain. The same year, the first fiber tracking in the human brain was performed [Conturo et al., PNAS 1999]. Tracts such as the optic radiation, corpus callosum, and subcortical association pathways were reconstructed, and validated against known anatomical knowledge. These studies opened a new window to see connections in the brain. As opposed to invasive tracer techniques in animals, this enabled noninvasive study of the fiber connections among brain regions in individual subjects.

Very quickly, it was realized that DTI was not able to accurately capture the complex geometry of many areas of the brain. For example, DTI assumes a single fiber population in an imaging voxel, however, the brain contains many regions where crossing fibers are expected to be present, or a distribution of fibers exists. This realization led a large number of more advanced reconstruction algorithms as well as more refined ways to propagate fiber tracks. One of the first methods proposed to resolve multiple fiber populations was named Q-ball imaging [Tuch et al., MRM 2002]. This acquisition scheme required more sampled diffusion directions and (typically) a larger diffusion weighting than DTI. Techniques like this that required a large number of acquisition directions and sometimes multiple diffusion weightings came to be known as high angular resolution diffusion imaging, or HARDI [Frank et al., MRM 2002], techniques. Some of the more common HARDI methods in the literature include Persistent angular structure MRI [Jansons et al., IPMI 2003], Spherical deconvolution [Tournier et al., Neuroimage 2004; Anderson, MRM 2005], and Diffusion Orientation Transform (Ozarslan et al., Neuroimage 2006], among others. These all vary in assumptions of diffusion in a voxel, and each has its own unique advantages as well as limitations. Finally, a method named Diffusion Spectrum Imaging (DSI) attempts to elucidate the full 3D diffusion propagator in each voxel (which is a function of both orientation/space and diffusion time) [Van Wedeen MRM 2005]. DSI is an adaptation of NMR work in the 1990's [Callaghan, JMR 1990] which describes 1D propagator imaging. DTI, HARDI, and DSI methods (in combination with various tractography algorithms) are now ingrained in the connectivity literature, are still the primary methods for probing structural connectivity in vivo. Recently, efforts have been made to create a comprehensive map of the neuronal connections of the brain. One of the largest – the Human Connectome Project [Van Essen et al., Neuroimage 2014], sponsored by the NIH and launched in 2009– has utilized all the above methods to perform fiber tractography, with the goal to shed light on connectivity of the healthy brain, as well as produce tractography data that will facilitate research on brain disorders such as dyslexia, autism, Alzheimer's disease, and schizophrenia.

### Microstructure Characterization

In addition to assessing structural connectivity using fiber tracking, diffusion is also unique in its ability to probe the tissue microstructure. Originally implemented in porous solids [Callaghan et al., 1990], measures of diffusion have been shown to be sensitive to material tortuosity, permeability, size, and density. Several methods have been proposed to model diffusion in biological tissue. A common strategy is to model different microstructural compartments with different geometric or biophysical properties. The first "multi-compartment" diffusion model was introduced by Aaron Szafer (Szafer et al., MRM 1995] - this modeled the apparent diffusion coefficient as a combination of intracellular and extracellular contributions. Surprisingly, it wasn't until a decade later that microstructural models became commonplace in dMRI research. In 2003, Behrens [Behrens et al., MRM 2003] proposed the "ball and stick" model which is able to account for one or more fiber directions in each voxel, assuming diffusion in axons is along a single direction (sticks) and extracellular diffusion is isotropic (ball). Daniel Alexander [Alexander et al., MRM 2008] investigated the ability of dMRI to measure axon radius using a two-compartment model that models the intra-axonal space as a cylinder with a non-zero pore size. Soon, these techniques were expanded to include cylindrical axons with a distribution of radii in a method called AxCaliber [Assaf et al., MRM 2008]. Models containing more than 2 compartments are also common, often including a CSF compartment [Alexander et al., NeuroImage 2010], or a dispersion of axon orientations ("orientation dispersion") in the

NODDI model [Zhang, NeuroImage 2011]. Recently, several models consider the diffusion data as a linear combination of multiple anisotropic compartments (myelinated and unmyelinated axons) and a spectrum of isotropic compartments (cells, sub-cellular structures, stationary water) in a technique known as diffusion basis spectrum imaging [Wang, Brain 2011]. Finally, as an alternative to compartment modeling, one can quantify features of the diffusion displacement function and relate these to tissue properties. For example, Diffusion Kurtosis Imaging [Jensen et al., MRM 2005] extends DTI by quantifying the non-Gaussianity of diffusion. Again, the Kurtosis metrics can be related to characteristics of tissue, including axonal water fractions, intra and extra-axonal diffusivities, and myelination [Fieremans et al., AJNR Am J Neuroradiol 2013].

### New Applications

The vast majority of Diffusion MRI studies have focused on tissue microstructure and connectivity with tractography. Recently, several new applications of diffusion in the brain have been explored. In 2006, Denis Le Bihan introduced diffusion *functional* MRI (dfMRI) [Le Bihan et al., PNAS 2006]. It is hypothesized that cells swell during neuronal activation, resulting in a decreased diffusivity coefficient, meaning that diffusion can act as a direct marker of cortical activation. DfMRI has been shown to have similar (yet more specific) activation patterns as BOLD responses, and to precede the BOLD vascular response. Because cell swelling may be more intrinsically linked to neuronal activation than blood oxygenation, dfMRI may provide improved functional resolution throughout the cortex.

A second application of diffusion MRI is anatomic labelling and parcellation of brain structures. Originally applied to the thalamus [Johansen-Berg et al., PNAS 2004], regions are defined as volumes having similar connectivity profiles, and anatomical borders are identified where connectivity changed. Similar methods have been applied across the human cortex [Anwander et al., Cereb. Cortex 2007]. By taking advantage of structural connectivity obtained through dMRI, these methods offer strategies for testing correspondences between structure and function in the brain.

One final exciting application of diffusion MRI is as a tool for surgical planning [Berman, FBTI 2014]. In Neurosurgery, it is critical to preserve functionally critical cortices and the underlying white matter tracts, and currently diffusion tractography remains the only noninvasive method of determining the course of these tracts. The use of tractography to complement surgical planning by localizing and visualizing white matter pathways has the potential to significantly improve surgical outcomes, and it is expected that tractography for surgical planning will become the standard of care in the near future [Berman, FBTI 2014]. However, it is essential that the capabilities and limitations of these techniques are understood before they can be routinely used in the clinic.

# CHAPTER 3: VALIDATING DIFFUSION MRI

## 3.1 What needs to be validated?

The potential of diffusion tractography to map the three-dimensional network of connections in the living human brain has opened up a large number of applications (see Section 2.5.3 Applications of Tractography). There exists evidence that the anisotropic diffusion of water largely reflects axonal geometry [18], and that many large tractography-defined pathways appear valid [67]. However, the process from data acquisition to generation of a 3D map of reconstructed pathways is a multi-step procedure, with numerous assumptions and uncertainties that can ultimately affect the ability of diffusion tractography to faithfully represent the true axonal connections of the brain (Figure 3.1). Thus, it is critical that tractography methods and experiments are carefully validated in order to provide proper interpretation of the results and to better understand the limitations of these techniques.

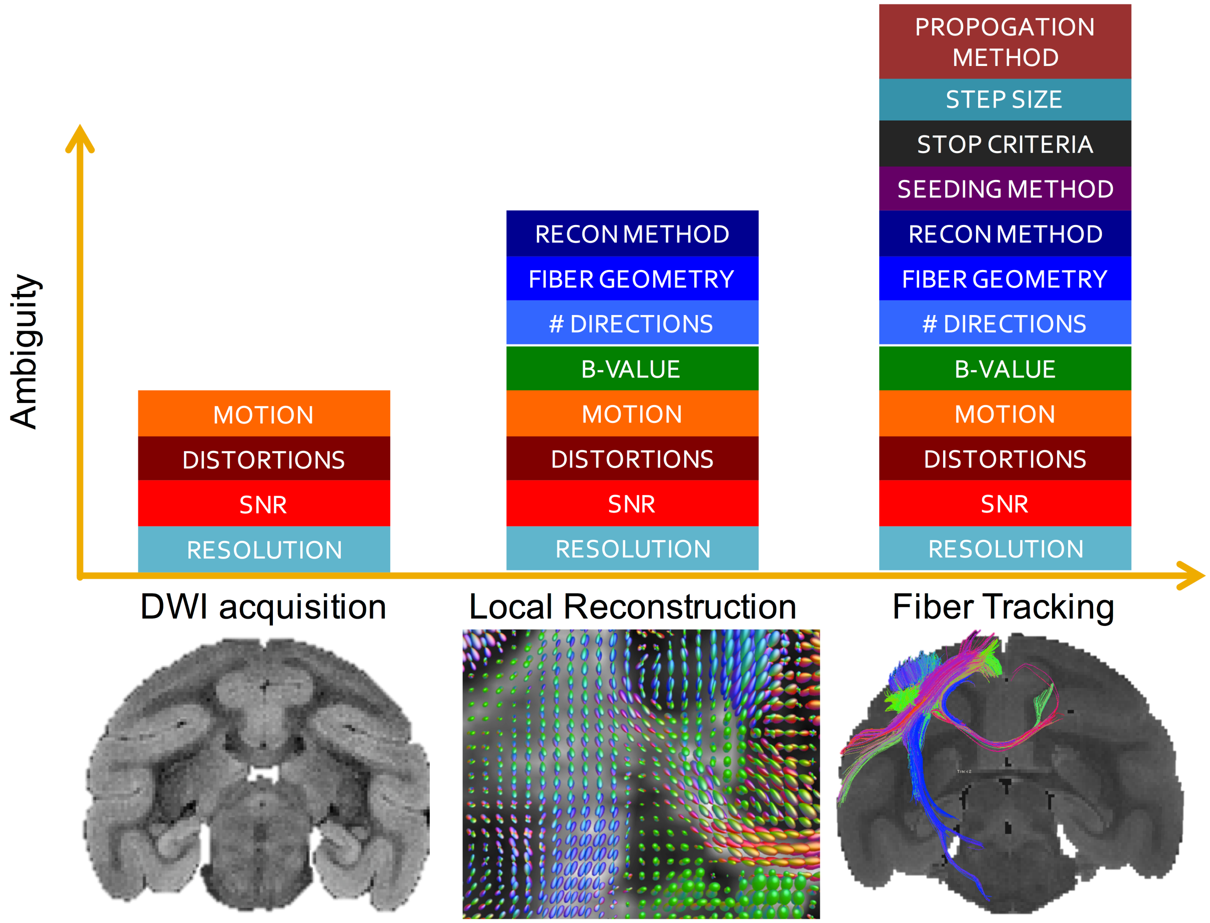

Figure 3.1 Sources of ambiguity, uncertainty, and error in diffusion MRI fiber tractography.

There are many potential sources of error and ambiguities that affect interpretation of the diffusion signal. As with any quantitative imaging approach, reliability of estimates is dependent on image signal-to-noise ratio (SNR), as well as image resolution which influences partial volume effects (as well as SNR) (Figure 3.1, left). In addition, image artifacts such as those from subject motion can corrupt results. Other artifacts particularly relevant to echo-planar imaging diffusion MRI are geometric distortions caused by susceptibility gradients, or induced by eddy currents due to the strong diffusion gradients. In order to eliminate some of these confounds, many of the experiments performed in this work are on ex vivo specimens. Imaging of fixed tissue has several experimental advantages including the feasibility of longer scanning times and the absence of motion. Together, this makes it possible to obtain data with high SNR at a much higher resolution compared to in vivo studies. The most critical advantage of ex vivo imaging relevant to our studies is the ability to compare diffusion data to histological data, which provides a gold standard for validation studies that are not available for the living human brain.

The next obvious source of error encountered in the tractography process is in the inference of fiber orientation (Figure 3.1, middle). While axons have diameters on the scale of ~1um, a typical MRI voxel is typically on the order of millimeters, and can contain hundreds of thousands of axons [104], with a wide range of possible configurations. This makes mapping from the diffusion signal to a fiber orientation distribution an ill-posed problem, with many patterns likely to give rise to the same MRI measurement. In addition to ambiguities associated with image acquisition (motion, distortion, SNR, resolution) and fiber geometry, the inference of fiber geometry in each voxel is dependent on the utilized dMRI reconstruction method, in combination with experimental conditions, including the number of DWIs and the amount of diffusion weighting (b-value). Because these estimates of fiber orientation form the input to all tracking algorithms, the validity of experimentally estimated orientation information must be checked and quantified against the true physical geometry of fibers under investigation. Thus, in Aim 1 of this thesis, we ask "can diffusion MRI accurately predict the fiber orientation distribution in each MRI voxel?". To do this, we investigate how well different HARDI models and reconstruction methods predict the ground-truth, histologically defined neuronal orientation distribution, as well as investigate their behavior over a range of physical and experimental conditions.

Finally, errors can be introduced in the fiber tracking process itself (Figure 3.1, right). Every stage in the tracking process, including seeding, track propagation, and stopping, influences the final results of the estimated fiber pathways. For example, varying tracking parameters such as curvature limits and path step length, in addition to potential integration of neighboring information, will likely result in differing estimates of white matter pathways. The effects of each of these components on the anatomical accuracy of tractography needs to be studied in order to allow the limitations, in terms of track specificity, sensitivity, and precision, to be understood.

When estimating some measure of point-to-point connectivity (for example, cortico-cortical connectivity), it is not only important to correctly follow white matter trajectories, but also to accurately map their gray matter origins and terminations. This is particularly problematic in areas of the cortex that exhibit complex folding and convolutions, necessitating sharp turns or crossing fibers at or near the white matter/ gray matter boundary. Recently, it has been shown that tractography streamlines have a tendency to terminate primarily on gyral crowns (Figure 3.2), rather than the walls of the sulci, or the sulcal fundi [105-107]. While these results could have significant implications regarding morphogenesis and development, it has been suggested that these observations likely reflect a bias in fiber tracking algorithms [108]. Clearly, a tendency for streamlines to track to certain regions of the brain could bias quantitatively connectivity studies.  In Aim 2, we investigate the “gyral bias” of tractography, by making direct comparisons of diffusion MRI and light microscopy to analyze discrepancies in connectivity measures and investigate the effects of tracking parameters and algorithms on observed biases.

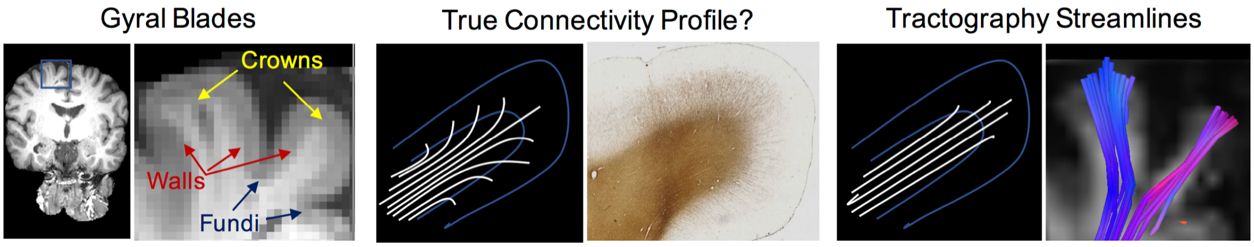

Figure 3.2 A "gyral bias" in diffusion tractography? An example coronal slice is shown highlighting gyral crowns, sulcal walls, and sulcal fundi (left). A potential white matter configuration along the gyral blade is depicted, along with a histological slice which indicates myelinated axons entering the cortex along the entire gyral blade (middle). Finally, tractography may result in overestimation of connectivity at the crowns, shown schematically and with experimental data (right).

## Addendum 2: Neuroanatomy Relevant to White Matter Connectivity

In addition to cadaveric dissection, much of what is known pertaining to white matter structural connectivity comes from tracer studies in animals. By capitalizing on cytoplasmic flow and the axoplasmic transport systems, these histological analyses can be very precise with regard to spatial localization, and allow reporting of the entire axon trajectory from source to target regions. For example, key studies in non-human primates utilize retrograde tracer injections to quantify strength of area-to-area connections [109], or anterograde injections to analyze axonal trajectories within the white matter [110]. These tracer studies allow us to make some general observations regarding anatomical connectivity.

First, we know that white matter appears to be grossly organized into a relatively moderate number of large fiber bundles (major tracts), however axons must follow more complex trajectories in order to reach their specific gray matter (or subcortical) targets. These pathways can largely be divided into association tracts, projection tracts, and commissural tracts. Association fibers are those that connect two cortical areas (cortico-cortical connection) with the same cerebral hemisphere. Examples of “long” association tracts are the fornix, uncinated fasciculus, cingulum, and superior longitudinal fasciculus. A class of association fibers called “short” association fibers, or U-fibers, lie immediately beneath the gray matter of the cortex, and connect together adjacent gyri, often passing from one sulcal wall to another. Projection fibers consist of afferent and efferent fibers connecting the cortex with either the spinal cord, or subcortical structures, such as the thalamus or brainstem. Examples of projection pathways are the motor tract (occupying part of the internal capsule), the fornix (containing efferent fibers from the hippocampus), and the optic radiation.  Finally, commissural fibers connect the two hemispheres of the brain. These include the corpus callosum (the largest commissural fiber system in the brain), the anterior commissure, and the posterior commissure.

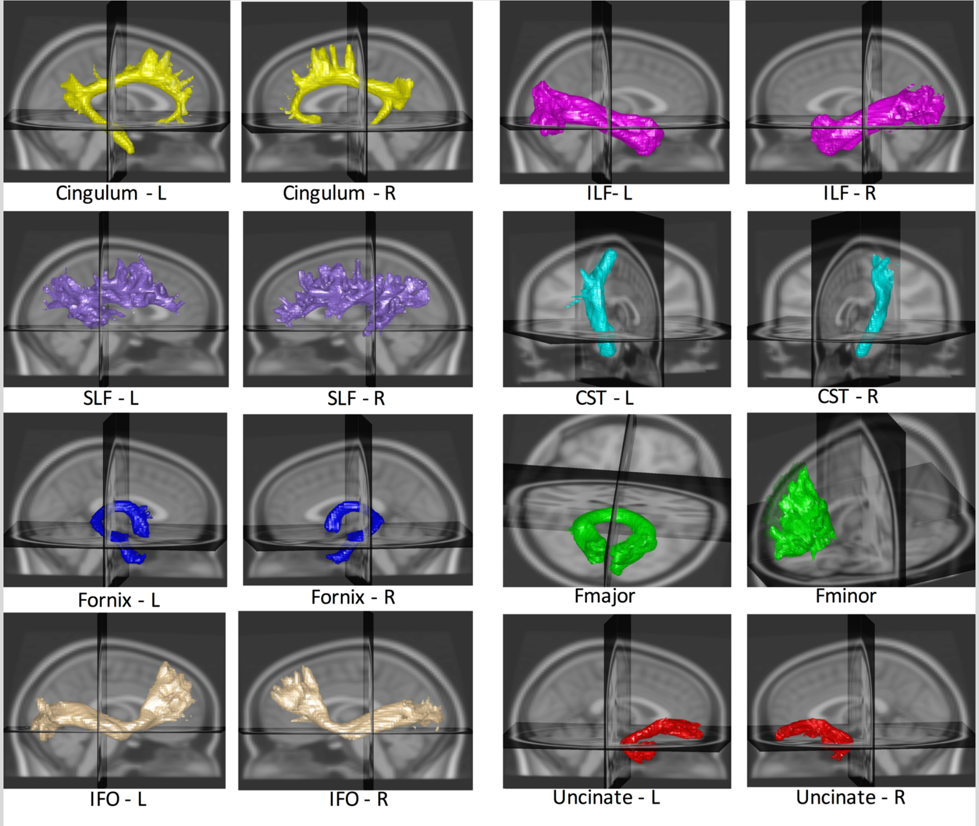

The axonal fiber bundles show a diverse pattern of geometries and trajectories within the white matter, and variations across pathways. Many white matter tracts are known to tightly fasciculate over long distances, remaining in a coherent bundle from injection site to termination in the gray matter [110]. Another geometry is fiber branching. Individual axons, or entire bundles, may branch at varying angles (from acute to near-orthogonal) into new pathways or into nearby cortical gray matter. In addition, there is evidence for a fiber dispersion, or fanning, from a tight bundle into a more diffuse pattern (or vice-versa) [110]. Finally, different pathways may cross others (again ranging from acute to orthogonal crossings), sometimes as adjacent, but separate, bundles, and other times as an interwoven “checkerboard” like pattern. Taken together, there is an extraordinary complexity of wiring of the brain, with a diverse range of bundle geometries, curvature, diameters, and lengths.

A second observation from tracer results is that cortico-cortical association circuits comprise the vast majority of long-distance pathways in the brain, relative to subcortical or commissural pathways. Qualitatively, for cortical injections (for example tracer reproductions from [109] supplemental figures) some labeled neurons are present in subcortical structures, but the vast majority of labeling occurs in the cerebral cortex. This predominance of cortico-cortical association fibers is expected to be even larger in humans due to the larger proportion of cerebral cortex in the human brain [111].

Finally, it is known that cortico-cortical connections vary in strength over a wide range (five orders) of magnitude. Connections tend to follow a distance-rule, where they are generally strongest between neighboring cortical areas, and the strength of connection declines progressively with increasing separation with an approximately exponential slope [109]. This may be particularly problematic for tractography algorithms, where the longest connections will be the weakest, and correspond to the largest streamline propagation, and consequently, the largest uncertainty in estimations.

In addition to this, there are a number of connection patterns that pose challenges to diffusion MRI. Long-range connections from across the brain may converge in a sulcus, yet their terminations show an interdigitating pattern, or topographic organization, with different paths exiting the stalk of the sulcus at different locations along the sulcal banks [112]. Diffusion MRI may not have the specificity to identify the converging, and subsequent branching, of pathways into the cortex. In addition to this, pathways are generally widely distributed across gyral and sulcal regions, and there is no obvious bias (or increased connection density) for gyral crowns, sulcal walls or sulcal fundi [108] (see Section 3.1 What needs to be validated? for a discussion of the gyral bias). However, there are currently no published studies which attempt to quantify the distribution of neurons across the gyral blades. Finally, in addition to a topographic organization of termination patterns across a gyral blade, there also exists a laminar organization of connection patterns along the depth of the cortex, as well as connections within and between the cortical layers themselves. Diffusion MRI would have to be able to distinguish separate connections to and from different cortical layers. At the current imaging resolution, gray matter is largely isotropic, however, evidence exists that diffusion MRI may be able to distinguish cortical lamina, with estimated fiber orientations running both tangentially and radially within the cortex [113-115], with some potential to reveal intra-cortical or lamina-specific connectivity [116].

To summarize, classical neuroanatomical studies have revealed that white matter pathways are organized into regular bundles, but can still have complex geometries and trajectories. Termination and connectivity patterns can have intricate organization, both within gyri and within cortical layers, and cortico-cortical connection strengths can vary over several orders of magnitude. Together, a precise quantification of axonal trajectories or connection strengths from diffusion MRI is a lofty goal, and tractography connectivity patterns must be validated in order to understand the sensitivity to different geometries and current limitations.

## 3.2 Validating Microstructure

It is important not only to test the ability of tractography algorithms to track pathways from voxel to voxel, but also to verify the accuracy of diffusion MRI to assess the fiber orientation within each voxel. To achieve reliable tractography, it is essential that the fiber reconstruction method is highly accurate, especially in the case of complex of crossing fibers. Several validation studies have been performed which check and quantify the match between the experimentally estimated orientation information, and the true orientation of fibers. For any validation method, a gold standard is needed from which to gather the ground truth orientation. The most common approaches are validation using software phantoms (numerical simulations), physical phantoms, and histology. Each method has contributed to our knowledge of the advantages and limitations of the wide variety of reconstruction algorithms.

### 3.2.1 Simulations and Software Phantoms

The validation framework of choice for the majority of reconstruction algorithms proposed in the literature has been through software phantoms using simulated data. Typically, the signal resulting from a fiber bundle (or bundles) is simulated based on some model of diffusion representing tissue microstructure or fiber orientation(s). The data are then analyzed using the given reconstruction method and compared to the ground truth microstructure/orientation(s). The synthetic signal is generally created in one of two ways: by test functions, or Monte Carlo simulations of spins undergoing Brownian motion within a user-defined environment. Most commonly, test functions are typically based on a mixture of user-defined Gaussian distributions simulating multiple fiber populations (i.e. crossing fibers) in a voxel [6]. Monte Carlo simulations allow highly complex physical environments to be formulated mathematically, generating synthetic datasets based on more “exact” models of diffusivity in the underlying environments [53, 117]. Simulations offer the user full control over all experimental conditions, including signal models, fiber configurations, sampling schemes, and noise levels. This enables a simple and versatile way to assess the performance of a reconstruction algorithm over a broad range of physical and acquisition conditions.

The major limitations of many algorithms are first identified using simulations. For example, several studies utilized simulations to highlight the failure of DTI to characterize intra-voxel orientation complexity when more than a single fiber population is present [118, 119]. A large number of HARDI methods intended to solve the crossing fiber problem first test their method on simulated data [36-38, 45, 120, 121]. The simulations are often used to optimize selection of algorithmic parameters, for example regularization constants and spherical harmonic order [36]. Another common use is to compare the performance of different algorithms under varying simulated physical conditions. In [6], the q-ball and PAS-MRI methods are compared using crossing Gaussian test functions across a range of simulated separation angles, fiber volume fractions, and noise levels. Here, they demonstrate the minimum resolvable crossing angle, and the accuracy and consistency in identifying both peaks of the fiber distribution. They determine that (a) PAS-MRI more consistently recovers the principal directions of the synthetic functions for typical clinical imaging conditions (SNR of 16 and 54 gradient directions), (b) an increase in either SNR (to 24) or gradient directions (>100) allows q-ball to recover directions with consistency comparable to PAS-MRI, and that q-ball gives the best performance with b-values in the range of 2,000-2,500 s/mm$^2$. The same group has also applied Monte Carlo simulations to investigate the optimal value of diffusion weighting (for both single and crossing fibers) for estimating the mean diffusivity, fractional anisotropy, and fiber orientations [122].

Finally, a recent challenge held by the diffusion MRI community, the “HARDI reconstruction challenge” [123] used fields of simulated Gaussian functions to compare the behavior of a large number of algorithms, including from DTI, sparse reconstruction methods, HARDI methods, and DSI-like methods. The two main criteria evaluated are the correct assessment of the number of fiber populations and the angular accuracy in their orientation. The comparative study highlighted the strengths and weaknesses of each approach and results in interesting considerations common to all algorithms. For example, (a) no method outperformed all others in every experimental condition, (b) accurate reconstruction using sparse-reconstruction schemes are possible with very few DWIs, (c) and inaccuracy in algorithms was caused by underestimation of fiber populations in high quality data, and over-estimation in low SNR acquisitions.

While computer simulations are useful to ensure a new method behaves as intended, and allows simple, inexpensive comparisons among methods, the simulations are only as good as the assumptions and approximations that lie behind the model from which the signal is derived. The results are likely to be highly dependent on the user’s knowledge and assumptions about how different anatomical compartments influence the diffusion signal. Thus, computer simulations are almost certainly an over-simplification of the diffusion process, and of limited use for validation in the living brain.

### 3.2.2 Physical Phantoms

In contrast to simulations, physical phantoms offer the generation of diffusion datasets based on the true Brownian motion of water molecules within a real model of underlying fiber orientations. An extra layer of realism is added in that the diffusion images are obtained on a real scanner and are subject to real data acquisition conditions (including noise and image artifacts inherent to diffusion MRI). A number of studies have been performed to validate the diffusion estimated fiber orientations utilizing physical phantoms. To date, most of these studies utilize capillary and synthetic based fiber phantoms to act as substitutes for axonal fibers.

Capillary-based phantoms, or hollow plastic cylindrical capillaries, were some of the first anisotropic structures used to mimic the geometry of axons. For example, an early study used water-filled capillaries to investigate the effects of different b-values on the apparent diffusion coefficient in given directions, demonstrating the alignment of diffusion peaks with the capillary orientations [124]. Similarly, using polytetrafluoroethylene capillaries, Lin et al. [125] showed that DSI was able to resolve sheets of fibers crossing at 90° and 45° (even when the narrow pulse approximation was violated), while DTI failed to resolve crossing fibers. Similar intersecting capillary set-ups investigated the ability of QBI and various implementations of CSD to resolve crossing fibers, showing the advantages of using sCSD to resolve crossings at acute angles (~30°). Although these phantoms allow assessment of fiber orientation information, they are limited in how well they geometrically match the characteristics of tissue. For example, the inner diameter can be an order of magnitude larger than that of axons (~50um), while the outer diameter is much larger, for example 325um in [125]. This certainly affects diffusion anisotropy, as a larger diffusion time is needed in order for spins to probe the local environment. Further, these structures possess no permeability to water, which may influence compartmental estimates depending on the diffusion time relative to the water exchange rates.

Investigation of the extracellular component of diffusion has been performed using synthetic fiber-based phantoms. These can be composed of rayon fibers [126] , hydrophobic acrylic fibers [127], or polyester yarn [128], which have fiber diameters closer to that of axons (~17 um in [126]), and increased densities relative to capillary phantoms, resulting in more biologically realistic values of FA (0.6-0.8) [128]. These synthetic phantoms offer the ability to vary fiber density, such as in the phantom developed by Farrher et al. [129]. This phantom not only has varying density from section to section (resulting in variable FA), but also regions of crossing fibers, as well as homogenous density fibers, and has been used to validate CSD and QBI, as well as investigate the effects of packing density on anisotropy. Finally, micron-sized, hollow, permeable fibers can be made using co-electrospinning of polymer solutions [130]. These techniques are capable of producing aligned fibers, with tuneable size distribution, and have been used to investigate the effects of inner diameter on DTI indices [131], although to date, there has been little validation of orientation information using the electrospun fibers. Although a step in the right direction in regards to replicating geometry and fiber densities, these synthetic fiber-based phantoms still fail to replicate the enormous complexity seen in tissue of the central nervous system.

### 3.2.3 Histological Validation

Finally, several studies have validated orientation measures using post-mortem histology. The imaging is performed on the tissue itself, which inherently contains the complex structural and biophysical characteristics of the central nervous system. From stained tissue sections, techniques such as manual tracing of fibers [132], filter matching [133], or structure tensor analysis [134] has been used to quantify the histological, ground-truth FOD. Studies in the owl monkey [133] and blocks of human cortical tissue [135] have investigated the angular accuracy of the DTI primary eigenvector, and probed the relationship between fiber density, fiber spread, and anisotropy with the angular orientation error. To date, the only histological validation of orientation information obtained through HARDI methods was done for high-b-value QBI in a study by Leergaard et al. [132], where they conclude that the fiber orientation distributions obtained from high dimensional diffusion data provide accurate representations of the myeloarchitecture, even in regions of crossing fibers.

Several disadvantages have plagued histological validation studies to date. First, most histological validation studies of orientation information have been limited to two-dimensional (2D), in-plane analysis of tissue sections. Thus, they rely on tissue sectioning in a plane parallel to the direction of fibers, and analysis is restricted only to fibers oriented in that plane.

Recently, 3D histology for the purposes of validation has been performed with the use of confocal microscopy [136] or optical coherence tomography [137], although these studies have been limited by resolution, estimating only a single dominant fiber orientation per voxel, rather than the full neuronal orientation distribution. Another histological technique, polarized light imaging – with contrast based on the birefringence of nerve fibers – has become popular because it allows 3D fiber orientation characterization of unstained brain sections at high resolution [138]. Three-dimensional polarized light imaging has been utilized to validate diffusion MRI orientation dispersion measures, however it has not yet been used to validate fiber orientation information. A second limitation of histological validation is that accurate alignment of the histological and MRI data is rarely addressed and, if performed, typically involves only manual alignment [132, 135, 136] of the data, which is prone to error and can lead to geometric mismatch and a bias in the validation results. Consequently, there is a need for a method to compare dMRI estimates of white matter pathways to direct measurements of axonal orientations on a voxel-by-voxel basis - one which allows three-dimensional (3D) analysis and addresses accurate, reproducible registration. We address these limitations in Aim 1 of this work, where we develop an approach to extend histological validation of orientation functions to 3 dimensions. Also, because a histological validation of many existing reconstruction methods is lacking, we utilize this approach in order to assess the reliability and accuracy of many of these techniques, as well as study the effects of acquisition parameters on their performance.

## 3.3 Validating Macrostructure (Connectivity)

Even perfect estimation of fiber orientation distributions on the voxel-scale does not guarantee success in fiber tracking. Each step in the tracking process has numerous assumptions and uncertainties that could result in potential errors in delineating pathways or connectivity estimates. Much like validation of orientation information, software and physical phantoms have been used as gold standards from which tractography algorithms can be validated. In addition, invasive tracers in animal models are commonly employed to visualize the true underling anatomical pathways for comparison with diffusion tractography. Together, these studies have advanced our understanding of the limitations and successes of various tracking algorithms.

### 3.3.1 Software Phantoms

Software phantoms for tractography are constructed choosing a “true” fiber trajectory or trajectories. For every voxel along that trajectory, a diffusion signal is simulated using some model of diffusion based on the simulated tissue, noise is added, and finally the tractography method under interrogation is applied and compared to the ground truth. Simulations are convenient in that they allow testing of a variety of methods, and the flexibility of assessing a broad range of experimental conditions by easily manipulating the trajectory itself or the acquisition conditions (noise, samples, b-value, etc.). A wide range of phantoms have been developed, varying from linear, to circular, to crossing and more complicated trajectories, with a range of anisotropies and varying partial volume effects. Again, however, simulations are limited in their validation ability because (a) they rely on a generative model of diffusion to create the signal, and (b) are certainly a simplification of the in vivo tissue geometry. Despite this, simulations have provided useful analysis of various approaches to tractography.

Early studies utilized simple geometries for simulations. For example, helical [139], circular, or semi-circular paths [140]. Studying the effects of experimental phantom designs, Lori et al. [139] showed that random tracking error is dependent on SNR, anisotropy, and voxel size, and accumulates with the square root of the track length (similar to a random walk process). This agrees with theoretical predictions [141]. Tournier et al. [140] find that the most reliable results are obtained with high SNR data, high anisotropy tracks, using interpolation (as opposed to FACT tracking), and smaller step sizes. They also show that partial volume effects can considerably bias results when tracking narrow fibers. Crossing fibers have been incorporated into simulations [142] to show advantages of using neighboring information to successfully track through ambiguous areas with DTI estimates. Simulations have played significant roles in fine-tuning the user-defined parameters of tractography, including regularization , step size, termination criteria, and tract curvatures [143]. In addition, some interesting tracts have been simulated, for example, a Canadian favorite: the maple leaf track [144].

Despite the wide number of simulation studies, these simulations still represent geometries that greatly over-simplify those of tissue. To overcome this partially, Close et al. [145] have developed a software tool that generates structures with a range of complexities (resembling a ball of spaghetti), that is flexible in generating a range of crossing and kissing tracks with densely packed bundles. Finally, a recent diffusion MRI community "challenge" was hosted using an open source simulation tool called Fiberfox [146] to replicate the well-known "FiberCup" physical phantom [147] (see Section 3.3.2 Physical Phantoms), which is intended to replicate a coronal slice of the brain, including 3 crossing bundles, 1 kissing bundle, and 3 bundles that split, covering a range of very straight, to U-shaped fibers. The simulated Fiberfox data was used to evaluate 12 tractography pipelines, each with different local models, tractography methods, and different open-source software implementations. However, even with these sophisticated simulations, results depend on the model used to generate the signal, which can show biases towards methods which also assume the same diffusion processes.

### 3.3.2 Physical Phantoms

Similar to validation of orientation information, physical phantoms for tractography have been constructed from a variety of materials including polyester [148], ultra-high molecular weight polyethylene, rayon, cotton, nylon [117], and hemodialysis fibers [126]. These phantoms can incorporate some complexity, for example crossing fibers at varying degrees to validate q-balls ability to track through crossing fiber regions [126, 127]. Recently, a physical "FiberCup" phantom was created using acrylic fibers packed into a polyurethane case to mimic a 2D slice of a coronal brain section [147]. A dMRI community challenge was organized using real MR-acquired data on this phantom, with 10 research groups submitting their own tractograms, and evaluation criteria including spatial overlap, orientation agreement, and curvature agreement with the ground truth acrylic fibers. This work has recently been extended with the "Tractometer" [149] to include a large number of algorithms (currently >57,000) on the FiberCup dataset. The Tractometer, in addition to spatial overlap, assesses the number of valid and invalid connections (end point analysis), number of missing connections (premature stopping), as well as valid and invalid bundles (whole tract analysis). Together, these results have provided valuable insight into the various sources of ambiguity in tracking. A meta-analysis of this data shows (a) seeding has a large impact on tractography output, (b) deterministic tractography produces fewer invalid tracts than probabilistic, c) averaging improves quality of all tractography, and (c) reconstruction methods that result in sharper angular profiles (for example FOD estimation rather than ODF) improve tractography. Yet, these phantoms still do not model fiber packing in a realistic way, and again, cannot capture the geometric complexity of the true connectivity in the brain.

### 3.3.3 Tracer and Histological Validation

Finally, validation using invasive tracers within tissue are the only validation approach that provides the possibility of visualizing the actual true underlying anatomical environment from which diffusion data is acquired. In addition to real imaging conditions with real biological diffusion physics, histological tracers have a low false positive rate (high specificity), meaning that detection of the compound away from the injection site is strong evidence for a connection. In addition, the spatial resolution allows the discovery of axon organization at a level of detail well beyond that of current MRI techniques. Because of this, neuro-tracing is considered the gold standard in measuring and validating connections.

There are a variety of classical tracers that have been used by neuroscientists to study the neuronal architecture of animal brains. Common tracers include Horseradish Peroxidase, lectins and toxins, fluorescent tracing compounds, and dextrans (for a review, see [150]), all of which have slightly different properties, for example anterograde vs. retrograde transport, cell body vs. axon vs. membrane staining, and single axon specificities. Traditionally, validating the prediction strength of tractography against tracers takes one of two forms. First, a measure of spatial overlap of the tract vs. tracer can be performed, which validates the overall layout and anatomical accuracy of tractography. Second, many studies measure connectivity measures, disregarding how tracts reached their destinations, and focusing only on the number of streamlines connecting different regions (for example cortico-cortical connectivity).

The cortico-cortical connections estimated from tractography have been compared with the results of invasive tracer data accumulated in web-based atlases or databases, for example the CoCoMac [151] database and Markov-Kennedy datasets [109, 152] for the macaque, or the Allen Brain Atlas of the mouse [153]. These databases are the results of a large number of tracer studies (126 studies for the CoCoMac database, 29 separate tracer injections for Markov dataset, and 488 tracer injections for the Allen Mouse Brain), with some quantification of connection strength to a number of parcellated cortical regions (39 regions, 91 regions, and 592 regions, respectively. Connection strength matrices (from tracer injection site to each cortical region) can be described as “strong”, “medium”, or “weak” (as in CoCoMac), or described by a continuous distribution such as the “fraction of labelled neurons” or staining intensity (as in the Markov and Allen Brain Atlas Datasets). These studies have provided encouraging results regarding the fidelity of tractography. For example, studying the detailed connections known in the macaque visual cortex, Azadbakht et al. [154] find that ~74% of known connections were successfully identified by probabilistic tractography, although this required optimization of FA thresholds, step size, and uncertainty thresholding (to minimize false positives). Further, although the tracts were identified, this was done in a binary fashion (exists, or doesn’t exist), whereas tracts actually vary in connection strength by orders of magnitude. In a study of the full macaque brain comparing the number of streamlines to connectivity measures from both the CoCoMac and Markov databases, van den Heuvel et al. [155] find positive correlation between tractography and connection strength, and conclude that the number of streamlines is a valid method of assessing projection strength of white matter pathways. Similarly, Donahue et al. [156], utilize ex vivo diffusion MRI probabilistic tractography and the same Markov atlas to show that tractography connection weights are only accurate to within one or two orders of magnitude to tracer ground truth, yet are a reliable predictor of connectivity strengths for strong connections, and less so for longer pathways (which have weaker connection strengths). Despite the fact that tractography was less correlated with tracer for weak connections, both the weak and strong pathways still contributed to the fairly high correlation (r=0.59). They also show that tractography results heavily depend on seeding, with seeding from the white-matter-gray-matter boundary have slightly higher correlations to ground truth, while seeding from all of white matter showed higher streamline densities in gyri rather than sulci (i.e. showed a gyral bias). Finally, comparing connectivity strengths with a comprehensive mouse atlas, Calabrese et al. [157]show modest correlation between tracer and tractography at a very high level parcellation (592 anatomic regions, r=0.42) but stronger correlations at coarser resolutions (for example, r=0.71 at a “structure-level” segmentation).

Studies using large-scale databases have the advantage of assessing connectivity of tens to hundreds of pathways at a time across many cortical areas, however they have several significant limitations. Most significantly, the tracer and MRI is not performed on the same animal, and pathway and connection strength can vary between animals. For example, repeated tracer injections into the same portion of the same area can vary by approximately an order of magnitude [158]. In addition, there can be heterogeneity in the connectivity of a given area, for example an injection in a specific location of a defined region may inadequately describe the connectivity to (or from) that region as a whole due to the known topographic organization of many cortical areas (see Addendum 2: Neuroanatomy Relevant to White Matter Connectivity). Variance in brain geometry between injected and scanned animals could also lead to mismatches in identifying injection regions (or seed locations) in the subject of interest. Finally, many atlases display asymmetric connection matrices, but are being compared to the inherently symmetric diffusion measures (which cannot identify anterograde vs. retrograde connections).

Very few studies perform diffusion MRI and histology in the same animal for validation. The first work to make direct comparisons of cortico-cortical connectivity and tractography in the same animal by Gao et al. utilized the squirrel monkey brain, and BDA injections into the primary motor area. By calculating BDA density maps from histology registered to diffusion data, Gao et al. [159, 160] show that DTI tractography strongly correlated with anatomical connectivity when measured on the scale of major cortical regions (defined by cytoarchitectural borders from Nissl stained slices), however was much less reliable measuring voxel-to-voxel connectivity. They also show that tractography was not reliable in ranking connectivity strength in regions with weaker connectivity result reproduced in macaques [156]. One limitation of this study is that the diffusion acquisition scheme consisted of a low number of DWIs, limiting analysis to DTI tractography. While not addressing cortico-cortical connectivity directly, a recent study by Reveley et al, utilize ex vivo macaque specimens to show that even with very high-resolution data with a large number of DWIs, large portions of the cortex were inaccessible to tractography, with streamlines never penetrating as much as half of the entire surface. Similarly, seeding in many of these regions leads to identification of only local fiber bundles, with streamlines never penetrating to deep white matter for long range tractography. Qualitatively, many of these cortical regions that pose challenges to tractography were observed near the sulcal fundi. These tracking limitations are attributed to the dense superficial white matter U-fibers, located immediately under the deepest cortical layer and running parallel to the gray matter surface, limiting tracking to and from the cortex nearest these layers. This work motivated much of the work presented in Chapter 8, which aims to quantify this gyral bias, as well as investigate the effects of tracking algorithms and image resolution on the observed bias.

In contrast to measures of connectivity, a number of studies have investigated spatial overlap of entire white matter trajectories with those from tractography. Validating these measures gives confidence in the ability to segment specific white matter pathways, with subsequent analysis usually assessing some quantitative imaging measure along that pathway, or characterizing the presence or absence of these tracts (see 2.5.3 Applications of Tractography). For example, Schmahmann et al. [161] compare DSI tractography to autoradiographic histological tract tracing [110], and identify 10 association fiber bundles using tractography that match the histological observations. They show that DSI tractography is able to replicate the major features of these tracks, and largely represents the geometrical organization of these large white matter pathways. However, no quantitative analysis is performed, and again, diffusion MRI and histology are from different specimens. In a series of studies on a macaque brain, Dauguet et al. [162, 163] inject a neural tracer, WGA-HRP, into three sites of the brain in three monkeys. They then reconstruct the histological sections of labeled fiber tracts in 3D, segment and register the fibers with the in vivo animal MRI, and perform DTI tractography using the injection sites as seeds. Visually, tractography correlated well with histology, and quantitative analysis showed Dice overlap coefficients ranging from as low as 0.2 to as high as 0.75 depending on FA threshold, radius of curvature, and step size. They then perform a voxel-wise analysis of false positive voxels (those that contain a DTI streamline, but do not contain histological WGA-HRP) and false negative voxels (those that do not contain a

DTI streamline, but do contain WGA-HRP stain), and conclude that DTI has difficulties when tracts cross or divide, and often stop prematurely due to low anisotropy. This was the first visualization of the crossing fiber problem as it relates to the failure of in vivo tractography.

From phantoms and simulations, tracking is known to be limited by technical factors affecting in vivo data acquisition, such as noise, artifacts, and data under-sampling resulting from scan time constraints. To investigate the anatomical accuracy of tractography with these limitations minimized, Thomas et al. [164] utilized the same high-quality macaque dataset as as in [107]. Comparing tractography to two tracer injections from a previous study [110], they investigated the sensitivity and specificity of a large number of advanced tractography algorithms. In contrast to previous histological validation studies where modest overlap or correlations were generally interpreted in an optimistic light, Thomas et al. [164] show that no tractography method showed a high accuracy, with methods that showed the highest sensitivity also showing the lowest specificity, and vice versa. The accuracy, again in agreement with previous studies, was highly dependent on a number of technical parameters (including diffusion model, angular threshold, and seeding strategy). The authors conclude that anatomically accurate results are an elusive goal, and will remain so even with advances in acquisition and imaging strategies.

Another method for validating tractography has been through the use of invasive Manganese (Mn) tracing. The paramagnetic Mn ion is an excellent T1 contrast agent, and injection into the animal brain has been shown to highlight many of the pathways connected to the administration site. This MR-visible tracer has several advantages, most notably it can be used in the same monkey in which diffusion MRI is performed, and is inherently registered to the same data (assuming similar imaging fields of view) allowing simple voxel-wise validation. The first study to compare tractography to Mn-enhanced MRI images investigated the optic tract of the rat using both DTI and DSI [125, 165], showing improved results in regions of crossing fibers with DSI. Two other studies, utilized three MR-visible tracer injections in the pig brain [166, 167] to validate various tractography algorithms. First, Dyrby et al. [166] used this technique to assess the performance of a multi-tensor probabilistic tractography method, showing generally high agreement between tracer and tractography, which was reproducible across brains. To extend this study, [167] implements more algorithms, both probabilistic and deterministic, with diffusion models including CSD, multi-tensor, and ball-and-stick compartment models. They conclude that tractography is capable of identifying major fiber tracts, and, as in [164], find that it is not possible to achieve high specificity and sensitivity at the same time, with problems arising in regions with complex fiber arrangements or high curvature (with different limitations associated with different white matter pathways). A major limitation of Mn tracing is the presence of false positive and false negative bundles identified due to enhanced transport and trans-synaptic capacity of Mn ions, as well as anterograde only projections identified using these tracers. Finally, there is a lack of specificity due to the somewhat arbitrary user-defined threshold applied to the T1-weighted images in order to identify signal enhancement, and thus isolate the white matter pathways. The extent and geometry of the pathways extracted is heavily dependent on the quantitative analysis of the T1 images [167].

In Aim 2 of this thesis, we use histology to validate various tractography measures obtained from diffusion MRI. As described above, histology is the only validation approach able to capture both the enormous complexity of the system of interest (brain white matter tissue) and biophysical or diffusion properties of the system, in addition to incorporating true imaging considerations (noise, artifacts, etc.). Specifically, we address limitations of previous histological validation studies: MRI and histology are performed on the same specimens, and image alignment is addressed through multi-step registration procedures. These validation studies are enabled through the construction and framework provided by the squirrel monkey digital brain atlas (Chapter 4). Specifically, aim 2 utilizes a myelin stain to quantify axonal density along gyral blades in order to assess errors and biases associated with gyral blade geometries (i.e. the "gyral bias" in tractography). In addition, the web-based atlas contains BDA tracer injections. BDA has the advantages of being transported both anterograde and retrograde, and is highly axon specific, identifying only regions connected to the injection location. This MRI-registered BDA tracer should facilitate future tractography validation studies, which can elucidate strengths and limitations of current tractography algorithms.

# CHAPTER 4: DIGITAL ATLAS OF THE SQUIRREL MONKEY BRAIN

## Prologue

The validation presented in this work is made possible through the use of non-human primates (NHP) as models for diffusion MRI of the brain. This chapter describes our work creating and disseminating a web-based, combined MRI-histology digital atlas of the squirrel monkey brain. Later chapters either use the data from this atlas directly, or utilize the atlas registration framework (on another NHP, the macaque), in order to facilitate comparisons of the MRI and histological imaging modalities. In addition, the database and front-end web viewer acts as a tool for other investigators to view and access the data to investigate questions well beyond the Aims of this work.

## Abstract

The squirrel monkey is a commonly-used surrogate for humans in biomedical research. In the neuroimaging community, MRI and histological atlases serve as valuable resources for anatomical, physiological, and functional studies of the brain; however, no digital MRI/histology atlas is currently available for the squirrel monkey. This chapter describes the construction of a web-based multi-modal atlas of the squirrel monkey brain. The MRI-derived information includes anatomical MRI contrast (i.e., T2-weighted and proton-density-weighted) and diffusion MRI metrics (i.e., fractional anisotropy and mean diffusivity) from data acquired both in vivo and ex vivo on a 9.4 Tesla scanner. The histological images include Nissl and myelin stains, co-registered to the corresponding MRI, allowing identification of cyto- and myelo-architecture. In addition, a bidirectional neuronal tracer, biotinylated dextran amine (BDA) was injected into the primary motor cortex, enabling highly specific identification of regions connected to the injection location. The atlas integrates the results of common image analysis methods including diffusion tensor imaging glyphs, labels of 49 white-matter tracts identified using DTI-tractography, and 18 cortical regions of interest identified from Nissl-revealed cyto-architecture. All data are presented in a common space, and all image types are accessible through a web-based atlas viewer, which allows visualization and interaction of user-selectable contrasts and varying resolutions. By providing an easy to use reference system of anatomical

information, our web-accessible multi-contrast atlas forms a rich and convenient resource for comparisons of brain findings across subjects or modalities. The atlas is called the Combined Histology-MRI Integrated Atlas of the Squirrel Monkey (CHIASM). All images are accessible through our web-based viewer (https://smda.vandyxnat.org/smda/), and data are available for download at (https://www.nitrc.org/projects/smatlas/).

## 4.1 Introduction

Non-human primates (NHP) are phylogenetically close to humans, sharing genetic, anatomical, and physiological similarities [168], making them a valuable model for biomedical studies of the brain. Numerous white matter pathways, as well as major functional subdivisions of the cortex, have been shown to have homologous counterparts in the human brain. This includes well defined lateral, central, and temporal sulci, as well as parietal, occipital, frontal, and temporal lobes. NHPs have sophisticated behavioral and cognitive capacities, and the use of NHPs allows access to “ground truth” anatomical or microstructural information via post-mortem histology, upon which experiments can be designed and evaluated.

One of the most commonly studied New World primates is the squirrel monkey (Saimiri sciureus). In addition to the above, squirrel monkeys have a relatively small, lissencephalic brain, making experimentation less cumbersome, and histological processing easier. Moreover, because of their small size they can be handled easily, trained to perform in behavioral experiments, and have relatively low resource requirements. Studies using the squirrel monkey are prevalent in neuroscience and related fields, including ophthalmology, toxicology, pharmacology, and psychiatry [169-180].

Brain atlases are useful for analyzing and identifying neurological structures. Currently, two stereotaxic atlases from the 1960’s are available for the squirrel monkey brain [181, 182]. Brain structures in these atlases are delineated based on cyto-architecture in Nissl stained sections and on myelo-architecture in myelin stained sections. However, these are printed atlases and, unlike digital atlases, do not facilitate spatial normalization of new image information for quantitative comparisons of brains across subjects, time, or differing experimental conditions. In other species, atlases based on magnetic resonance imaging (MRI) have become valuable tools to reference the anatomy of the brain. Recently, we have introduced the first MRI atlas of the squirrel monkey brain to facilitate three-dimensional (3D) anatomical localization or segmentation, and to enable comparisons of experimental data across different subjects [183].

While MRI allows for 3D viewing of the brain and specific structures within it, precise spatial relationships between structures and differentiation between types of tissue, the image resolution is somewhat limited. Stained tissue sections, on the other hand, offer high spatial resolution, and the ability to identify individual cells and fiber systems, however, there are often spatial distortions inherent in histological sectioning, staining, and processing. Here, we present a web-based digital atlas of the squirrel monkey brain that combines aligned MRI and histology data. The MRI includes anatomical and diffusion contrasts, and histology includes Nissl and myelin stains. In addition, a bi-directional (anterograde and retrograde) tracer is injected into the primary motor cortex of the subjects, and histologically processed in order to identify white matter pathways associated with the injection location. All histological contrasts are registered to the corresponding MRI data of the same specimen. The atlas also includes post-processed results, including diffusion tensor imaging glyphs, diffusion tractography-defined white matter labels, and cyto-architecturally defined cortical regions. This atlas is designed to provide an easy to use resource for anatomical, functional, and physiological studies of the squirrel monkey brain that may benefit from information gathered through either histological or MRI modalities. Thus, the atlas provides a convenient medium for comparisons of brain findings across subjects or modalities. To highlight typical usage, we also present three illustrations of the application of data contained in this atlas to neuroscience research, with a focus on diffusion MRI fiber tractography. All images are accessible through our web-based atlas viewer (https://smda.vandyxnat.org/smda/).

## 4.2 Methods and Materials

### 4.2.1 Data Acquisition Overview

Figure 4.1 shows an overview of the atlas data acquisition pipeline. Each squirrel monkey was imaged in at least two in vivo scan sessions. Following scanning, a bidirectional tracer, biotinylated dextran amine (BDA) was injected into the left hemisphere primary motor cortex (M1). One to three weeks after surgery the monkey was sacrificed. The brain was then removed from the skull and scanned ex vivo. After this session, the brain was frozen and cut serially on a microtome in the coronal plane. For registration purposes, the surface of the frozen tissue block (i.e. the “block face”) was photographed using a digital camera prior cutting every third section. Next, series of sections were processed for BDA histochemistry, Nissl, and myelin stains. Finally, borders of cortical regions of interest were manually labeled by an expert based on cyto-architecture provided by Nissl stains. Each data acquisition step is described in full detail below.

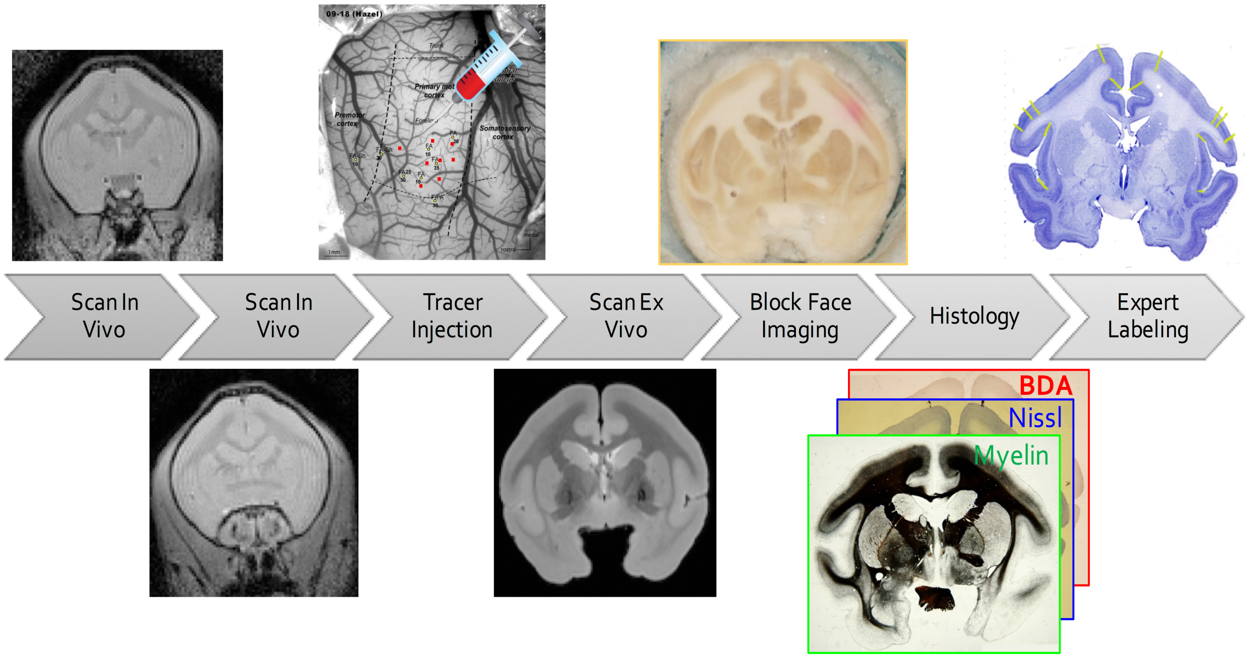

Figure 4.1 Atlas data acquisition pipeline.

### 4.2.2 MRI Methods

*Animals*

The full acquisition pipeline (Figure 4.1) was completed for three subjects (subjects #1-3), while three additional subjects (#4-6) were acquired only after sacrifice and did not undergo in vivo scans nor tracer injections. The data used to construct the atlas were acquired as part of a longer-term study validating the biological basis of diffusion MRI, hence additional subjects will be continually added to the database.

*In Vivo Imaging*

All in vivo imaging procedures were performed on a Varian 9.4 T, 21 cm horizontal bore imaging system, using a quadrature birdcage volume coil (inner diameter = 85mm). The two (or more) in vivo sessions were separated by at least a 20-day interval. During MRI data acquisition, each monkey was maintained under stable anesthesia (isoflurane 0.5%- 1.0%) and mechanically ventilated (40 respiration cycles/min), with head and body stabilized in an MR compatible frame. Vital signs including heart rate (Nonin), core body temperature (SA Instruments), respiration pattern and EKG (SA Instruments), end tidal CO2, and SpO2 (SurgiVet) were monitored and maintained at normal levels throughout the imaging session. Both structural and diffusion-weighted images were acquired in vivo. Structural images were acquired with a standard T1-weighted gradient echo multi-slice (GEMS) sequence (TR = 404ms, TE = 2.4ms, flip angle = 20˚, 630µm isotropic voxels, 64×64×80 matrix). Diffusion-weighted images were acquired using a pulsed gradient spin echo (PGSE) echo planar imaging (EPI) sequence (TR=5.5s, TE=44ms, 32 gradient directions, 630um isotropic voxel, 64×64×65 matrix) with a b-value, or diffusion weighting, of 1000 s/mm$^2$.

*Ex vivo Imaging*

Four weeks after the second in vivo scan, the monkey was given a lethal dose of barbiturate, and perfused through the heart. All blood was rinsed out with physiological saline (0.9% NaCl) followed by fixative (4% paraformaldehyde). The brain was removed from the skull and stored in buffered saline overnight. Ex vivo imaging was performed on the same Varian 9.4 T magnet and also included both structural and diffusion-weighted contrasts. Structural contrasts were acquired with a GEMS sequence with full brain coverage (TR = 963ms, TE = 4ms, flip angle = 20˚, 300µm isotropic voxels, 192×128×115 matrix). Diffusion weighted scans were performed using a PGSE multi-shot spin-warp imaging sequence with the same FOV as the structural images (TR=4.6s, TE=42ms, 32 gradient directions, b≈1000s/mm2, 300µm voxel, 192x128x115 matrix).

A slightly different protocol was followed for the three additional subjects (subjects #4-6) that were acquired only after sacrifice (and hence did not have in vivo scans). These brains were also perfusion fixed with 4% paraformaldehyde preceded by rinse with physiological saline. Brains were then removed and immersed for 3 weeks in phosphate-buffered saline (PBS) medium with 1mM Gd-DTPA in order to reduce longitudinal relaxation times [184]. The brains were then placed in liquid Fomblin (California Vacuum Technology) prior to scanning. For these specimens, structural imaging was performed using a 3D gradient echo (GE3D) sequence (TR = 50ms; TE = 3ms; flip angle = 45°) at 200um isotropic resolution. Diffusion data were acquired using a 3D spin-echo multi-shot diffusion weighted EPI sequence (TR = 410ms; TE = 41ms; NSHOTS = 4; NEX = 1; Partial Fourier k-space coverage = 0.75) at 300um isotropic resolution. Diffusion gradient duration and separation were 8ms and 22ms, respectively, and 101 diffusion weighted images with uniformly spaced directions were acquired at b-values 3,000, 6,000, 9,000, and 12,000 s/mm2. Use of increased numbers of DWIs and larger diffusion weightings allows advanced diffusion processing techniques that require more directions and/or b values than common DTI.

### *MRI data processing*

Diffusion MRI pre-processing was performed in the coordinate system the data were acquired in. Steps included correction for movement, susceptibility induced distortions, and eddy currents using FSL's *topup* and *eddy* algorithms [185]. The gradient tables were rotated based on the transformations obtained from the corrections. Next, for web visualization, processing is performed in "block-space" (see Section 4.2.4 Atlas Framework, Registration), although the registration procedure allows data to be moved to any space (i.e. histology, block, or MR-space) for comparison or overlay between modalities. Diffusion tensors were calculated using weighted-linear least squares fitting, from which maps of mean diffusivity (MD), fractional anisotropy (FA), and diffusion-encoded color-maps were computed. Tensor results are visualized as ellipsoidal glyphs, representing the proton displacement isosurfaces. Constrained spherical deconvolution (CSD) was performed for the high angular resolution datasets (monkeys 4-6) using MRTrix software [186]. CSD results are visualized as glyphs representing the estimated fiber orientation distributions. Finally, structural contrasts for all monkeys are also visualized in block-space.

*White Matter Labels*

The atlas contains individual white matter labels for three monkeys (#1-3), based on processed ex vivo diffusion weighted images using diffusion fiber tractography [55]. Detailed procedures are described in [187]. Due to structural similarities between the macaque and squirrel monkey brain, the results of a comprehensive set of histological tracer injections of the macaque brain, described in [110],were used as a reference for both seeding and refining tracts. Deterministic fiber tractography, and subsequent tract trimming and editing, were performed in DSI Studio [188]. Tracking parameters (including FA threshold, step size, angular threshold) were manually tuned according to the characteristics of each white matter bundle. All 3D fiber tracts were stored as tract density maps, and thresholded, resulting in a binary mask for each white matter pathway. All white matter pathways were checked by a neuroanatomist with expertise in nonhuman primate brain structure, assessing the coarse shape and orientation of each tract, the gray matter structures next to each bundle, and the cortical regions connected by the pathways. This procedure resulted in 57 white matter labels for each monkey.

### 4.2.3 Histological Methods

*Tracer Injection*

BDA is a commonly utilized neuroanatomical tracer for studying neural pathways. Because it can be transported both anterograde and retrograde, BDA can yield sensitive and detailed labeling of both axons and terminals, as well as neuronal cell bodies [189]. This tracer relies on axonal transport systems; thus, BDA injection is performed prior to ex vivo scanning (see Figure 4.1). Under general anesthesia using aseptic techniques, BDA (Molecular Probes Inc., Eugene, OR) was injected (as a 10% solution in phosphate buffer) into left hemisphere M1 cortex of three monkeys (subjects #1-3). Surgical, microstimulation, and injection procedures were performed following those described in [160, 190]. Pressure injections of BDA were carried out using a 2 ul Hamilton syringe. Eight injections (1 ml/ site) were made in order to cover a large M1 region representing the forearm as identified by intracortical microstimulation. After surgery, the monkey was allowed to recover from the procedure, giving the tracer sufficient time to be transported along axons to all regions connected to M1.

### *Histological Acquisition*

Following ex vivo MRI scanning, the brain was frozen and cut serially on a microtome in the coronal plane at 50 um thickness. All sections were collected in phosphate buffer, but prior to cutting every third section (i.e., at 150 mm intervals), the surface of the frozen tissue block was photographed using a Canon digital camera (image resolution = 50 um/pixel, image size = 3330×4000 pixels, number of images per brain ~ 280), mounted above the microtome. These block-face images have been shown to produce more robust inter-modality registration results by providing a relatively undistorted intermediate reference space between the histological and MRI data [191].

Three stains were performed for each brain. A cresyl violet Nissl stain [192] for identification of cell bodies, a Gallyas silver stain [193] to identify myelinated axons, and processing for BDA [189] to trace pathways associated with M1 cortex. Sections were divided into six series, and every sixth tissue section was processed for a given stain (for example sections #1, 7, 13 for Nissl).

Whole-slide brightfield microscopy was performed using a Leica SCN400 Slide Scanner at 20x magnification, resulting in a maximum in-plane resolution of 0.5um/pixel. The images are stored in the Leica image file format (file extension: SCN), which stores a hierarchical series of images at varying resolution levels. Each series has the associated size, position, and resolution, as well as the image data stored as TIFF data. For example, there are five levels, ranging from level #0 at 0.5 um/pixel (typical size ~80,000×80,000 pixels) to level #4, down-sampled by a factor of 256 to a resolution of 128 um/pixel (typical size ~300×300 pixels). Each level has ¼ the resolution of the previous level.

### *Cortical Labels*

The atlas contains cortical labels for three monkeys (#1-3) that were histologically defined based on cytoarchitectural features revealed in Nissl-stained sections. Eighteen cortical regions of interest (ROIs) in the frontal and parietal lobes were manually labeled by an experienced neuroanatomist on the digitized Nissl-stained slides. Labelling was performed using ITK-SNAP (Version 2.4.0), and labels were digitized to create masks for each ROI.

### 4.2.4 Atlas Framework

In order to transfer information between high-resolution microscopy and MRI data, a multi-step registration scheme was utilized. Figure 4.2 summarizes the steps of this procedure. The aim is to provide an atlas framework which facilitates comparisons across modalities.

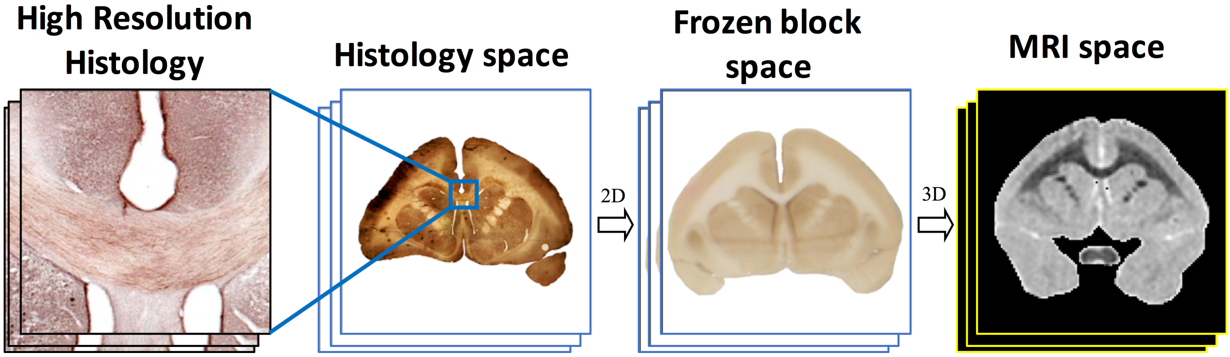

Figure 4.2 Atlas framework. Registration from one space to another allows comparisons across modalities.

*Registration*

The multi-step registration utilized here is very similar to the registration procedure validated in an earlier study [194], which showed that the accuracy of the overall registration was approximately one MRI voxel (~0.3mm). From the Leica image file, the TIFF image stored at 128um/pixel (down-sample factor 256) was extracted and registered to the down-sampled photograph (256×256 pixels at a resolution of approximately 128um/pixel) of the corresponding tissue block using a 2D affine transformation followed by a 2D non-rigid transformation, semi-automatically calculated via the Thin-Plate Spline algorithm [195]. Next, all down-sampled block face photographs were assembled into a 3D block volume and registered to the corresponding 3D MRI volume using a 3D affine transformation followed by a non-rigid transformation automatically calculated via the Adaptive Bases Algorithm [196]. The deformation fields produced by all registration steps are saved in order to transfer any set of acquired data (or processed data) to any desired space for comparisons.

For the web-interface, we have chosen to display all data (high resolution histology, block-face photographs, in vivo and ex vivo MRI) in the intermediate block-space.

*Layer construction*

As described above, the histology images are captured at a resolution of 0.5um/pixel. For comparisons of high-resolution histology with MRI images that have fields-of-view on the order of tens-of-millimeters (for example ~40 mm), the histology file would contain billions of pixels (~80,000×80,000 pixels), making the image much larger than is reasonably handled in a browser viewport, and hindering interactive panning or zooming functions. For this reason, all images are "shredded" into smaller PNG files (on the order of ~256×256 pixels) which are dynamically loaded and stitched together for viewing (see Web Viewer Tool section for details). In this way, the user can assess the data at a resolution suitable for the task at hand, loading and manipulating millions of pixels rather than billions.

All histological images were shredded in block-space, and in the coronal plane. For histological level #4, the OpenSlide [197] library (a C-based library for whole-slide digital images) was used to read and extract the corresponding image matrix from the SCN file, and the image was deformed to block-space using the appropriate 2D deformation field. Finally, the 256×256 image was saved as a PNG. For higher-resolution levels (levels #3 through #0), the deformation field was up-sampled to the appropriate spatial resolution, the corresponding image matrix was read from the SCN file, and the deformation field was applied to this image. The final histological images (now in block-space) were saved as a series of 256×256 PNGs covering the entire field-of-view. For example, level #3 contains 16 PNGs (four rows by four columns), while level #0 (at 0.5um/pixel) contains 65,536 PNGs (256 rows by 256 columns). This procedure was repeated for every slice in block space. Finally, all PNGs were stored on a CentOS 7 web-server, and a Postgres database created to store meta-information about image locations and spatial positions

Similar shredding was performed for MRI and block-face data. Because these are not acquired at high resolution, they are saved as PNGs at the resolution of the block-face image only, corresponding to histology level #4. In addition to coronal images, these two modalities are also shredded in axial and sagittal views to facilitate 3D localization and visualization.

### *Web Viewer Tool*

The web interface aims to support exploring the squirrel monkey brain through both MRI and histological imaging modalities, as well as the relationship between them. Functionality includes the ability to page through MRI volumes in coronal, axial, and sagittal orientations, with cross-hairs showing the 3D position in the brain, displayed with a tri-planar viewer. Drop-down menus allow navigation through different contrasts, sessions, and subjects. Overlays include DTI and CSD diffusion glyphs, as well as both white matter and gray matter labels.

On the histological side, the website displays slices, and facilitates navigating across slices with a slider, as well as scrolling or panning across a slice. Zooming can be performed through sliders and mouse functionality, with a mini-map utilized to display current screen position in the image. Again, drop-down menus allow navigation through different staining contrasts.

Finally, registration of the histology and MRI data supports overlays between the aligned modalities, showing the differing contrasts in the same parts of the same brain. Histology can be overlaid on MRI contrast, with the ability to switch between the various contrasts, as well as change the transparency of the histology modality.

The web viewer is a Python Flask web server that uses PostgreSQL to access the database of images. The web frontend uses HTML5 and the javascript library AngularJS and makes requests to the web server in order to dynamically retrieve images. Specifically, the frontend requests information in the form of JSON text data (image size, number of slices, etc.) and uses this information to form a URL to a specific image on the web-server. The images are rendered using WebGL, including the histology mosaic and the different MR contrasts. When zooming, the frontend uses the magnification factor to determine which histological level to load, and interpolates the images until the magnification reaches the next highest histological level.

All data, including shredded images, processed and unprocessed histology and MRI, block-face images, and deformation fields, are made available at (https://www.nitrc.org/projects/smatlas/). The back-end currently includes upwards of 1.2TB of data.

### 4.2.5 Additional content

Additional content was added to the atlas web-viewer in the form of the VALiDATe29 multi-channel atlas of the squirrel monkey brain [183]. This atlas is based on multiple types of MRI contrast acquired on 29 squirrel monkeys, and created using nonlinear registration techniques, resulting in a population-averaged stereotaxic coordinate system. The MRI-based atlas contains T1, T2, T2*, and diffusion-weighted MRI templates, as well as population averaged cortical and white matter labels. The atlas facilitates spatial normalization for comparisons of data across subjects or differing experimental conditions, as well as label propagation to identify regions of interest. The VALiDATe29 atlas is presented in the web-viewer in its own space (as opposed to all other data in block-space), in sagittal, coronal, and axial orientations. Functionality includes scrolling, zooming, and panning throughout the atlas-space as well as overlays of labels and differing contrasts. VALiDATe29 data is made available with all other data content (https://www.nitrc.org/projects/smatlas/), as well as downloadable separately at https://www.nitrc.org/projects/validate29/ as described in [183].

## 4.3 Results

The squirrel monkey atlas is available at https://smda.vandyxnat.org/smda/, and the complete set of images upon which the atlas is based is freely available at (https://www.nitrc.org/projects/smatlas/). This includes shredded images of all imaging modalities, as well as processed and unprocessed histology and MRI, deformation fields, as well as VALiDATe29 atlas and templates.

### 4.3.1 Atlas Contents

All data in the web-viewer are aligned to each subject’s block-face images.  Figure 4.3 shows a selection of MRI (top) and histology (bottom) data for a single subject. MRI data for all subjects, all sessions, and all contrasts (both acquired and calculated contrasts) are presented in a tri-planar viewer. Figure 4.3 (top) shows the mean ex vivo diffusion weighted image, the ex vivo T2 contrast, the in vivo (session 1) T2 contrast, and the in vivo (session 2) processed FA maps for a selected subject, which demonstrates excellent alignment across sessions and across modalities. In addition to these, contrasts of MD, diffusion tensor elements, mean b0 images, radial anisotropy, diffusion weighted images, RGB color maps, and primary eigenvector maps are also available and viewable.

Histological data for each subject are displayed as coronal slices (Figure 4.3, bottom), and currently include Nissl, Myelin, and BDA contrasts. Again, contrasts demonstrate excellent alignment in most areas of the brain, even at increased levels of magnification.

Additional content includes block space images, as well as all MRI contrasts made available through the VALiDATe29 squirrel monkey atlas [183]. In addition, white matter and gray matter labels, as well as DTI (and CSD) glyphs are viewable, although these will be utilized most often as overlays on histological or MR modalities (see Section 4.3.2 Atlas Interface and Functionality).

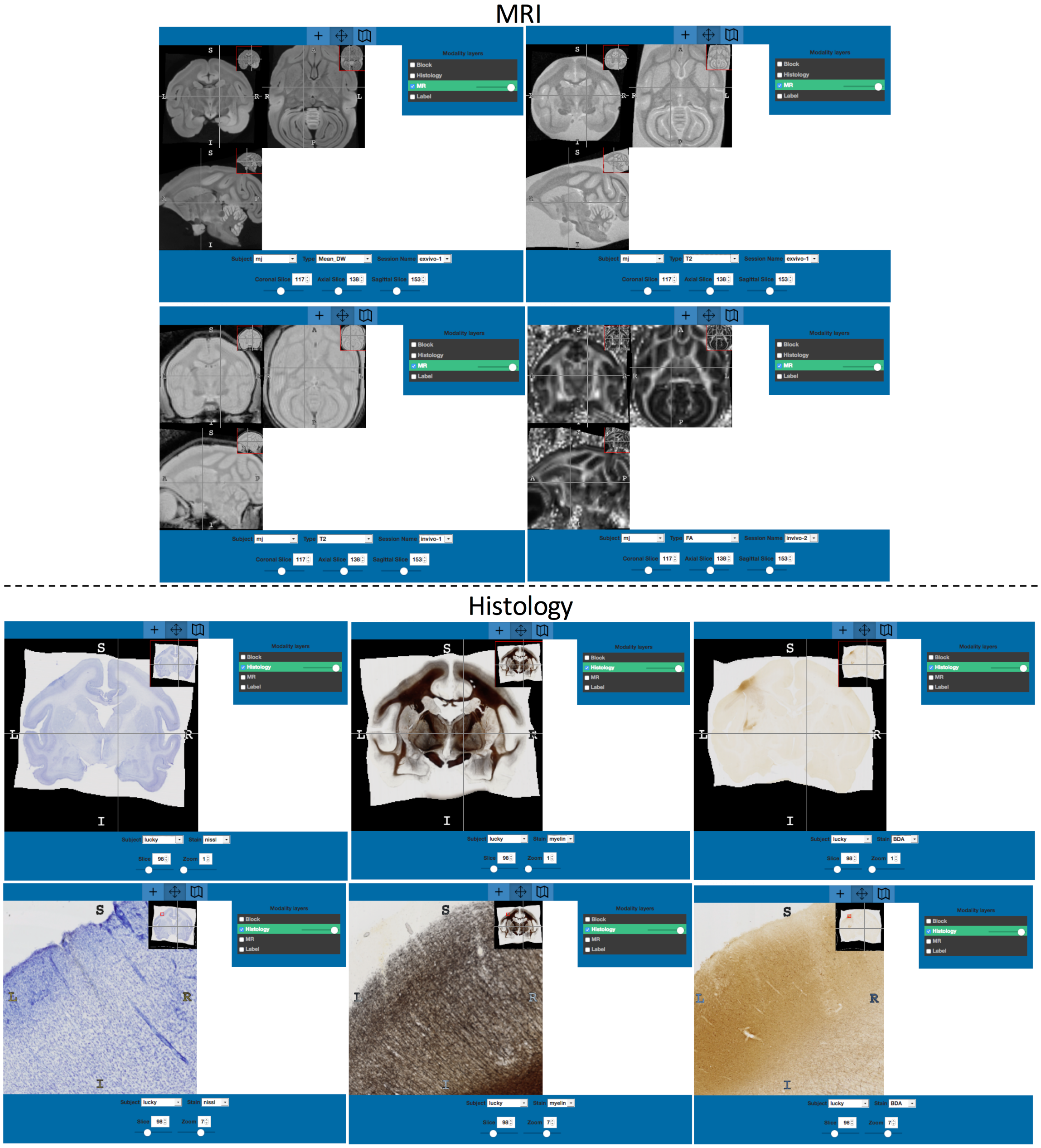

Figure 4.3 Atlas Contents. For all subjects and sessions, the atlas contains both MRI (top) and histological (bottom) data. Here, selected MRI contrasts are shown for a single subject for the same coronal, sagittal, and axial slices. Similarly, histological contrasts of Nissl, myelin, and BDA stains are shown for the same single subject.

### 4.3.2 Atlas Interface and Functionality

Figure 4.4 shows the basic atlas interface for visualizing MRI, histology, and block face data. The image type is selected using the "Modality Layers" menu. For MRI contrast (Figure 4.4, A), the "Selection" menu below the image display window contains drop-down menus that allow selection of subject, MR contrast type, and session, as well as sliders to facilitate scrolling through the 3D volume. In addition, a crosshair tool, pan tool, and minimap tool are selectable in the toolbar above the image display, which facilitate navigation and localization within the image volumes.

For histological contrast (Figure 4.4, B), images are displayed as coronal slices, and the Selection menu allows choice of subject, stain, and slice. In addition, the menu contains a slider for zoom, which allows viewing histology at a range of magnification levels. Zoom can also be controlled through mouse wheel scrolling, with panning controlled by dragging the mouse. By default, the minimap is displayed, which shows the current location and field of view. Finally, the toolbar again allows selection of crosshair and panning tools, as well as the ability to enable/disable the minimap.

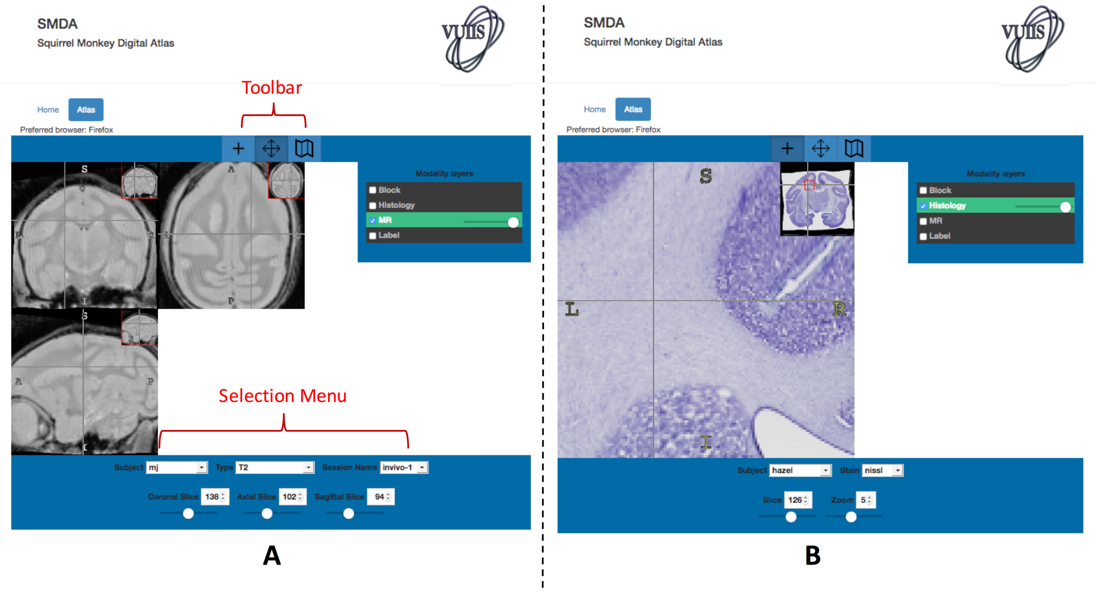

Subject mj
Type T2
Session Name invivo-1
Coronal Slice 138
Axial Slice 102
Sagittal Slice 94

Subject hazel
Stain nissl
Slice 126
Zoom 5

Figure 4.4 Atlas interface and functionality. The toolbars, menus, and display associated with MRI (A) and histology (B) modalities are shown.

Multiple modalities can be displayed simultaneously. For example, any histological stain can be overlaid onto any coronal MRI contrast. Figure 4.5 (A and B) shows an example overlay of a Nissl-stained histological slice overlaid on an ex vivo FA map. The transparency of each layer can be adjusted using the slider bar (note differences between Figure 4.5 A and B). In addition, the overlay order can be changed by dragging and dropping the label in the “Modality Layers” menu, with the order of the labels corresponding to the order of the layers.

Finally, various derived maps can be displayed and/or overlaid on images. For example, anatomical labels (Figure 4.5, C) can be shown in order to identify the region of the brain currently under investigation. Finally, DTI glyphs, which highlight the direction of greatest diffusivity, can be shown over both MRI and histology (Figure 4.5, D).

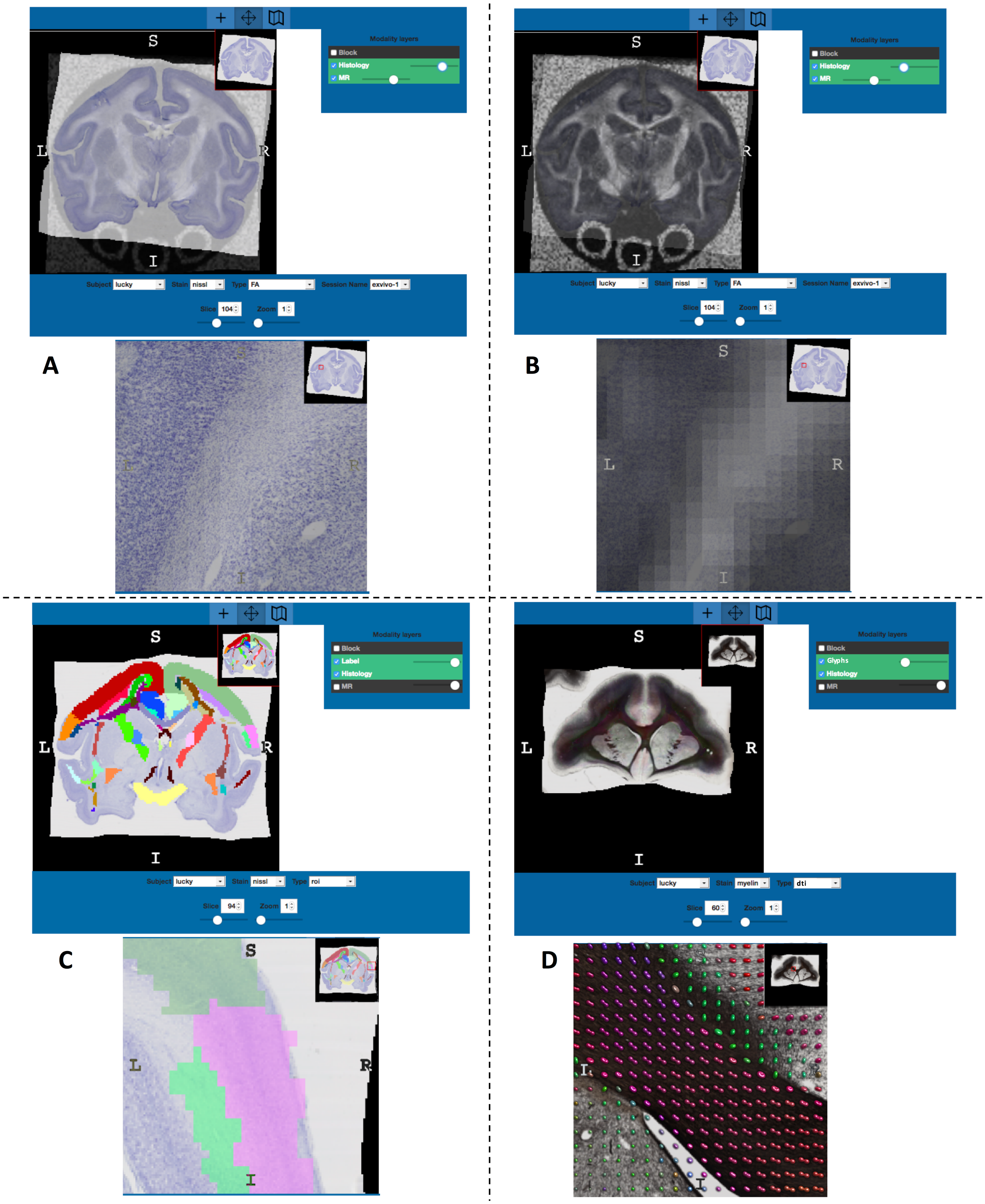

Subject lucky Stain nissl Type FA Session Name exvivo-1
Slice 104 Zoom 1

Subject lucky Stain nissl Type FA Session Name exvivo-1
Slice 104 Zoom 1

Subject lucky Stain nissl Type roi
Slice 94 Zoom 1

Subject lucky Stain myelin Type dti
Slice 60 Zoom 1

Figure 4.5 Image overlays. Overlays of Nissl-stained histology and FA maps from MRI (A and B) at low (top) and high (bottom) zoom levels. Overlays of ROI labels (C) and DTI glyphs (D) at low (top) and high (bottom) zoom levels. Alpha levels can be adjusted for each contrast/overlay independently.

### 4.3.3 Applications

The data in this atlas can be utilized for a broad range of neuroscience investigations. Here, we briefly describe three studies which have utilized the data contained in this atlas: (A) validation of fiber tractography, (B) comparison of fiber orientation and DTI measurements, and (C) label propagation for fiber tractography.

Using the BDA stained histology in this atlas, Gao et al. [160] compared DTI tractography to “ground truth” M1-cortical connectivity revealed by the tracers. By segmenting BDA from histological sections and running tractography algorithms directly on the aligned MRI data, comparisons are easily made between the two modalities (Figure 4.6, A). Doing this, the authors found that DTI tractography of major pathways predicted inter-regional connectivity comparable to the histological connectivity, but was less reliable in measuring voxel-wise connectivity strengths. Future tractography validation studies with these data could investigate newer high angular resolution algorithms, or other tractography methods [167].

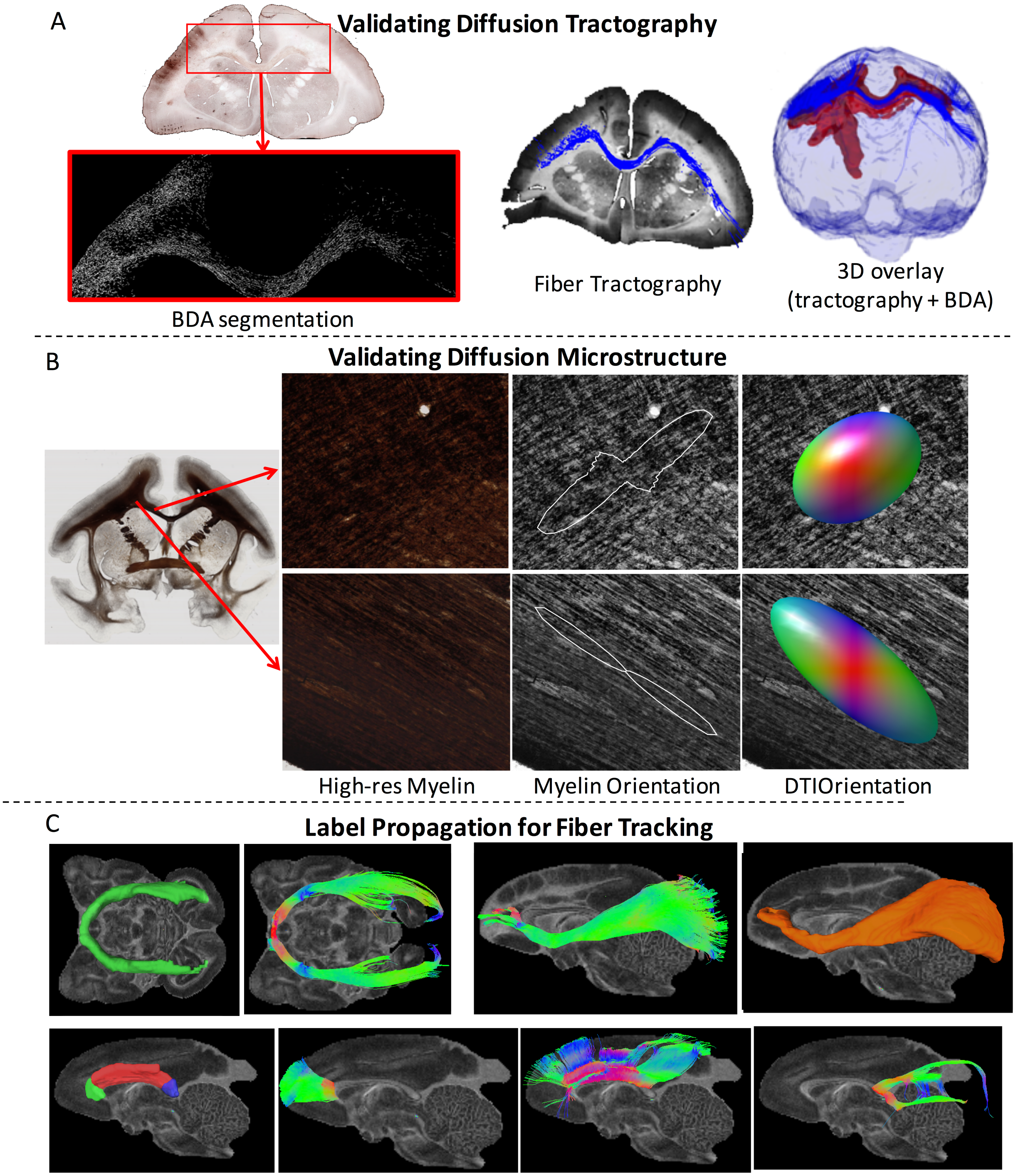

Figure 4.6 Atlas applications. The data in this atlas can be used for validation of diffusion tractography (A) by comparing BDA stains (red in the overlay) to fiber tractography (blue) algorithms; validating diffusion microstructure measurements (B) through comparisons with myelin or Nissl stained sections; and (C) label propagation to new subjects for fiber tracking or region of interest delineation. Here, fiber tractography for the Optic Tract (top left), inferior occipito-frontal fasciculus (top right) and genu, body, and splenium of the corpus callosum (bottom) are shown. We note that, in these examples, the BDA (A), myelin (B), and labels (C) are directly from our atlas data, while the tractography (A and C) and orientation maps (B) are calculated results not currently in the atlas, but easily derived from atlas data.

Choe et al. [133] used a framework similar to that in this atlas in order to compare myelin-stained brain sections directly to the diffusion parameters from registered DTI (Figure 4.6, B shows similar results based on atlas data). Using a Fourier-based image processing technique to extract myelin orientations, the authors found that the major eigenvector of the tensor aligned well with the underlying myelinated fibers in voxels with highly coherent fibers, and was able to identify regions of complex fiber structures via a reduced FA (Figure 4.6, B for examples using atlas data). The myelin data in our atlas could be processed using similar techniques, in combination with the co-aligned MRI data, to validate both DTI and higher order diffusion models.

A final example application of the atlas is in identifying regions of interest. In addition to the web-based label overlays to localize regions of interest on the histology or MRI, these labels can also be propagated to new datasets for comparisons of data across different subjects or across varying experimental conditions [183, 187]. The atlas labels can be registered to an individual squirrel monkey brain (or vice-versa) and used for delineating regions of interest, or as seeds for fiber tractography. For example,  Figure 4.6C shows fiber tractography performed after labels for the optic tract, inferior occipito-frontal fasciculus, and corpus callosum were registered to a squirrel monkey diffusion dataset, and used as seed regions for tractography.

## 4.4 Discussion and Conclusion

Here we present the construction of a web-based multi-modal atlas of the squirrel monkey brain, called the Combined Histological-MRI Integrated Atlas of the Squirrel Monkey (CHIASM). The atlas data include both in vivo and ex vivo MRI scans (including anatomical and diffusion contrasts), tracer injections, and a variety of histological stains. Calculated parameters, including diffusion MRI glyphs and region of interest labels, are also included in the atlas. All data are presented in a common space, a framework which facilitates comparisons across imaging modalities. Data from all subjects are accessible through a web-based atlas viewer, which allows visualization and interaction with data, allowing the user to select contrasts, locations, and varying resolutions. This multi-contrast atlas provides a convenient medium for comparisons of neuroanatomical findings across subjects or modalities, for example, validating MRI measurements with histological correlates. The web-viewer is accessible at https://smda.vandyxnat.org/smda/, and the complete set of images upon which the atlas is based are freely available at (https://www.nitrc.org/projects/smatlas/).

Future work will include more comprehensive MRI protocols on a larger set of animals, both in vivo and ex vivo. Larger b-values and more diffusion directions will facilitate implementation and validation of a larger selection of high angular resolution diffusion techniques [198]. In addition, multiple MRI modalities can be incorporated, including BOLD contrast, susceptibility imaging, or myelin volume fraction imaging. For histology, more stains will be included, for example acetylcholinesterase to facilitate identifying thalamic nuclei [190]. In addition to wide-field light microscopy, high resolution 3D confocal images can be included to facilitate comparisons of fiber orientation information estimated from diffusion MRI [199]. Finally, new forms of processed data, including fiber orientation maps [200] or quantified BDA tracer densities, should be included in future iterations of the atlas.

# CHAPTER 5: THE CROSSING FIBER PROBLEM

## Prologue

The most commonly implemented diffusion MRI method, diffusion tensor imaging (DTI), cannot adequately describe voxels with complex fiber geometries (see Section 2.4.2 The Crossing Fiber Problem and Figure 2.3), which can ultimately affect the fidelity of fiber tractography. One may expect that technological advances in MRI (including higher field strengths, stronger gradients, and faster imaging) may lead to a decreased prevalence of the crossing fiber problem by enabling an increased spatial resolution of images. Here, we investigate the prevalence of this crossing fiber problem using both histology and MRI of a macaque, using the acquisition and processing framework developed in the atlas. We ask at what resolution we expect this crossing fiber problem to be solved, if any. If unresolved, higher order models of diffusion become crucial to the successful implementation of tractography.

## Abstract

It is now widely recognized that voxels with crossing fibers or complex geometrical configurations present a challenge for diffusion MRI (dMRI) reconstruction and fiber tracking, as well as microstructural modeling of brain tissues. This “crossing fiber” problem has been estimated to affect anywhere from 30% to as much as 90% of white matter voxels, and it is often assumed that increasing spatial resolution will decrease the prevalence of voxels containing multiple fiber populations. The aim of this study is to estimate the extent of the crossing fiber problem as we continually increase the spatial resolution, with the goal of determining whether it is possible to mitigate this problem with higher resolution spatial sampling. This is accomplished using ex vivo MRI data of the macaque brain, followed by histological analysis of the same specimen to validate these measurements, as well as to extend this analysis to resolutions not yet achievable in practice with MRI. In both dMRI and histology, we find unexpected results: the prevalence of crossing fibers increases as we increase spatial resolution. The problem of crossing fibers appears to be a fundamental limitation of dMRI associated with the complexity of brain tissue, rather than a technical problem that can be overcome with advances such as higher fields and stronger gradients.

## 5.1 Introduction

Diffusion-weighted magnetic resonance imaging (dMRI) is a technique sensitive to the random thermal motion of water [22], providing contrasts that give unique insights into tissue architecture. In the neuroimaging community, dMRI research can loosely be divided into two main classes [201]. The first concerns mapping the neural fiber pathways, or connectivity, of the brain. These fiber “tractography” techniques exploit diffusion anisotropy to infer the orientation of the underlying white matter (WM) in each voxel, and use the field of these discrete orientation estimates to reconstruct continuous trajectories called streamlines (for review, see [8]). The second class concerns mapping microstructural properties of the tissue. Rather than focusing on fiber orientation estimation, these techniques attempt to extract properties such as axon diameter, axon density, or degree of myelination – measures serving as biomarkers for WM and gray matter (GM) physiology and pathology. Despite significant progress in assessing microstructure and connectivity, both areas of research are complicated when voxels contain complex fiber configurations, an issue that has generically been referred to as the “crossing fiber problem” [201-203].

This crossing fiber problem typically refers to the situation where there are two or more differently oriented fiber bundles located in the same dMRI imaging voxel [202, 203]. This causes a partial volume effect, with multiple fiber bundles contributing to the dMRI signal. In general, this partial volume effect can occur in any situation where axons within a voxel do not all run parallel to each other. Therefore, the ‘crossing fiber’ problem encompasses not only crossing fibers, but also fibers of bending, fanning, or kissing geometries.

It is now widely recognized that these geometries can lead to ambiguous or incorrect estimates of fiber orientation [33, 120, 204] and subsequent failure of tractography [34, 59], as well as misleading microstructural indices. This is particularly true for one of the earliest, yet arguably the most common, dMRI technique, diffusion tensor imaging (DTI) [30], which models a single primary fiber direction per voxel. While a plethora of methods have been introduced to resolve crossing fibers for tractography [24, 40, 41, 43, 58, 120, 205], they are still plagued by assumptions on the signal, lengthy acquisition requirements, and limited ability to resolve fibers crossing at acute angles. Similarly, methods have been introduced to describe axon diameters, dispersion, and density [48, 52-54, 206-208], but typically assume a single known orientation of axons in the model, limiting their use to small regions of the brain with known orientation, or leading to ambiguous measurements in crossings between tracts with different orientations.

Given its implications on dMRI neuroimaging studies, it is important to fully investigate the scope of the crossing fiber problem. With axon diameters on the order of microns [209], fiber tracts (i.e., bundles of axons) often less than a few millimeters wide, and dMRI voxels typically 2-3 mm in each dimension on clinical scanners, it is not unreasonable to expect crossing fibers to be widespread throughout the brain. In fact, fitting dMRI data to multiple tensors, Behrens et al. [34] found that nearly one-third of voxels contain 2 fiber populations. Moreover, using data acquisition and modeling techniques specifically designed to estimate the prevalence of crossing fibers, Jeurissen et al. [210] found that as many as 90% of white matter voxels are affected by crossing fibers. However, these results have yet to be validated through histology. Also, because these results were obtained using dMRI methods designed for detecting discrete sets of fiber orientations, or discrete “peaks” in the fiber orientation distribution (FOD), it is unclear whether these fractions represent true crossing fibers, or something like fiber “spreading” that is interpreted as multiple distinct fiber populations using these dMRI techniques.

It is often assumed that increasing the spatial resolution will decrease the prevalence of voxels containing multiple fiber populations. If true, there would be a tradeoff between minimizing the crossing fiber problem (increasing spatial resolution), and increasing signal-to-noise ratio (SNR), increasing angular resolution (number of diffusion weighting directions), and increasing diffusion weighting (or b-value, which has been shown to provide greater sensitivity to fiber orientations). At present, there is little consensus on the optimal acquisition protocol, which is typically determined based on the type of questions to be answered from the data. Moreover, it is unknown what resolution is necessary to ameliorate this crossing fiber problem, or if it is at all feasible with advances in imaging methods in the foreseeable future.

In this study, we set out to estimate the extent of the crossing fiber problem as a function of spatial resolution. Specifically, our goal is to determine whether it is possible to significantly mitigate the problem by increasing spatial resolution. This is performed using both ex vivo MRI data from the macaque brain, followed by histological analysis of the same specimen. Ex vivo dMRI offers several experimental advantages including longer scanning times and absence of motion, allowing acquisition of data with much higher SNR at a resolution currently unachievable in the clinic. Histological methods allow us to further extend this analysis to resolutions not possible even on pre-clinical scanners. In addition, it serves as a validation of the current standard MRI techniques for resolving crossing fibers. For dMRI, we report the fraction of crossing fibers in WM and GM, as well as the inter-fiber angle of crossing fibers in each voxel, as a function of acquisition resolution. For histology, we report the fraction of voxels with a "complex" geometry at varying resolution levels. In addition, in direct analogy to dMRI, we report on a subset of these complex voxels – those that exhibit distinct "crossing" fibers. Finally, we also describe the histological inter-fiber angle of these fibers at each resolution level.

## 5.2. Methods

### 5.2.1 MRI acquisition

MRI experiments were performed on a single hemisphere of an adult Rhesus Macaque (Macaca Mulatta) brain that had been perfusion fixed with physiological saline followed by 4% paraformaldehyde. The brain was then immersed for 3 weeks in phosphate-buffered saline (PBS) medium with 1mM Gd-DTPA in order to reduce longitudinal relaxation time [184]. The brain was placed in liquid Fomblin and scanned on a Varian 9.4 T, 21 cm bore magnet. For WM/GM segmentation, a structural image was acquired using a 3D gradient echo sequence (TR = 50ms; TE = 3ms; flip angle = 45°) at 200um isotropic resolution.

Diffusion data were then acquired with a 3D spin-echo diffusion-weighted EPI sequence (TR = 340ms; TE = 40ms; NSHOTS = 4; NEX = 1; Partial Fourier factor = .75). Diffusion gradient duration and separation were 8ms and 22ms, respectively, and the b-value was set to 6,000 s/mm$^2$, which has been shown to be in the optimal range for modeling multiple fiber populations in ex vivo specimens [198]. A gradient table of 101 uniformly distributed directions [211] was used to acquire 101 diffusion-weighted volumes with four additional image volumes collected at b=0. This acquisition protocol was performed at imaging resolutions ranging from 800um isotropic to 300um isotropic, in 100um increments. All acquisition parameters were kept constant (including diffusion times), except for the field-of view and the number of phase encoding and readout samples required to achieve the intended resolution. Total acquisition time was approximately 48 hours.

### 5.2.2 MRI fiber orientation estimation

Fiber orientations were estimated using constrained spherical deconvolution (CSD) [45], and following the procedures developed and outlined in [210]. The diffusion-weighted signal was first deconvolved with the single-fiber response function [43, 45], estimated from all WM voxels with an FA > 0.7, to obtain the FOD fit to spherical harmonics of degree 8 (the response function was derived independently for each dataset). A peak-finding procedure was then performed to identify distinct fiber orientations. This algorithm uses a Newton optimization algorithm to identify local maxima of the FOD that meet a specific threshold criterion. As in [210], maxima in the FOD are included if the peak amplitude is >10% of the maximum peak amplitude. The number of unique peaks is then counted and assumed to be equal to the number of fiber populations in each MRI voxel. This procedure was performed in all voxels, for datasets at all acquired resolutions. In this study, we refer to voxels containing >1 discrete peaks as voxels with "*crossing fibers*" (peaks in directions $\hat{r}$ and -$\hat{r}$ are considered the same).

### 5.2.3 Histology Acquisition

After imaging, the brain was embedded in dry ice and sectioned on a microtome at a thickness of 25um in the coronal plane. Sixteen slices, covering the entire brain, were selected for this study. The selected tissue sections were stained for myelin using the silver staining method of Gallyas [193] and mounted on glass slides. Whole-slide brightfield microscopy was performed using a Leica SCN400 Slide Scanner at 20x magnification, resulting in an in-plane resolution of 0.5um/pixel.

### 5.2.4 Histological fiber orientation estimation

The histological fiber orientations were defined on myelin-stained slices using structure tensor (ST) analysis [134, 200, 212]. ST analysis is an image processing technique based on the dyadic product of the image gradient vector with itself, resulting in an orientation estimate of objects in every pixel in the image. These techniques have previously been performed on histological samples in the brain of rats [134], squirrel monkeys [199], macaques [136], and humans [200, 213].

Histological fiber orientation distributions were calculated by combining pixel-wise estimates of orientation over larger volumes of tissue, constructed to match potential MRI voxels. For example, a voxel with a resolution of 32um would be created by combining all orientation estimates in an area with a 32um by 32 um field of view. The FOD in each "voxel" was computed as the histogram of orientation estimates using 64 equally spaced bins, as performed in [200]. These FOD's were then fit to a von Mises distribution [214]

$$f(\theta;\mu,\kappa) = \frac{e^{\kappa cos\ 2(\theta-\mu)}}{2\pi I_0(\kappa)} \tag{19}$$

and a mixture of two von Mises distributions. Here, $\mu$ is center of the distribution with concentration parameter $\kappa$, and $I_0$ is the modified Bessel function of order 0. Also note the factor 2 in the exponent, which was included because the orientation distributions in this study are pi-periodic. Both distributions also included an isotropic component. Fitting was performed using the Matlab Curve Fitting Toolbox (The MathWorks, Natick, MA, USA).

Model selection was performed using the Akaike information criterion (AIC) [215]. The AIC is a measure of the quality of a given model, and quantifies the trade-off between model complexity and goodness-of-fit:

$$AIC = -2\,log(L) + 2K + \frac{2K(K+1)}{N-K-1} \tag{20}$$

where L is the likelihood of obtaining the data given the current model, K is the number of estimated parameters, and N is the number of measurements [215]. The lower the AIC, the more predictive the model is. Thus, the AIC was calculated for both the single and mixture von Mises distributions for each voxel, and the model with the lowest AIC was selected to represent the FOD in that voxel.

We then classified the histological voxels based on model selection and the resulting FOD. If a single von Mises distribution was the best fit, the voxel was classified as a "*single* *fiber*” voxel. In this case, the parameter θ reflects the dominant fiber orientation. If a mixture model was the best fit, the voxel was classified as a “*complex fiber*” voxel. To further classify the complex configuration, we performed a procedure analogous to that for MRI and searched for local maxima, or peaks, in the FOD that were >10% of the maximum peak amplitude. If two distinct peaks existed, the voxel was classified as a “*crossing fiber*” voxel. Thus, “crossing fibers” are a subset of “complex fibers”. Complex fibers that did not contain two distinct peaks in the FOD (i.e. not crossing) could be the result of asymmetric FOD’s due to geometries like fiber fanning or bending (see Discussion). The fiber classifications and definitions for both dMRI and histology are summarized in Table 5.1.

For all complex fiber voxels (including crossing fibers), we calculated the inter-fiber angle, or the angle that the parameter θ from the two distributions make with each other. These histological procedures were performed at “voxel” sizes ranging from 32 um isotropic to 1024 um isotropic, doubling the linear dimensions at each step. For both MRI and histological analysis, we present results on WM voxels only, as the crossing “fiber” problem refers specifically to axons in the WM tissue.

Table 5.1 Fiber classification definitions for MRI and histological analysis

| | | |
|---|---|---|
| **MRI** | Single Fiber | Voxel where FOD derived from CSD has 1 local maximum (1 peak) |
| | Crossing Fiber | Voxel where FOD derived from CSD has >1 local maximum (>1 discrete peaks) |
| **Histology** | Single Fiber | FOD derived from ST Analysis best fit to single von Mises distribution (1 peak) |
| | Complex Fiber | FOD derived from ST Analysis best fit to mixture of Von Mises distributions |
| | Crossing Fiber<br>(Crossing ⊆ Complex) | FOD derived from ST Analysis best fit to mixture of Von Mises distributions<br>**AND** FOD dervied from ST Analysis has >1 local maximum (>1 discrete peaks) |

## 5.3 Results

### 5.3.1 Fiber Orientation Estimation in Crossing Fiber Regions

A region of the brain containing crossing fibers of the superior corona radiata (SCR) and the body of the corpus callosum (BCC) is examined in detail in Figure 5.1. A color-coded orientation map at native resolution (Figure 5.1, A) demonstrates the ability to detect the orientation of individual myelinated fibers in these intersecting fiber bundles. Zooming in on a region of fiber crossings (yellow box), the left-right fibers of the BCC (blue/red) and superior-inferior fibers of the SCR (green/yellow) are intersecting in a woven “checkerboard-like” pattern, highlighting the stereotypical “crossing fiber” problem. Interestingly, even in the BCC (blue box), a region typically assumed to contain a single homogenous fiber population, ST analysis is able to capture a dispersion, or heterogeneity of orientations, on a microscopic scale.

To identify voxels in this region containing crossing or complex fiber configurations, the FODs were fit to a single von Mises and a mixture of von Mises distributions (Figure 5.1, B) at all resolution levels. At the coarsest resolution (1024um) the predominant white matter tract orientations are visible, even with broad peaks (low κ), and throughout the entire region of intersection. At increasing resolutions levels (256um and 64um) there is still evidence of crossing fibers. The peaks become narrower, yet there is still spatial coherence in peak orientations.

Maps of the types of fiber populations detected in histology (Figure 5.1, C, D) similarly show a high degree of structural coherence. As the voxel size decreases, there is evidence of crossing fibers in the BCC, whereas at a coarse resolution typical of dMRI, these regions do not contain multiple (distinct) peaks in orientation (Figure 5.1, C). However, at these coarse resolutions, nearly all voxels suggest a complex geometry (Figure 5.1, D). The orientations become less complex at the higher spatial resolutions, particularly in the BCC. However, a large percentage of voxels still do not support a simple single fiber geometry. The results of MRI data in the same region show trends qualitatively similar to that of the “crossing” fiber histological analysis; specifically, the BCC is composed of largely single fiber regions, yet, even at the highest spatial resolutions, crossing fibers still persist throughout the region of interest.

Figure 5.1, F summarizes the results in this region in plot form. From dMRI, the fraction of voxels with crossing fibers in this region increases as the image resolution increases. Similarly, the fraction of histological voxels exhibiting multiple peaks (i.e. crossing fibers) also increases at higher resolutions. Conversely, the histological “complex” fibers decreases as the resolution increases.

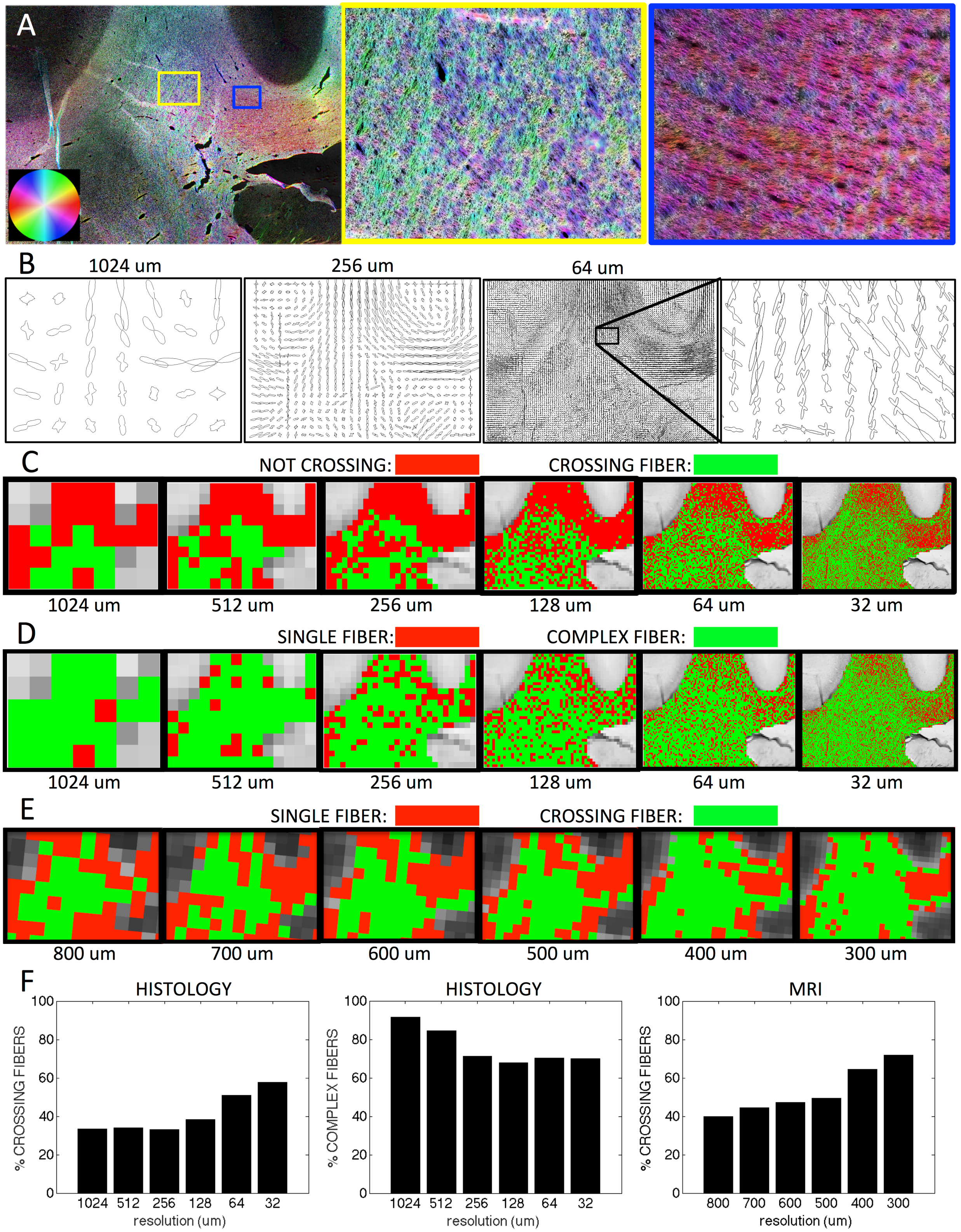

Figure 5.1 Fiber orientation estimation in a crossing fiber region. The results of structure tensor analysis on a myelin-stained histological slice shown as a color-coded orientation map (A), and shown zoomed in on two regions containing crossing (yellow box), and disperse (blue box) fibers. The resulting FODs are displayed at varying resolution levels (B). From the resulting FODs,

voxels are characterized as crossing fiber (C; green) vs. not-crossing fibers (C; red), as well as single fiber (D; red) vs. complex fibers (D; green), at all resolutions. Note that “not-crossing” voxels are those that with single fiber populations in addition to complex fibers that do not contain two discrete local maxima. Voxels from diffusion MRI in the same region are also displayed as single fiber (E; red) vs. crossing fibers (E; green). Histograms for this specific region of interest show percentages of crossing fibers (F; left) and percentages of complex fibers (F; middle) for histology, as well as percentage of crossing fibers (F; right) for dMRI.

### 5.3.2 MRI crossing fiber analysis

The prevalence of crossing fibers was determined for all voxels in the WM, at all resolution levels. Maps of the number of fiber populations detected in the WM are shown in Figure 5.2, A. At all spatial scales, large clusters of voxels containing two or more orientations are present throughout the brain. Examples of regions with two fiber populations include the BCC and anterior corona radiata (ACR) (label 1), BCC and ACR (label 2), and posterior thalamic radiation (PTR) and the superior longitudinal fasciculus (SLF) (label 3). Although labeled in the highest resolution dataset, these clusters appear structurally quite similar and of comparable size at all resolutions, although a slight reduction in the area of these crossing fiber regions at more coarse resolutions is discernable. A cluster of 3 fiber populations is shown at the intersection of the posterior corona radiata (PCR), the BCC, and the dorsal posterior corona radiata (DPCR) (label 4). Interestingly, this cluster nearly disappears in the 800 and 700 um datasets.

Figure 5.2, B displays the FOD glyphs that are typical of dMRI, at both the lowest and highest resolution levels. At both resolutions, we see orientation coherence across space in regions containing both single and crossing fibers. However, the 300um glyphs indicate a higher prevalence of voxels with multiple fiber populations (particularly those with 3 peaks), and qualitatively the glyphs appear shaper, with more concentrated orientation distributions.

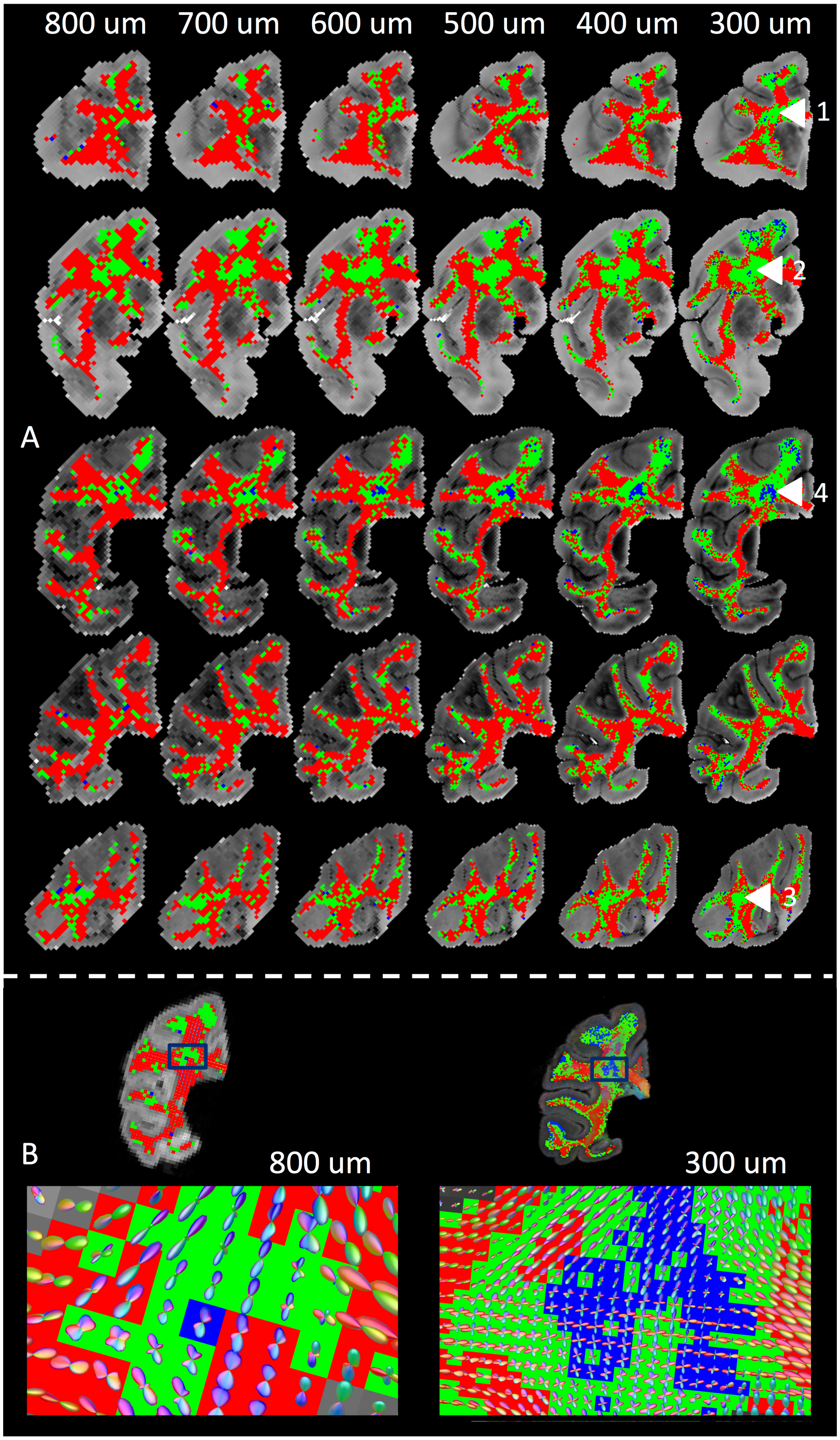

Figure 5.2 MRI crossing fibers. (A) Number of fiber orientations per voxel (red: 1, green: 2, blue: 3) estimated using CSD. Numbered arrows highlight regions of crossing fibers and are described in the text. (B) Glyphs highlighting FODs estimated using CSD for voxels at 800 um and 300 um isotropic. Note that background color corresponds to that in (A), while glyph color is

based on fiber orientation, where red, green, and blue represent fibers running right/left, anterior/posterior, and superior/inferior.

Figure 5.3 summarizes the incidence of crossing fibers for all acquired image resolutions. Consistent with the qualitative results of Figure 5.2, the fraction of crossing fibers increases as the voxel size decreases. Multiple fiber populations were found in 23% of all WM voxels at 800um isotropic resolution, and in 51% at 300um isotropic resolution.

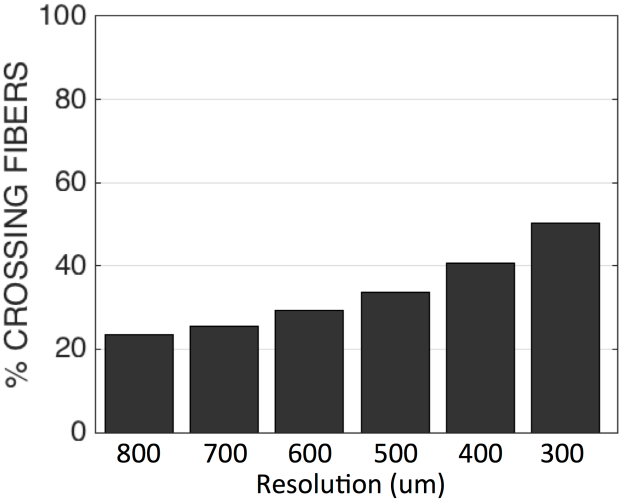

Figure 5.3 Percentages of crossing fiber voxels throughout the WM as determined using CSD, for different MRI acquisition resolutions.

The inter-fiber angle of all voxels with crossing fibers was investigated, and summarized as histograms in Figure 5.4. For all cases, a majority of the resolved fiber crossing occurred at nearly orthogonal angles. The 1st, 2nd, and 3rd quartile of crossing angles, in all cases, was in the range of 63-69°, 75-78°, and 83-85%, respectively. Similarly, for all datasets, almost all crossing angles detected (95% of all crossings) are greater than ∼47°.

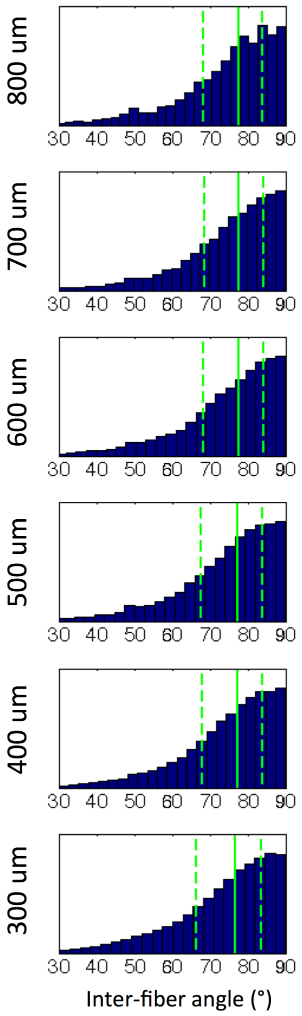

Figure 5.4 Histograms of inter-fiber angle for crossing fiber voxels in WM, at all acquired dMRI resolutions. The 1st, 2nd, and 3rd quartiles are shown as dashed, solid, and dashed lines, respectively.

### 5.3.3 Histological Crossing/Complex Fiber Analysis

To validate the dMRI measurements, as well as identify and quantify crossing fibers at resolutions currently unachievable with even preclinical imaging, ST analysis of histological sections was performed for all slices. Visual inspection of maps displaying crossing fibers (Figure 5.5) shows crossings in regions previously identified in MRI. These regions still show evidence of multiple, distinct fiber bundles down to resolutions of 32um. As in the dMRI data, these maps show spatial coherence, suggesting genuine anatomical features.

Visual inspection of “complex” fibers (Figure 5.6) shows that a large majority of the voxels meets this criterion, particularly at lower resolutions. Very few regions meet the definition of a voxel containing only a single fiber bundle. In fact, the only regions in Figure 5.6

that show large areas without complex fibers are the corpus callosum (label 1), the external capsule (label 2), the SLF III (label 3), and the middle longitudinal fasciculus (label 4). Even these regions become more complex as the spatial resolution decreases towards those currently achievable with dMRI. Further yet, these regions may still contain complex geometries that are unable to be captured using 2D brightfield microscopy, and the number of regions with a single dominant orientation may be overestimated on histology.

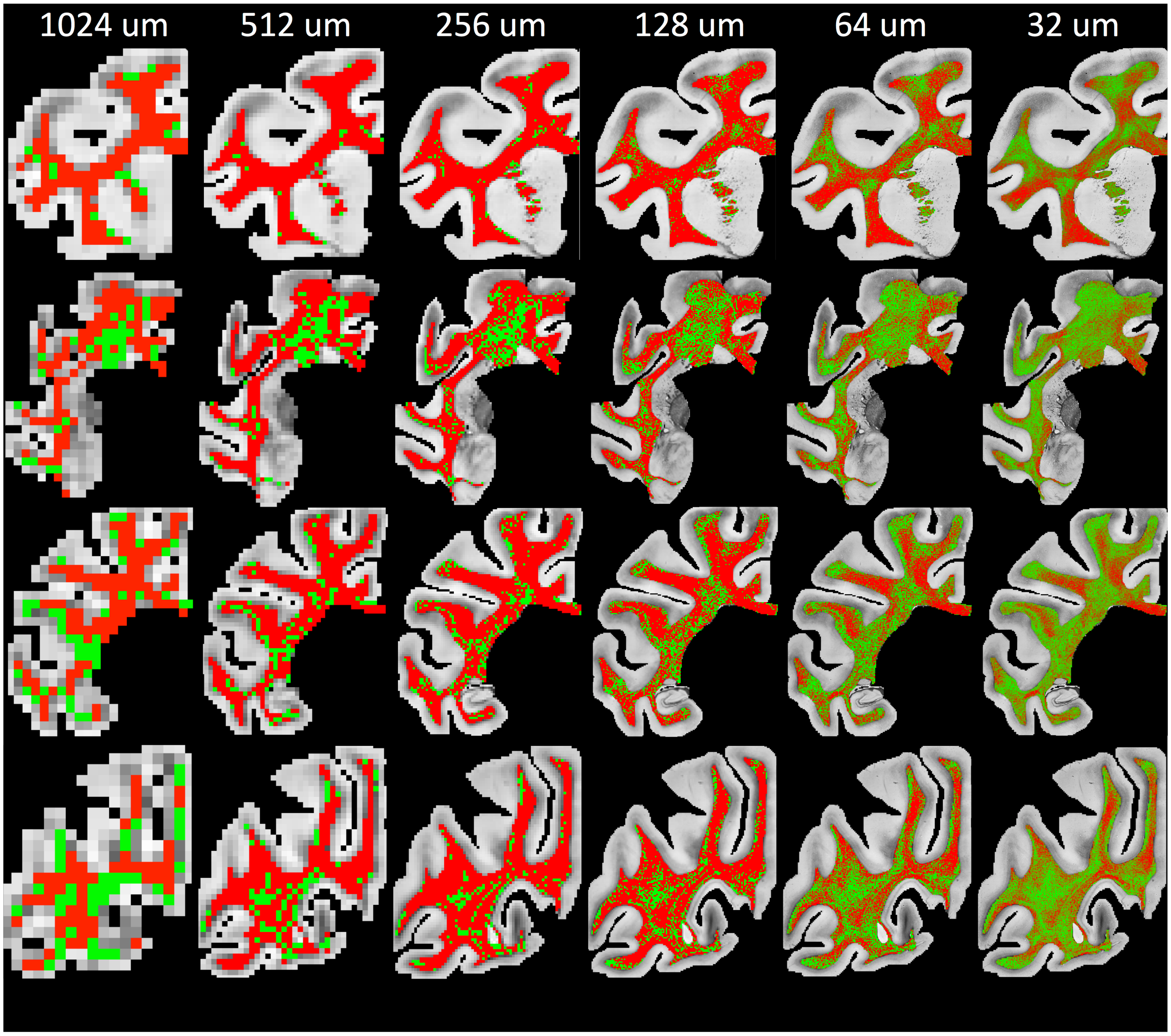

Figure 5.5 Histological maps of crossing fibers (green) vs. voxels without crossing fibers (red). Crossing fibers are defined as voxels whose FOD contains two distinct local maxima, or peaks. Note that red voxels are those with single fiber populations in addition to complex fibers that do not contain two distinct local maxima.

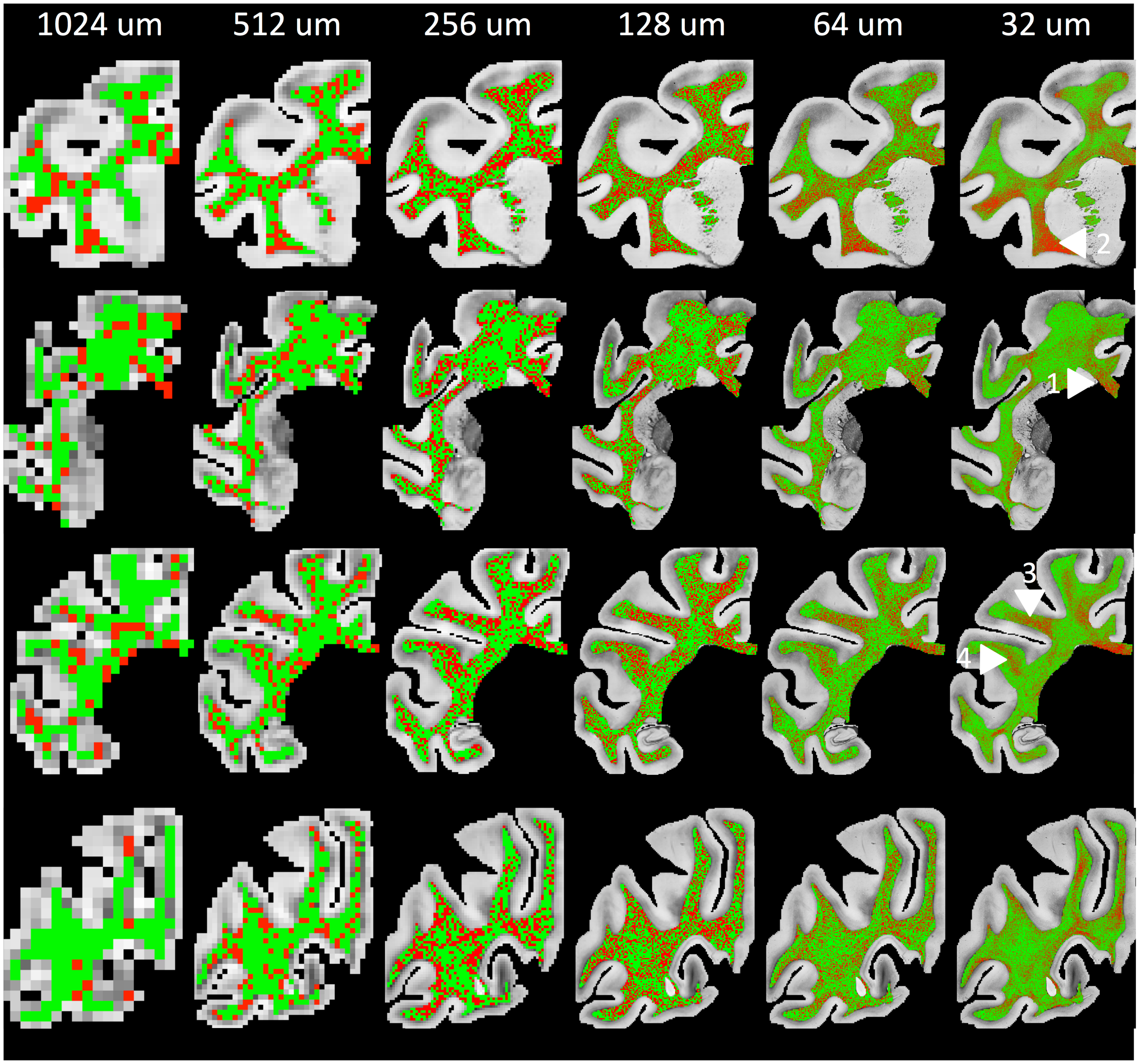

Figure 5.6 Histological maps of complex fibers (green) and single fibers (red). Complex fibers are defined as voxels whose FOD supports fitting to a mixture of von Mises distributions, and may or may not contain two distinct peaks in the FOD.

Figure 5.7 quantifies these results in histogram form. These results confirm that, in general, the fraction of voxels with crossing fibers increases at higher resolutions . Crossing fibers are most prevalent at 32um resolution, affecting as much as 52% of voxels in the WM. In contrast, the fraction of voxels with complex geometries tends to decrease somewhat at the higher resolutions, leveling off at approximately 128um resolution.

Figure 5.8 shows histograms of inter-fiber angles for crossing fibers and complex fibers. For crossing fibers, the histograms shift to the left (toward smaller angles) at the highest resolutions. From coarse to fine resolutions, the median crossing angle decreases from 65° to 29° in the WM. The angular difference between the centers of the two von Mises distributions shows similar trends for the complex distributions, although with much lower angular differences. The median inter-fiber angle is reduced from 37° at 1024um resolution, to 23° at 32um resolution.

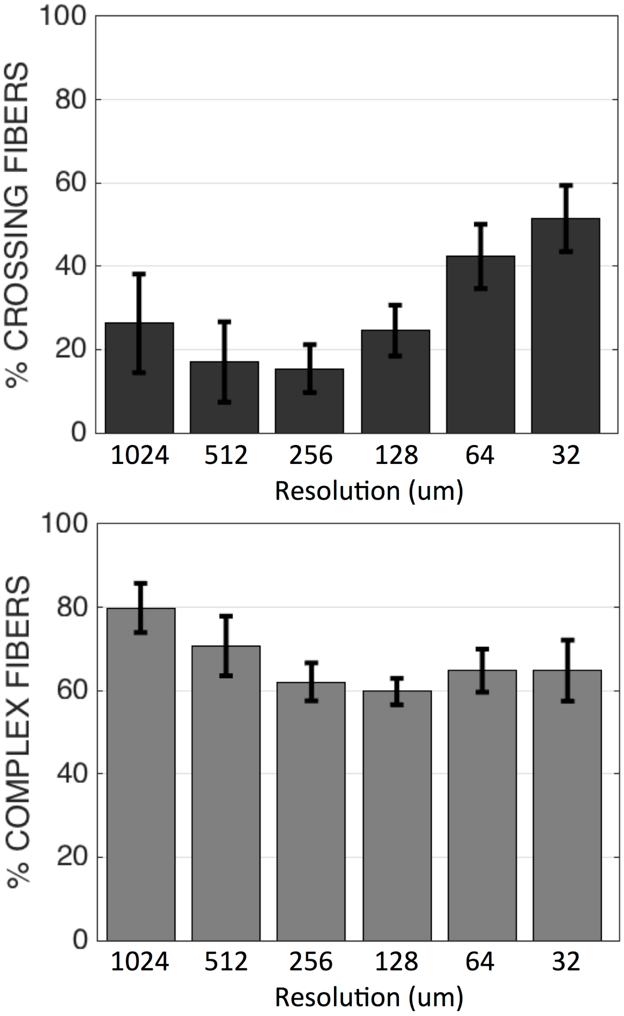

Figure 5.7 Percentages of crossing fibers and complex fibers throughout WM as determined through ST analysis of histology, for different “voxel” sizes. Error bar shows standard deviation across 16 histological slices.

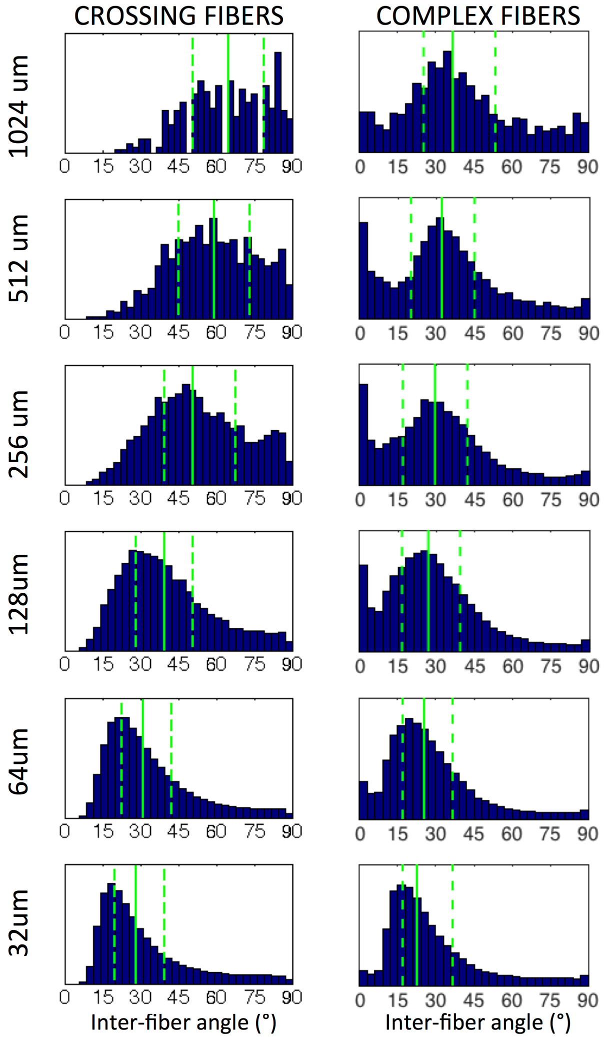

Figure 5.8 Histograms of inter-fiber angles for crossing fibers and complex fibers in WM, at all resolutions, as determined using ST analysis of histological sections. The 1st, 2nd, and 3rd quartiles are shown as dashed, solid, and dashed lines, respectively.

### 5.3.4 Qualitative Analysis

To understand these trends, two more regions (each 1024um across) are further analyzed, including a region with two non-overlapping fiber populations (Figure 5.9) and one with two interwoven fiber populations (Figure 5.10). For both figures, the original gray scale image (A) is shown along with the color-coded orientation maps (B). The FOD's at all resolutions are shown (C), along with fiber classification (D), and (if crossing fibers exist), the crossing angle (E).

Figure 5.9 shows the case of an apparent orthogonal crossing voxel at larger voxel sizes (Figure 5.9, C, D, E). As the voxel size decreases, the intersection of the two bundles is highlighted (Figure 5.9, E, white oval), where most crossing angles are nearly orthogonal. However, at even higher spatial resolutions, multiple fiber populations are detected in areas not along the interface of the two bundles, and at more acute angles. This is caused by the spatial averaging of incoherent fibers within the same fiber “bundle”. This figure demonstrates that crossing fibers are more prevalent at higher spatial resolutions, and that higher spatial resolutions typically resolve fibers crossing at more acute angles.

Figure 5.10 shows a fiber geometry typical in many regions of the brain, a so-called “checkerboard-like” crossing. The solid box around an example FOD shows a crossing fiber region. When the four neighboring regions (dashed box) are averaged to go to the next coarser resolution level (i.e. larger voxel size), the ability to distinguish separate fiber populations is lost, and the voxel is now a complex fiber (rather than complex-crossing). This is because the inter-voxel angular dispersion of the individual fiber populations becomes larger than the crossing angle of the two fiber populations, and it blurs the FOD, reducing the ability to resolve discrete peaks. This, again, explains why crossing fiber populations may be more prevalent at higher spatial resolution.

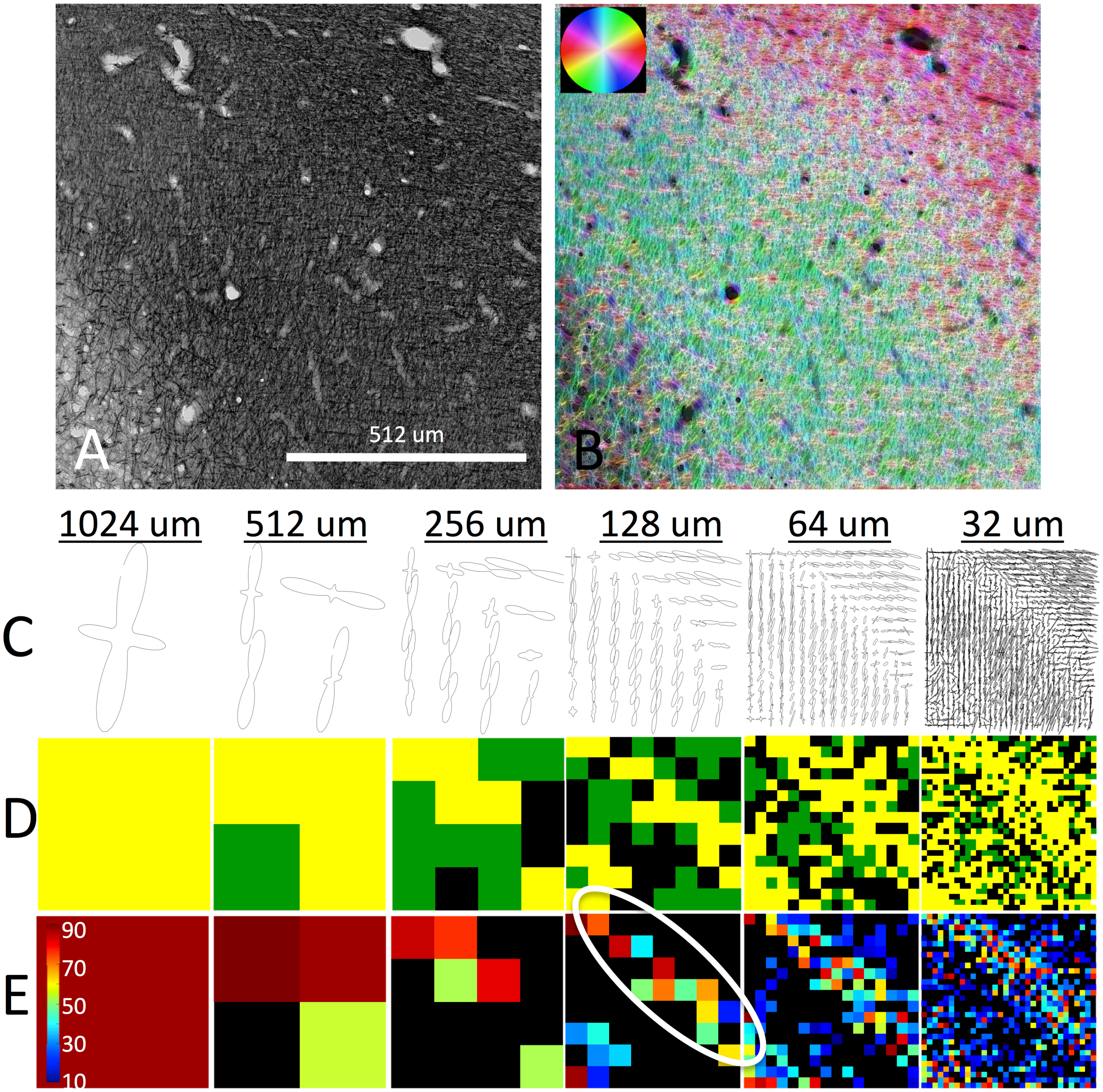

Figure 5.9 Histological analysis of region with two non-overlapping fiber populations. Structure tensor analysis on myelin-stained region of interest (A) is shown as color-coded orientation map (B). For all spatial resolutions, 2D FODs are displayed (C). Voxels are characterized as single fiber (D; black), complex fibers (D; green), or complex "crossing" fibers (D; yellow). In voxels with crossing fibers, the inter-fiber angle (in degrees) is shown in (E). White oval highlights the interface between the two fiber populations.

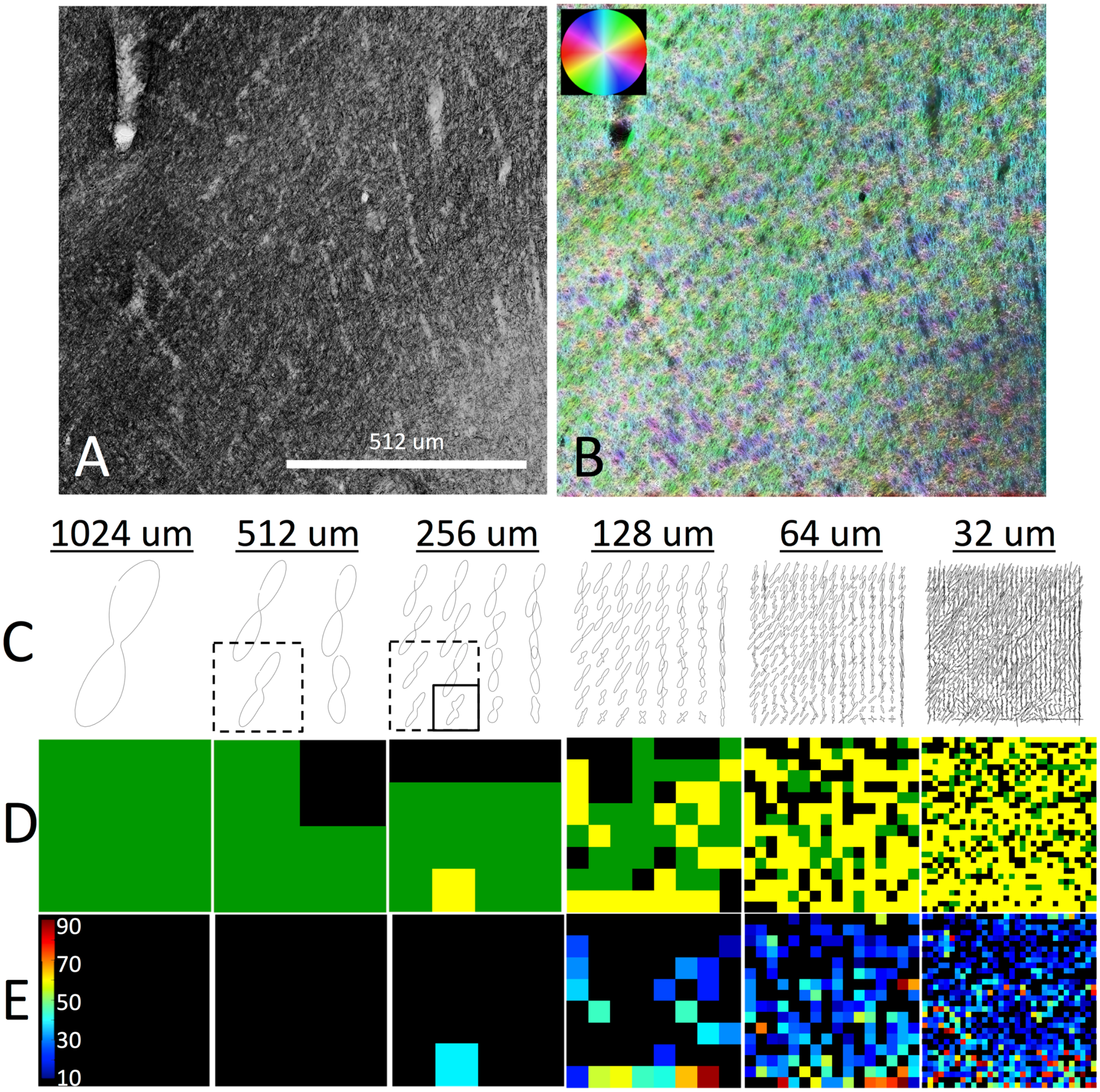

Figure 5.10 Histological analysis of region with two overlapping fiber populations. Structure tensor analysis on myelin-stained region of interest (A) is shown as color-coded orientation map (B). For all spatial resolutions, 2D FODs are displayed (C). Voxels are characterized as single fiber (D; black), complex fibers (D; green), or complex "crossing" fiber (D; yellow). In voxels with crossing fibers, the inter-fiber angle (in degrees) is shown in (E). Solid box highlights a crossing fiber voxel at 256um resolution. At a coarser spatial resolution (512um), the ability to detect discrete fiber populations is limited by partial volume effects (dashed box).

### 5.3.5 Crossing Fibers and SNR

The role of SNR on CSD reconstruction has been studied in great detail [45, 216], and it is well known that a decreased SNR can results in spurious, false-positive peaks. To examine whether our findings of an increased prevalence of crossing fibers at higher resolution could be due to the comparatively lower SNR, we assess the effects of SNR on our MRI data directly.

Gaussian random noise was added in quadrature to the lowest resolution dataset (800 um isotropic) in order to make datasets with equivalent SNR to all other resolutions. The effects of SNR on crossing fibers is shown in Figure 5.11. As the SNR decreases towards that of the highest resolution dataset, the prevalence of crossing fibers increases from 23% to 29% of all WM voxels. This increase is much smaller than that found for increasing resolution, shown in Figure 5.3.

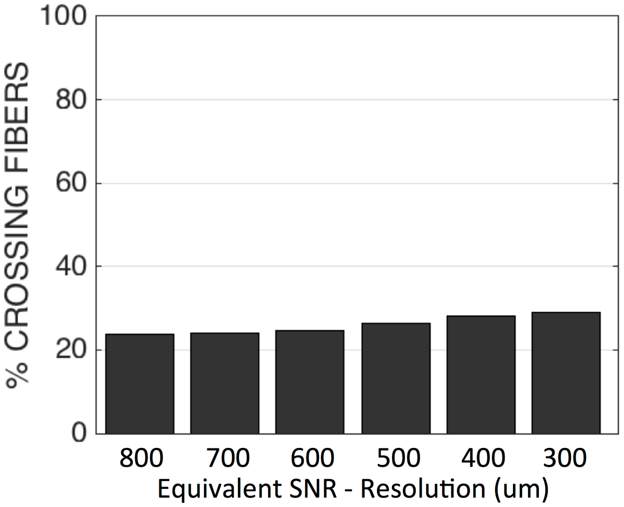

Figure 5.11 Percentages of crossing fiber voxels throughout the WM determined using CSD, for varying SNR levels. SNR levels were simulated by adding Gaussian random noise in quadrature to all DWIs of the 800um isotropic dataset in order to obtain an SNR equivalent to all other acquired resolutions.

### 5.3.6 2D projection of MRI FOD

One discrepancy between MRI and histology is the lower fraction of crossing fibers in histology relative to MRI at similar resolutions (for example, compare 512um histology in Figure 5.9 with 500um MRI in Figure 5.5). To determine whether this is due to the 2D nature of the histology, we performed a projection of all MRI-derived 3D FOD's onto the coronal plane, and the same 2D fitting procedures used for histology.

Figure 5.12 shows the fraction of crossing and complex fibers for the 2D FOD projections in WM. Similar to the results from 3D MRI and 2D histology, these figures show an increase in the fraction of crossing fibers at increasing resolutions. These values are much closer to the results from the 2D histological analysis at similar resolution levels (compare to Figure 5.7), and confirm that the discrepancy between 3D MRI and 2D histology is largely due to the projection of orientation information into a 2D plane.

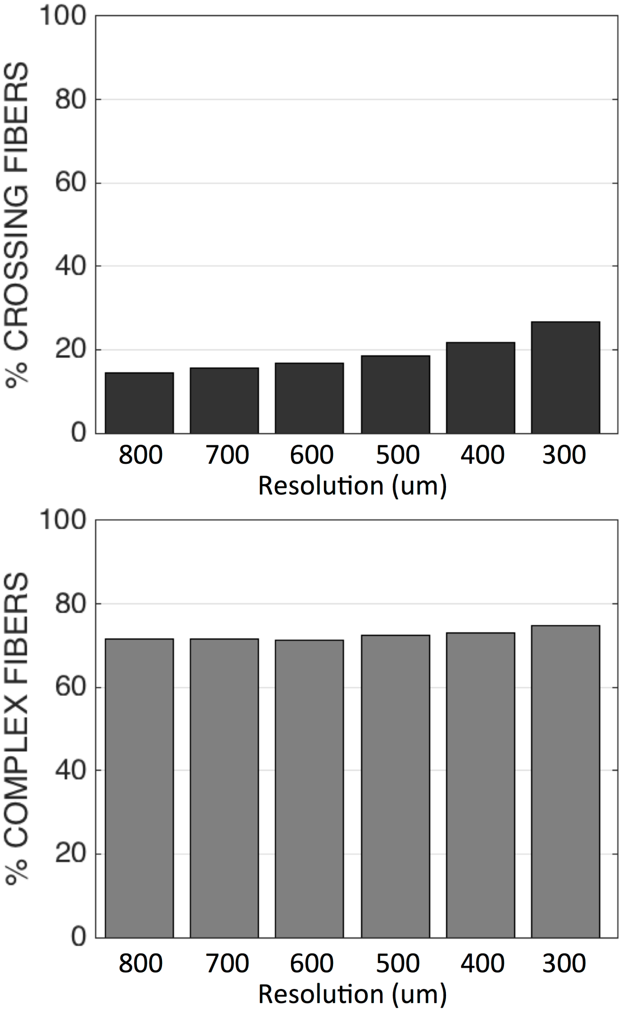

Figure 5.12 Percentages of crossing fibers and complex fibers throughout WM as determined after 2D projection of the CSD FOD, and fitting to a 2D circular distribution (in a manner equivalent to analysis of histological data).

## 5.4 Discussion

The aim of this study was to investigate the prevalence of crossing fibers in the brain as the spatial resolution is continually increased. Using both dMRI and subsequent histology, we find that the fraction of voxels with crossing fibers varies with resolution, but in an unintuitive way – the percentage of crossing fibers *increases* as the resolution increases (Figure 5.3 and Figure 5.7). The problem of crossing fibers appears to be a fundamental limitation of dMRI associated with fiber microstructure, rather than a technical problem that can be overcome with higher fields, stronger gradients, or technological advances that may increase spatial resolution. This limitation is likely shared by any imaging method (e.g., polarized light imaging) that is subject to partial volume averaging of fiber orientation information.

One potential explanation for these results could be an artefactual increase in voxels with false-positive peaks caused by a decreased SNR of the high-resolution datasets. While an analysis of SNR-equivalent datasets does show a small increase in WM crossing fibers (Figure 5.11), this increase is only a small fraction of that due to increased resolution (compare to Figure 5.3), and the resultant decreased partial volume averaging. It is important to note that even our highest resolution MRI dataset (300um isotropic) had an SNR of ~38 in the WM of the b0 image, a value much higher than is expected in typical human DWIs. Finally, the finding that the prevalence of crossing fibers increases as resolution increases is also validated using histological analysis at spatial scales over a range an order of magnitude greater than the dMRI data.

A surprising result was that even at voxel size as low as 32um on histology, a size much smaller than the scale of WM fiber tracts, crossing fibers are found in >50% of voxels in the WM. So, although there is a much finer delineation of structures, resolutions much higher than currently achievable on pre-clinical scanners still will not eliminate the crossing fiber problem. In fact, our data suggest that with smaller voxels and the consequent finer delineation of structures, there is less partial volume averaging of axon orientations between and within tracts. As voxel size increases, the within-voxel angular dispersion of individual fibers can become larger than the crossing angle of the two fiber populations, which reduces the ability to resolve discrete peaks in the fiber orientation distribution. This implies that the minimum detectable crossing angle depends on both the within-voxel orientation dispersion and the intrinsic angular resolution of the imaging method. Increased spatial resolution leads to less ambiguous orientation estimates in regions containing complicated fiber geometries (fiber dispersion, fiber splaying, fibers crossings at very acute angles), which are eventually resolved into multiple distinct fiber populations at higher spatial resolutions. These results, however, do not imply less accurate fiber tracking at higher resolutions. Because there is less partial volume averaging, and more voxels containing pure crossing fibers, it makes the crossing fiber model more valuable at these resolutions.

While many dMRI techniques are geared towards resolving crossing fibers, histological analysis was able to capture a range of complex fiber geometries. Figure 5.7 shows that the fraction of fibers containing complex geometries does decrease at higher spatial resolutions, yet remains as high as ~60% at 32um. Our definition of “complex” fibers not only includes voxels with distinct crossing fibers, but also includes any situation where partial volume effects arise between multiple, or even within single, fiber populations. This could include asymmetries in the FOD due to fibers with high curvature or fiber fanning. These complex fibers represent regions where the diffusion tensor (and any metrics derived from it) will fail to accurately capture the underlying fiber distribution, even if the region still contains only a single fiber population. In addition, the regions described by complex, but not crossing fibers, are regions where even methods developed to resolve crossing fibers [24, 40, 41, 43, 58, 120, 205] may fail to characterize the true tissue complexity, which cannot be adequately described by a simple count of the number of discrete peaks. It is interesting to note that these complex configurations can take place in regions typically assumed to contain single fiber populations (e.g., the corpus callosum), where heterogeneous fiber orientations are apparent in histological sections (see Figure 5.1).

These results have implications for the future development of dMRI acquisition methods. Because voxels with complex fiber configurations will *always* exist in datasets, even at resolutions far beyond current dMRI capabilities, it may be more beneficial to focus on appropriate tissue models for describing fiber geometry in voxels rather than focus on pushing resolution (and sacrificing SNR), where the gains in fiber reconstruction accuracy may be minimal. For dMRI sessions, rather than acquiring high spatial resolution data, time may be better spent on acquiring high angular resolution data or more unique diffusion weightings, at a higher SNR, to accommodate biophysical modeling, although specific acquisition requirements are likely to depend on the intended goal of the individual study, in addition to the implemented diffusion reconstruction method. Also, because of the pervasiveness of complex fiber configurations, significant emphasis could be placed on models with fiber fanning and curving [62, 217, 218], as well as those containing multiple compartments, allowing both fanning and crossing [50].

An interesting discrepancy between MRI and histology is the inter-fiber angle in voxels containing crossing fibers. Figure 5.4 shows that dMRI tends to resolve crossing fibers when the fibers are crossing at nearly orthogonal angles, at all resolutions. Many dMRI techniques are limited by the minimum angle that can be resolved reliably. While dependent upon acquisition parameters, this minimum resolvable angle is typically in the range of 40-60°. A similar distribution of crossing angles has been previously described [210], and if the observed orthogonal crossings are the result of genuine anatomical structures, they could have significant implications for evolution, development, and brain connectivity [219]. However, our results suggest that when voxels are large enough (i.e., when intra-voxel orientation dispersion grows large), then near-orthogonal crossings will be most common. Hence, the 'blurring' of FODs (and other orientation distribution functions) due to intra-voxel fiber dispersion biases measurements of the prevalence of orthogonal fiber crossings. Analysis of histological sections (Figure 5.8) shows that the mode of the inter-fiber angle distribution is much smaller than 90°, and actually decreases at higher spatial resolutions, for both crossing and complex configurations. CSD has an intrinsic angular resolution limit defined by the deconvolution kernel [45], meaning that this technique cannot model crossing fibers (i.e., will not find two local maxima) that have a crossing angle smaller than the width of the kernel. While we do not attempt to state an optimal resolution for dMRI (as this will surely depend on the goals of the individual study), in regards to the crossing fiber problem, there may be little advantage in increasing the spatial resolution beyond the point where the intrinsic angular resolution of the reconstruction algorithm is able to detect true crossing angles.

The second discrepancy between MRI and histology was the lower percentage of crossing fibers in histology relative to MRI at similar resolutions. While histological measurements are often considered a "gold standard" from which to validate diffusion MRI measurements, they may come with their own set of limitations. In addition to potential geometric tissue distortion and a limited tissue slice thickness (25um), a major limitation of this study is the use of inherently 2D histological analysis. There is no information on the 3rd dimension (in this case anterior to posterior); all fiber orientations derived from histology are instead projections onto the histological plane. After projection of the 3D MRI data onto a 2D plane (Figure 5.12), we find much better agreement in percentage of crossing fibers – for example the 2D projection of the 500um dataset decreases the percentage of crossing fibers from 30% to 16%, a value in good agreement with the 17% indicated by the 512um histological analysis (Figure 5.7). Note, however, that 2D and 3D histological FODs still exhibit similar partial volume averaging effects as voxel size increases, so the 2D calculations can be used to predict general features of the dependence of 3D FODs on voxel size. It is also possible that dMRI actually overestimates the fraction of crossing fibers in regions with highly curved or fanning structures that are resolved into two discrete fiber bundles due to modeling strategies employed with CSD. In addition, we have only implemented one variant of one reconstruction algorithm (CSD), whereas a multitude of techniques exist for the purposes of resolving crossing fibers. Different algorithms and different diffusion kernels are expected to vary in performance when estimating tissue microstructure. Future studies should acquire and derive the 3D histology FODs [199] for comparisons with CSD and other analysis methods in order to quantify both fiber orientation accuracy and the ability to identify voxels with multiple fiber populations. These data could also be used to test whether brain fiber pathways are truly arranged in orthogonal grid-like structures [219].

A final limitation is the use of the macaque brain, whereas studying human brain connectivity, structure, and function is commonly the ultimate goal of non-invasive neuroimaging. However, the time required to scan a human at the resolutions acquired in this study is not feasible, and there would be no histological gold standard with which to validate the dMRI measurements.  Furthermore, the ex vivo macaque brain is a common model for validating dMRI measurements [154, 157, 164, 220, 221] because it contains a functional and microstructural organization similar to humans'. Despite this similarity, it seems that the fraction of crossing fibers identified through dMRI (ranging from 23% to 51% in WM) is less than that using similar methods in the human (between 63% and 90% in WM) [210].

### 5.5 Conclusion

In this work, we investigate the prevalence of crossing fibers and complex fiber configurations in WM tissue using both dMRI and histological analysis of the same brain. Our results indicate that increasing spatial resolution does not completely eliminate the crossing fiber problem. In fact, the frequency of crossing fibers increases at higher spatial resolutions in both histology and MRI. Our histological results highlight the fact that complex fiber configurations will always exist in dMRI data, even at resolutions that far surpass today’s technology. These findings have implications for future generations of tractography algorithms as well as microstructural models, and highlight the importance of both crossing and more complex fiber geometries.

# CHAPTER 6: COMPARISON OF 3D ORIENTATION DISTRIBUTION FUNCTIONS WITH CONFOCAL MICROSCOPY AND DIFFUSION MRI

## Prologue

Because fibers with crossing or complex fiber configurations will always exist in datasets of the brain, it is critical that diffusion reconstruction algorithms adequately capture the distribution of neuronal fibers in each voxel in order for fiber tractography to be successful. In this chapter, we develop an approach to validate the accuracy of diffusion reconstruction algorithms. We extract the histological fiber orientation distribution from 3D confocal data by extending the image processing techniques (structure tensor analysis) from Chapter 5 to three dimensions. We also utilize the spatial registration techniques developed in the atlas to facilitate comparisons of histology and MRI of the same tissue volumes. While no direct validation is performed in this chapter, the developed techniques are benchmarked and assessed by comparing histology to both DTI and spherical deconvolution. The methodology developed in this chapter will be implemented in Chapter 7 for the first 3D histological validation of a large number of commonly implemented diffusion techniques.

## Abstract

The ability of diffusion MRI (dMRI) fiber tractography to non-invasively map three-dimensional (3D) anatomical networks in the human brain has made it a valuable tool in both clinical and research settings. However, there are many assumptions inherent to any tractography algorithm that can limit the accuracy of the reconstructed fiber tracts. Among them is the assumption that the diffusion-weighted images accurately reflect the underlying fiber orientation distribution (FOD) in the MRI voxel. Consequently, validating dMRI's ability to assess the underlying fiber orientation in each voxel is critical for its use as a biomedical tool. Here, using post-mortem histology and confocal microscopy, we present a method to perform histological validation of orientation functions in 3D, which has previously been limited to two-dimensional analysis of tissue sections. We demonstrate the ability to extract the 3D FOD from confocal z-stacks, and quantify the agreement between the MRI estimates of orientation

information obtained using constrained spherical deconvolution (CSD) and the true geometry of the fibers. We find an orientation error of approximately 6° in voxels containing nearly parallel fibers, and 10-11° in crossing fiber regions, and note that CSD was unable to resolve fibers crossing at angles below 60° in our dataset. This is the first time the 3D white matter orientation distribution is calculated from histology and compared to dMRI. Thus, this technique serves as a gold standard for dMRI validation studies - providing the ability to determine the extent to which the dMRI signal is consistent with the histological FOD, and to establish how well different dMRI models can predict the ground truth FOD.

## 6.1 Introduction

Diffusion magnetic resonance imaging (dMRI) has the ability to estimate the distribution of neuronal fiber orientations in each voxel from a set of diffusion measurements, an object often referred to as the *fiber orientation distribution* (FOD). By following these fiber orientation estimates from voxel to voxel throughout the brain, intricate maps of brain connectivity can be created. This process of mapping brain connectivity using dMRI data has been termed “fiber tractography” [8, 55], and has been used in applications ranging from delineating brain networks [222], to studying the changes associated with disease [78, 93], psychiatric disorders [223], and traumatic brain injury [224].

Diffusion tensor imaging (DTI) was the first MRI method to allow mapping of fiber orientations throughout the brain[225], and remains the most common. However, this uni-modal Gaussian diffusion model is known to be inadequate for characterizing diffusion in voxels with complex fiber structure [204] and has been shown to lead to erroneous tractography results. A number of methods have been introduced to address this “crossing fiber” problem [24, 34-36, 38, 40, 41, 43, 49, 61, 120]. Typically, these approaches solve for the fiber orientation by estimating the FOD or the orientation density function (ODF) – another spherical function, which reflects the relative number of spins that have diffused in any given direction. Tractography algorithms then exploit local peaks in the FOD or ODF to propagate tract streamlines.

While these techniques have produced improvements in white matter tractography, there has been no clear consensus on a “gold standard” for validating the underlying orientation distributions. The most common method to date has been validation using synthetic data [6, 226]. However, these simulations rely on assumptions and approximations to generate the modeled MR signal, and are likely to be inadequate for validation in the living brain. Physical phantoms can be used to provide more realistic experiment conditions (including artifacts inherent to dMRI) and allow control of the ground truth orientation distribution. Yet, these capillary-based [125, 227] or synthetic fiber-based [117, 126, 129] phantoms can still fail to replicate the structural characteristics typical of neuronal tissue, including axon diameter, membrane permeability, and most importantly, the enormous geometric complexity seen in the central nervous system.

To overcome these limitations, several studies have validated orientation measures using post-mortem histology. From stained tissue sections, techniques such as manual tracing [132], structure tensor analysis [135], and Fourier analysis [133] have been used to quantify the histological FOD. However, two potential disadvantages have plagued histological validation studies to date. First, many have been limited to two-dimensional (2D), in-plane analysis of tissue sections. Thus, they rely on tissue sectioning in a plane parallel to the direction of fibers, and analysis is restricted to fibers oriented in that plane. Recently, this limitation of validation studies has been circumvented through the use of confocal microscopy [115, 136] and optical coherence tomography [137]. However, no method has been presented which characterizes the full fiber orientation distribution in white matter voxels, but rather recent studies estimate a single dominant orientation in areas equivalent in size to an MRI voxel [136, 137], or determine the orientation distribution in axons and dendrites of the cerebral cortex [115]. Second, comparing MRI and histology is often done through manual alignment [132, 136, 228] of the data , which is prone to error and can lead to geometric mismatch and a bias in the validation results. Consequently, there is a need for a method to compare dMRI estimates of white matter pathways to direct measurements of axonal orientations on a voxel-by-voxel basis - one which allows three-dimensional (3D) analysis and addresses accurate, reproducible registration.

In this study, using post-mortem histology and confocal microscopy, we develop an approach to extend histological validation of orientation functions to 3D. We also describe appropriate alignment and orientation of the histological data to MRI data. The intention of this work is not a comprehensive validation of the strengths and weaknesses of the various dMRI algorithms, nor determination of optimal acquisition parameters. Rather, the focus is on the technique itself, which represents an advance in the development of a “gold standard” for the purposes of validating fiber orientation information. We begin with an in-depth description of the method, which employs a common image processing technique - structure tensor analysis - in order to extract the 3D FOD in areas equivalent in size to an MRI voxel. Next, we describe the sensitivity of this approach to confocal acquisition and image processing parameters. Finally, we apply this technique to both single fiber and crossing fiber white matter (WM) regions, and, as a methodological benchmark, make quantitative comparisons of the histological-FOD to the corresponding MRI-FOD derived using constrained spherical deconvolution (CSD) with the damped Richardson-Lucy algorithm [44].

## 6.2 Materials and Methods

### 6.2.1 MRI Acquisition

Diffusion MRI experiments were performed on an adult squirrel monkey brain that had been perfusion fixed with physiological saline followed by 4% paraformaldehyde. The brain was then immersed in 4% paraformaldehyde for 3 weeks. The brain was transferred into a phosphate-buffered saline medium for 24 hours and scanned on a Varian 9.4 T, 21 cm bore magnet using a multi-shot multi-slice spin echo EPI sequence (TR = 6.7s; TE = 42ms; $\delta$ = 8ms; $\Delta$ = 27ms; max gradient strength = 30G/cm; voxel size = 400um isotropic; partial Fourier = .75; NEX = 5). A 30-direction diffusion-sampling scheme based on an electrostatic repulsion algorithm [229] was used to acquire 30 diffusion-weighted images at a b-value of 3200 s/mm$^2$, and 2 additional images were collected with b=0. This set of data was used for calculating diffusion tensors using a weighted linear least squares fit. Next, a 90-direction scheme was used to acquire diffusion weighted-images at a b-value of 6400 s/mm$^2$, and 6 additional images at b=0. From this data set, the MRI-FOD was estimated using constrained spherical deconvolution with the damped Richardson-Lucy algorithm [44] and fit to 8th order spherical harmonic (SH) coefficients. MRI data processing was done using the high angular resolution diffusion imaging (HARDI) toolbox for MATLAB, available at http://neuroimagen.es/webs/hardi_tools/.

### 6.2.2 Histological Procedures

After imaging, the brain was sectioned on a cryomicrotome at a thickness of 80um in the coronal plane and mounted on glass slides. Using a Canon EOS20D (Lake Success, NY, USA) digital camera with a zoom lens of 70-300 mm, the tissue block was digitally photographed prior to cutting every other section, resulting in a 3D “block-face” volume with a through-plane resolution of 160um.

The tissue sections were mounted on glass slides and stained following the procedures outlined in [134]. Briefly, tissue sections were rinsed in PBS and dehydrated through graded ethanol solutions. The fluorescent lipophilic dye, “DiI”, (1,1’-dioctadecyl-3,3,3’3’-tetramethylindocarbocyanine percholarate) in 100% ethanol (.25mg/mL) was rinsed over sections for 1 minute. The stained sections were then rehydrated through graded ethanol solutions, and coverslipped with Fluoromount-G mounting medium.

### 6.2.3 Confocal Acquisition

All histological data were collected using an LSM 710 inverted confocal microscope (Carl Zeiss, Inc. Thornwood, NY. USA). For all selected tissue slices, confocal acquisition consists of two protocols: [1] creating a 2D montage of the entire tissue and [2] constructing a 3D high-resolution image in a selected region of interest. The 2D montage (Figure 6.1, A) consists of approximately 600-900 individual tiles acquired using a 10x oil objective at a resolution of $0.80\mu m^2$, which are stitched together using Zeiss software, ZEN 2010. Acquisition for a single slice takes approximately 30 minutes. To correct for image inhomogeneity and tiling effects in the image, we found it useful to increase the zoom feature to 1.5x or higher at the expense of collecting more tiles. This 2D montage is used for image registration, and for localizing the 3D high-resolution region of interest.

Prior to 3D z-stack acquisition, two steps are performed. First, tissue thickness in the z-dimension is determined by adjusting the focal plane depth to determine where fluorescence begins and ends. This thickness is used to correct orientation estimates for tissue shrinkage (see *Histological FOD* below). Second, it is necessary to increase the laser output as deeper layers are imaged due to the increases in light scatter and absorption at greater tissue depths (see *Confocal Pre-Processing*). The laser power is adjusted for approximately 5 different depths ranging from the coverslip to the end of the tissue, at each step ensuring that the image intensity range will cover the full 8-bit depth from 0-255 units. The LSM 710 interpolates the laser output between depths.

The 3D z-stack (Figure 6.1, B) is then collected using a 63x oil objective at a nominal resolution of 0.18µm×0.18µm×0.42µm. Typical acquisition time to acquire the entire section thickness with an in-plane field of view of 1.6mm × 1.6mm (equivalent to 16 MRI voxels) is approximately 8 hours. The through-plane resolution is the “optimal” slice-thickness, calculated from the LSM710 software based on a 1.0 Airy unit pinhole diameter and an excitation wavelength of 543nm. Stitching, again, is performed using ZEN 2010 software to create a single 3D z-stack.

Finally, all confocal data are converted from the LSM file format to TIFF images and imported into MATLAB for further processing.

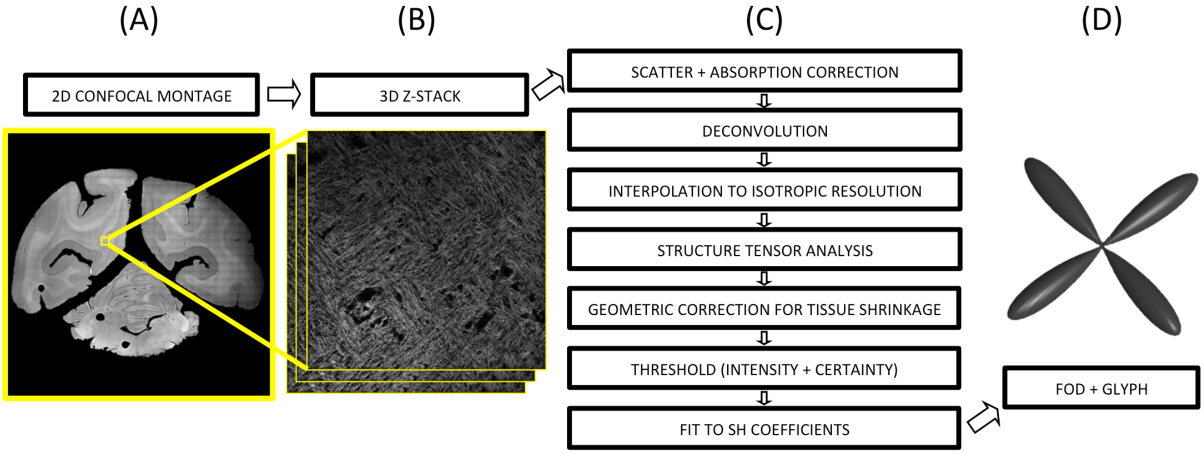

Figure 6.1 Estimating the fiber orientation distribution from confocal z-stacks. Confocal acquisition includes a 2D low-resolution montage (A) and a high-resolution 3D z-stack (B). Image pre-processing (C) comprises light scatter and absorption correction, deconvolution, and interpolation. Next, structure tensor analysis is performed (illustrated in Figure 2 on a simulated fiber), and the tertiary eigenvector extracted for all pixels. This is followed by geometric correction for tissue shrinkage, thresholding fibers, and fitting to spherical harmonic coefficients. The resulting FOD is displayed as a 3D glyph (D).

### 6.2.4 Confocal Pre-processing

The aim here is to extract the histological-FODs from the 3D z-stacks in areas equivalent to the size of an MR voxel. To do this, we use structure tensor analysis to obtain an orientation estimate for every pixel in the 3D z-stack that is occupied by a fiber.

Prior to structure tensor analysis, four sources of anisotropy inherent to confocal microscopy must be accounted for (Figure 6.1, C). Three corrections are performed directly on the confocal z-stack prior to structure tensor analysis, and the final correction performed post-analysis. The first is an attenuation of the image intensity as a function of tissue depth. This effect is caused by light scatter and absorption which decreases the intensity of excitation light penetrating to the deeper layers of the tissue, and consequently, the fluorescence of these layers. Because structure tensor analysis is based on image intensity gradients, this artifact could result in a bias in fiber orientation estimates [136]. The attenuation correction is performed in the *Confocal Acquisition* stage described above. Increasing the laser power for deeper layers generates a z-profile that has a relatively constant mean intensity in each x-y plane containing fibers.

The second source of anisotropy arises from the confocal microscope's point spread function (PSF). The PSF is the 3D diffraction pattern resulting from the systems response to an infinitely small point source of light. This diffraction pattern is known to be nearly three times wider through-plane than in-plane [230], leading to anisotropic blurring of the image; in-plane structures will be better resolved than those oriented through-plane. To deblur the confocal data, we use the iterative Lucy-Richardson algorithm [231] and a computed theoretical model of the confocal microscope's PSF [230]. This model takes into account various confocal parameters including the numerical aperture, refractive index, wavelength of light, and the acquired image resolution. The Lucy-Richardson deconvolution algorithm is a maximum-likelihood approach to find the statistically most likely image, given the blurred image and assuming Poisson noise [231, 232], which is an appropriate noise model of the photon-counting process of confocal imaging [230].

The final pre-processing step is to correct for the anisotropic acquisition resolution. This ensures that fibers oriented laterally in the image will contain an equivalent number of pixels per length as fibers oriented axially. Interpolation to isotropic resolution is accomplished using cubic interpolation.

### 6.2.5 Structure Tensor Analysis

The structure tensor was introduced in the late 1980's for point and edge detection [212, 233], and has since become popular in image processing and computer vision, with applications including texture analysis and materials science [234, 235]. This analysis technique is applied to our entire 3D confocal image, f(x,y,z). The structure tensor [236] is based on the gradient of f:

$$\nabla f_{\sigma} = (f_x, f_y, f_z)^T \tag{21}$$

which is calculated with Gaussian derivative filters:

$$f_x = g_{x,\sigma} * f, \qquad f_y = g_{y,\sigma} * f, \qquad f_z = g_{z,\sigma} * f \tag{22}$$

where $*$ denotes the convolution operation and $g_{x,\sigma}$, $g_{y,\sigma}$, and $g_{z,\sigma}$ are the spatial derivatives in the x, y, and z-direction, respectively, of a 3D Gaussian with standard deviation σ:

$$g_{\sigma}(x,y,z) = \frac{1}{(\sqrt{2\pi\sigma^2})^3} e^{-\frac{(x^2+y^2+z^2)}{2\sigma^2}} \tag{23}$$

For illustration purposes, we show this step as performed on a simulated cylindrical fiber (Figure 6.2, A), representative of the neuronal structures seen in the 3D confocal image (similar illustrations appear in [136] and [237]). Ideally, the image gradients are orthogonal to the fibers at all points (Figure 6.2, B). Next, an object known as the gradient square tensor, is calculated for each point in the image by taking the dyadic product of the gradient vector with itself:

$$GST(x,y,z)_{\sigma} = \nabla f_{\sigma} \nabla f_{\sigma}^{\ T} = \begin{pmatrix} f_x^2 & f_x f_y & f_x f_z \\ f_x f_y & f_y^2 & f_y f_z \\ f_x f_z & f_y f_z & f_z^2 \end{pmatrix} \tag{24}$$

Each tensor element is averaged over a local neighborhood to create the pixel-wise structure tensor. For spatial averaging, we choose a 3D Gaussian filter with standard deviation ρ:

$$ST_{\rho}(\nabla \mathrm{f}_{\sigma}) = g_{\rho} * (\nabla f_{\sigma} \nabla f_{\sigma}^T) \tag{25}$$

This results in a 3-by-3 symmetric, semi-positive definite, rank-two tensor. Much like the diffusion tensor, this matrix will have three positive eigenvalues, and can be visualized as an ellipsoid (Figure 6.2, C). In DTI, one is typically interested in the largest eigenvalue and eigenvector, which points in the direction of greatest diffusion, and is usually assumed to be parallel to the primary structure orientation in the MR voxel. However, in structure tensor analysis, the image intensity gradients are strongest perpendicular to the fibers, which means the largest two eigenvectors will also be perpendicular to the fiber bundles. Hence, we make the assumption that the direction of minimal intensity variation is parallel to the fiber orientation at each pixel, a direction given by the eigenvector corresponding to the smallest eigenvalue.

The certainty in estimated fiber orientation can be described by the Westin-measure [238] defining how planar the structure tensor is:

$$c_p = \frac{\lambda_2 - \lambda_3}{\lambda_1} \tag{26}$$

where $\lambda_1$, $\lambda_2$, and $\lambda_3$ are the primary, secondary, and tertiary eigenvalues of the structure tensor. This value varies from 0 to 1 and will be large in areas, like that depicted in Figure 6.2, C, where the first two eigenvalues are much larger than the third. This measurement is used to threshold the confocal image, so voxels with low certainties are not included in the final orientation distribution.

For the results presented in this paper, the spatial derivatives were calculated using a Gaussian with standard deviation $\sigma = 1\mu m$, and spatial averaging performed using a Gaussian with standard deviation $\rho = 2.5\mu m$ (these values were chosen based on comparisons to distributions of manually traced fibers – see Section 6.3.1 Sensitivity Analysis).

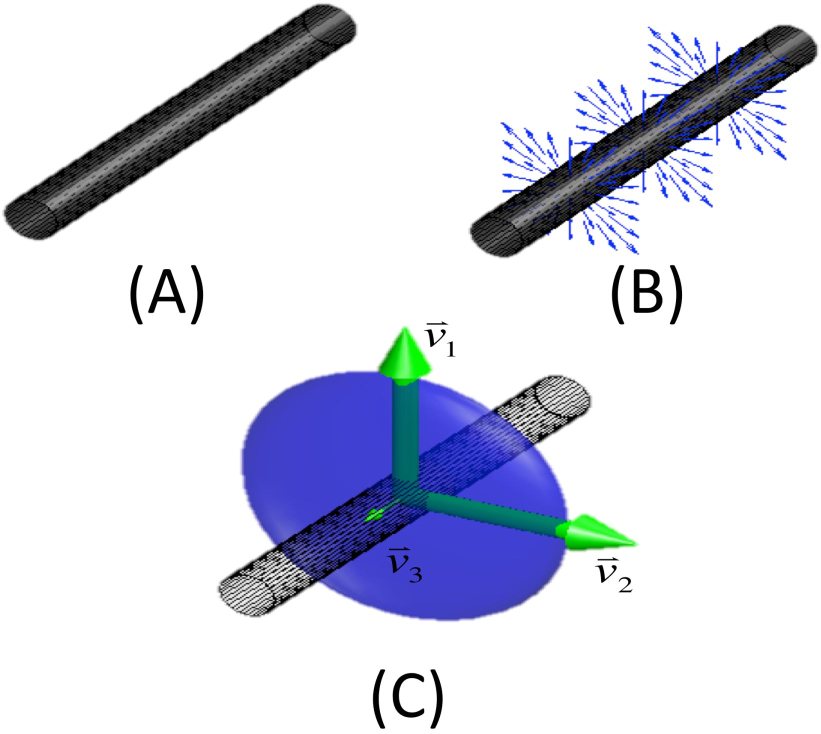

Figure 6.2 Structure tensor analysis illustrated on a simulated cylindrical fiber (A). The structure tensor is derived from the image intensity gradients (B), which should be orthogonal to the fiber at all points. The Cartesian product of the gradient vector with itself is taken, and averaged over a local neighborhood to derive the structure tensor, which has 3 eigenvalues and 3 eigenvectors (C). The tertiary eigenvector, $v_3$, will point in the direction of minimum intensity variation – parallel to the fiber.

### 6.2.6 Histological-FOD

After a fiber orientation has been extracted for all pixels in the image (Figure 6.1, C) one final correction for anisotropy must be performed. It is known that tissue samples may shrink due to processing, sectioning, and staining [239, 240]. These effects are mainly a result of fixation and dehydration in alcohol solutions during the staining procedure [241, 242]. We use the thickness measurement before acquisition of each 3D z-stack to perform a geometric correction to the orientation estimate for every pixel in the image by assuming linear shrinkage in the through-plane (z) direction.

Once all estimated vectors have been appropriately re-oriented to account for tissue shrinkage, the results are thresholded using both image intensity and the certainty value. This yields an orientation estimate for every pixel in our z-stack that is occupied by a fiber.

A histogram representing the histological-FOD is then created as a function of polar and azimuthal angle, where the orientation estimates are placed into bins that cover constant solid angles over a sphere. This FOD is fit to high order (20) SH coefficients, and throughout this dissertation is displayed as a three dimensional glyph (Figure 6.1, D) in the same way that the MRI-FOD's are typically displayed.

### 6.2.7 Image Registration

In order to make a quantitative comparison of the histological-FOD and the MRI-FOD, the data must be aligned and oriented appropriately. A multi-step registration procedure [194] was used to align histology to MRI data. The first step is registration of the 2D confocal montage to the corresponding block face image using mutual information based 2D linear registration followed by 2D nonlinear registration using the adaptive bases algorithm (ABA) [196]. Next, all block face photographs were assembled into a 3D block volume, which is registered to the MRI b=0 image using a 3D affine transformation followed by 3D nonlinear registration with ABA. Given the location of the 3D z-stack in the 2D confocal montage, we can use the combined deformation fields to determine the MRI signal from the same tissue volume. The MRI signal of interest is analyzed in MRI native space. As described above, we derive the tensor using a WLLS fit, and estimate the MRI-FOD using constrained spherical deconvolution. The final step is to transform the diffusion tensor and MRI-FOD to histological space to facilitate comparisons with the histological FOD. For the tensor, we apply the preservation of principal directions (PPD) strategy [243] twice: once to transform the tensor from MRI-space to block-space, and again to transform to histological space. For the MRI-FOD, we choose the approach developed in Hong et al. [244]. This method takes into account rotation, scaling, and shearing effects of the spatial transformations, and can be applied to any orientation distribution on a sphere. After these corrections, both the histological-FOD and the MRI-FOD are in histological space, and quantitative analysis can be performed.

## 6.3 Results

### 6.3.1 Sensitivity Analysis

We begin by reporting the sensitivity of this technique to acquisition and image analysis parameters. First, three single fiber regions (with three different primary orientations) were acquired at in-plane resolutions ranging from 0.08µm×0.08µm to 0.42µm×0.42µm. The through-plane resolution was set to 0.42µm for all sets. Structure tensor analysis was performed on all datasets with parameters σ = 1µm and ρ = 2.5µm. To determine the ground truth fiber distribution, 100 fibers (seeded from 100 random voxels) were manually traced in the highest resolution dataset, the corresponding histogram fit to spherical harmonic coefficients, and the primary orientation extracted as performed above. The angular error between the ground truth orientation and the results from structure tensor analysis is shown in Figure 6.3 (left). It is clear that higher resolution provides the most accurate representation of fiber direction, however, even isotropic resolution had an average error of less than 5.0°.

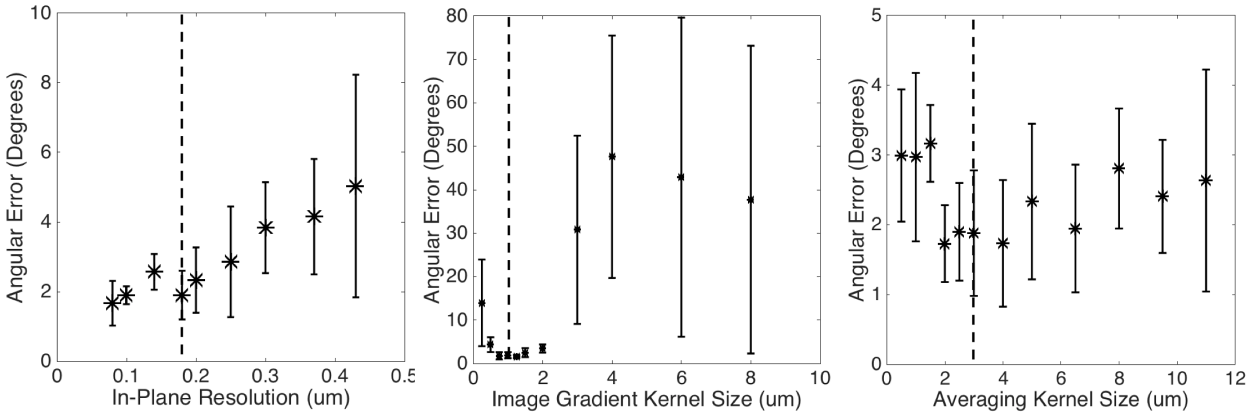

Figure 6.3 Sensitivity of structure tensor analysis to imaging and image processing parameters. Ground truth fiber orientation distribution was determined for three confocal z-stacks by manually tracing 100 fibers per confocal volume. Angular error in the primary fiber orientation is plotted as a function of the in-plane confocal resolution (left), the standard deviation (σ) of the Gaussian kernel used for calculating spatial derivatives (middle), and the standard deviation (ρ) of the Gaussian kernel used for spatial averaging (right). Dashed lines indicate the parameters chosen for this study.

Next, the sensitivity of the analysis to the standard deviation of the first derivative Gaussian, σ, was analyzed. This was done using the z-stacks acquired at 0.18µm×0.18µm×0.42µm, ρ = 2.5µm, and a range of σ (Figure 6.3, middle). We find a range of kernel sizes, with σ between 0.5µm and 2µm that result in accurate orientation results. This optimal range closely matches the size of the myelinated fibers in the image, which we found to have diameters in the range of 0.5µm-1.5µm. Outside this range, the results become unreliable. In particular, too large a kernel will result in a significant blurring of the image, which leads to large areas of isotropic intensity, and an almost random orientation estimate for all pixels. The error begins to approach the expected value for the angle between two randomly oriented lines through the origin, 1 radian or 57.3° [245].

Finally, we find that the method is relatively robust to the averaging kernel size, ρ (Figure 6.3, right). With a resolution of 0.18µm×0.18µm×0.42µm and σ=1µm, all values of the averaging kernel gave an estimate of the primary fiber direction accurate to within 4°.

### 6.3.2 Image Registration

An example of the correspondence between histology and MRI after registration is shown in Figure 6.4. The top row shows the 2D confocal montage (A1), the corresponding block-face image (A2), and the MRI data (A3), all aligned in the intermediate “block-space”. These whole-slice images show agreement of large-scale features, including sulci and gyri, and major white matter tracts. A magnified region of interest is also shown for each modality (A4-A6). The asterisk indicates the location of the center of the 3D confocal z-stack acquired and displayed in Figure 6.9, E. The arrows highlight anatomical landmarks and are drawn at the same position on each image. It is clear that smaller scale features still share precise shape, position and alignment on all three modalities.

Similarly, panels (B1-B3) assess the registration accuracy from the slice corresponding to that shown in Figure 6.9, A. While not strictly necessary, we chose to manually remove the cerebellum from the confocal and block images to facilitate registration, as is commonly done in studies where this structure is of no interest [246, 247]. Again, we see excellent agreement between histology, block, and MRI on the scale of the full slice (B1-B3) and at the voxel-wise scale (B4-B6).

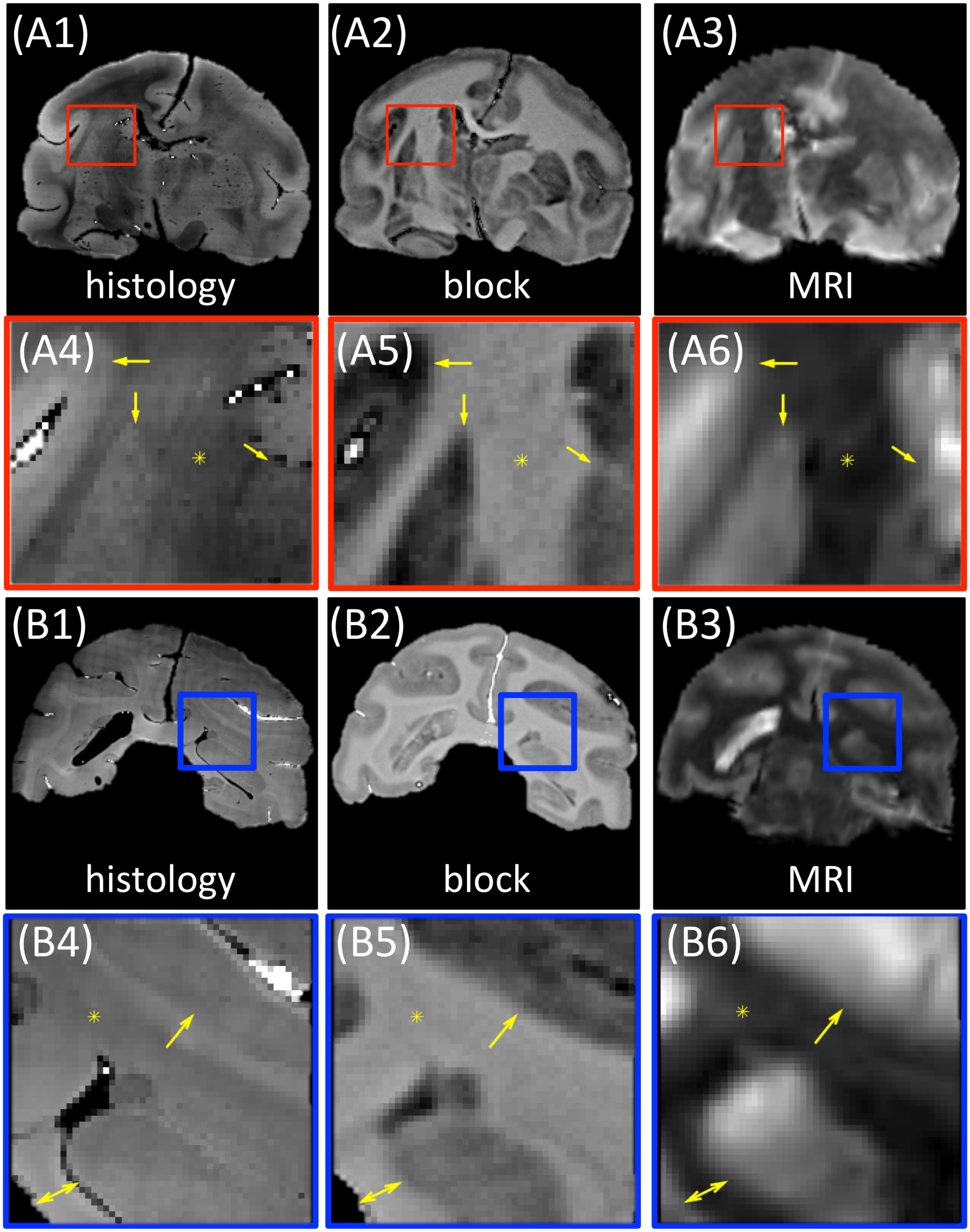

Figure 6.4 Image registration quality. Selected histological slices show the correspondence of matching between MRI and histology of the full slice and magnified views. The top two rows correspond to the histological slice shown in Figure 6.9, E, and displays histology (A1), the matching block-face (A2) and the non-diffusion weighted MRI images (A3), all registered to the

intermediate “block space”. The magnified views (A4-A6) show that MRI can be correlated on the voxel level to histology. The arrows highlight anatomical borders or edges between white and gray matter, while the asterisk indicates the location of the center of the acquired 3D z-stack. The lower two rows show the slice from Figure 6.9, A (note the cerebellum was removed to facilitate registration). Again, there is a large scale agreement between histology (B1), block-face (B2), and the registered MRI (B3). Magnified views are displayed in figures (B4-B6) and show agreement on the voxel-wise scale. The asterisk, again, indicates the center of the 3D z-stack, while arrows facilitate comparisons by highlighting anatomical similarities.

### 6.3.3 Single Fiber Analysis

The results of 3D structure tensor analysis in regions of the brain containing predominantly single fiber populations are shown in Figure 6.5 (rows 1 and 2). Structure tensor analysis demonstrates the corpus callosum (Figure 6.5, A) is composed of fibers running in the right-left orientation and remaining largely in-plane. Visually, this corresponds well with the primary fiber orientation derived from MRI, including the CSD-FOD (row 3) as well as the apparent diffusion coefficient profile of the diffusion tensor (row 4), calculated as the negative log of the normalized diffusion signal. Histological results from the optic tract (Figure 6.5, B) and external capsule (Figure 6.5, C) demonstrate the ability of this technique to describe obliquely-oriented, or slightly through-plane, fibers as well as those oriented completely through-plane, respectively. Again, the 3D structure tensor results qualitatively agree well with both the MRI-derived FOD and diffusion tensor.

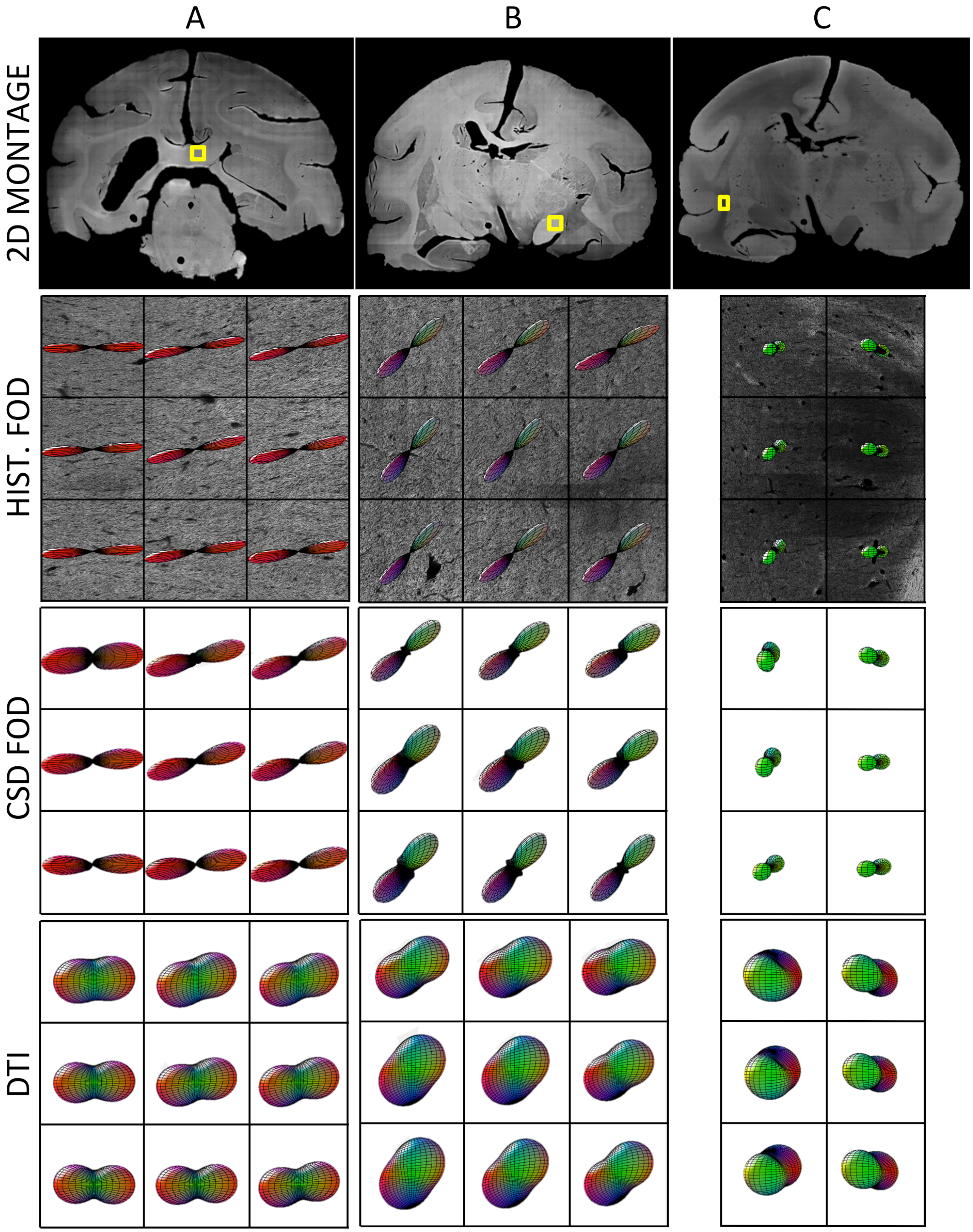

Figure 6.5 Qualitative single fiber analysis. Three large white matter tracts containing a single fiber population are shown, including the corpus callosum (A), optic tract (B), and external capsule (C). The 2D confocal montage of the tissue for each slice (row 1) highlights the locations of the 3D-confocal z-stack (yellow box). Histological FOD (row 2) is shown overlaid on a single slice of the z-stack. The MRI-FOD (row 3) and tensor (row 4) for corresponding voxels are displayed as 3D glyphs. All glyphs are color coded based on orientation, where red, blue, and green represent orientations in the left-right, superior-inferior, and anterior-posterior directions, respectively. Note that the third column from the external capsule (C) contained predominantly gray matter and has been excluded from analysis.

Figure 6.6 shows cloud plots of angular error in peak orientations between diffusion MRI and histology for 74 voxels in 10 different regions of the brain containing only a single fiber population. The average magnitude angular error (in 3D) was 6.4°±4.0° for CSD and a larger error of 11.2°±5.9° for DTI. For CSD, the mean in-plane orientation error was -0.8°±6.5°, and through-plane was 1.7°±4.0°. The mean DTI error was -3.8°±6.5° in-plane and -6.6°±7.9° through-plane.

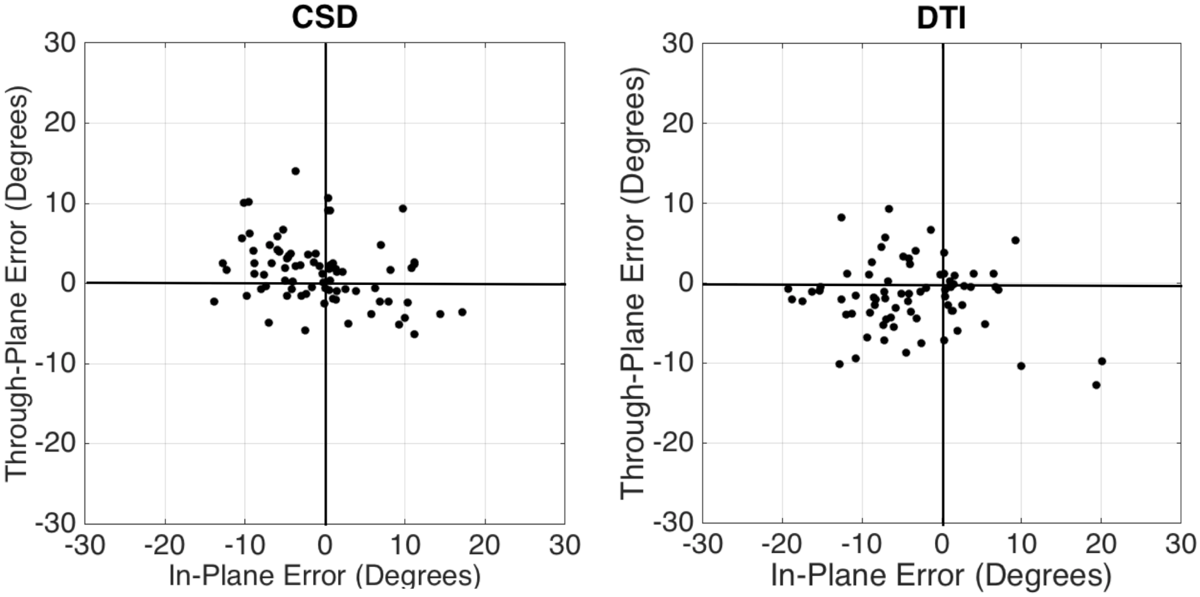

Figure 6.6 Quantitative single fiber analysis. Cloud plots display angular error between MR and histology for CSD (left) and DTI (right) derived orientation estimates. Orientations are projected onto the xy-axis (in-plane) and the yz-axis (through-plane).

While the regions in Figure 6.5 represent voxels containing classic single fiber populations, an in-depth examination of the histology depicts a "spread" of orientations in these imaging voxels. For example, structure tensor analysis of the corpus callosum voxel (Figure 6.7, A) shows an anisotropic fanning of the fibers while the optic tract voxel (Figure 6.7, B) shows axonal orientation dispersion symmetric around the predominant orientation. A common analysis approach in the literature is to fit these to a distribution on a sphere in order to extract parameters that can be used to describe geometric patterns [248]. One such distribution is the Bingham distribution [249], an antipodally symmetric distribution with elliptical contours on the sphere that is well suited for representing asymmetric or anisotropic dispersion [50]. If fit to the Bingham distribution, the voxel in the corpus callosum results in anisotropic concentration parameters: $\kappa_1$=21, $\kappa_2$=12, confirming slightly anisotropic fanning geometry (fanning in the S/I direction). The optic tract voxel has slightly larger, but isotropic, dispersion: $\kappa_1$=10, $\kappa_2$=9, consistent with a symmetric orientation dispersion.

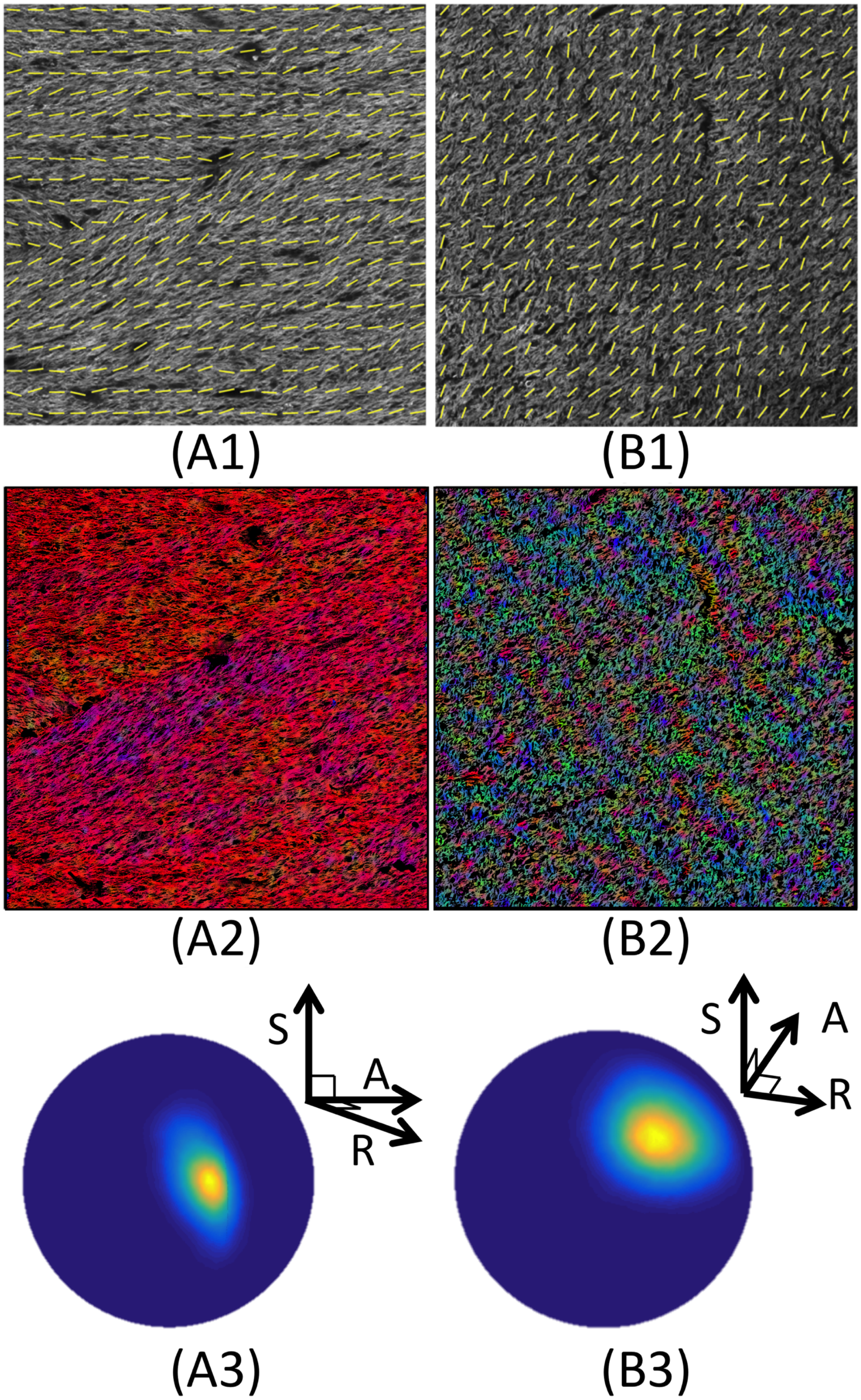

Figure 6.7 Orientation dispersion in single fiber regions. Vector maps (A1, B1) display fiber orientation projected onto xy plane. In colormaps (A2, B2) fibers are orientationally color-coded using the coloring scheme described in Figure 6.5. The FOD is

further displayed as a distribution over the unit sphere (A3, B3). These have been rotated to better visualize the dispersion patterns. The blue-yellow color codes from 0 to high values of the distribution. The voxel from the corpus callosum (A) is the center voxel depicted in Figure 6.5A, while that from the optic tract (B) is also the center voxel from Figure 6.5B.  Note that both voxels display a spread of orientations.

### 6.3.4 Crossing Fiber Analysis

Figure 6.8 demonstrates the advantages of using 3D acquisition and analysis over previous studies limited to 2D. The confocal montage (Figure 6.8, A) was used to choose a voxel for high-resolution acquisition that visually appeared to contain fibers oriented both in-plane and through-plane (Figure 6.8, B). The middle slice of the z-stack was chosen for conventional 2D analysis using the methods described in Budde and Frank, 2012 [134]. These results (Figure 6.8, C) suggest a single fiber population in this voxel, oriented primarily in the superior-inferior direction. However, the MR data indicate the presence of multiple fibers (Figure 6.8, D), which is verified with 3D structure tensor analysis, shown as a color-coded fiber map (Figure 6.8, E) and 3D glyph (Figure 6.8, F).

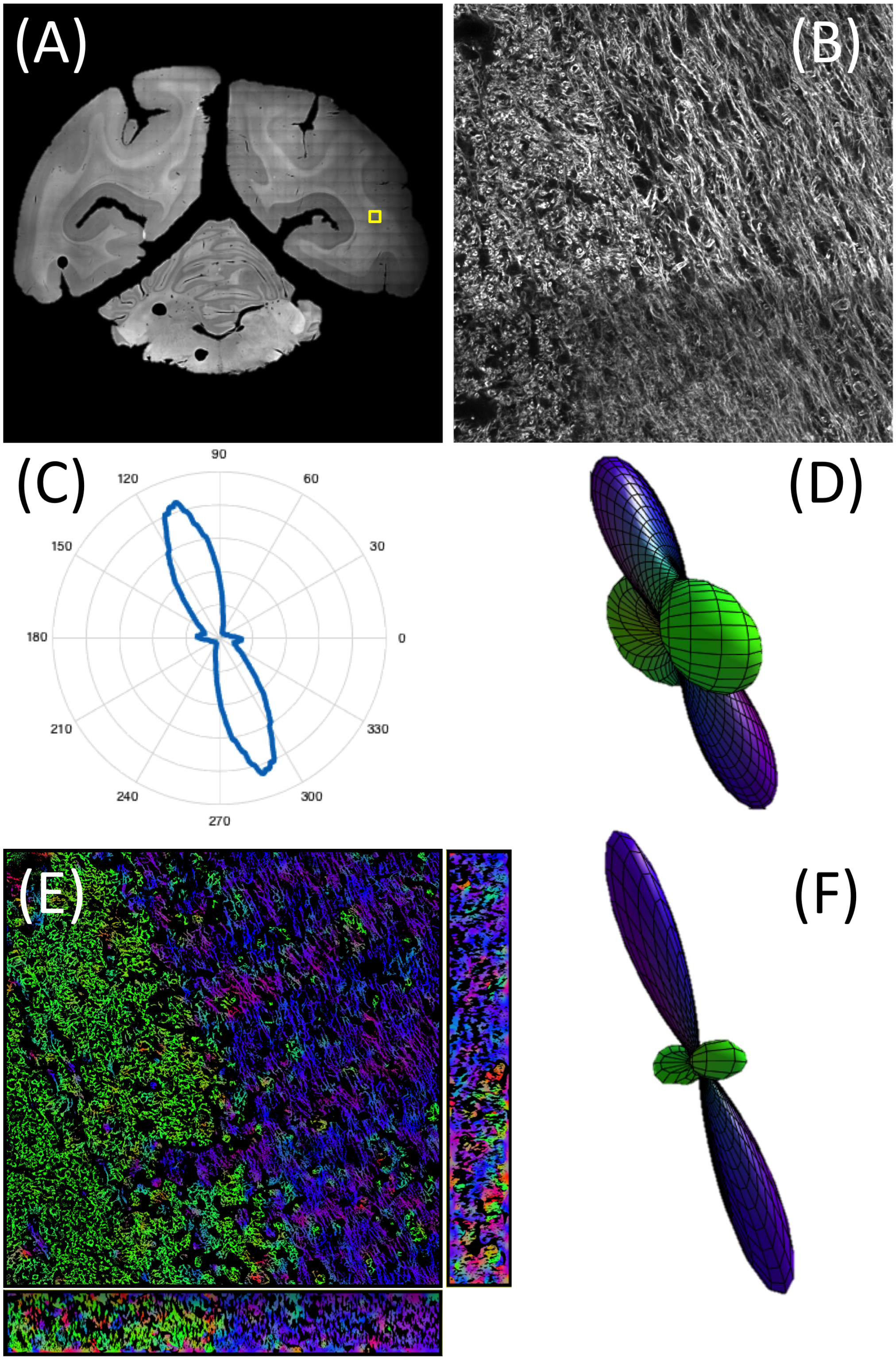

Figure 6.8 Crossing fiber analysis in 2D and 3D. The 2D confocal montage (A) highlights the location of the high-resolution 3D z-stack (B). 2D structure tensor analysis was performed on a single slice and the results shown in the 2D rose plot (C) suggest a single fiber population, while CSD-MRI data (D) suggest two fiber populations. Results from 3D structure tensor analysis are displayed as a colormap of the slice (E), along with the two orthogonal views, using the color scheme described in Figure 6.2, as well as FOD glyph (F), both of which highlight the fact that two distinct fiber orientations are present.

Figure 6.9 further demonstrates the ability of 3D structure tensor analysis to capture the crossing of fiber bundles in 3D. A 3.2mm×1.2mm region where the corpus callosum meets the corona radiata is highlighted (Figure 6.9, A) along with the structure tensor results from the histological z-stack (Figure 6.9, B), where the two dominant fiber bundles and their intersection are readily apparent. These results qualitatively agree with the FODs derived from MRI data (Figure 6.9, D).

The ability to extract orientation information from complicated crossing geometries is highlighted in Figure 6.9, C, where fibers running right to left (Figure 6.9, C, red) interdigitate with the majority of fibers which run superior to inferior (Figure 6.9, C, blue). Further, regions with very sharp crossing angles can be identified (Figure 6.9, E) and resolved with structure tensor analysis (Figure 6.9, F). The dominant orientations again agree well with those from CSD (Figure 6.9, G), however, regions with multiple crossings at acute angles are often not identified in MRI as having multiple fiber populations.

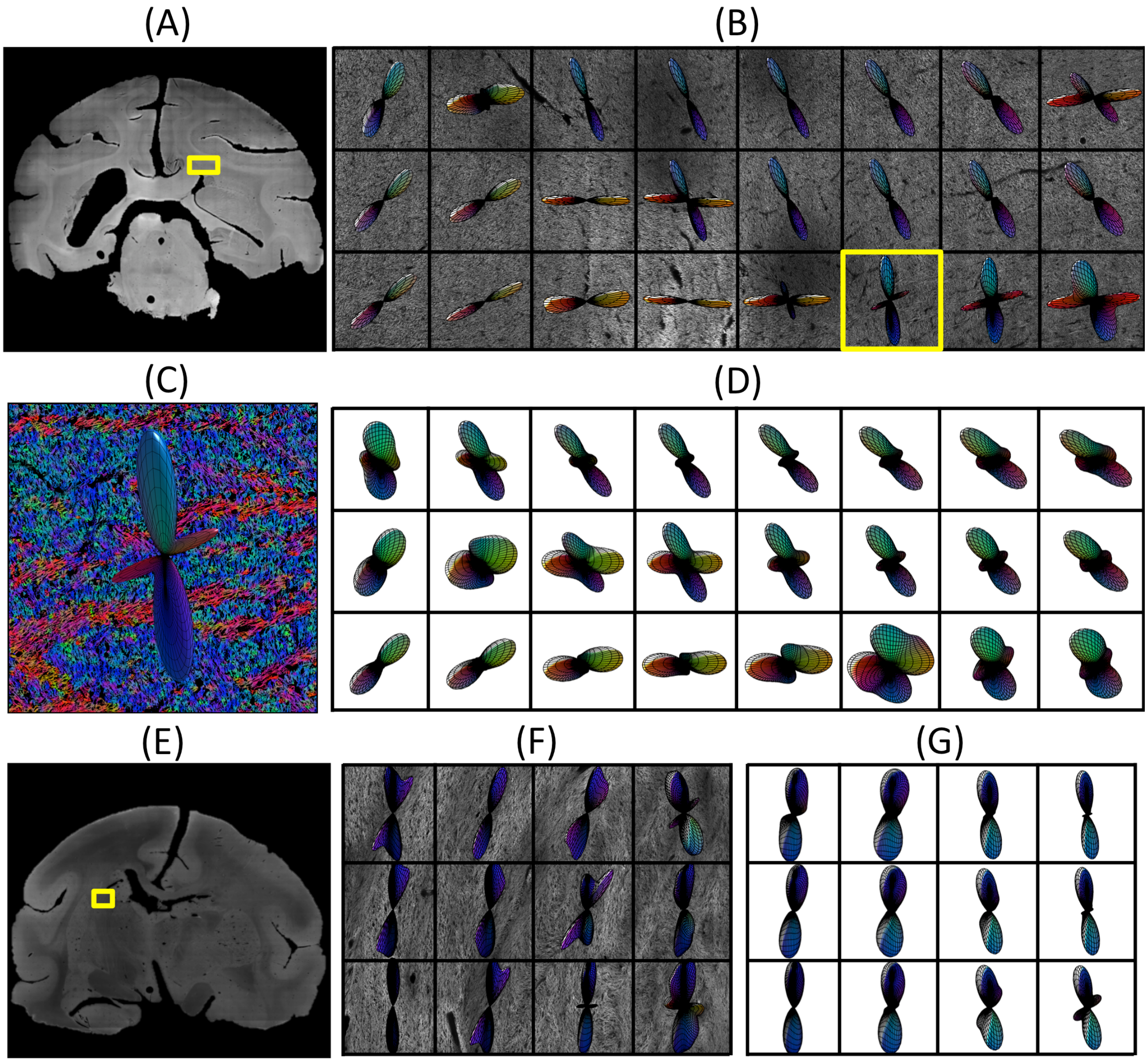

Figure 6.9 Qualitative crossing fiber analysis. The intersection of the corpus callosum and corona radiata (A) was imaged in 3D, and FOD's from structure tensor analysis are displayed (B). The yellow box highlights the voxel displayed in (C) where interdigitating fibers running right-left are visible in both the colormap and the 3D glyph. The MRI results using CSD (D) appear to be a blurred version of the histological FOD, where primary orientations largely agree. The region identified in (E) is shown to contain fanning structures and bundles crossing at sharp angles (F), while the MRI data (G) fail to resolve sharp crossing angles.

Forty histological voxels were identified through structure tensor analysis as having multiple fiber populations, and quantitatively compared to CSD results. The algorithm to determine whether a voxel contains crossing fibers is described in [40]. Briefly, the histological FOD is sampled in a large number of evenly distributed directions on a unit sphere and local maxima identified (local maxima are defined to be greater than any other samples within a search radius of 0.25 radians). Similarly, the FOD's of the corresponding MRI-CSD results were analyzed. In order to remove spurious peaks, those with amplitude less than 10% of the amplitude of the largest peak, as well as peaks that did not correspond with any histological peak to within an angular error of 30°, were discarded. The results of this analysis are shown in Figure 6.10. The average magnitude angular error was 10.4°±5.1° for the primary (largest amplitude) fiber orientation (Figure 6.10, left), and 11.6°±7.0° for the secondary orientation (Figure 6.10, right), both of which are larger than the error associated with single fiber regions. For the primary direction, the mean in-plane orientation error was -0.1°±9.7°, and through-plane was 3.5°±5.7°, while that for the secondary direction was -0.2°±10.4° and 3.6°±8.4°, respectively. Finally, we employ a commonly used measure, the success rate, as a function of fiber crossing angle (Figure 6.10). The success rate measures the proportion of voxels containing two fiber orientations (as identified by histology) where two peaks could also be identified by the chosen MRI algorithm. From the 40 identified voxels with multiple fiber populations, only 29 of the corresponding MRI voxels exhibited the presence of crossing fibers after spherical deconvolution. With this data set, CSD consistently failed (<20% success rate) to resolve crossing fibers in regions where histology identified crossing at angles below 60 degrees, while the success rate was high for fibers crossing at angles above 70°. Further, DTI failed to resolve crossing at all angles, which was expected [204], as the tensor model represents only one dominant direction.

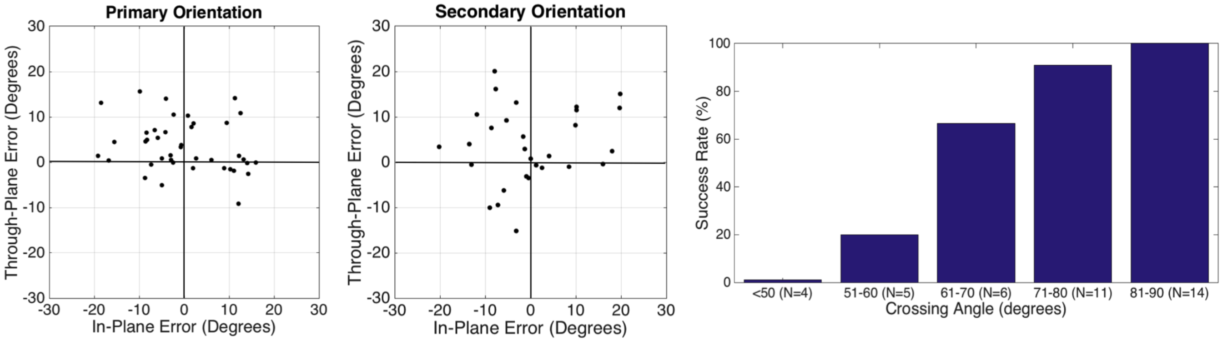

Primary Orientation

Secondary Orientation

Figure 6.10 Quantitative crossing fiber analysis. Cloud plots display angular error between MR and histology for the primary fiber orientation (left) and secondary fiber orientation (middle) in regions with crossing fibers. Orientations are projected onto the xy-axis (in-plane) and the yz-axis (through-plane). The success rate of CSD with the damped Richardson-Lucy algorithm is reported as a function of fiber crossing angle as identified by histology (right). The sample size is also noted for each crossing angle bin.

## 6.4 Discussion

Diffusion MRI-based non-invasive mapping of the three-dimensional network of connections in the brain has gained widespread use in the neuroimaging community. These tractographic reconstructions result in exquisite images of the human brain that can easily be over-interpreted or misinterpreted. Thus, validating diffusion imaging's ability to assess the underlying fiber orientation in each voxel is critical for its use as a biomedical tool.

The use of ex vivo histology as a "gold standard" holds promise, as it provides true axonal characteristics at the micron and voxel-sized scales, including microstructural compartments, biophysical properties, and complex tissue geometries. This work presents an extension of histological validation of orientation functions to three dimensions. Previous orientation validation studies have been limited in that they required identification of suitable regions of interest where 3D FODs could be compared to the inherently 2D coronally sectioned histological data. This also necessitated sectioning the tissue block paraellel to the primary directions of interest for adequate analysis, as any through plane fibers would be undetected [134] and could lead to misleading orientation results (Figure 6.8, C). While the use of 3D optical imaging to validate dMRI has recently gained traction, determination of the white matter histological fiber orientation distribution has not yet been reported. For example, the current study shares many methodological similarities with Khan et al., 2015, including structure tensor analysis of confocal data. However, rather than assessing the orientation of all individual axons, the focus in that study was on quantitative comparisons of dMRI and structure tensor measures (FA, eigenvalues) on the scale of 10's-100 microns. Similarly, Jesperson, 2012, performed a 3D analysis of Golgi-stained tissue, but with aim of deriving the dendritic and axonal orientations in the cerebral cortex.

The use of histology for validation studies presents several potential limitations. Two of these are the data registration problem, and the imaging depth limitation inherent to confocal microscopy. Mapping high resolution histological data onto the MRI images is known to be a challenge because of the many differences between the histological slices and the original brain tissue [247]. The process of fixation and brain extraction can lead to mechanical distortions in the tissue, while cutting, placing slices on slides, and staining can cause contractions, nonlinear distortions, and separation of the hemispheres [247]. In this study, these problems are addressed through the use of linear and non-linear registration of the data sets. For data alignment, the acquisition of the block-face image data is crucial; it provides an undistorted 3D image of the brain before sectioning, and operates as an intermediate step in registration of the potentially distorted histology to the MR data [191]. Previously, this technique has been shown to provide registration accurate to approximately the size of the MRI voxel [194]. Tissue contraction (shrinkage) is further accounted for in the confocal pre-processing steps (and discussed in section 6.4.4 Data Pre-Processing). The imaging depth limitation of confocal microscopy is also discussed in Section 6.4.4 Data Pre-Processing.

### 6.4.1 Single Fiber Analysis

The peaks of the histological FOD correspond well with those obtained with DTI and CSD in regions containing predominantly a single fiber population. While DTI had a larger angular error than CSD reconstruction (11.2° versus 6.4°, respectively), this is potentially a result of differing acquisition protocols (lower b-value and fewer sampling directions for DTI) rather than DTI being an inferior technique in single fiber regions. These mean angular errors are slightly larger than simulation [250] and phantom [227] studies with similar imaging conditions, emphasizing the importance of incorporating the complex tissue geometries seen *in vivo*. Further, the in-plane orientation errors agree well with previous 2D histological validation studies [132, 133], which were only able to capture in-plane orientation estimates. These results verify that confocal analysis and image processing are able to extract fiber orientation distributions in 3 dimensions from histological data, thus serving as a methodological benchmark.

A closer look at these regions shows that the underlying geometry may be more complex than an idealized single fiber bundle where all fibers are assumed to be running parallel within the voxel. For example, histology (Figure 6.7) depicts a spread of orientations in the form of fiber-fanning, or in wave-like undulations. Recently, there has been interest in characterizing this spread by using dispersion indices in order to infer the underlying fiber geometry [54, 206, 251]. While the CSD and DTI methods implemented assume axially symmetric profiles, 3D structure tensor analysis is well suited for studying the axonal angular dispersion, even in highly organized white matter tracts. Thus, the methods presented in this study can provide a valuable resource in validation of this challenging inverse problem.

### 6.4.2 Crossing Fibers

Understanding the limitations of dMRI in crossing fiber regions is an active area of research. Here, we chose to analyze our data using a spherical deconvolution model, which aims to reconstruct the FOD directly. However, there are a variety of high angular resolution approaches to reconstruct orientation estimates that could be validated against histology, including, but not limited to, Q-ball Imaging [35], DSI [24], multi-tensor [120] or ball-and-stick models [61], persistent angular structure models [40], diffusion orientation transform [38], and the CHARMED model [49]. While this study does not present a full validation, it is important to point out that with the current imaging parameters (SNR ~15, sampling directions = 90, b-value = 6400 s/mm$^2$, roughly equivalent attenuation profile as an in vivo value of ~2000 s/mm$^2$), CSD was not able to consistently resolve fibers crossing at angles below 60°. This is in close agreement with simulations [123] which found a success rate of approximately 20% for constrained spherical deconvolution [45] at crossing angles below 60° with an SNR of 30, b-value of 3000 s/mm$^2$, and 60 sampled directions. Additionally, simulating crossing fibers with equal fiber volume fractions, an SNR of 30, and a b-value of 1000 s/mm$^2$ [252] find an angular resolution limit using CSD of 54°.

It is important to emphasize that we do not want to draw broader conclusions regarding this reconstruction method without larger sample sizes and an optimized acquisition protocol that would be appropriate to validate this (and other) models and parameters. Thus, future work will determine the relationship between the MRI signal and the histological FOD as a function of diffusion model, b-value, number of diffusion encoding directions, SNR, and scan time equivalence. Validation using structure tensor analysis is not limited to CSD methods, and can easily be applied to any of the existing techniques for modeling orientation functions in order to test the limitations of these techniques or to determine optimal acquisition parameters.

### 6.4.3 Sensitivity

Figure 6.3 shows that 3D structure tensor analysis is relatively robust to the resolution of the confocal z-stack. The angular error closely follows intuition – the higher the image resolution, the more accurate are the orientation measurements. The final choice of in-plane resolution, 0.18μm×0.18μm, was a compromise between orientation accuracy and scan time. A more than two-fold reduction in resolution from $0.08\mu m^2$ to $0.18\mu m^2$ leads to a minimal loss of accuracy, yet allows acquisition of a field of view greater than 4 times larger in a given scan time.

We found our technique is quite sensitive to the kernel used for calculating spatial derivatives. While this step can be performed using a simple finite difference kernel (e.g. forward, backward, central difference) along all three axes, a Gaussian derivative is most commonly used as a regularization step to improve SNR and decrease sensitivity to noise. This also makes the algorithm sensitive to structures that correspond to the size of the Gaussian derivative. This explains the lower angular error when the kernel size is approximately the size of the myelinated fibers, which are the objects we wish to detect in the image.

Finally, the structure tensor analysis was not particularly sensitive to the averaging kernel size. This kernel serves to combine all orientation information in a local neighborhood, which leads to better estimates and reduced local errors in orientation estimates. Any low-pass filter can accomplish this smoothing operation, however, if two distinct orientations exist in a neighborhood, an averaging operation could lead to erroneous estimates. Thus, we chose an averaging kernel large enough to encompass the surfaces normal to the fiber, but small enough to resolve fibers interdigitating on scales as small as 2.5μm.

For fiber orientation estimation from 3D data using structure tensor analysis, we advise acquiring data at the highest resolution that time permits. We recommend calculating the spatial derivatives using a filter matched to the size of the structures of interest, while ensuring that the averaging kernel is slightly larger than the structure of interest. For future work, an adaptive approach may prove fruitful. Iterating through a range of spatial derivative kernels and keeping the estimate that maximizes the orientation certainty could lead to more accurate estimates in the presence of a distribution of fiber diameters.

### 6.4.4 Data Pre-Processing

To obtain reliable FODs using structure tensor analysis we found it necessary to perform 4 corrections, similar to those found in Khan et al., 2015 [136]. First, image intensity variation as a function of depth must be corrected as it could bias orientation estimates. Existing corrections include dividing each slice of the z-stack by the mean intensity within that slice [136], or estimating the extinction coefficient of light in the tissue [253] and correcting each slice using this decaying exponential, both of which should result in a constant intensity profile. Here, we chose to increase the laser power as a function of tissue depth. However, additional analysis (not shown) indicates that all three methods yield similar orientation results. Our current implementation was chosen to ensure that all slices make use of the entire 8-bit intensity range, which preserves detail as well as SNR as a function of depth. Light scattering is one of the major limitations of the current technique, as it limits the tissue depth that can reasonably be imaged. Optical clearing to minimize light scattering is one possible solution, and will be a focus of future work.

The second pre-processing step, deconvolution, is necessary because PSF anisotropy will bias orientation estimates. For this, Khan et al., 2015 chose to measure and approximate the PSF with an anisotropic 3D Gaussian function, then blurred their image in the xy plane to create an image effectively convolved with an isotropic PSF. This is an appropriate approach for their analysis, as they are interested in answering questions regarding a single dominant orientation in the MR-voxel rather than the full orientation distribution. However, our analysis requires the ability to distinguish individual fibers, and necessitates deconvolution. Using the same data from the sensitivity analysis, we performed analysis without the deconvolution step (but all other parameters constant), and find a significant bias in the through plane direction, with an average of 16° angular error towards the A/P direction, or towards the third dimension (data not shown). Interestingly, the in-plane error remained minimal (<4°).

The third operation, interpolation to isotropic resolution, is necessary (as described before) to ensure that in-plane and through-plane fibers are weighted equally in the final distribution. The final correction is a simple geometric correction to account for tissue shrinkage. The thickness after histological processing was consistently found to be between 50 and 55um, or 62-68% of the thickness of the original section. These values, again, are in line with those obtained from Khan et al., 2015, where similar processing and staining techniques were used.

## 6.5 Conclusion

We have demonstrated the ability of structure tensor analysis to extract the 3D FOD from confocal microscopy z-stacks and compared these to FODs calculated via constrained spherical deconvolution for the same voxel locations. Agreement is good (5-11 degrees) for both single and crossing fibers, except when the crossing angle is less than about 60 degrees. This technique represents a considerable advancement in the development of a “gold standard” for validating fiber reconstruction methods, and could be used to assess and improve the various “crossing fiber” algorithms that attempt to recover the FOD or ODF on a voxel-wise scale. Further, by extracting features such as the spread of fiber orientations and the fractions of fibers in each direction, these methods could be the basis of detailed studies of the relationship between the diffusion MRI signal and the underlying tissue microstructure.

# CHAPTER 7: HISTOLOGICAL VALIDATION OF DIFFUSION MRI FIBER ORIENTATION DISTRIBUTIONS AND DISPERSION

## Prologue

Using the methodology developed in Chapter 6, and the squirrel monkey MRI data from Chapter 4, this chapter presents a full validation of a large number of commonly implemented algorithms for recovering intra-voxel fiber structures from diffusion MRI data. This study represents the first 3D histological validation of diffusion MRI techniques, and the first validation to quantitatively compare a large number of competing algorithms to direct measurements of histologically-derived axonal orientations.

## Abstract

Diffusion magnetic resonance imaging (dMRI) is widely used to probe tissue microstructure, and is currently the only non-invasive way to measure the brain's fiber architecture. While a large number of approaches to recover the intra-voxel fiber structure have been utilized in the scientific community, a direct, 3D, quantitative validation of these methods against relevant histological fiber geometries is lacking. In this study, we investigate how well different high angular resolution diffusion imaging (HARDI) models and reconstruction methods predict the ground-truth histologically defined fiber orientation distribution (FOD), as well as investigate their behavior over a range of physical and experimental conditions. The dMRI methods tested include constrained spherical deconvolution (CSD), Q-ball imaging (QBI), diffusion orientation transform (DOT), persistent angular structure (PAS), and neurite orientation dispersion and density imaging (NODDI) methods. Evaluation criteria focus on overall agreement in FOD shape, correct assessment of the number of fiber populations, and angular accuracy in orientation. In addition, we make comparisons of the histological orientation dispersion with the fiber spread determined from the dMRI methods. As a general result, no HARDI method outperformed others in all quality criteria, with many showing tradeoffs in reconstruction accuracy. All reconstruction techniques describe the overall continuous angular structure of the histological FOD quite well, with good to moderate correlation (median angular correlation coefficient >

0.70) in both single- and multiple-fiber voxels. However, no method is consistently successful at extracting discrete measures of the number and orientations of FOD peaks. The major inaccuracies of all techniques tend to be in extracting local maxima of the FOD, resulting in either false positive or false negative peaks. Median angular errors are ~10° for the primary fiber direction and ~20° for the secondary fiber, if present. For most methods, these results did not vary strongly over a wide range of acquisition parameters (number of diffusion weighting directions and b value). Regardless of acquisition parameters, all methods show improved successes at resolving multiple fiber compartments in a voxel when fiber populations cross at near-orthogonal angles, with no method adequately capturing low to moderate angle (<60 degrees) crossing fibers. Finally, most methods are limited in their ability to capture orientation dispersion, resulting in low to moderate, yet statistically significant, correlation with histologically-derived dispersion with both HARDI and NODDI methodologies. Together, these results provide quantitative measures of the reliability and limitations of dMRI reconstruction methods and can be used to identify relative advantages of competing approaches as well as potential strategies for improving accuracy.

## 7.1 Introduction

Diffusion magnetic resonance imaging (dMRI) has proven a valuable neuroscience tool due to its unique ability to provide information about tissue composition, microstructure, and structural connectivity of the brain non-invasively [25, 254]. In the white matter, the diffusion-driven displacements of water molecules are hindered by the organization of intra and extra-cellular tissue components [18], making it possible to infer the distribution of neuronal fiber orientations in each voxel from a set of diffusion measurements, an object often referred to as the *fiber orientation distribution* (FOD). Fiber tractography can then be performed by following these fiber orientation estimates from voxel to voxel throughout the brain in order to reconstruct the structural connections between different brain areas [8, 55].

There are a number of assumptions and uncertainties that can affect the ability of fiber tractography to faithfully represent the true axonal connections of the brain. The most obvious potential source of error is in the inference of fiber orientation in each MRI voxel [32, 255]. The challenge here lies in the fact that axons have diameters in the micron range, while a typical

MRI voxel can be on the order of millimeters and contain hundreds of thousands of axons [104, 256] with a wide range of possible configurations, which makes the mapping from diffusion signal to axon orientation an ill-posed problem (where many patterns are likely to give rise to the same MRI measurement). In addition, the choice of dMRI reconstruction method in combination with experimental conditions, including the number of diffusion weighted images (DWIs) and the amount of diffusion weighting (the “b-value”), are expected to result in different inferences of the fiber geometry in each voxel. Because these estimates of fiber orientation form the input to nearly all fiber tracking algorithms, it is critical that the validity of experimentally estimated orientation information be checked and quantified against the true physical geometry of fibers under investigation.

Diffusion tensor imaging (DTI), the first reconstruction method to allow mapping of fiber orientations throughout the brain, models diffusion as a 3D Gaussian distribution [225]. While the fiber orientation estimates from DTI have been validated in large coherent fiber bundles, a significant limitation of DTI is that it cannot adequately capture the underlying structure in voxels containing complex white matter architectures or multiple fiber populations. This “crossing fiber” problem has motivated the development of a large number of reconstruction methods which aim to resolve multiple fiber orientations and recover complex fiber configurations [24, 35-41, 43-45, 49]. These algorithms, typically referred to as high angular resolution diffusion imaging (HARDI) methods, differ in a number of aspects, including acquisition requirements, fundamental assumptions on diffusion processes, and the representation of orientation information. Some techniques estimate the FOD directly, whereas others estimate a diffusion orientation distribution function (dODF) describing the probability of diffusion in a given direction, with the assumption that fiber orientations coincide with the peaks of the dODF. Finally, while some reconstruction methods do not explicitly model diffusion in white matter, others model distinct tissue compartments and fiber populations separately. For example, a common compartmental model, termed NODDI (neurite orientation dispersion and density imaging) [54], utilizes a fiber orientation dispersion index (ODI) to characterize the geometrical angular variation of the fiber populations. Similarly, measures of dispersion can be extracted from the FOD and ODF directly [257-259] as a way to characterize the fiber geometry in a voxel. Due to the large number of reconstruction methods, and differences among them, a direct validation and comparison among techniques remains very difficult.

The validation method of choice for most reconstruction algorithms [36-38, 45, 120, 260], or comparison of algorithms [6, 123], is through numerical simulations. Simulations offer the versatility of assessing performance across a broad range of physical and experimental conditions. However, they rely on assumptions and approximations to generate the modeled dMRI signal that are likely to be over-simplifications of complex biological tissue. Physical phantoms add additional complexity and realism to the validation process by incorporating practical effects of image acquisition. Yet, these synthetic fiber-based [117, 129] and capillary-based [125, 227] phantoms can still fail to replicate the biological characteristics of brain tissue, including membrane permeability, axon diameters, and the geometric complexity of the central nervous system. Finally, validation of orientation information has been performed by comparisons with the results of histological analysis [132, 133, 135, 261]. While offering exquisite detail of the tissue microstructure, these studies have been limited to two-dimensional analysis of tissue sections, restricting investigation to only those fibers oriented parallel to the plane of sectioning. Recently, several groups have explored the use of confocal microscopy [115, 199], optical coherence tomography [137], and polarized light imaging [138, 262] as a means of extracting the 3D histological FOD for direct comparison with dMRI. Despite these advances, most histological validation studies have studied only a few axonal tracts or MRI voxels, and none have investigated the performance of multiple reconstruction algorithms, nor studied the effect of varying acquisition parameters on their performance.

Thus, there is a need to characterize the distribution of neuronal fibers in 3D using histology and make direct comparisons to the corresponding dMRI estimated orientation distributions. With this in mind, the aim of this study is to determine how well different dMRI models and reconstruction methods predict the ground truth FODs, as well as investigate the effect of fiber geometry, b-value, and number of gradient directions on the accuracy of the reconstruction methods. This is done by extracting the ground truth FOD from 3D confocal data of *ex vivo* tissue followed by spatial registration of the dMRI data to the z-stacks to facilitate comparisons of the same tissue volume. The results of this study are measures of reliability and accuracy of competing intra-voxel fiber reconstruction methods, as well as highlights of the relative merits and limitations of state-of-the-art techniques for analysis of dMRI data.

## 7.2 Methods

### 7.2.1 MRI acquisition

MRI acquisition was performed on three adult squirrel monkey brains, and implemented as described in the squirrel monkey atlas, Section
4.2.2 MRI Methods (Ex Vivo Imaging, subjects #4-6). Briefly, diffusion data were acquired on a Varian 9.4T magnet with a 3D spin-echo diffusion-weighted EPI sequence at 300um isotropic resolution, with 101 uniformly distributed diffusion gradient directions, and the b-value set to 6,000 s/mm$^2$.

In order to assess the effects of diffusion weighting on reconstruction accuracy, the full diffusion acquisition was repeated with b-values of 3,000, 9,000, and 12,000 s/mm$^2$, while keeping all other acquisition parameters (including diffusion times) constant.

### 7.2.2 Histological Procedures

Here, we aim to extract the histological FOD from 3D confocal z-stacks in areas equivalent to the size of an MRI voxel [199]. To do this, we utilized an image processing technique, structure tensor analysis [212], which results in an orientation estimate for every pixel in the 3D z-stack that is occupied by a fiber. All histological procedures are performed as described in Section 6.2 Materials and Methods, and shown in Figure 7.1 for convenience. This includes block-face photographs, tissue sectioning and staining, and both 2D and 3D confocal acquisition (Figure 7.1, A, B). Similarly, confocal pre-processing (correcting for inherent sources of anisotropy), structure tensor analysis, and image thresholding (Figure 7.1, C) are performed as described in Chapter 6. Finally, the histological FOD is then computed as the histogram of the extracted fiber orientations, and fit to high order spherical harmonic (SH) coefficients (Figure 7.1, E). Throughout this chapter, the FODs are displayed as 3D glyphs (Figure 7.1, F) in the same way that the MRI-FOD's are typically displayed in literature.

Four slices were randomly selected for each monkey (12 total slices) for confocal imaging. For each slice, multiple regions of interest were chosen to image (using the above protocol) in order to capture both voxels with coherent single fiber populations, as well as expected regions of crossing fibers. This was done using prior anatomical knowledge of squirrel monkey white matter bundles. For crossing fiber regions, sampling was continued until a sample size of at least N>10 was collected for each histogram bin of crossing angles, ranging from <30° to 90°, with a bin width of 10°.

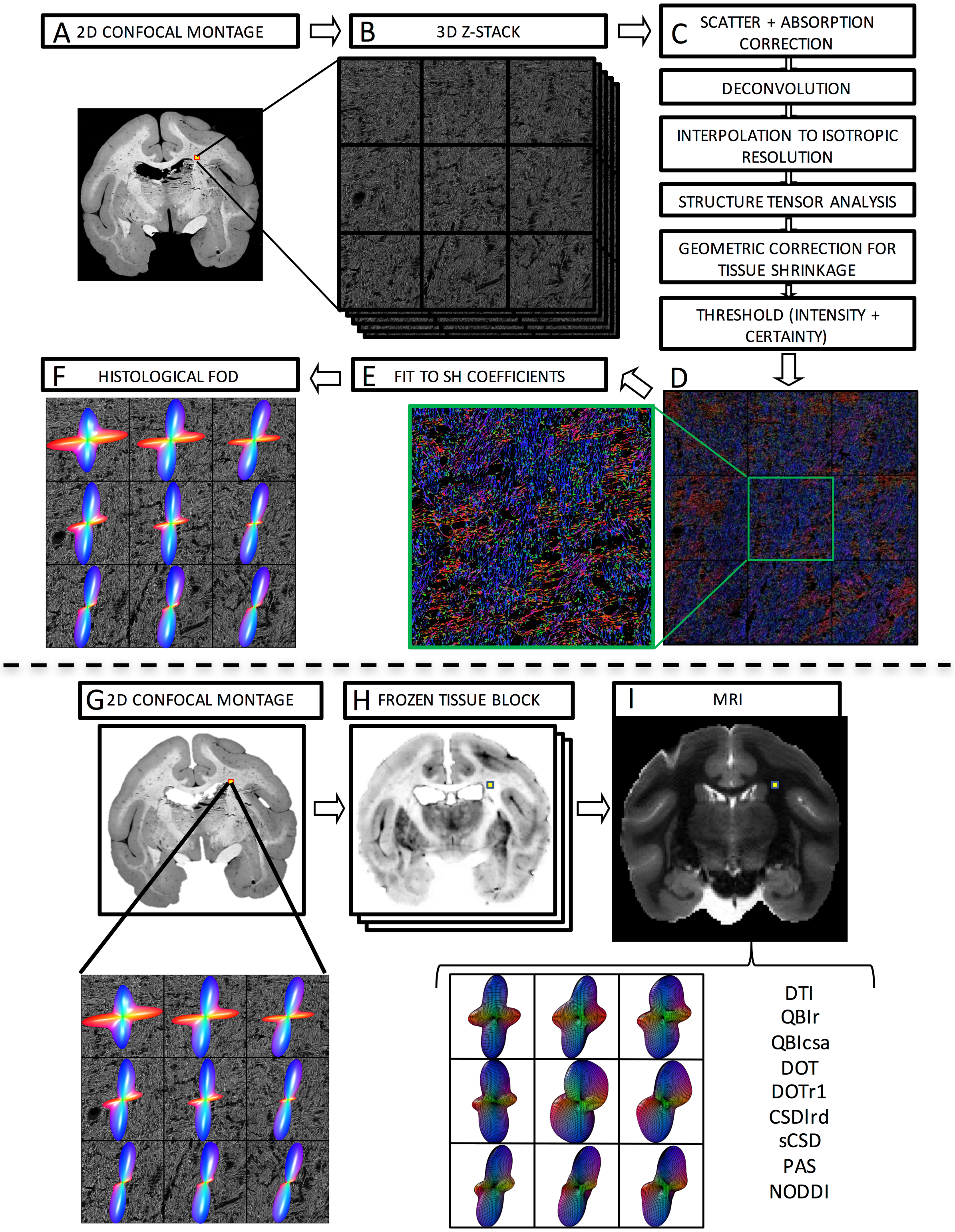

Figure 7.1 Histological procedures and image registration. Confocal acquisition includes a 2D low-resolution montage (A) and a high-resolution 3D z-stack (B). Image pre-processing (C) comprises light scatter and absorption correction, deconvolution, and interpolation, followed by structure tensor analysis. This is followed by geometric correction for tissue shrinkage and thresholding fibers. This results in an orientation estimate for every pixel in the z-stack occupied by a fiber, here shown as an

RGB color map (D) where red, green, and blue represent fiber oriented right/left, anterior/posterior, and superior/inferior. Zooming in on the center voxel shows crossing fibers oriented primarily left/right and superior/inferior. Fitting the orientation distribution to spherical harmonic coefficients (E) results in the histologically defined ground truth FODs, displayed as 3D glyphs (F). The registration procedure involves 2D registration of the 2D confocal montage (G) to the corresponding frozen tissue block (H) and subsequent 3D registration to the non-diffusion weighted image (I). From this, the signal corresponding to the high-resolution z-stack can be determined and processed using a chosen reconstruction method for direct voxel-wise comparison of histology and dMRI.

### 7.2.4 Image Registration

In order to make quantitative comparisons of the histological FODs with estimates derived from MRI, the data must be aligned and oriented appropriately. The multi-step registration procedure used to align histology to MRI data is described in detail in Section 6.2.7 Image Registration. Briefly, the registration included both 2D linear and nonlinear registration of the confocal montage (Figure 7.1, G) to the corresponding block-face image (Figure 7.1, H), followed by 3D linear and nonlinear registration of the block stack to the MRI volume (Figure 7.1, I). Given the location of the 3D z-stack in the 2D confocal montage, we can use the combined deformation fields to determine the MRI signal from the same tissue volume. The MRI signal of interest is analyzed in MRI native space using the chosen reconstruction method (Figure 7.1, I), and transformed to histological space in order to facilitate comparisons with the histological FOD.

### 7.2.5 MRI Reconstruction Methods

The reconstruction models implemented in this study include DTI, Q-ball imaging (QBIr: regularized;  QBIcsa: constant solid angle), diffusion orientation transform (DOT and DOTr1), constrained spherical deconvolution (Richardson-Lucy regularization: CSDlrd; super-resolved: sCSD), and persistent angular structure (PAS). In addition, the biophysical model, NODDI, is also investigated. Detailed descriptions of each method are given in Section 2.4.3 HARDI models and Section 2.4.4 Biophysical models. Again, the focus is on those that attempt to describe the underlying fiber orientation information. Because of the large number of these techniques proposed in the literature, the assessment presented in this work is not exhaustive, yet comprises some of the more commonly implemented reconstruction techniques. All MRI techniques resulting in a function over a sphere are represented as SH series, where the SH order is determined by the number of DWI's utilized in calculation, up to a maximum of order 8 [263]. All reconstruction algorithms are implemented using the Matlab HARDI Toolbox (freely available at NeuroImageN.es), Camino Diffusion MRI Toolbox [264], and MRtrix3 software [186], with default reconstruction parameters.

### 7.2.6 Orientation and Fiber Geometry Measures

For each histological FOD, and all MRI reconstructions (FOD, ODF, etc.), a number of measures were extracted. First, a peak finding algorithm [43, 210] was used to identify distinct fiber populations, and the orientations of each. In order to avoid including small peaks introduced by noise [210], only peaks whose values are larger than a threshold percentage of the largest FOD/ODF value are counted (this threshold is often heuristically chosen – we have chosen 0.2 in this study, a value commonly seen in literature [123]). In this study, voxels where the *histological FOD* contains >1 local maxima (>1 peaks, counting peaks at $\vec{r}$ and $-\vec{r}$ as one) are considered "crossing fiber" voxels while those with a single maximum are considered "single fiber" voxels. In the case of crossing fibers, we also calculate the intra-voxel crossing angle as the angular difference between the two peaks (i.e. fiber populations). The same peak finding procedures and fiber classification schemes are applied to both histological and MRI FODs (or ODFs). These procedures resulted in a sample size of 383 histologically defined single fiber voxels, and 181 crossing fiber geometries.

Next, measures of orientation dispersion were determined for each peak. The ODI is calculated by fitting a Watson (or a multi-Watson, if >1 peak) distribution directly to the SH representation of the function [257] (note that for the NODDI model the ODI is estimated as part of the model-fitting procedure). The Watson distribution, a spherical analogue of the Gaussian distribution, is described by two parameters, the mean orientation (or peak orientation), and a concentration parameter, $\kappa$. As in the NODDI model [54], $\kappa$ is mapped to the ODI:

$$ODI = \frac{2}{\pi} arctan\left(\frac{1}{\kappa}\right) \tag{27}$$

The ODI ranges from 1 for isotropic distributions, to 0 for perfectly parallel fibers.

### 7.2.7 Evaluation Criteria

To assess the quality and accuracy of the reconstructions, we have implemented a variety of metrics that focus on [A] overall agreement in shape of the histological FOD and dMRI spherical function, [B] correct assessment of the number of fiber populations in each voxel, [C] angular error in orientation estimation, and [E] correlation between histological and MRI measures of dispersion or fiber spread.

In order to evaluate agreement in overall shape with the histological FOD, we implemented the angular correlation coefficient (ACC) and the Jensen-Shannon divergence (JSD) (See Appendix 7.A for mathematical descriptions). The ACC, like the linear correlation coefficient, measures the degree to which two functions over a sphere are correlated and can be calculated directly from the spherical harmonic coefficients of the two functions [41]. The JSD measures the distance between two probability distributions (in this case, over a sphere) and has been used in the dMRI literature to compare ODFs from different reconstruction methods [265], and to quantify reproducibility of dMRI algorithms [266, 267]. The JSD is bounded between 0 and 1, where lower values indicate greater similarity of distributions.

To assess the estimation of the number of fiber populations, we employ the commonly used success rate (SR) [123] and consistency fraction (CF) [6]. Here, a reconstruction algorithm is a “success” if it successfully detects all peaks identified with histology, within a given angular tolerance (in this study, 25°). A value of 20° has been previously employed in simulation studies [123]; our tolerance includes this 20° plus an additional uncertainty of ~5° expected due to the registration and pre-processing steps [199]. A voxel is then consistent if it successfully detects all histological peaks within a given angular tolerance (25°) *AND* if the number of estimated peaks equals the number of peaks identified in histology. In both cases, a 1-to-1 correspondence is established between peaks in histology and dMRI, meaning that 2 histological peaks cannot be “successfully” identified by the same MRI peak, even if it happens to be within the given angular tolerance from both peaks. To understand reasons for non-successful or non-consistent voxels, we also calculated the number of false positive (FP) and number of false negative (FN) peaks identified with the given reconstruction method. The number of FP peaks in a voxel is the number of peaks in MRI that do not have a corresponding peak in histology (within an angular tolerance). The number of FN peaks is the number of histological peaks that do not have a corresponding peak in MRI (within an angular tolerance).

The angular accuracy of orientation estimation is measured as the error (in degrees) between the estimated fiber directions and the histological FOD peaks, again ensuring a 1-to-1 mapping between histological and MRI peaks. The angular error is calculated separately (i.e. not averaged over a voxel) for the primary, and (if it exists) the secondary fiber orientations in a voxel.

Finally, to compare estimates of white matter dispersion from diffusion MRI to the true histological fiber dispersion, simple linear correlation coefficients were utilized.

We begin by implementing the above metrics in order to assess the effects of fiber geometry on reconstruction accuracy. Specifically, we first computed metrics in single fiber and crossing fiber regions for all methods. To further elucidate limitations in crossing fiber regions, we assess the quality metrics as a function of the intra-voxel crossing angle. We then investigate the effects of fiber dispersion on angular error and MRI ODI estimates. Next, we examine the effects of the number of DWIs acquired on reconstruction accuracy. To do this, the full 100 gradient directions were re-ordered to minimize the electrostatic potential energy of any partial set of “N” directions, ensuring that these “N” directions are maximally uniformly distributed [268]. From this, subsets of DWIs from 20 to 100 directions (in increments of 4) were created and quality assessed using the above metrics. Finally, we end by investigating the effects of b-value on accuracy and quality of reconstruction.

## 7.3 Results

### 7.3.1 Effects of Fiber Geometry on Reconstruction Accuracy

*Qualitative Results*

Representative confocal data are shown in Figure 7.2 for a single fiber region (A), and a crossing fiber region (B) that contains two local maxima in the histologically defined FOD. The 2D confocal montage highlights where the 3D z-stack was acquired. A zoomed-in view of the middle voxel-equivalent (Figure 7.2, middle column) shows the high-resolution of the confocal data, in which individual myelinated axons are discernable. The results from structure tensor analysis are shown as color-coded maps (Figure 7.2, right column) where each axon contributes to the voxel-wise FOD, overlaid on the image as a 3D glyph. The single fiber region (Figure 7.2,

A) is composed of fibers coherently oriented in the left/right direction, while the crossing fiber region (Figure 7.2, B) is predominantly composed of fibers oriented left/right with a smaller volume fraction oriented superior/inferior and slightly through-plane.

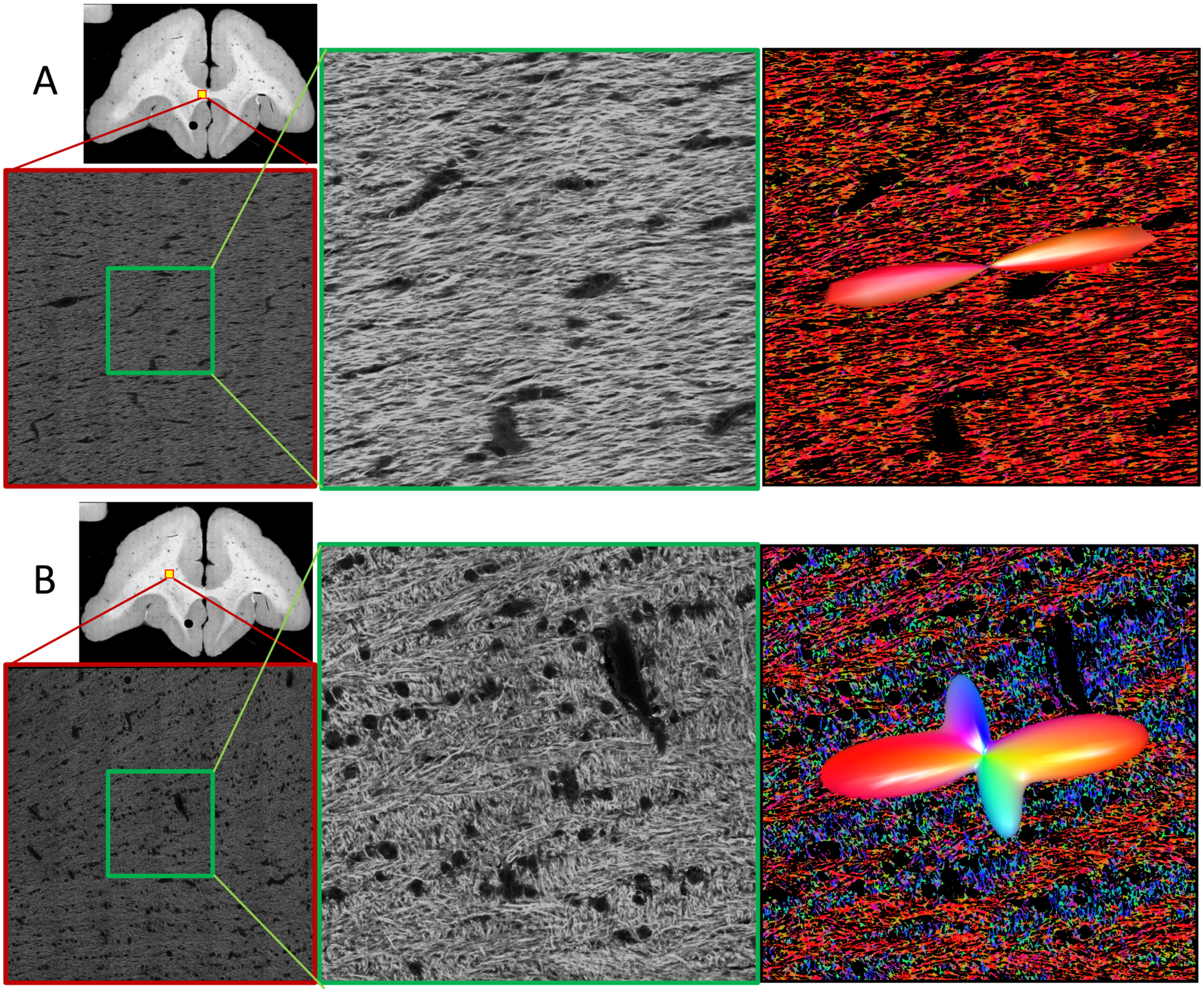

Figure 7.2 Qualitative confocal images. Representative confocal data (of a single slice) are shown for single (A) and crossing (B) fiber regions. Overview images highlight location of full 3D z-stacks (shown as a single, middle slice). A zoomed region of interest in the middle of the z-stack (equivalent in size to an MRI voxel) are shown in the middle column. Results from structure tensor analysis are shown as color-coded images (with colors scheme as described in Figure 7.1), with the histologically-defined FOD overlaid as 3D glyphs (right).

Histological 3D FODs derived from ST analysis are shown as glyphs overlaid on histology in Figure 7.3, displaying two regions containing crossing fibers (left and middle columns) and a single fiber region (right column). This highlights the ability of our histological procedures to resolve fibers crossing within a voxel where both fibers are in-plane (left), as well as the ability to detect bundles of fibers crossing in a plane orthogonal to confocal acquisition (middle). In addition, the results from all eight reconstruction methods are displayed below the corresponding histological FOD. All methods (except DTI) demonstrate some ability to resolve the crossing fibers in generally the same orientations as revealed by the histological FOD. However, differences between dMRI methods are apparent, particularly in the sharpness and number of peaks. For example, at the two extremes, QBIr results in a smoother function over a sphere than PAS, which results in distinct, sharp peaks. Similarly, in the single fiber region, all methods show qualitative agreement with histology in fiber orientation, with the only differences being overall lobe width (or dispersion), and sometimes small spurious peaks (most readily apparent in PAS and DOT).

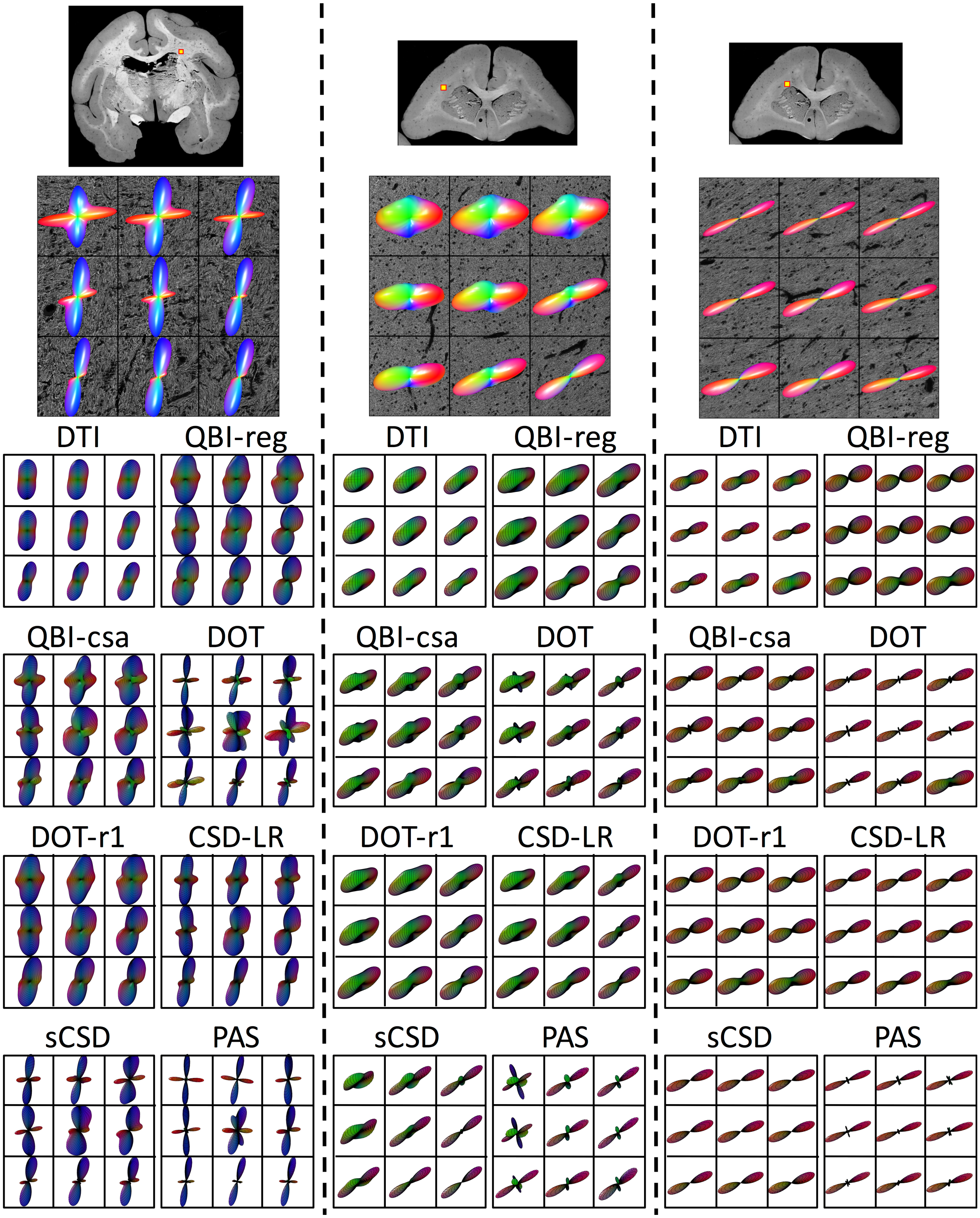

Figure 7.3 Effects of fiber geometry on reconstruction accuracy - qualitative results. Histological FODs are shown overlaid on confocal images for three z-stacks. Z-stack locations are shown as yellow boxes overlaid on 2D confocal montages (top). The voxels represent typical crossing fibers (left), fibers crossing both in-plane and through-plane (middle), and a typical single fiber regions (right). MRI data was analyzed at corresponding locations, and glyphs for all eight reconstruction methods are shown below each histological slice. Note that DTI results are displayed as the ADC profile.

### *Single Fiber and Crossing Fiber Regions*

Quantitative comparisons between reconstruction methods for voxels containing single fiber geometries (N=383) and those containing crossing fiber geometries (N=181) are shown in Figure 7.4. All methods indicate good to moderate overall angular agreement with the histological FOD in single fiber regions, showing similar ACC results with median values between 0.73 and 0.80 for all methods. The one exception is PAS with a lower median ACC of 0.56 (Figure 7.4, A). The two methods with the highest ACC are those that estimate the FOD directly, sCSD and CSDlrd. Similarly, most methods show low JSD of <0.05, with the largest deviations occurring for PAS, DOT, and sCSD, respectively. The performance of each method with respect to estimation of the number of fiber populations in single fiber regions (Figure 7.4, C) shows that most methods consistently estimate a single peak. However, QBIcsa, DOT, and PAS consistently show the presence of FP peaks, with an average of ~2 peaks in these single fiber regions. The ability of all methods to successfully identify the single peak remains high (SR>93% for HARDI models) for all methods (including DTI) (Figure 7.4, D), however, the CF varies dramatically across models (Figure 7.4, E). For example, PAS, QBIcsa, and DOT have low CF, largely due to the prevalence of false positive peaks. Finally, the angular error in single fiber regions is remarkably consistent across all methods, with a median value of ~10° (Figure 7.4, F).

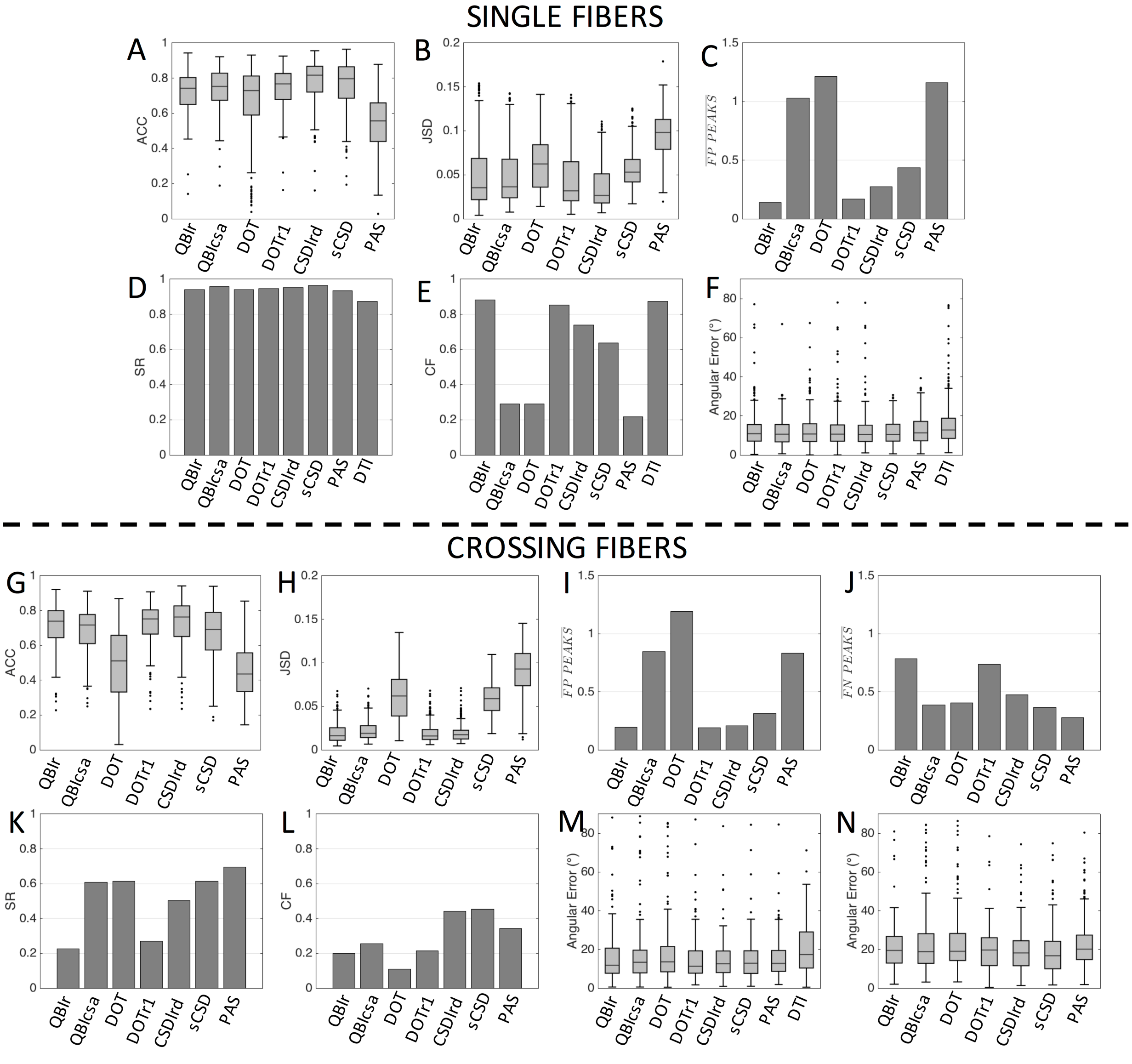

Figure 7.4 Effects of fiber geometry on reconstruction accuracy in single fiber and crossing fiber regions. Quality metrics describing overall agreement with the histological FOD (ACC: angular correlation coefficient, JSD: Jensen-Shannon Divergence), correct assessment of number of peaks (FP: false positive, FN: false negative, SR: success rate, CF: consistency fraction), and orientation accuracy (angular error), are shown for all HARDI methods, and DTI where appropriate.

The quantitative metrics show similar trends in crossing fiber regions (Figure 7.4, G-N). The ACC is decreased slightly compared to that in single fiber regions (Figure 7.4, G) with a median ACC between 0.7 and 0.76 for all methods except DOT and PAS, which indicate a lower overall angular correlation with the ground truth FOD. Similarly, the JSD remains low for all methods, with the largest deviations occurring for PAS, DOT, and sCSD, respectively (Figure 7.4, H). In these regions, QBIcsa, DOT and PAS still contain a large number of FP peaks (Figure 7.4, I), while QBIr and DOTr1 show the largest prevalence of FN peaks (Figure 7.4, J), indicating the lowest ability to resolve crossing fibers. These two methods also show the lowest SR (Figure 7.4, K) with all other methods able to resolve the multiple fiber populations >50% of the time. However, all methods have low CF in crossing fiber regions (Figure 7.4, L), due to the frequency of FP and FN peaks. The median angular error of the primary peak (defined by histology) is consistently between 11-13°, a value slightly higher than that in single fiber regions. The exception to this is DTI (median value of 18°), which is unable to resolve multiple fiber populations, and the primary orientation is expected to lie somewhere between the two dominant peaks. The angular error of the non-dominant peaks is larger still, with a median value between 16° and 20° for all HARDI methods (we note that if a given reconstruction method did not contain multiple peaks, its lone peak is included only in one of the angular metrics, the one giving the lowest error).

### *Crossing Angle*

To assess under which geometrical conditions these methods succeed/fail in crossing fiber regions, we re-examine the quality metrics as a function of fiber crossing angle (Figure 7.5). First, voxels were grouped by crossing angle and placed into bins with a width of 10°, ranging from those with intra-fiber angle <30° to a maximum angle of 80-90°. Each bin had a sample size of 10 or greater (Figure 7.5, J).

Crossing angle has very little effect on ACC (Figure 7.5, A) and JSD (Figure 7.5, B) measures, although a slight increase in ACC with increasing angle is noticeable for PAS, QBIcsa, DOT, and sCSD. For all methods, the number of FP peaks is dramatically reduced as fibers cross at more orthogonal angles (Figure 7.5, C), with a similar reduction in FN peaks for QBIcsa, DOT, CSDlrd, sCSD, and PAS at larger angles (Figure 7.5, D). The reduction in both FP and FN peaks leads to a significant increase in SR (Figure 7.5, E) and CF (Figure 7.5, F) for all methods. In fact, QBIcsa, DOT, CSDlrd, sCSD, and PAS are able to successfully resolve nearly all peaks (SR near 1) at angle >80°. Besides angles <40°, the angular error for both primary (Figure 7.5, G) and secondary (Figure 7.5, H) fiber orientation is not dramatically affected by crossing angle. The increased angular error at small crossing angles is likely caused by reconstruction methods resolving multiple fiber populations, with only one accurately corresponding to one of the two histological peaks, and the other being a spurious peak and contributing to a larger error, or the dMRI finding only one peak with a primary orientation somewhere between the two true peaks.

Finally, Figure 7.5,I shows boxplots of the MRI-resolved angles (if the given reconstruction method was able to resolve multiple fiber populations) versus the histologically defined crossing angle. The shaded box highlights where the range of crossing angles should be if there was a perfect match in each histological angular bin. First, many methods do not show boxplots (or only have a single data point) in voxels with low crossing angles (in agreement with the low SR with these fiber geometries). Second, it is obvious that nearly all methods over-estimate the intra-voxel crossing angle. This effect is most noticeable in the 40-50° and 50-60° range. With very few exceptions, the MRI reconstruction methods consistently resolve fibers crossing at a more orthogonal angle than is suggested by the histological FOD.

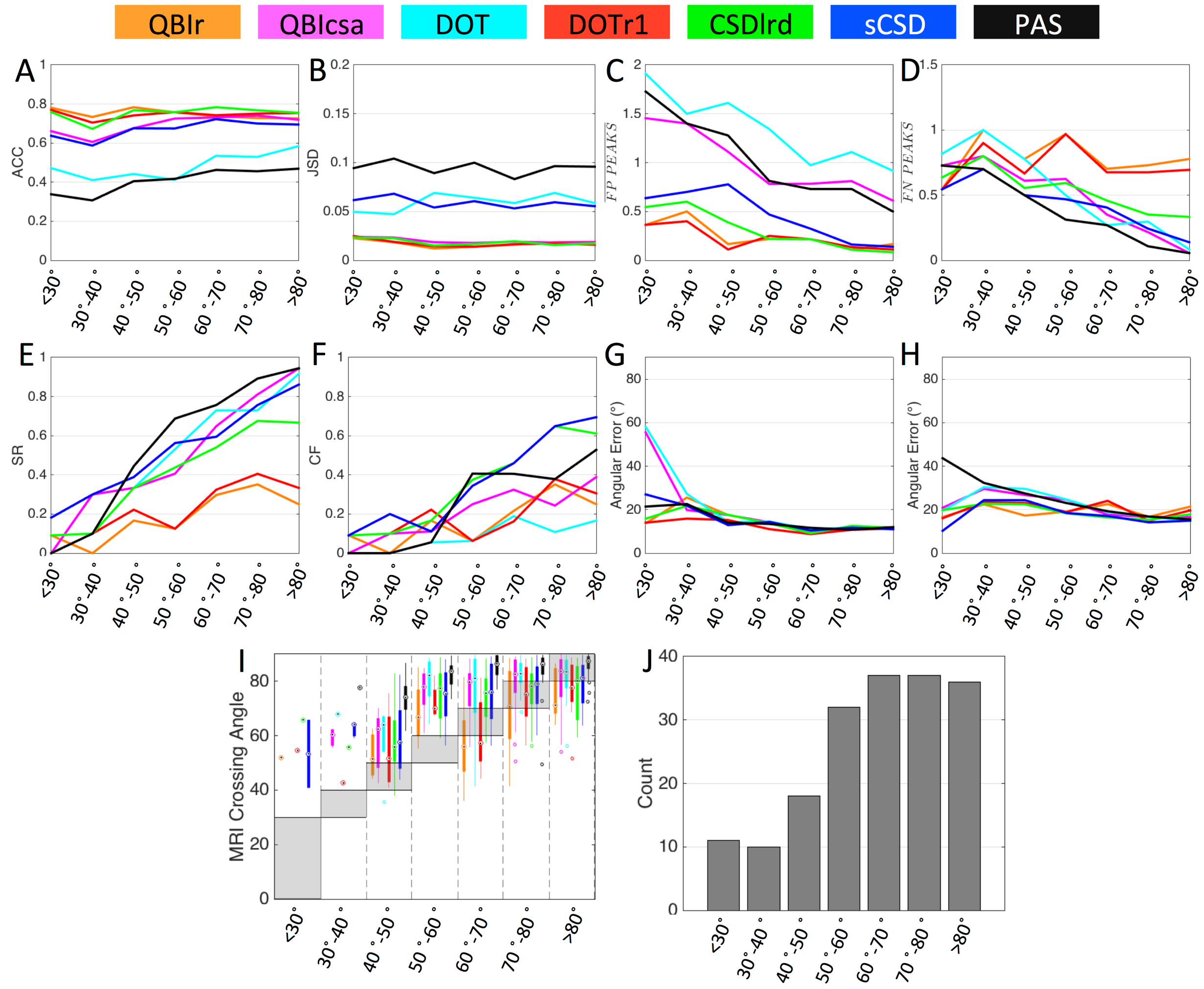

Figure 7.5 Effects of crossing angle on reconstruction accuracy in crossing fiber regions. Quality metrics (A-H) are evaluated for all reconstruction methods as a function of histologically defined crossing angle, grouped into bins with widths of 10°. In addition, MRI-resolved crossing angle is compared to that from histology (I), and sample sizes for each angular bin (J) are shown. Reconstruction methods are designated by color.

### *Fiber Dispersion*

We next examine the effect of fiber orientation dispersion on accuracy of MRI reconstruction methods. Histological analysis revealed a range of dispersion in the confocal z-stacks. Figure 7.6 provides a qualitative reference for the dispersion values investigated in this study, visualized as both 3D glyphs as well as surface distributions over a sphere. The ODI ranges from very highly aligned bundles with a low ODI (0.02-0.03, corresponding to a fiber spread of ~7-9°), to ODI more typical of WM voxels (0.08-0.13, a fiber spread of ~17-19°), to ODI > 0.40 (a fiber spread >37°).

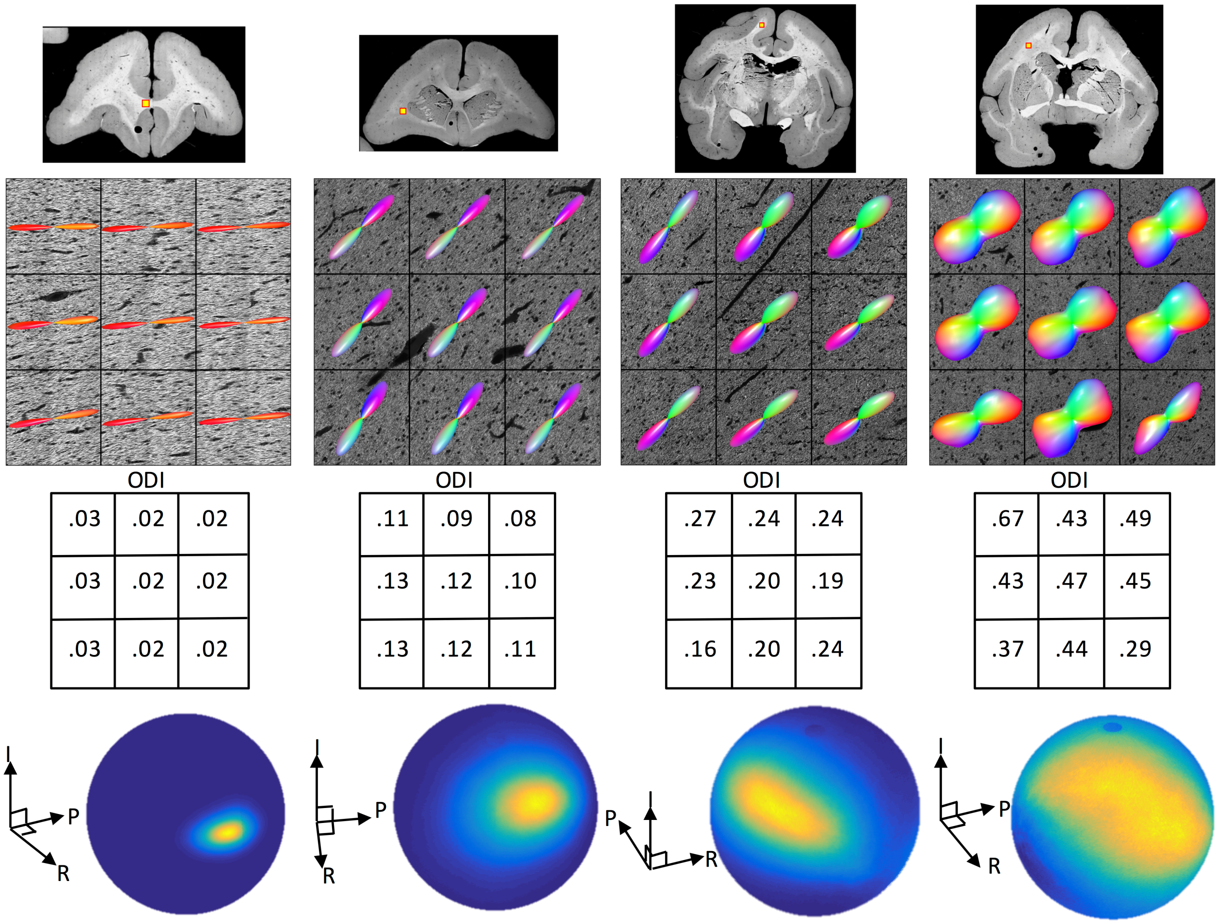

ODI

| | | |
|---|---|---|
| .03 | .02 | .02 |
| .03 | .02 | .02 |
| .03 | .02 | .02 |

ODI

| | | |
|---|---|---|
| .11 | .09 | .08 |
| .13 | .12 | .10 |
| .13 | .12 | .11 |

ODI

| | | |
|---|---|---|
| .27 | .24 | .24 |
| .23 | .20 | .19 |
| .16 | .20 | .24 |

ODI

| | | |
|---|---|---|
| .67 | .43 | .49 |
| .43 | .47 | .45 |
| .37 | .44 | .29 |

Figure 7.6 Histological dispersion in the brain WM. A range of fiber orientation dispersion is shown, ranging from low ODI (left) to high ODI (right). Dispersion is visualized with 3D glyphs as well as orientation distributions on a sphere (for the center voxel of each stack). We note that ODI values between 0.08-0.13 are most typical of WM encountered in this study (in voxels containing single fiber populations).

We begin by examining the relationship between fiber dispersion derived from the 3D histological FOD (in single fiber regions only) and those derived from MRI reconstruction methods, as well as the relationship between dispersion and accuracy of fiber orientation estimates. (Figure 7.7). Plots of histological ODI versus orientation error indicate a low, but significant, positive correlation for all methods (Figure 7.7, A). Plotting the MRI-estimated ODI versus that from histology (Figure 7.7, B) shows moderate correlation for all methods, except for DOT. While correlation coefficients are similar, differences between methods are noticeable. For example, sCSD and PAS consistently result in low dispersion indices, while the QBI methods tend to overestimate ODI. Finally, for most methods, some form of an ODI lower bound is present, below which a resulting ODI is not possible due to either modeling assumptions, or the truncated spherical harmonic representation of the function.

A potential source of discrepancy between MRI and histological measures of dispersion could be the presence of false positive peaks estimated with dMRI, causing a bias in ODI estimation. We find that many of the histological single fiber voxels with larger dispersion were separated into two or more distinct FP peaks using all reconstruction methods (Figure 7.7, D). In all cases, larger dispersion was significantly more likely to result in resolving 2 or more peaks. When voxels with FP peaks were removed from the analysis, all methods estimated dispersion indices with a much stronger correlation with histology (Figure 7.7, C), with correlation coefficients ranging from 0.52 for PAS to 0.74 for QBIcsa. Next, DTI FA shows a moderate, negative correlation with histological ODI, and the DTI angular error shows a small positive correlation (Figure 7.7, E). Finally, the NODDI multi-compartment model has a much stronger overall correlation with histological ODI (Figure 7.7, F) than the HARDI models (compare to Figure 7.7, B). We note that NODDI systematically overestimates the true ODI in our ex vivo experiments, although the line of best fit retains a slope near unity (m=1.09). However, there is also some low, but significant, correlation with the estimated intra-cellular volume fraction (ICVF) and isotropic volume fraction (ISOVF).

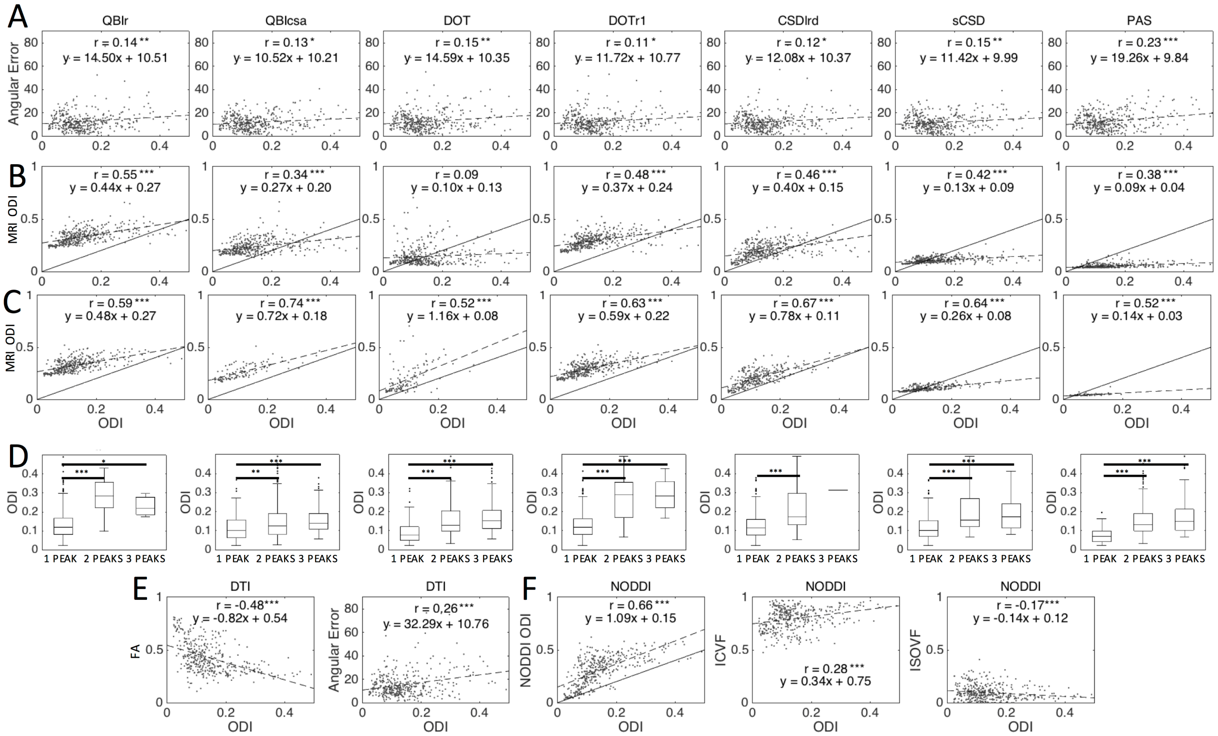

Figure 7.7 Effects of histological dispersion on MRI orientation and dispersion measures. MRI angular error (A) and MRI ODI estimates (B) are plotted against histological ODI in single fiber voxels. For all methods, large histological ODI consistently

resulted in two or more distinct MRI peaks (D), and when FP voxels are removed, MRI-ODI correlations with histology-ODI are increased (C). DTI measures of FA and angular error (E), and NODDI measures of ODI, ICVF, and ISOVF (F) are plotted against histology-ODI. Significance levels are indicated by asterisks (*p<0.05; **p<0.01; ***p<0.001).

### 7.3.2 Effects of Number of DW Directions on Reconstruction Accuracy

#### *Qualitative Results*

We next examine the effects of the number of acquired DWIs (gradient directions) on reconstruction accuracy and quality metrics. Qualitative results are shown in Figure 7.8 for three selected HARDI methods. Here we focus on a region with fibers crossing at acute angles (top), a region containing fibers crossing at near-orthogonal angles (middle), and a single fiber region (bottom). For sharp crossing angles (top), while significant differences exist between methods, there is very little noticeable change between the 64 and 96 direction glyphs within methods. At 32 directions, peaks tend to “blend” into each other (see QBI-csa and DOTr1) or orientations are no longer consistent with histology (sCSD). Remarkably, at regions of orthogonal crossings (middle) almost no difference is observable across gradient directions, with all methods visually indicating the presence of crossing fibers. Similarly, in single fiber regions (bottom) no difference is observed as the number of DWIs varies.

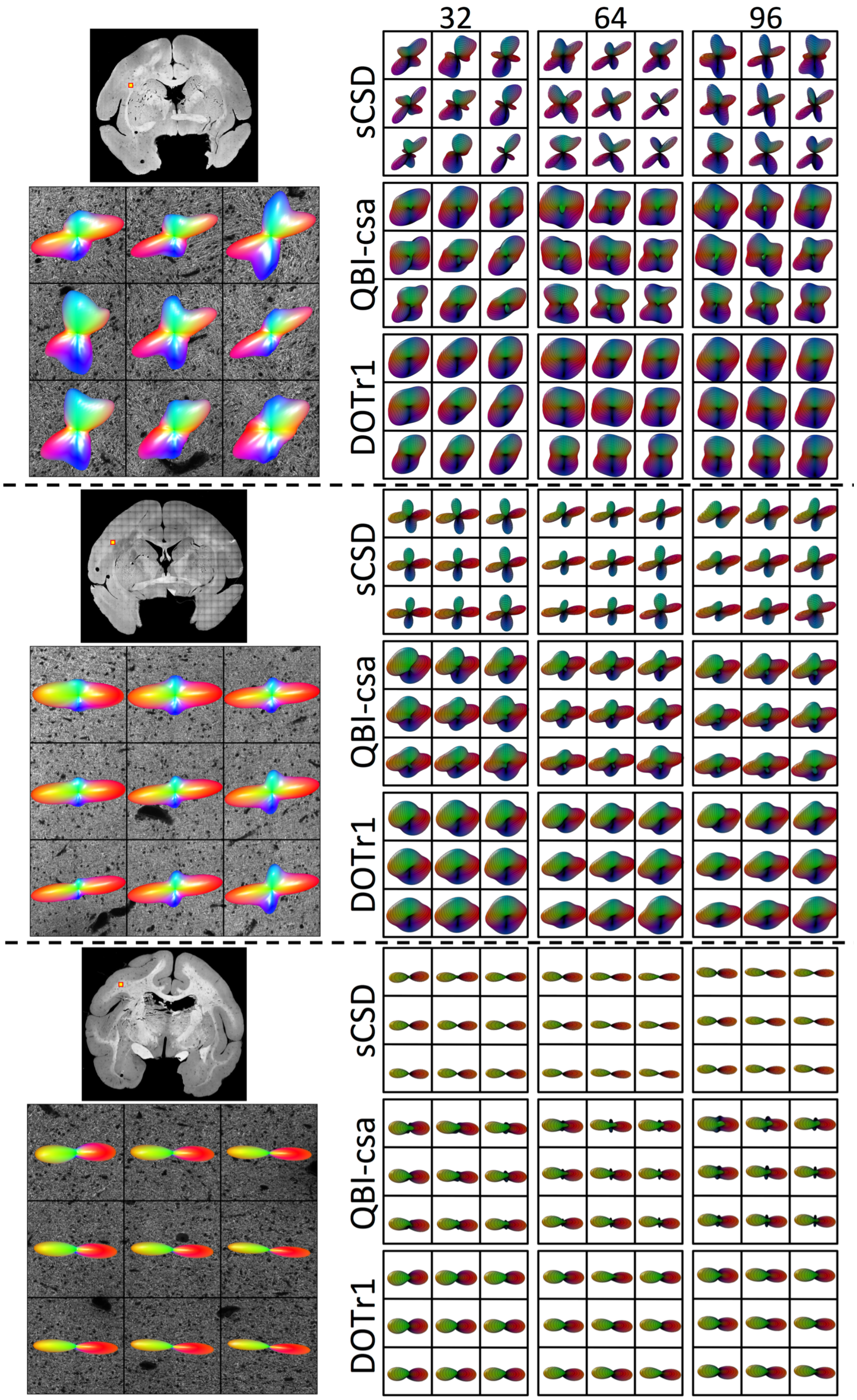

Figure 7.8 Effects of number of DW directions on reconstruction accuracy - qualitative results. Histological FODs are shown overlaid on confocal images for three z-stacks. The voxels represent fibers crossing at sharp angles (top), fibers crossing at near-orthogonal angles (middle), and a typical single fiber region (bottom). MRI-derived glyphs for three selected reconstruction methods are shown for each histological slice.

*Single Fiber and Crossing Fiber Regions*

Quantitative analysis of the effects of number of DW directions is shown in Figure 7.9. For these results, it is important to point out that the SH representation of all functions over a sphere use a maximum SH order of 4 for 20-24 directions, a maximum order of 6 for 28-44 directions, and a maximum order of 8 for 48 directions, or greater.

For single fiber regions, all methods show a slight decrease in ACC (Figure 7.9, A) from 24 to 28 directions, and a slow, but consistent increase in ACC as directions increase (except for PAS). Also, there is little to no change in the rankings of the models across directions, for example sCSD and CSDlrd retain the highest ACC at all directions. Results for JSD (Figure 7.9, B) show very distinct changes when changing the SH order used to represent the functions. Specifically, the changes as the number of DW directions vary is much smaller than the changes in JSD when changing SH order, with noticeable increase in JSD at a 6th order representation. The response to changing number of directions as it relates to FP peaks varies across methods (Figure 7.9, C). DOT and QBIcsa show an increasing prevalence of FP peaks as the number of DWIs increase, while PAS and CSDlrd show decreasing number of FP peaks, and QBIr and DOTr1 show very little change. The SR shows continuous improvement with increasing directions, with the greatest improvement apparent between 20 and 30 directions (Figure 7.9, D). The CF (Figure 7.9, E) shows trends inversely mirroring that of the FP peaks; QBIr and DOTr1 retain high, but consistent CF, PAS and CSDlrd show increasing CF with directions, with DOT and QBIcsa decreasing in CF. Finally, the angular error (Figure 7.9, F) continually decreases with increasing directions, with all HARDI methods showing very similar results, and DTI indicating the largest overall error.

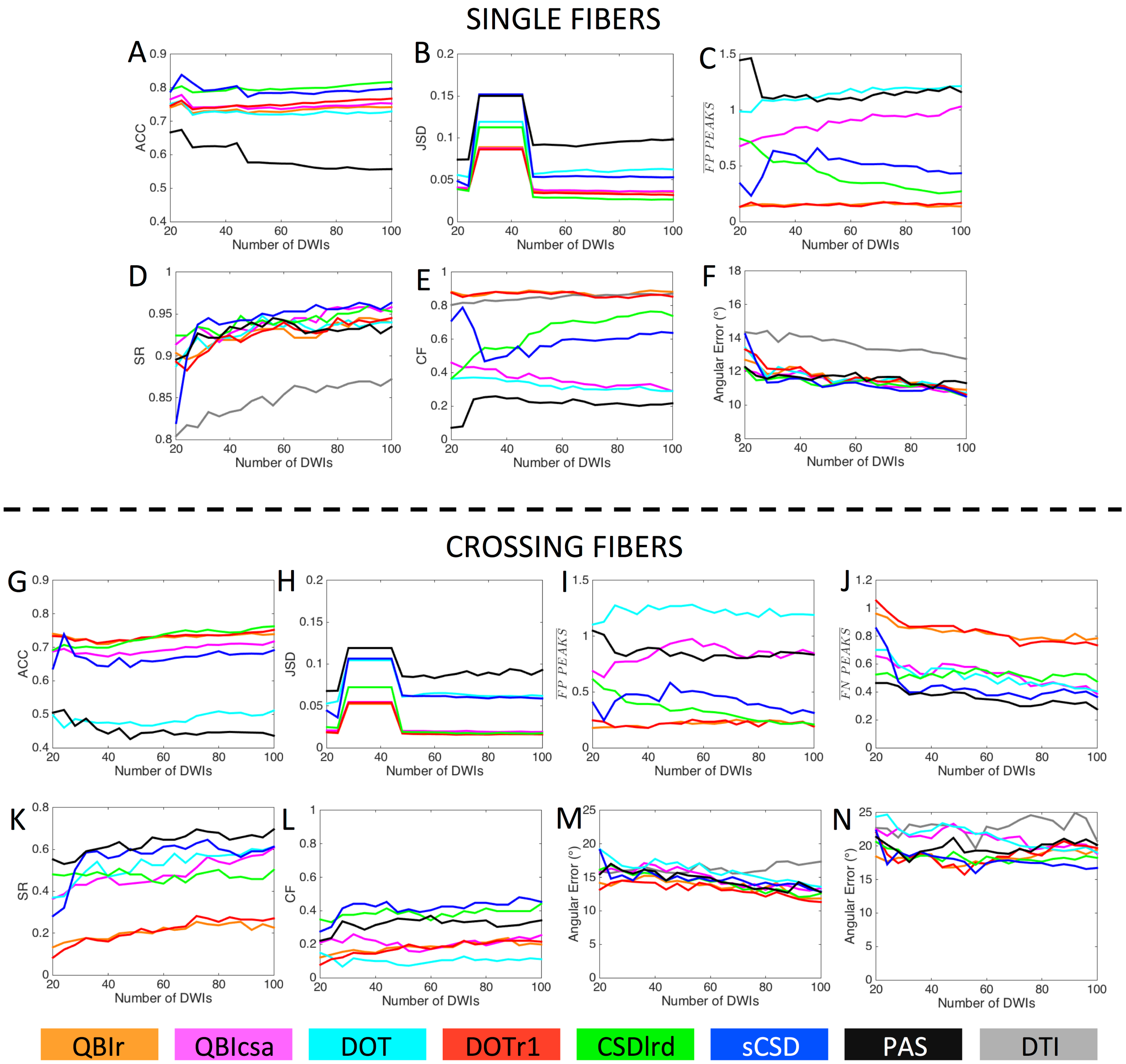

Figure 7.9 Effects of number of DW directions on reconstruction accuracy in single fiber and crossing fiber regions. Quality metrics are evaluated for all modeling methods as a function of the number of DWIs (i.e. number of gradient directions) used in reconstruction. Reconstruction methods are designated by color.

Results in crossing fiber regions show similar trends. All methods (except for PAS) indicate a slight increase in ACC (Figure 7.9, G) with increasing directions, with the greatest increase occurring for CSDlrd (overtaking all other methods after 52 directions). Again, JSD is most sensitive to the SH order (Figure 7.9, H), rather than number of directions, with 6th order showing the largest divergence from ground truth data. The number of FP peaks (Figure 7.9, I) again varies between methods, mirroring the trends seen in the single fiber analysis (see Figure 7.9, C). In all cases increasing image volumes regularizes the reconstruction, resulting in decreasing FN peaks (Figure 7.9, J), with the largest changes occurring between 20 and 30 directions, most notably for sCSD. Both the SR (Figure 7.9, K) and CF (Figure 7.9, L) for all methods show consistent increases as DW directions increase, continuing all the way to the full 100 directions. All methods show consistent behavior in these trends, with no obvious “optimal” number above which increases are diminishing. Finally, all methods (except DTI) show a slow, but continuous increase in orientation accuracy for both primary (Figure 7.9, M) and secondary (Figure 7.9, N) fiber orientations, with larger improvements apparent for the primary fiber orientations.

### *Number of DW directions and Crossing Angle*

The SR for all methods is plotted as a function of histological crossing angle and number of DW directions in Figure 7.10 for all reconstruction methods. A few general trends are noticeable. Unsurprisingly, the SR increases as the intra-voxel angle increases (in agreement with Figure 7.5, E), and increases as the number of DW directions increases. Interestingly, for many methods, one can appreciate a sharp increase in SR at 70-80° and >80° range as the number of directions reaches 28 or greater. In addition, a similar increase in SR is apparent for the intermediate crossing angles (50-60° and 60-70° range) at numbers of directions ranging from as low as ~36 for PAS to approximately 60-64 directions for sCSD, QBIcsa, DOT, and CSDlrd. Finally, methods such as PAS, sCSD, QBIcsa, and DOT consistently show greater SR than QBIr and DOTr1, regardless of fiber geometry and acquisition parameters.

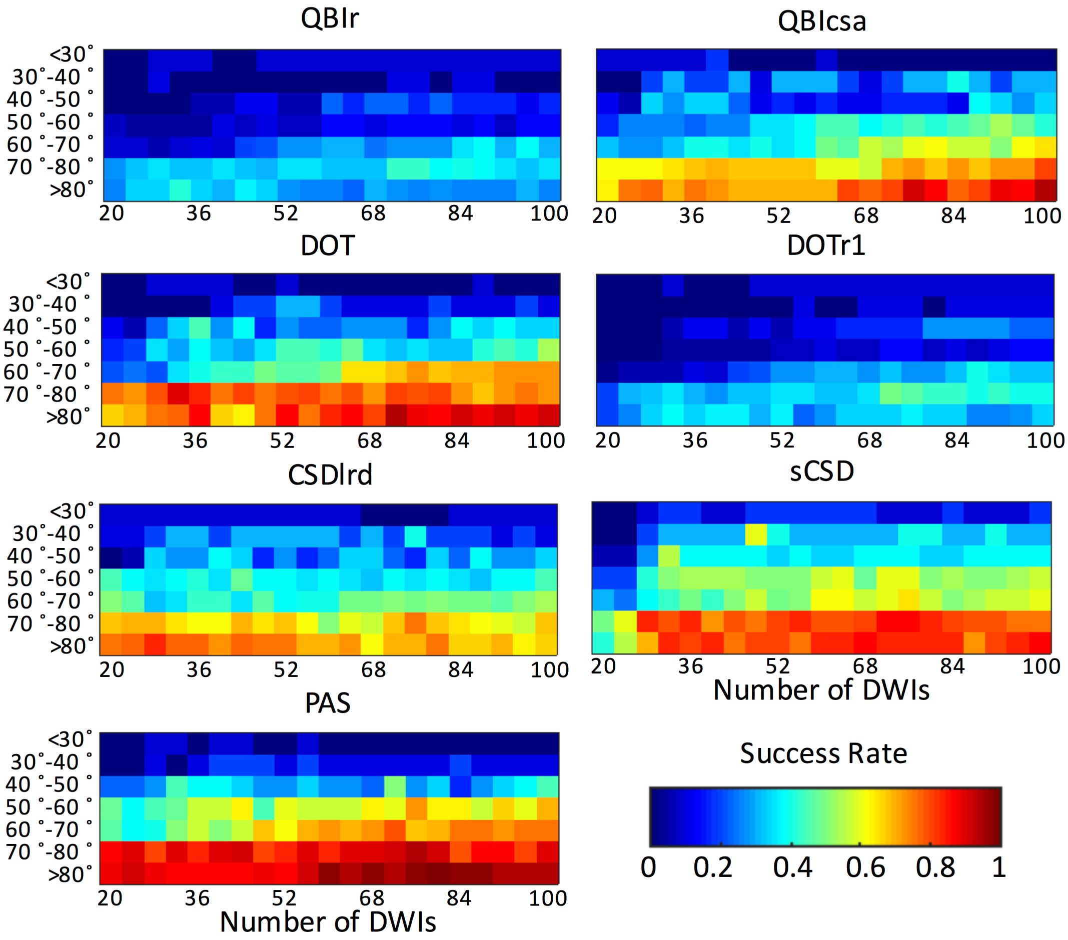

Figure 7.10 Effects of histological crossing angle and number of DWIs on SR of reconstruction methods.

### 7.3.3 Effects of b-value on Reconstruction Accuracy

*Qualitative Results*

Finally, we examine the effects of diffusion weighting (b-value) on the MRI reconstruction methods. Qualitative results are shown in Figure 7.11 for 3 select HARDI methods, in 3 different anatomical locations. Again, we have a region with near-orthogonal, clearly separated fibers (top), a region of sharp crossing fibers (middle), and a region with single fiber voxels (bottom). In these figures, it is apparent that the QBIr and CSDlrd methods are better able to resolve crossing fibers at higher b-values (>6,000 s/mm$^2$ in these regions), which also result in sharper FOD/ODF profiles. For PAS, the profiles do not appear to get "sharper", but the orientations seem to differ across diffusion weightings. However, even at low b-values, all methods show a general agreement with the histologically defined FOD in crossing and single fiber regions. There are no readily apparent differences in the spherical profiles of the methods in the single fiber regions.

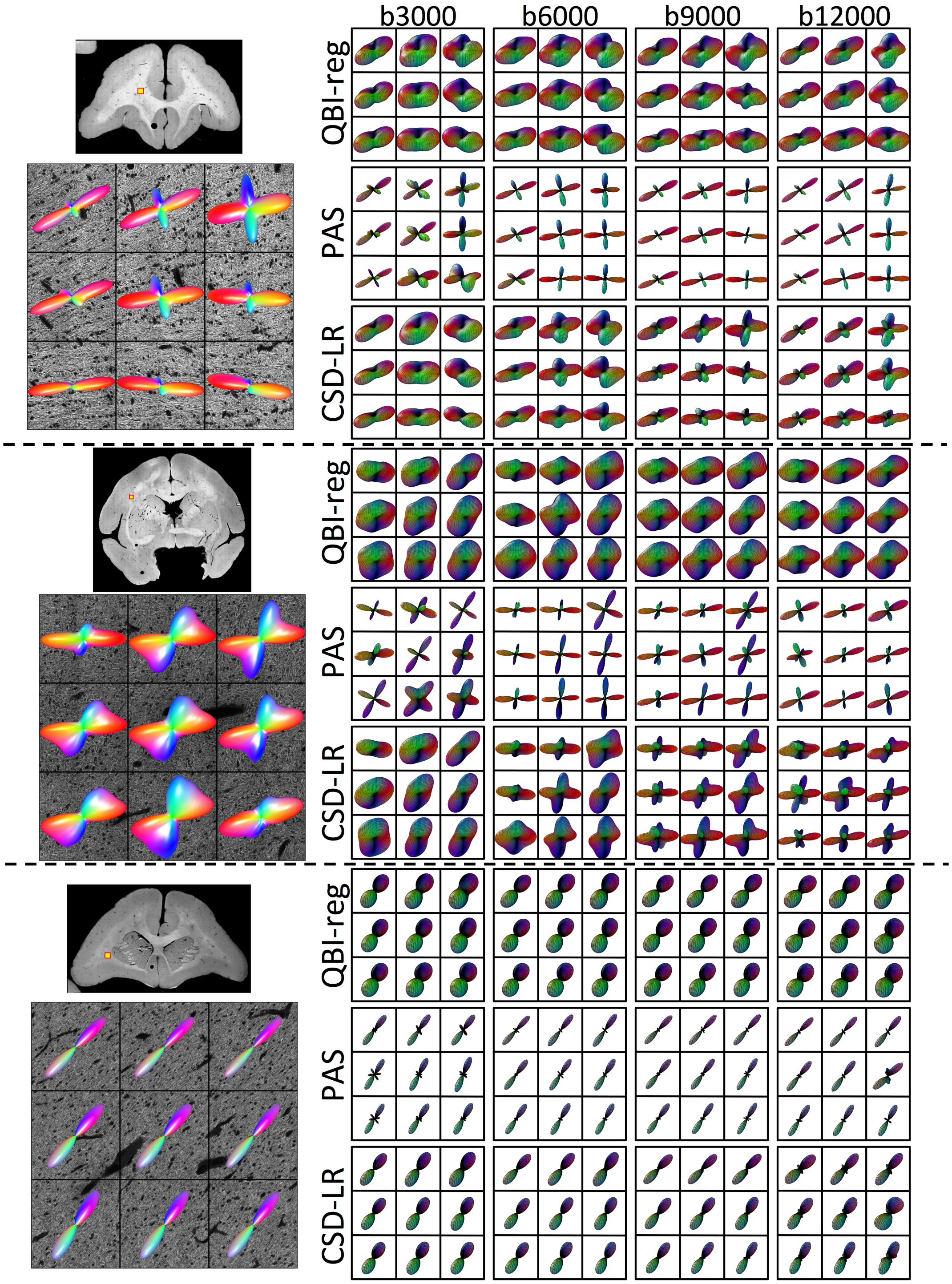

Figure 7.11 Effects of b-value on reconstruction accuracy - qualitative results. Histological FODs are shown overlaid on confocal images for three z-stacks. The voxels represent fibers crossing at near-orthogonal angles (top), fibers crossing at acute angles (middle), and a typical single fiber region (bottom). MRI-derived glyphs for three selected reconstruction methods are shown for each histological slice.

*Single Fiber and Crossing Fiber Regions*

The effects of b-value on accuracy of MRI-reconstructions are shown in Figure 7.12 for single fiber (top) and crossing fiber (bottom) voxels. For single fiber regions, the b-value has varying effects on ACC (Figure 7.12 , A), with methods like QBIr and DOTr1 showing clear improvement as b-value increases, while DOT and sCSD show improvement at lower b-values. For JSD (Figure 7.12 , B), most methods show an increased divergence at higher b-values, with exceptions for QBIr and DOTr1. QBIr retains a low number of FP peaks at all diffusion weightings (Figure 7.12 , C), PAS shows a decreasing FP rate once the b-value is increased above 3,000 s/mm$^2$, and all other methods show a clear increase in FP prevalence at higher b-values. The SR (Figure 7.12 , D) remains high for all methods, with very little difference between methods, and little difference between b-values from 6,000-12,000 s/mm$^2$. However, the CF (Figure 7.12 , E) is affected by the increased FP rate at high b-value, showing significant decreases for all HARDI methods. Finally, the angular error shows minor improvements at increasing b-values (Figure 7.12 , F), for all methods.

The effects of b-value on MRI-reconstructions in crossing fiber regions show similar trends. The ACC (Figure 7.12 , G) closely mirrors that in single fiber regions, although at a lower overall correlation. The JSD (Figure 7.12 , H) indicates decreased performance at higher b-values for most methods, in particular DOT and PAS. Again, most methods show an increased number of FP peaks at larger diffusion weightings (Figure 7.12 , I), with the largest increases observed for CSDlrd and sCSD. PAS shows the opposite trend, with the QBI methods showing a decreased FP rate at b-values of 6,000 and 9,000 s/mm$^2$. All methods show significant decreases in the number of FN peaks with b-values greater than 3,000 s/mm$^2$ (Figure 7.12 , J). At a b-value of 3,000 s/mm$^2$ all methods consistently result in a single fiber population (a FN rate near 1). The decreased FN rate leads to increases in SR (Figure 7.12 , K) for all methods at higher b-value, with the largest differences seen between 3,000 and 6,000 s/mm$^2$. Similarly, the CF (Figure 7.12 , L) remains low at a b-value of 3,000 s/mm$^2$, peaking at either a b-value of 6,000 or 9,000 s/mm$^2$ for all methods. Finally, the angular error is largest in both the primary (Figure 7.12 , M) and secondary (Figure 7.12 , N) peaks for the b-value of 3,000, with little change seen when increasing diffusion weightings beyond 6,000 s/mm$^2$.

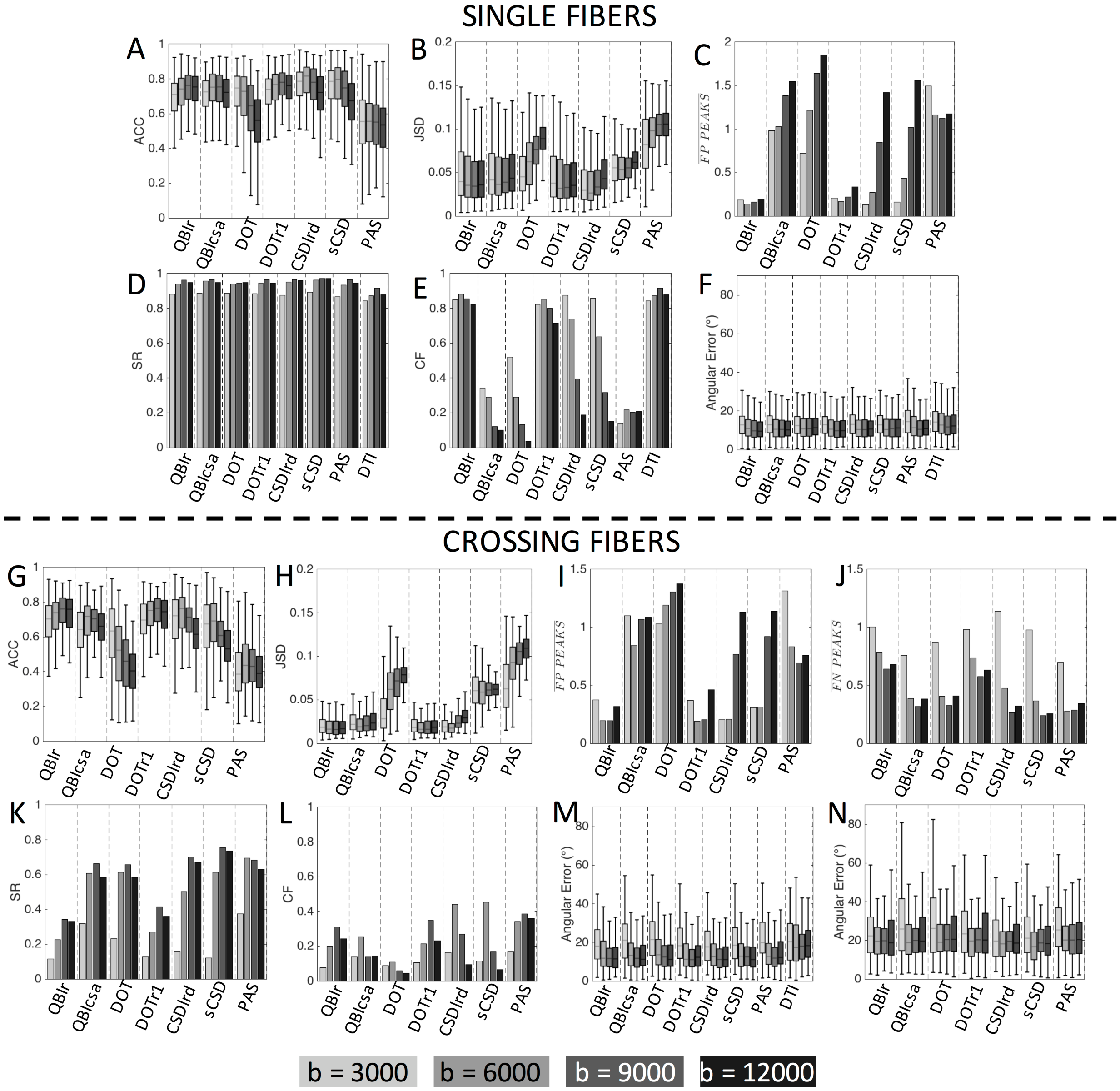

Figure 7.12 Effects of b-value on reconstruction accuracy in single fiber and crossing fiber regions. Quality metrics are evaluated for all modeling methods as a function of the diffusion-weighting used in reconstruction. b-values (in s/mm$^2$) are indicated by gray-scale level.

### *b-value and Crossing Angle*

The SR of all-reconstruction methods at all b-values is plotted as a function of histological crossing angle in Figure 7.13. As before, and for all b-values, the resolving ability of all reconstruction methods increases as the crossing angle becomes larger. Also, for all methods, the data at b=3,000 s/mm$^2$ consistently has the lowest SR for all fiber configurations. At the low b-value, PAS tends to be the most successful at resolving fibers, at all crossing angles. For all methods, the SR generally increases at higher b-values, with smaller differences between b=6,000 and b=12,000 s/mm$^2$. At the lower crossing angles, sCSD tends to have the highest success (at b-values of 6,000 s/mm$^2$ or greater).

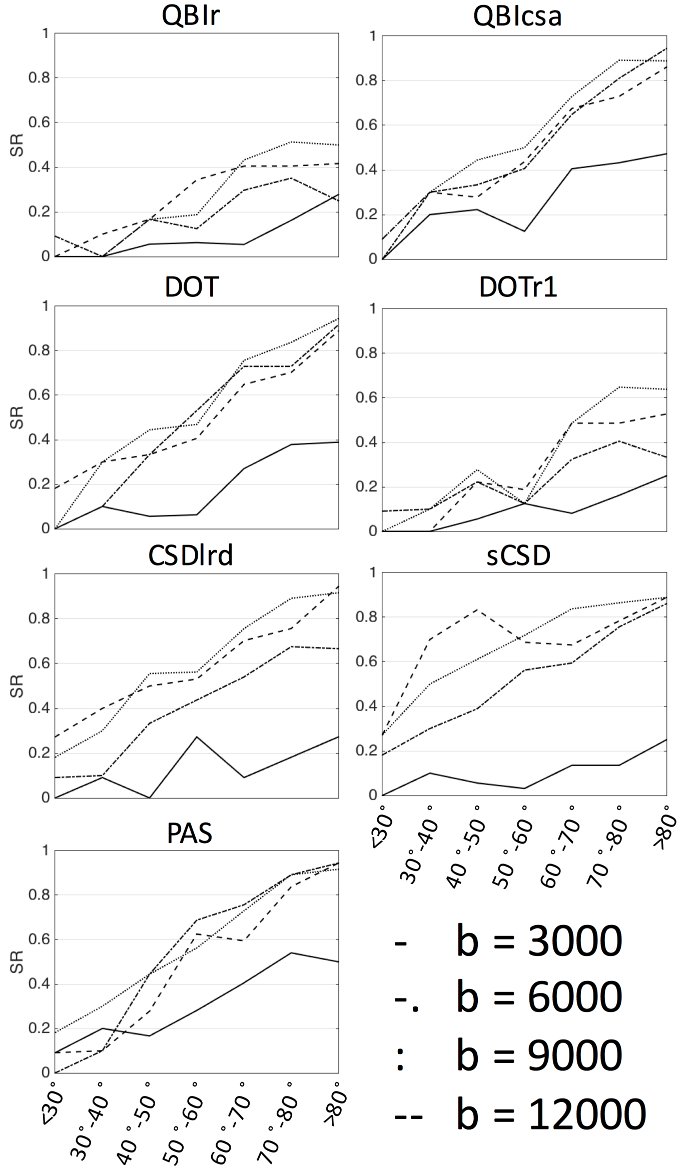

Figure 7.13 Effects of histological crossing angle and b-value (in s/mm2) on success ratio (SR) of reconstruction methods.

## 7.4 Discussion

While there are a large number of dMRI methods for estimating neuronal fiber orientation distributions, the correspondence between dMRI measures and realistic biological fiber architectures remains unclear. Towards this end, this study investigated the relationship between the 3D histologically-defined distribution of neuronal fibers (the FOD) and the corresponding dMRI estimated orientation distributions, implementing a wide range of high angular resolution diffusion imaging techniques. Estimates of fiber orientation and anisotropy have previously been reported in biological tissue [200], and compared to DTI indices [132, 133, 135] and a high angular resolution QBI model [132]; however, these methods have been limited to 2D histological measurements and small sample sizes. Recent work with confocal microscopy [115, 199], optical coherence tomography [137], and polarized light imaging [138, 262] extend the ability to extract the fiber orientation distributions to 3 dimensions. Still, no 3D histological validation of orientation and dispersion measures has been performed for any existing dMRI reconstruction techniques. Further, no histological validation study has presented a comparison of models, nor studied the effects of fiber geometry (crossing fibers, fiber dispersion) and acquisition parameters (number of DWIs, b-value, etc.) on their performance.

The most pertinent questions addressed in our study are whether the current generation of dMRI reconstruction methods allow us to adequately infer the underlying voxel-wise fiber orientations, and how algorithmic differences (including acquisition schemes, assumptions in modeling, descriptors used to characterize the intra-voxel structure, etc.) affect the fidelity of the resulting reconstruction. While we do not attempt a final ranking of the models (because the optimal technique is almost certainly going to depend on the intended goals and interests of the specific study) we are able to make some general observations, and report on the strengths and weaknesses of the tested dMRI algorithms.

All HARDI models are shown to describe the overall angular structure of the FOD, as evidenced by high ACC and low JSD in voxels containing both simple and complicated figure geometries (shown qualitatively in Figure 7.3, and quantified in Figure 7.4). Despite correlating well with the overall FOD shape, no method is consistently successful at extracting discrete measures of the number and orientations of FOD peaks. The major inaccuracies of all techniques tend to be in extracting or capturing local maxima of the FOD, resulting in either false positives and false negatives. Regardless of acquisition parameters, all methods show improved successes at resolving multiple fiber compartments in a voxel when fiber populations cross at near-orthogonal angles (Figure 7.5, Figure 7.10, Figure 7.13). This is consistent with the literature on both phantoms [125, 216] and simulations [6, 123] and describes one of the major hurdles to resolving crossing fiber populations. In addition, the ability to resolve crossing fibers increases for all reconstruction methods at increased diffusion weightings (Figure 7.13), often at the expense of increased FP peaks and an overall lower overall angular agreement with the histological FOD (Figure 7.12). Thus, although techniques tend to capture the overall continuous shape of the FOD, care must be taken when evaluating diffusion results, particularly with respect to estimates of number of fibers or fiber orientation based on local maxima of the FOD or ODF alone.

A comparison across methods showed that no HARDI model outperformed others in every quality criteria or experimental condition. There was nearly always a tradeoff in measures of accuracy. For example, PAS regularly had the highest rate of success in resolving crossing fibers, at acute angles with low b-values and fewer gradient directions, however it is plagued with FP peaks in all conditions, and consistently had the lowest overall angular agreement with the FOD in both single and crossing fiber regions. On the other end of the spectrum, QBIr rarely resulted in identification of multiple maxima of the ODF, however, resulted in some of the highest ACC and lowest JSD values in all acquisition conditions. At first glance, the lack of consistency across models and wide range of accuracy in describing the FOD may be disheartening, the most commonly implemented (single-shell) HARDI methods for the last decade give varying results, and will almost certainly result in even more dramatic differences with subsequent fiber tracking. However, these results are unsurprising; the techniques all differ a great deal not only in modeling assumptions, but also what they aim to represent. One could envision a model based on the empirically derived FODs in this study, or some combination of techniques to obtain an optimal reconstruction. Another reassurance is that techniques show robustness to acquisition parameters including b-value ($\geq$ 6,000 s/mm$^2$ for most methods in this ex vivo study) and number of DW directions, indicating that studies implementing the same reconstruction technique are likely to be comparable even with somewhat different acquisition parameters.

The robustness to the number of acquired DW directions is particularly surprising. Upon introduction of many techniques, a large number of directions are used. For example, 492 [58], 252 [35], and 80 directions [216] for QBI methods, 60 [43], 92 [41], and 80 directions [216] for spherical deconvolution methods, and 82 [38] directions for DOT methods. For many methods, validation studies (often through simulation) show that with a moderate number of directions (>~50), methods show success at describing fiber geometries[6, 122, 269, 270] . Our results are generally in agreement with this observation, suggesting that many methods show an improvement at moderate numbers of directions (particularly in resolving intermediate crossing angles, Figure 7.10). However, the overall correlation with the histological FOD and other quality metrics (SR, false peaks) remain high for as few as 28 directions (Figure 7.9), a protocol common in many DTI schemes. Further, we find that some measures of quality (i.e. JSD and FP peaks) are largely influenced by the fit SH order used to represent that function on a sphere, an effect observed in previous reproducibility studies [267].

In addition to validating HARDI methods' ability to capture orientation and number of fiber populations, we also validate the ability to capture another descriptor of fiber geometry, orientation dispersion. We tested a popular multi-compartment diffusion technique (NODDI) that estimates indices of neurites that may be more directly related to, and provide specific markers of, brain tissue microstructure. Measures of orientation dispersion may provide specificity for various pathologies [271-274], as well as provide fiber "tract-specific" indices that can again correlate to pathology, or increase fiber tracking specificity [257-259]. Validation of dispersion measures has been performed for NODDI in the ex vivo spinal cord [275] and on a 2-compartment dispersion model in the human corpus callosum [262]. In this study, we evaluate both signal models (which primarily aim to recover only the angular component of the diffusion profile) and the NODDI multi-compartment model (Figure 7.7). We find that the FOD and ODFs from signal models can provide more information that just number of peaks and peak directions. Specifically, the width of the FOD (or ODF) lobe is correlated with the histological fiber dispersion, for all reconstruction methods (significant correlations from r=0.34-0.55). High dispersion typically results in false positive peaks which can lead to errors in dispersion measures when fitting to Watson (or multi-Watson) distributions. When removing false positive peaks from analysis, the correlation is much stronger (r=0.52-0.74). Despite the high correlation, there is an overall limited range of dispersion identifiable with these techniques. For example, PAS and sCSD result in consistently low ODI (and sharp peaks), while QBIr and

QBIcsa consistently result in larger ODI values. In addition, we find that increasing dispersion leads to greater uncertainty in estimating the primary fiber orientation in a voxel. For the NODDI model, which explicitly estimates a dispersion index, we find a much greater overall correlation (without the removal of FP peaks because NODDI estimates only a single fiber compartment). Overall, this demonstrates that the orientation dispersion estimates from dMRI correlate well with tissue architecture, using both HARDI and the multi-compartment NODDI model.

A recent study [219] proposed that the brain's white matter structure is organized in a pattern of parallel sheets by analyzing crossing fiber pathways using dMRI tractography. It was found that incident pathways cross nearly orthogonally in a grid-like or sheet-like structure, with this pattern found throughout white matter and across species. This pattern has significant implications with regard to development, evolution, and structural connectivity. However, it has been argued [276] that this grid pattern is likely an artifact due to the inherently low angular resolution of the proposed dMRI technique (which estimated the diffusion ODF), causing a bias towards orthogonal angles, making the grid pattern a likely apparent geometric configuration. Our results indicate that all methods studied show a bias towards orthogonal crossings (Figure 7.5, I), regardless of true histological crossing angle, and regardless of whether the FOD or ODF (or any other function) is estimated. This would seem to argue in favor of a technical limitation causing an artefactual grid. However, we note that (although we did not perform systematic random sampling) it was much easier to find near-orthogonal crossings than crossing angles less than 50° in the histological sections we studied (Figure 7.5, J).

Future work should investigate the effects of reconstruction accuracy as spatial resolution varies. Because of the tradeoffs in spatial resolution, signal to noise ratio, and imaging time, optimizing the resolution for diffusion MRI (and subsequent analysis and/or tractography) is highly relevant to human in vivo imaging. Interestingly, recent work using MRI and high resolution histology has shown that the crossing fiber problem is not eliminated even with very high spatial resolution data [277]. However, it is expected that the angular accuracy of diffusion MRI estimates will increase at high spatial resolution [261] due to reduced geometric complexity or decreased fiber dispersion [261, 277].

While validation comparing dMRI and histology is the only validation method able to capture both the enormous complexity of the white matter and the practical effects of image acquisition, it is not without limitations. Histology is technically complex due to tissue deterioration during preparation (shrinking, deformation, etc.). We have attempted to ameliorate the shrinkage with confocal image pre-processing, and a previous study describing the methodology [199] shows an expected error of less than 5° when compared to manually traced fibers. In addition, to assess whether residual anisotropy or bias is introduced during confocal processing, we have evaluated the angular error as a function of the z-component of the histological FOD (data not shown) and found only very low correlations (maximum correlation of coefficient of $|r| = 0.20$). Only one reconstruction method (DTI) showed a statistically significant correlation (interestingly, a negative correlation as through-plane orientation increased). Together, this suggests that the angular error is largely independent of the histological FOD orientation. The multi-step registration procedure accounts for both deformation and tissue placement on the slide, and can result in localization errors on the order of the size of MRI voxels [194], 300 um in our study. Together, these may account for the slightly larger angular error than that seen in simulation studies [122, 123, 278, 279], however, a median angular error of 10° is consistent with previous 2D histological validation studies on DTI [132, 133]. Thus, rather than a methodological limitation, this could indicate that the models used in simulation (often mixtures of Gaussians) are overly simplistic relative to the complicated true FOD that may not only contain disperse mixtures of fiber populations, but also varying microstructure affecting the motion of water, and anisotropic dispersion causing differences between the peak amplitude and something similar to an angular “center-of-mass” of the FOD. A further limitation is that confocal data, acquired in 50 micron tissue sections was compared to dMRI data acquired in 300 micron thick MRI sections. This comparison is based on the assumption that histological FODs change slowly in the slice direction, which is likely false in some fraction of voxels (and may account for some of the outliers in Figure 7.4 and Figure 7.12, for example). While the present research focused on distinguishing “single” and “crossing” fibers, this may be an oversimplification of the true geometry. For example, in our confocal data, fibers are often seen bending throughout the field of view, and even within a voxel.

Voxels can have both a dispersion and/or bending of fibers, yet result in a single local maximum of the FOD. Future work should utilize confocal data to quantify not only fiber curvature and bending, but also characterize how fibers cross and fan out (or in) within the voxel, and how these geometries relate to the diffusion signal. One final limitation of our study is extrapolation of the ex vivo tissue and imaging conditions to that of in vivo. However, previous studies indicate that anisotropy and the angular dependence of the signal is preserved [113, 198, 280], albeit at a lower diffusivity, thus care must be taken in interpreting the equivalent in vivo diffusion weightings for this study. Overall, there is no perfect validation method for dMRI, and we must rely on the accumulation of evidence from all approaches to validate and better understand the relationship between the dMRI signal and the tissue microstructure.

## 7.5 Conclusions

This work compared and evaluated fiber orientation distributions and orientation dispersion values derived from a number of diffusion MRI algorithms with those derived from histology. The algorithms included commonly implemented high angular resolution techniques for recovering intra-voxel fiber geometries, as well as a multi-compartment model. All reconstruction techniques are able to recover the overall angular structure of the FOD with some accuracy, with weaknesses in extracting discrete orientations and numbers of peaks. In addition, both HARDI methods and the microstructural model show high correlations with histologically defined orientation dispersion. These results can be used to identify the relative advantages of competing approaches, potential strategies for improving accuracy, and appropriate techniques to implement for answering specific research questions.

## Appendix 7.A Measures of similarity on the unit sphere (ACC and JSD)

A method for calculating the correlation of functions over a sphere given the SH expansions of both functions is given in [41]. Given two spherical functions and their spherical harmonic expansions:

$$U(\theta,\varphi) = \sum_{l=0}^{\infty}\sum_{m=-l}^{l} u_{lm} Y_{lm}(\theta,\varphi)$$

$$V(\theta,\varphi) = \sum_{l=0}^{\infty}\sum_{m=-l}^{l} v_{lm}Y_{lm}(\theta,\varphi) \tag{A.1}$$

The ACC of the functions is calculated as:

$$ACC = \frac{\sum_{l=1}^{\infty}\sum_{m=-l}^{l} u_{lm}v *_{lm}}{\left[\sum_{l'=1}^{\infty}\sum_{m'=-l'}^{l'}|u_{l'm'}|^2\right]^{1/2}\left[\sum_{l''=1}^{\infty}\sum_{m''=-l''}^{l''}|v_{l''m''}|^2\right]^{1/2}} \tag{A.2}$$

The JSD was used to quantify the similarity between two FODs (or ODFs). Similar to [266], we projected both FODs onto 724 values distributed equally over a sphere. The JSD is defined as

$$JSD(P,Q) = \frac{D_{KL}(P,M) + D_{KL}(Q,M)}{2} \tag{A.3}$$

with

$$M(i) = \frac{P(i) + Q(i)}{2} \tag{A.4}$$

and P(i) and Q(i) are the magnitudes of the histological and MRI FODs (or ODFs) along index i (i=1…724), and $D_{KL}$ is the Kullback-Leibler divergence:

$$D_{KL}(P,Q) = \sum_{i} P(i)\log\left(\frac{P(i)}{Q(i)}\right) \tag{A.5}$$

# CHAPTER 8: A GYRALBIAS IN DIFFUSION MRI FIBER TRACTOGRAPHY

## Prologue

Assessing the performance of diffusion MRI techniques to estimate fiber orientation information is an essential step in the validation process; however, it is not in itself sufficient to predict the performance of the tractography process. In this chapter, we investigate the anatomical accuracy of tractography methods and potential sources of error in connectivity estimates. Specifically, by comparing diffusion MRI to myelin-stained histology, we ask if tractography results are related in any way to histologically derived measures of axon counts or densities. Doing so, we find several sources of bias in tractography algorithms.

## Abstract

Diffusion MRI fiber tractography has been increasingly used to map the structural connectivity of the human brain. However, this technique is not without limitations, for example, there is a growing concern over anatomically-correlated bias in tractography findings. In this study, we demonstrate that there is a bias for fiber tracking algorithms to terminate preferentially on gyral crowns, rather than the banks of sulci. We investigate this issue by comparing diffusion MRI (dMRI) tractography with equivalent measures made on myelin-stained histological sections. We begin by investigating the orientation and trajectories of axons near the white matter/gray matter boundary, as well as the density of axons entering the cortex at different locations along gyral blades. These results are compared with dMRI orientations and tract densities at the same locations, where we find a significant gyral bias in many gyral blades across the brain. This effect is shown for a range of tracking algorithms, both deterministic and probabilistic, and multiple diffusion models, including the diffusion tensor and a high angular resolution diffusion imaging technique. Additionally, the gyral bias occurs for a range of diffusion weightings, and even for very high-resolution datasets. The bias could significantly affect connectivity results using the current generation of tracking algorithms.

## 8.1 Introduction

It has long been recognized that a detailed map of the structural connections in the brain would be of great value for understanding cognition, brain function, normal development and aging, as well as neurological disease and disorders [110, 281, 282]. Thus, creating a comprehensive description of the neuronal connections in the brain (i.e. the human connectome [283]) has been a major scientific goal for decades [281]. Early investigators relied on techniques performed on post-mortem tissue that limit analysis to small brain areas, or one system of pathways at a time (see [110, 281] for historical reviews). The advent of diffusion MRI (dMRI) [3] and dMRI fiber tracking [55] opened up the possibility of studying white matter anatomy on living subjects, and across the entire brain, in a matter of minutes.

The ability to non-invasively study the human brain has made dMRI one of the main tools used in Connectomics research for inferring anatomical pathways connecting brain regions. Significant progress has been made in modeling the network architecture of the brain [66, 222, 284], parcellating the cortex into functionally and anatomically distinct subregions [285, 286], and making detailed measurements of white matter microstructure [114, 287, 288]. However, despite its widespread use in inferring the "connectedness" between brain regions, dMRI fiber tracking is not without its limitations [201].

For an accurate connectivity map of the brain, estimated dMRI fiber trajectories (streamlines) must be able not only to follow major fiber bundles through the deep white matter, but must also correctly follow fibers as they cross the white matter/gray matter (WMGM) boundary. This is particularly problematic in areas of the cerebral cortex that exhibit complex folding and convolutions. Recently, it has been shown that tractography streamlines have a tendency to terminate primarily on gyral crowns, rather than the walls of sulci, or the sulcal fundi [105-107, 289]. These results could have significant implications regarding cortical development and morphogenesis [105, 106]. However, it has been suggested that, rather than an anatomical reality, this likely reflects a bias in fiber tracking algorithms [108]. Clearly, a tendency for streamlines to track towards certain regions of the brain could significantly bias quantitative connectivity studies using dMRI, including network connectome profiles and brain parcellation results.

The observation that tractography streamlines are denser in gyri than in sulci could have several explanations. For one, it could have genuine anatomical underpinnings. Due to their convexity [290, 291], the cortical volume (per unit surface area of the WMGM boundary) at gyral crowns would be greater than at the relatively flat sulcal walls or concave fundi [108]. If the axonal density associated with a unit volume of the cortex were to be relatively homogenous, as is often assumed [108, 156, 292], this would imply that the number of axons crossing the WMGM boundary at the gyral crowns would have to be higher than those along the banks or fundus of sulci [108].

On the other hand, the “gyral bias” could be an artifact of tracking algorithms, due either to technical limitations or inherent simplifying assumptions. Analysis of myelin-stained sections has shown that many fibers follow a sharply curved trajectory as they enter the cortex, particularly those near the sulcal walls [108, 200, 293]. Because of the large voxel size of dMRI acquisitions (typically 2-3mm), these areas are prone to partial volume effects. This could bias orientation estimates along the WMGM border to point in the direction of the adjacent white matter (which is often tangential to the boundary [108, 294]), rather than correctly pointing towards the sulcal cortical surface [108]. Because these orientation estimates form the input of most tracking algorithms, any fiber tracking would subsequently exhibit a bias.

Even if fiber orientations were estimated perfectly, tracking algorithms might still not be able to propagate correctly into the cortex. Tracking usually involves choosing a curvature threshold, a maximum angle that the trajectory is able to turn through over a certain distance [201]. This parameter is often justified on the basis that fibers in the brain typically do not exhibit sharp bends; however, this will clearly preclude accurately tracking fibers that truly exhibit curvatures greater than this threshold. Similarly, in voxels where multiple “crossing” fibers are detected, many algorithms will propagate in the direction with the least angular deviation from the previous tracking step. Again, along the cortex, this could lead to streamlines continuing to follow the direction of the white matter bundles, rather than exiting the white matter to enter the cortex [108], even if these fibers were correctly detected.

In addition to limitations of the dMRI acquisition and tracking algorithm, bias can be introduced in part by the strategy used to begin streamline propagation. Some of the most common seeding strategies include propagating streamlines from every voxel in the brain ("whole brain" seeding), or seeding from every voxel in the white matter ("white matter' seeding). Because longer white matter pathways occupy a greater volume from which to seed, these pathways tend to be over-represented in streamline reconstruction [295, 296]. If these pathways were to terminate more frequently in specific regions (i.e. gyral crowns), this could, again, lead to a larger number of streamlines entering this area. To compensate for this, it is common in many brain network studies to heuristically scale the contribution of each streamline to the overall connection density by the reciprocal of the streamline length [65, 66]. Several groups have attempted to bypass this potential source of bias by seeding only from the WMGM boundary [297, 298]. However, it is unclear what effect the seeding strategy, and subsequent quantification, have on potential gyral biases in diffusion tractography.

Taken together, it is clear that dMRI tractography has limitations that could produce significant bias in certain anatomical regions, and prevent creation of accurate connectivity maps of the brain. Hence, there is a need to better understand to what extent, and under which circumstances, these biases occur.

In this study, using histology as a validation tool, we compared dMRI fiber tractography to myelin histology performed on a Rhesus macaque brain to investigate gyral bias. We first asked how the true (histologically defined) density of fibers entering the cortex varies along the gyral blade, and if this "fiber density profile" varies between different gyri. Next, we asked whether fiber tracking using the very commonly used diffusion tensor imaging (DTI) model is biased towards the gyral crowns, relative to histological measurements, and if this bias is dependent on seeding or fiber quantification strategies. We then investigated the axonal trajectories near the WMGM boundary along gyral blades by assessing fiber curvature, the effects of the tractography curvature threshold, and the agreement with dMRI estimated fiber orientations. We then assess whether the b-value, or diffusion-weighting, affects the results in any way. In addition, intuition suggests that increasing the spatial resolution of dMRI images would lead to more accurate fiber tracking [108, 299] and a reduced gyral bias. Hence, we analyze different tractography methods using data-sets acquired at varying spatial resolutions to test this hypothesis. Finally, we then move away from the commonly used diffusion tensor and assess tractography based on a higher-order algorithm (constrained spherical deconvolution [45]) for estimating fiber orientation, and use this to construct 3D fiber pathways.

## 8.2 Methods

### 8.2.1 MRI acquisition

MRI experiments were performed on a single hemisphere of an adult Rhesus macaque (Macaca Mulatta) brain on a Varian 9.4T magnet following perfusion, Gd-DTPA immersion, and Fomblin preparation described in Section

4.2.2 MRI Methods. A structural image was acquired using a 3D gradient echo sequence (TR = 50ms; TE = 3ms; flip angle = 45°) at 200um isotropic resolution.

Diffusion data were then acquired with a 3D spin-echo diffusion-weighted EPI sequence (TR = 340ms; TE = 40ms; NSHOTS = 4; NEX = 1; Partial Fourier k-space coverage = .75) at 400um isotropic resolution. Diffusion gradient pulse duration and separation were 8ms and 22ms, respectively, and the b-value was set to 6,000 s/mm$^2$. This value was chosen due to the decreased diffusivity of ex vivo tissue, which is approximately a third of that in vivo [198], and is expected to closely replicate the signal attenuation profile for in vivo tissue with a b-value of approximately 2,000 s/mm$^2$. A gradient table of 101 uniformly distributed directions [211] was used to acquired 101 diffusion-weighted volumes with four additional image volumes collected at b = 0. Unless otherwise noted, all fiber tractography was performed on this dataset.

In order to assess the effects of the diffusion weighting on any potential gyral bias, the full diffusion acquisition was repeated with b-values of 3,000, 9,000, and 12,000 s/mm$^2$, while keeping all other acquisition parameters (including diffusion times) constant. Higher b-values have been shown to be beneficial for several advanced diffusion (and fiber) reconstruction algorithms [122, 198, 263]. Finally, to assess the effects of image resolution, the full acquisition was repeated with resolution ranging from 300um isotropic to 800um isotropic, in 100um increments. Here, all b-values were set to 6,000 s/mm$^2$. Again, all acquisition parameters were kept constant (including diffusion times), except for field-of-view and number of phase-encoding and readout points required to achieve the intended resolution.

The signal-to-noise ratio in the white matter of the non-diffusion weighted images ranged from approximately 36 in the 300um isotropic images, to approximately 310 in the 800um isotropic images, values much higher than those typical of diffusion MRI on clinical scanners (approximately 16-20). Comparing the macaque and human brain based on volume only (approximately 80mL and 1200mL [300], respectively), our 300um isotropic voxels would be roughly equivalent to ~740um isotropic in the human, while our 800um isotropic scans would resemble human voxels at approximately 2mm isotropic.

### 8.2.2 Histology

Tissue sectioning, and block-face photography, were performed following the methodology described in Section 4.2.3 Histological Methods. Thirty-five slices, with an effective slice gap of 1.8mm, were selected for this study. The tissue sections were then stained for myelin using the silver staining method of Gallyas [193] and mounted on glass slides. Whole-slide brightfield microscopy was performed using a Leica SCN400 Slide Scanner at 20x magnification, resulting in an in-plane resolution of 0.5um/pixel.

### 8.2.3 Registration

In order to transfer the MRI information into high-resolution histological space (or vice-versa), the multistep registration procedure introduced for the atlas construction was used (see Section 4.2.4 Atlas Framework, registration). Briefly, this included 2D linear and nonlinear registration of each histological slice to the corresponding block-face image, followed by 3D linear and nonlinear registration of the block volume to the mean MRI b=0 image. The block to MRI registration was performed for all MRI acquisitions separately. Concatenation of these two deformation fields allows any scalar MRI information (i.e. labels for the crown and walls) to be transformed into histological space. For orientation information derived from MRI, the data were transformed and re-oriented appropriately using the preservation of principal directions (PPD) strategy [301].

### 8.2.4 Data Processing

From the histological and MRI datasets, six pieces of information were obtained (Figure 8.1).

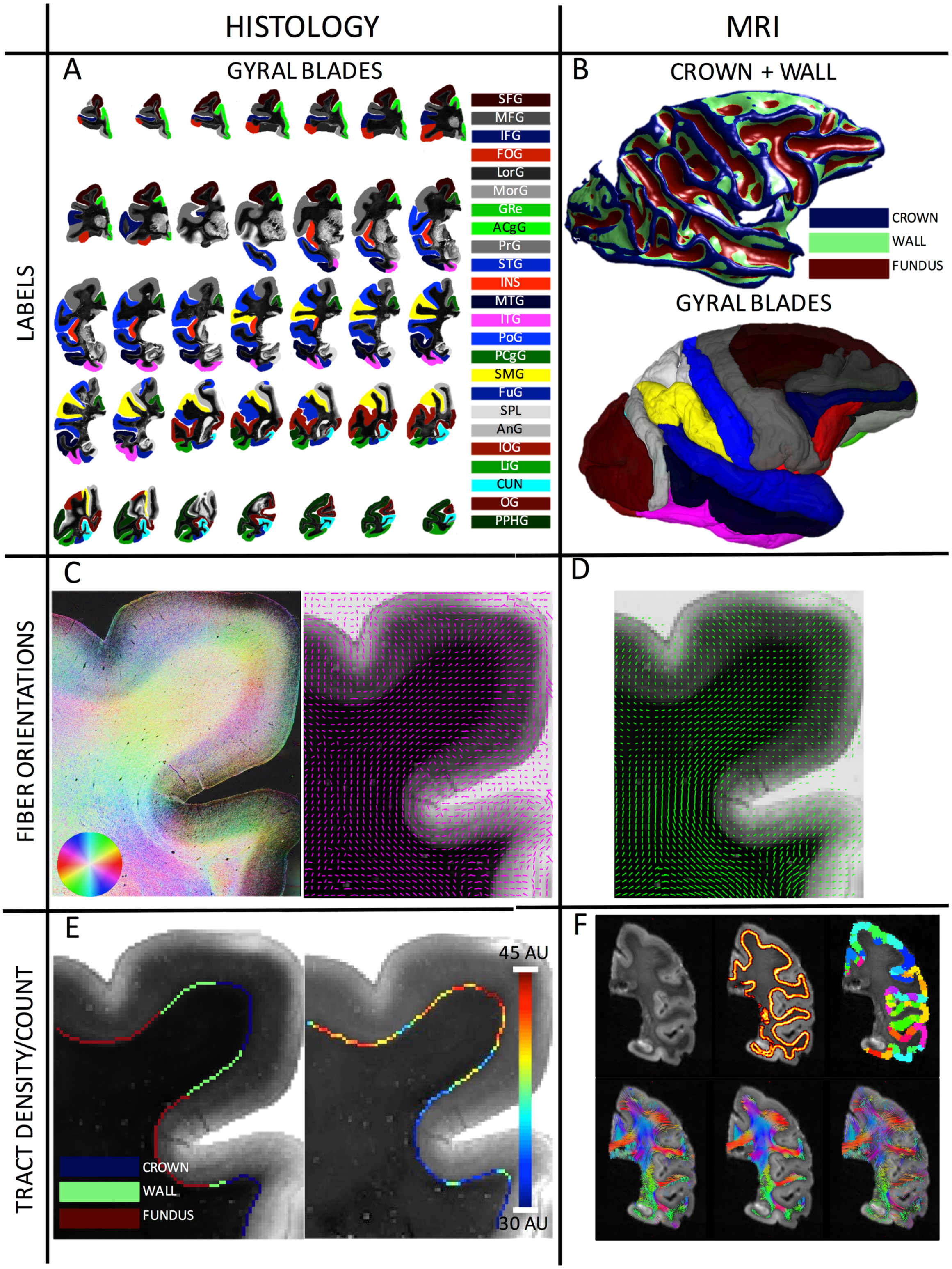

Figure 8.1 Data processing pipeline. From the histological (left column) and MRI (right column) datasets, six pieces of information are extracted. Twenty-four gyral blades are manually defined on histological slices (A), while labels for the crown, walls, and fundi are defined based on convexity measures from 3D MRI data (B). The 3D WMGM surface colored with the crown/wall/fundus labels are shown on top, while the gyral labels transferred to MRI space are shown below (note color scheme is same from part 1). Structure tensor analysis (C, left) is used to extract the myelinated, or ground truth, axon

orientations (C, right), for comparisons with dMRI estimated fiber orientations (D) after transformation to histological space. A count of axons entering the cortex is made along the entire gyral blade, in gyral crowns and sulcal walls (left) for the myelinated tract density measurement (right) (E), for comparisons with the dMRI tractography connectivity and fiber density measures (F). Shown on top are a select slice from the b0 image, the WMGM boundary, and gyral labels segmented into crowns, walls, and fundi. On bottom are shown results from various tractography algorithms (from left to right: DTI, M1; DTI, M2; CSD, M1).

#### *8.2.4.1 Definition of Gyral Blades*

Gyral blades were defined on the histological sections. Manual labeling of 24 gyral blades across all slices (Figure 8.1, A) was performed by a neuroanatomist (IS), with the help of existing macaque atlases [302, 303]. Each gyral region of interest was represented on a minimum of 4 slices, and all described procedures were performed for all regions on all slices.

Gyral blades and abbreviations are as follows: Superior Frontal Gyrus (SFG); Medial Frontal Gyrus (MFG); Inferior Frontal gyrus (IFG); Frontal Orbital Gyrus (FOG); Lateral Orbital Gyrus (LorG); Medial Orbital Gyrus (MorG); Gyrus Rectus (Gre); Anterior Cingulate Gyrus (ACgG); Precentral Gyrus (PrG); Superior Temporal Gyrus (STG); Insula (INS); Middle Temporal Gyrus (MTG); Inferior Temporal Gyrus (ITG); Postcentral Gyrus(PoG); Posterior Cingulate Gyrus (PCgG); Supramarginal Gyrus (SMG); Fusiform Gyrus (FuG); Posterior Parahippocampal Gyrus (PPhG); Superior Parietal Lobule (SPL); Angular Gyrus (AnG); Inferior Occipital Gyrus (IOG); Lingual Gyrus (LiG); Cuneus (CUN); Occipital Gyrus (OG). Note that one gyrus, PPhG, was removed from analysis as it was determined to be defined only on gyral crowns (see 2.4.2), and had no data from sulcal walls for comparison.

The gyral labels were transferred to MRI space (Figure 8.1, B, bottom) using the transformations described above (see Section 8.2.3 Registration). Transferred labels were visually inspected, and manually corrected as necessary.

#### *8.2.4.2 Defining Gyral Crowns and Sulcal Walls*

Labels for gyral crowns and sulcal walls were defined from the structural MRI data. Taking advantage of the 3D architecture provided from MRI, many groups have developed methods to reconstruct gyral and sulcal parcellations using mesh-based, or surface-based, analysis derived from either mean curvature or convexity measures [304-310]. Traditionally, the *crown* of the gyrus is defined by its convexity (negative curvature) [291, 308]. The *sulcal walls*, or banks of the sulci, are the areas of cortex along opposing sides of adjacent gyri [291] and are characterized by a low curvature [308]. Finally, the *fundus* describes the deepest part of the sulcus [291] and are regions with positive curvature [308]. In this study, we began with a joint segmentation and bias field correction based on integrated local intensity clustering [311] to create a white matter mask. Next, a mesh of the WMGM boundary was created, and for every vertex, the mean curvature [304, 305] is calculated. Then, a simple threshold was applied at the 33rd and 66th percentile of the mean curvatures to segment the surface into crown, walls, and fundi (Figure 8.1, B, top). After registration, the labels derived from 3D MRI data were transferred into 2D histological space (Figure 8.1, B, bottom). At this point, we have labels for gyral blades defined in both histological and MRI space, and each blade is segmented into crown(s), wall(s) and fundus (fundi).

#### 8.2.4.3 Myelinated Fiber Orientations

The ground truth fiber orientations were defined on histological myelin-stained slices using structure tensor (ST) analysis [212]. The ST has been employed on histological sections in 2D on rat [134] and human [200, 213] brains, and in 3D on macaque [136] and squirrel monkey [199] brains. ST analysis is a technique based on the dyadic product of the image gradient vector with itself, and results in an orientation estimate for every pixel in the image (Figure 8.1, C, left). Downsampling of the high-resolution orientation estimates was employed to determine the primary fiber orientation in 150um$^2$ areas (Figure 8.1, C, right). These were then used for comparison with the primary orientation estimated from MRI using the diffusion tensor model (see Section 8.2.4.4 dMRI Estimated Fiber Orientations), as well as for analysis of fiber curvature along the WMGM boundary. For visualization, ST values of orientation, anisotropy, and staining intensity are displayed as hue, saturation, and brightness (HSB) images (Figure 8.1, C, left), respectively, at native resolution [134].

#### 8.2.4.4 dMRI Estimated Fiber Orientations

We chose to use the tensor model for comparisons of orientation with histology (although any local reconstruction algorithm can be processed and compared in a similar way). The tensor was estimated using a NLLS DT fit [312]. After transformation to and reorientation in histological space (see Section 8.2.3 Registration), the primary eigenvector of the diffusion tensor was projected onto the 2D histological plane [133] (Figure 8.1, D). This 2D projection was then compared to the histological fiber orientations estimated using ST analysis.

#### *8.2.4.5 Myelinated "Tract Density"*

An automatic count of the axons leaving the white matter and entering the cortex was made along the entire WMGM boundary mesh surface for every gyral blade (Figure 8.1, E). This was performed by dilating the WMGM boundary 50um into the cortex (to ensure we were not counting axons in the white matter) and taking the intensity profile along this band. Because the myelinated axons appear as low intensities, the intensity values were inverted, and a count of the number of peaks meeting an (empirically derived) intensity threshold was made. This threshold was kept constant across the entire slice, and for all slices. The fiber density was then the average axon count over a specific distance. For each gyral blade, this measurement was summarized by taking the ratio of the average fiber density at the crown(s) over the average fiber density at the wall(s). We refer to this quantity as the "connectivity profile" of each gyral blade. For statistical analysis, we took the natural log of this ratio. This makes the ratios additive, the variance homogenous, and the distribution symmetric [313], which allows for standard parametric hypothesis testing. A positive log-ratio (ratio>1) suggests higher fiber connectivity at the crown(s), while a negative value (ratio<1) suggests higher connectivity at the wall(s).

#### *8.2.4.6 Diffusion MRI Tract Density*

We begin our study by choosing fiber tractography based on (arguably) the most commonly used local reconstruction technique, diffusion tensor imaging [30, 225]. Three tracking strategies that are ubiquitous in the field are employed, distinguished largely by the strategy for seeding streamlines. Each method is performed using both deterministic and probabilistic propagation techniques. Finally, for each method, four connectivity "scaling" measures are performed.

Method 1 (M1) is based on *whole brain* seeding. This means seeds are initiated from all voxels in the brain, and terminate only when they exit the brain, or exceed the maximum curvature threshold. This method is consistent with analysis based on tract-density imaging [314], and most commonly applied in studies where whole-brain seeding is used in combination with waypoints to select specified white matter pathways [167, 315]. For each region of interest (i.e. the crowns and walls for each gyral blade), the number of streamlines ending within the region volume are counted. Method 2 (M2) is seeded throughout the *white matter*. White matter seeding is the most common strategy for studies mapping the human connectome [222, 316, 317], and again, is also commonly performed before addition of inclusion/exclusion masks for extracting specific fiber pathways. For M2, tracking is stopped once the voxel leaves the WM (crosses the WMGM boundary), and the number of pathways terminating on the surface of each label is counted. Method 3 (M3) then seeds from the interface of the *WMGM boundary*. The method has been proposed as a way to bypass potential seeding biases [297, 298], and is gaining in popularity in structural connectivity pipelines. Again, tracking is terminated when the pathway crosses the WMGM boundary, and the number of pathways terminating on the surface of each label is counted. In all cases, tracking was performed using the publically available software package MRTrix3 [56, 186], and seeding was repeated until 2,500,000 streamlines were created. Streamlines that did not meet the minimum length criteria of 5x the voxel size were discarded.

The four connectivity scaling measures are as follows. The first option is no normalization at all. This number then represents the raw “count” of streamlines entering each region of interest. The second scaling mechanism is to scale the contribution of each streamline to the total count by the reciprocal of its length. As described above, this is intended to compensate for biases introduced by homogenous seeding throughout the brain, which leads to over-representation of the long fiber pathways. Third, the number of streamlines can be scaled by the reciprocal of the total node volume. This is intended to compensate for the fact that larger target regions are more likely to be intersected by an overall greater number of streamlines. The results are traditionally interpreted as a connection density (count per volume), which is more of an analogue to our histological measurements (fiber density). (Note that, for M2 and M3, the data are normalized by GMWM surface area, rather than volume). The final scaling option we assess is to scale the contribution of each streamline by the streamline length (exactly the inverse of the second normalization mechanism). Although not as commonly used in literature, this scaling could be justified on the basis that longer connections are harder to reconstruct than shorter ones due to tract dispersion (uncertainty) and tract deviation (errors in orientating estimation) [57, 141, 318]. Thus, this scaling would emphasize these longer, harder to reconstruct connections as an attempt to correct for the path-length dependency inherent in fiber tractography [156, 319].

In order to assess the effects of curvature criteria on DTI tracking, tractography was performed with no stopping criteria other than curvature threshold, or leaving the brain mask. The curvature thresholds chosen for analysis were 15°, 30°, 45°, 60°, 75°, 90°, 135°, and 180° (equivalent to no stopping criterion). Similarly, the effect of b-value and resolution were assessed by performing repeating tractography for all b-values (3,000–12,000 s/mm$^2$) and for the entire range of resolutions (300-800um isotropic). In order to eliminate the effects of the step size on analysis of acquisition resolution, the step size was fixed for all tracking algorithms, at all resolutions, to 10% of the smallest voxel size (i.e. 30um step size). Finally, to test tracking biases using a reconstruction method capable of resolving multiple fiber populations, we have chosen a commonly used higher order algorithm, constrained spherical deconvolution (CSD) [298], implemented in MRTrix3.

Figure 8.1, F shows the WMGM boundary used for seeding and stopping, the gyral blades segmented into crowns, walls, and fundi, and 3 representative tractograms.

## 8.3 Results

### 8.3.1 Histological Density Profile

The results of histological analysis are shown in Figure 8.2. We find that many gyral crowns do have more dense connectivity than neighboring sulcal walls. Eleven of the 23 regions of interest have a significantly higher fiber count at the crowns, and all but one have a higher average fiber count at the crown (one-sample t-test; $p<0.05$). Across all gyri, we find an overall log-ratio value of 0.12 (average ratio of 1.13) suggesting an average 13% increased fiber density at the crowns relative to walls. Finally, a 1-way ANOVA with the gyral blades as factors suggests that the histological fiber density profile is not the same across all gyri ($F=3.27$, $p<.001$).

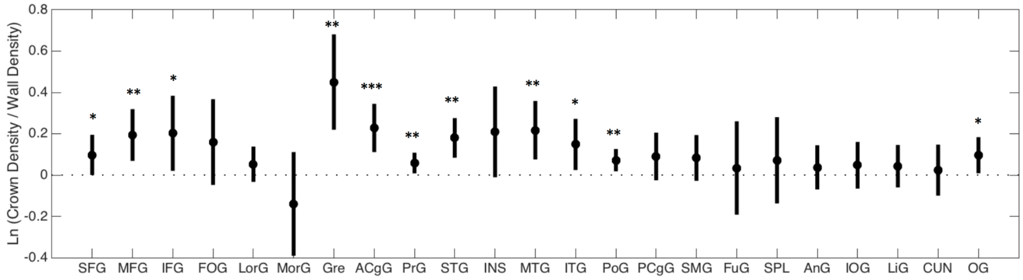

Figure 8.2 Histological density profile across 23 gyral blades. Average log-ratio (circles) and 95% confidence intervals (lines) are shown for each region of interest. The value of 0 (ratio = 1) is shown as a horizontal dotted line. Asterisks indicate that log-ratio is significantly greater than 0 (* p<.05; ** p<.01; *** p<.001), which means the gyral crown has significantly higher density than neighboring sulcal wall(s).

### 8.3.2 DTI tractography

Figure 8.3 shows the tractography-derived fiber density profiles (ratio of crown measure to wall measure) for all gyral blades. Results are shown for all 3 seeding methods, each with both deterministic and probabilistic propagation, and with 4 scaling methods applied to each. It is clear that DTI streamlines are biased towards the gyral crown relative to histology in many gyral blades, for all 3 tracking strategies. No combination of seeding method and quantification is consistently non-biased across all gyral blades. In fact, many gyral blades show a bias of as much as much as 12x more “connectivity” at crowns that at the corresponding walls.

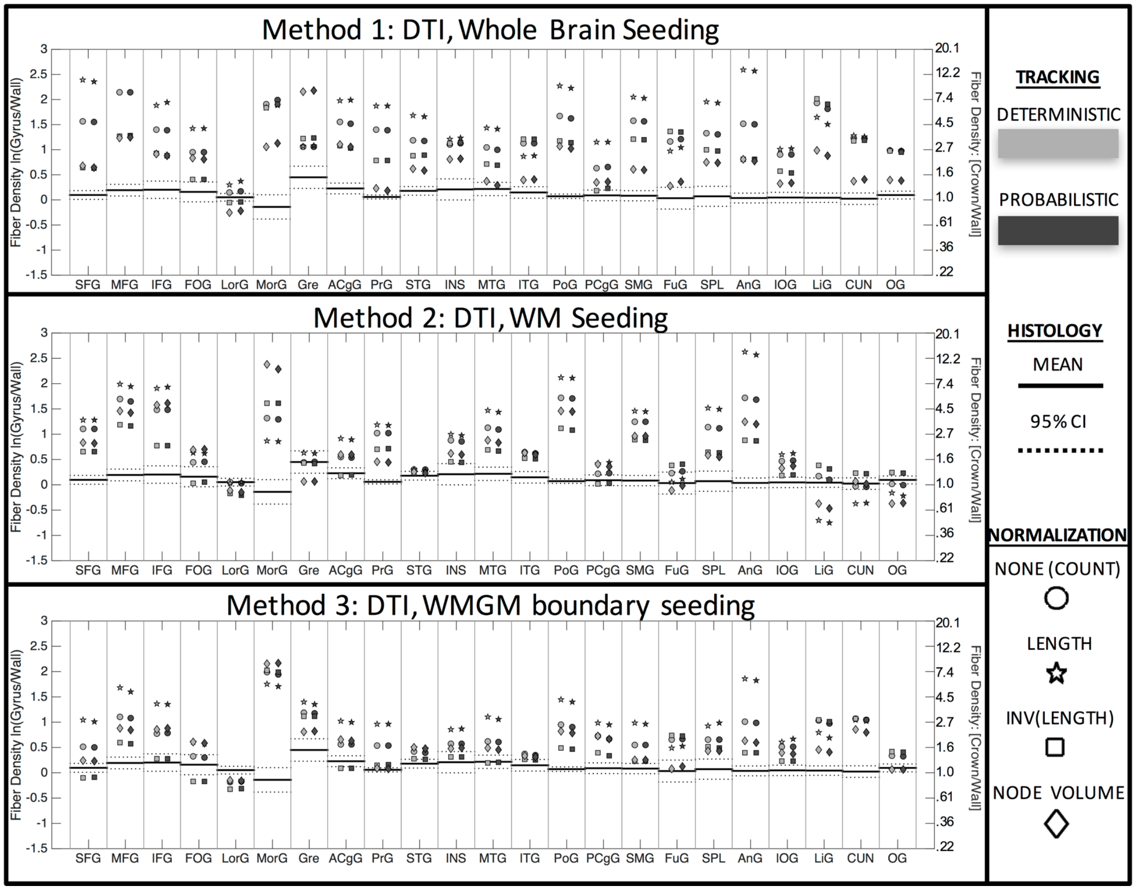

Figure 8.3 DTI streamlines are biased towards gyral crowns in many gyral blades, for all tracking strategies. The ground truth density profile is shown as horizontal lines (mean +/- 95% confidence interval). DTI tractography-derived densities for whole brain seeding (top), white matter seeding (middle), and WMGM boundary seeding (bottom) are shown for each gyral blade, for both deterministic (light gray) and probabilistic (dark gray) propagation. Data are shown as (1) no normalization (circle), normalized by length (star), inverse length (square), and inverse node volume (diamond). Log-ratio scale is shown on left vertical axis, while the ratio measure is shown on the right. A tractography-derived value greater than the histological range indicates a bias towards the gyral crowns.

Condensing this information across all gyri (Figure 8.4) shows that across the whole brain, all algorithms are significantly biased relative to histology, and consistently overestimate connectivity at the gyral crowns by a factor of between 1.5 and 5. Several trends are apparent. First, bias is dependent on seeding method ($p<.001$, $F=17.64$, $df=5$), for example M1 (whole brain seeding) has significantly higher bias than M2 and M3. Second, there is no significant difference between deterministic and probabilistic DTI tractography. Finally, there are significant effects of scaling mechanism on the gyral bias ($p<.001$, $F=27.89$, $df=5$). For all cases, scaling by length leads to the largest bias, followed by no normalization, then inverse length and inverse node volume. It is important to point out that the methods resulting in a fiber profile most similar to histology - M3 with scaling by inverse length - has no biological, anatomical, or technical basis for scaling by inverse length. This scaling mechanism is tailored to address biases inherent to homogenous white matter seeding, which is not performed in M3. Thus, this combination of seeding and quantification is unlikely to be performed in practice.

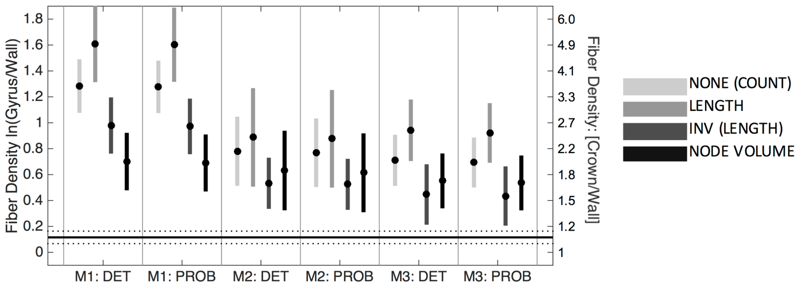

Figure 8.4 DTI streamlines are more dense in gyri than sulci for all three seeding strategies, regardless of subsequent fiber quantification. Mean (circle) and 95% confidence intervals (vertical line) are shown over all gyri for each DTI tracking algorithm. Four quantification strategies include (1) no scaling, (2) scaling by length (3) inverse streamline length, (4) and inverse node volume. Histological mean and 95% confidence intervals across all gyri are shown as horizontal solid and dotted lines.

Inspection of the resulting fiber pathways gives insight into potential sources of the bias. Figure 8.5 shows a select coronal slice, with labels for the crown and walls highlighted. All streamlines are colored by their endpoints, meaning groups of fibers with similar endpoints will share similar colors. For M1, the most striking feature is the densely populated gray matter in the crown, with sparse fibers throughout the wall. Even more striking, there are areas of the fundus (dotted arrow), where no fibers are able to propagate, a characteristic described in [107], and attributed to the superficial U-shaped fibers just beneath the infragranular layers of the cortex. In addition, we see relatively sharp curvature into the cortex at the walls (solid arrow), a feature similar to that described in histological sections [108, 200, 293]. This motivates an analysis of the effect of curvature threshold on tractography results (described later). M2 shows features similar to M1. As in M1, it is clear there is an over-representation of some of the longer pathways which tend to orient towards the gyral crown. For example, seeding anywhere in the oval leads to an excessively dense representation of tracts in the stalk of the gyrus, which all terminate in the same vicinity.

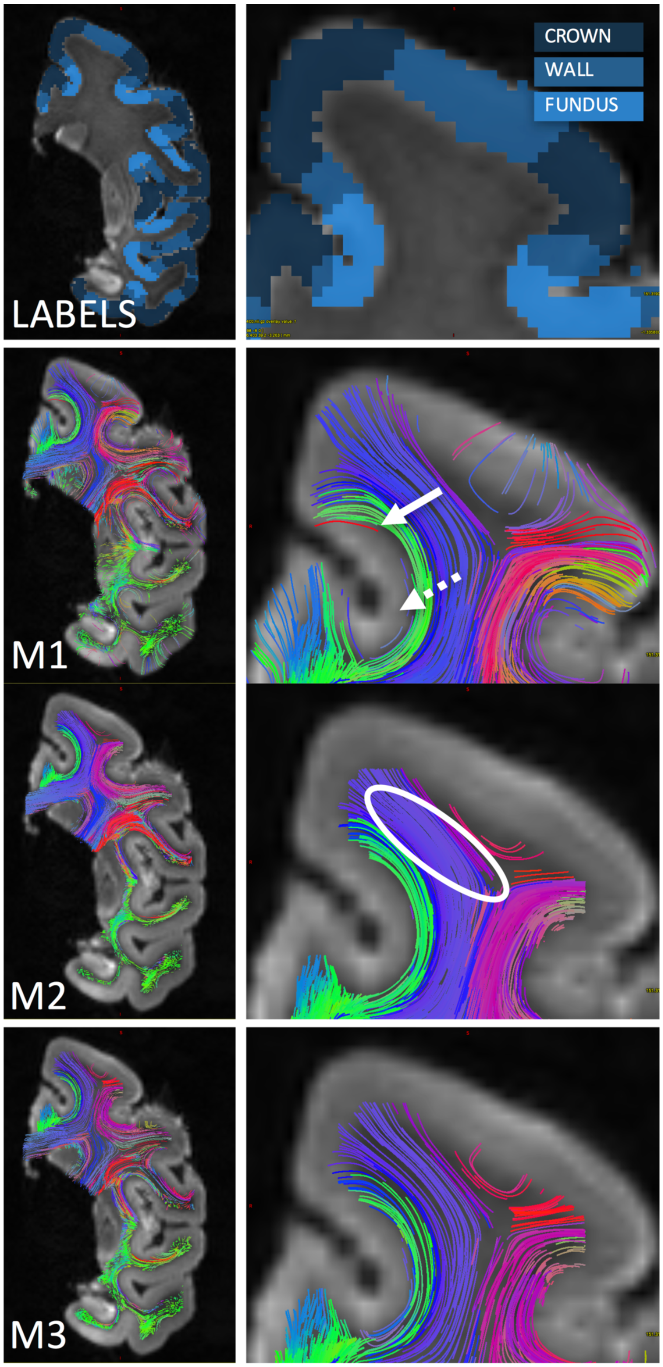

Figure 8.5 Subset of DTI streamlines for each tracking strategy. Labels for crown, wall, and fundi are shown with a zoomed in view of the SFG. DTI streamlines are shown for M1 (whole brain seeding), M2 (WM seeding), and M3 (WMGM boundary seeding), and are colored based on streamline end points. The dashed arrow highlights a fundus, where no streamlines are able to propagate. The solid arrow points towards the increased curvature of streamlines entering the GM. And the oval highlights a large, homogenous, area of WM, where seeding will contribute to over-representation of fibers terminating at the crown.

To confirm that the dominant source of bias comes from the longer fibers, we separate streamlines by length into short, medium, and long fibers (binned by 33rd and 66th percentiles), and repeat the analysis. Figure 8.6 shows the results (without scaling), for all algorithms. In all cases, the longer fibers are more biased towards the crowns than medium and short fibers. In agreement with known anatomy [110], the short streamlines consist of the short association fibers (U-fibers) connecting the same or adjacent gyri, while the medium and long fibers are composed of the long association fibers (connectivity of different lobes) and commissural fibers. However, unlike the results of anterograde and retrograde tracer studies [110], there is a clear penchant for the association and commissural streamlines to terminate on the gyral crowns. Despite the fact that increased seeding in longer pathways is the dominant source of bias, applying inverse-length scaling does not eliminate the bias (Figure 8.6).

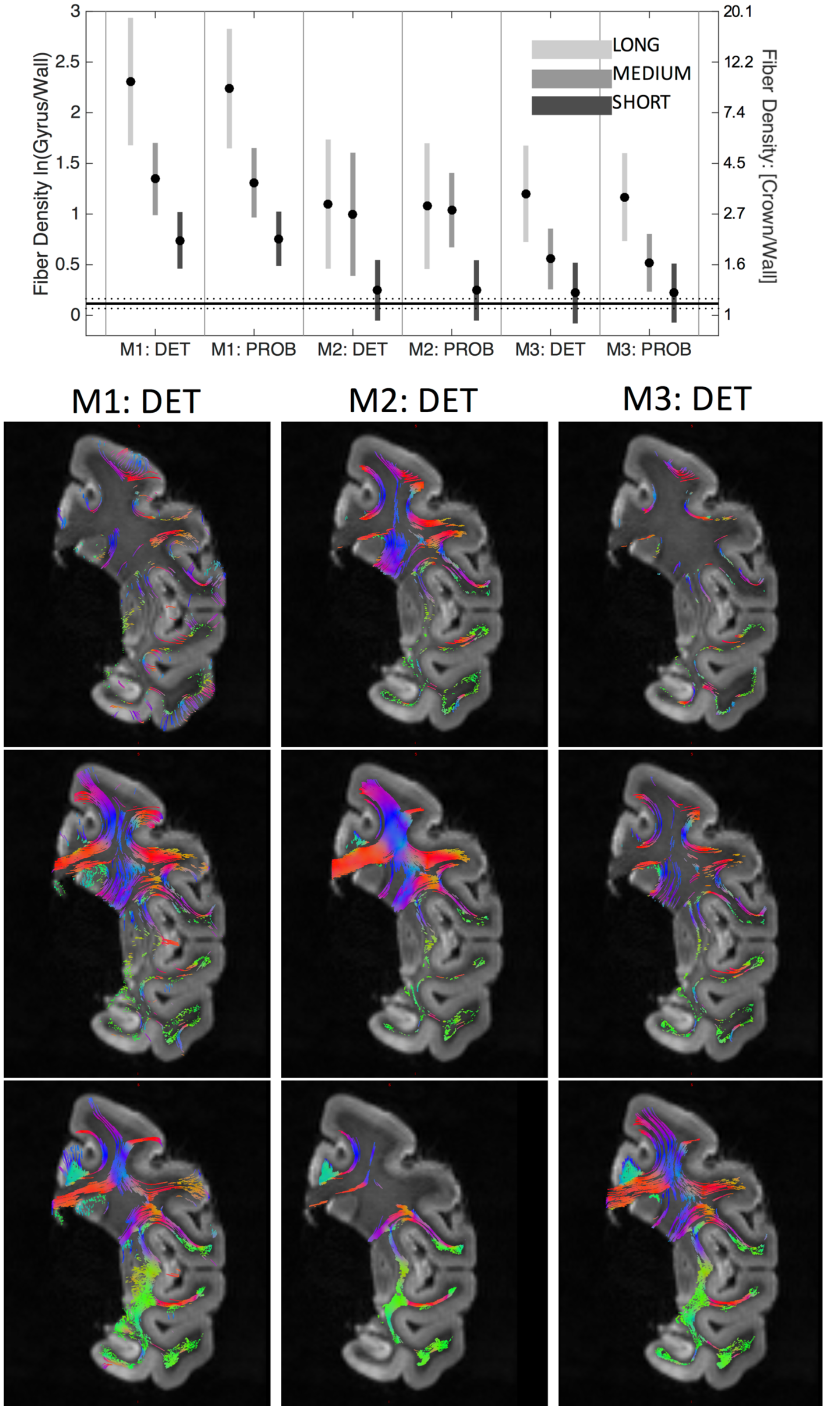

Figure 8.6 The effects of fiber length on gyral bias. The (unscaled) fiber-density profile across all gyral blades is shown for long, medium, and short fibers (top). A subset of long, medium, and short fibers is shown for each of the three tracking strategies for a select coronal slice (bottom).

### 8.3.3 Fiber Curvature at the cortex

Two examples highlighting a potential anatomical cause of this bias are shown in Figure 8.7. Here, we focus on the curvature of fibers as they enter the cortex, taking as examples a slice showing the SFG (A-C) as well as a slice containing the IFG and FOG areas (D-F). Figures A and D show the WMGM boundary (blue voxels) along the gyral blades, as well as the normal to the boundary (yellow sticks). ST analysis, along with the HSB images, qualitatively highlights the high curvature of fibers entering the cortex along the sulcal wall (B and E), and the relatively low curvature at the crown (C and F).

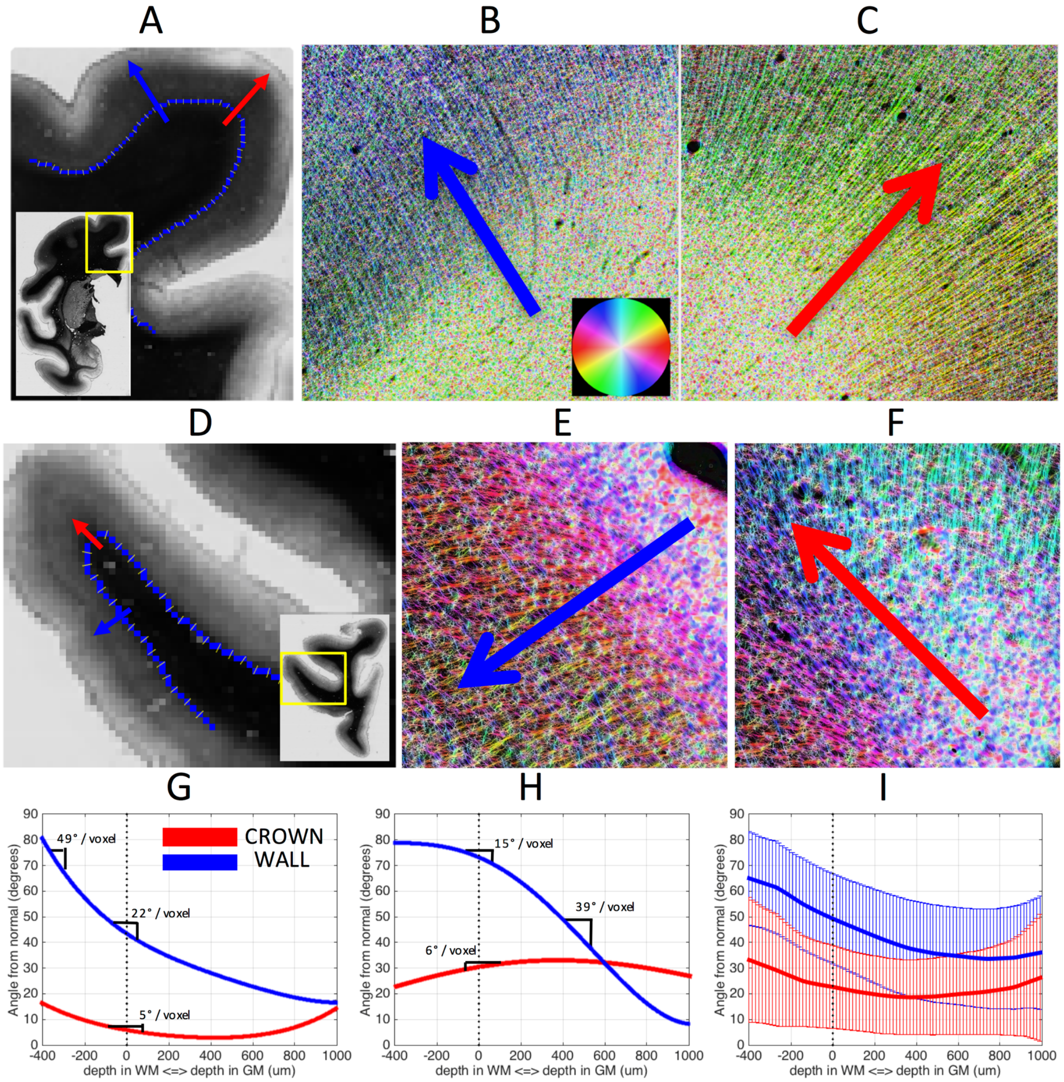

Figure 8.7 Fibers typically curve more at the sulcal wall than they do at gyral crowns. A histological slice containing the SFG (A) is shown, along with the WMGM border (blue) and the normal to the border (yellow lines). Arrows are shown at the wall (blue) and crown (red) going from white matter into gray matter. Both arrows are perpendicular to the WMGM boundary. High-resolution HSB images in the same places at the wall (B) and crown (C) demonstrate the high curvature of fibers entering the cortex at the walls (B) and the long, straight fibers at the crown (C). A myelin-stained slice containing IFG and FOG regions (D), and high-resolution HSB images at the wall (E) and crown (F), show similar trends. The fibers from A-C are tracked from white matter, into gray matter, and the angle these fibers make with the normal to the WMGM border is recorded (G) for the wall (blue) and crown (red). The slope of this curvature is marked in various locations. The fibers from D-F are similarly tracked, and the angle at these locations from the wall (blue) and crown (red) are plotted (H). Finally, the results from all gyral blades analyzed (I) are shown for the crown (red) and wall (blue) with the mean (solid line) and standard deviations (vertical lines) plotted for each.

To quantify the fiber curvature (G and H), the angle the fibers make relative to the normal to the WMGM boundary is plotted as they traverse from white (negative distance) into gray matter (positive distance). In these regions, fibers at the crown stay relatively parallel to the normal (red arrows) throughout the entire path, and are curving at only 5° and 6° per 400um as they enter the cortex. At the wall, the fibers bend from nearly perpendicular to the normal, to almost parallel, within a distance of less than 1.5mm. In these specific slices, the wall of the SFG (G) is curving at a larger 22°/400um entering the cortex, while the highest curvature happens just inside the white matter at nearly 49°/400um. For the wall of the IFG and FOG (H), the highest curvature takes place about 400um into the cortex, curving at approximately 39°/voxel. Thus, in these two examples, the fibers curve more at the sulcal walls than they do at gyral crowns.

While these examples highlight two slices with high curvature at the walls, there is high variability across slices and across gyral blades. Figure 8.7 (I), shows the mean and standard deviation of the angle relative to the WMGM normal across all analyzed gyral blades. Despite the wide range, two trends are apparent. Fibers at the crown enter the cortex at a smaller angle (relative to the WMGM normal) than those at the walls (22° ± 15° and 50° ± 17°, respectively), and curve less upon entering the cortex than those at the walls.

### 8.3.4 Effects of curvature threshold

We next test the effects of curvature threshold on the gyral bias, by performing tractography with varying curvature thresholds (data not shown). We find that for all 3 methods, with all 4 quantification techniques, there is no significant effect of pathway curvature threshold on the bias (F ranged from 0.50-0.81, $p>0.05$).

### 8.3.5 Angular agreement between histology and dMRI

To assess whether the diffusion *orientation* estimates are biased towards the gyral crowns relative to the true fiber orientations, we compared the primary diffusion directions (projected onto the 2D histological plane) with the histological fiber orientations estimated using ST analysis (calculated in the 2D plane). Figure 8.8 (top) shows the angular differences for all voxels along the WMGM boundary, in each of the gyral blades. A positive angular difference indicates that the fiber orientation from diffusion is angled more *towards* the apex of the gyral blade (relative to ST orientation), while a negative angular difference means it is angled *away* from the apex. The first, second (median), and third quartiles of this dataset are -8.6°, 2.2°, and 13.7°, respectively. This indicates a slight bias for estimated fiber orientations, the inputs for fiber tracking algorithms, to be oriented slightly more towards the crown than they should be. However, as the tensors become more isotropic, particularly near the cortex, the ambiguity in fiber orientation increases, and could account for much of the angular differences measured.

Figure 8.8 (bottom) shows the absolute angular deviation of voxels in the white matter (this does not include all white matter, only that which is contained within the gyral stalks). The median absolute angular difference in the white matter is 9.2°, indicating that, on average, the tensors differ from the true fiber orientation by less than 10°, a value in good agreement with previous histological validation studies [132, 133].

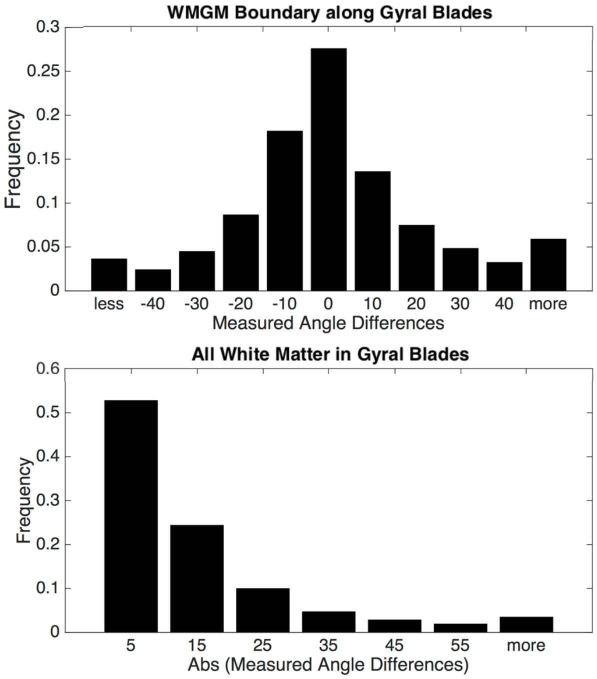

Figure 8.8 Histograms of measured angle differences. The differences between the true fiber orientation measured with high-resolution micrographs and the fiber orientation estimated from diffusion imaging are shown for both the voxels comprising the WMGM boundary (top), and those that are in pure WM (bottom). The top figure shows both positive and negative angular differences along the WMGM border, indicating estimated orientation error towards and away from the gyral crown, respectively. The bottom figure shows the absolute value of angular differences in white matter regions contained within the gyral blades.

### 8.3.6 Effect of b-value

Next, DTI tractography was repeated for all acquired b-values (data not shown). For all methods, and all quantification strategies, the diffusion weighting did not have a significant effect on the gyral bias (F ranged from 0.02-0.33, p>.05).

### 8.3.7 Effect of image resolution

Figure 8.9 shows the results (over all gyri) of running all tractography algorithms for all acquired resolutions ranging from 300um isotropic to 800um isotropic voxels (shown ranging from light to dark grays). It is interesting that for M2, increasing the resolution (i.e. reducing voxel size) does not improve the fiber density profile along the gyral blades. In fact, the opposite happens - the observed bias consistently decreases as the resolution decreases. This however, does not mean the streamlines produced from lower resolution data are more anatomically accurate (see Discussion), only that the measured tractography density along the WMGM border more closely approximates the histological densities as the voxel size increases. In contrast, the observed bias in M1 and M3 trend in the opposite direction.

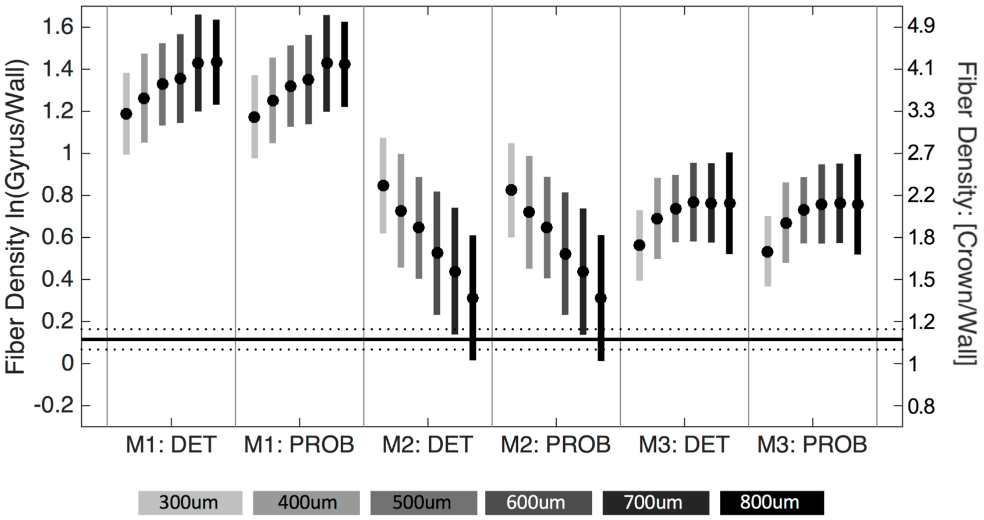

Figure 8.9 Gyral bias is dependent on MRI resolution. Fiber tracking is performed using three tracking strategies, at image resolutions ranging from 300um isotropic to 800um isotropic. The log-ratio of density at the gyral crowns to that at the walls is shown for all algorithms, and all resolutions. Results are shown with no scaling factor.

### 8.3.8 Effect of higher order diffusion model

We next ask whether the ability to detect multiple fiber orientations in a voxel enables more anatomically correct streamline propagation into the cortex. CSD has been shown to be both accurate and consistent in resolving multiple intra-voxel fiber populations, and has been used extensively to study crossing fibers throughout the brain[45, 210, 216]. Figure 8.10 shows the voxel-wise reconstruction results for both DTI and CSD in two gyral blades. For DTI (middle column), 3D ellipsoids are shown representing the mean-square diffusion distance in each direction. WM glyphs show the typical “cigar” shape, while more isotropic ellipsoids are apparent along the WMGM boundary along with a lower FA, likely indicating larger geometric fiber dispersion or multiple fiber populations. The CSD glyphs (right column) show the estimated fiber orientation distributions. Many areas in both WM and GM show multiple fiber populations. In addition, in agreement with previous studies [114, 116, 198], we see fibers largely oriented radially (perpendicular) to the WMGM boundary, particularly in the crowns (solid arrows), and crossing fibers oriented tangentially to the boundary that are especially prevalent in the walls (solid arrows). Also of note, the short U-shaped fiber tract occurring between the faces of adjacent sulci (white brackets) are apparent in both diffusion techniques. Even here, CSD often shows the presence of a second fiber population oriented perpendicular to the surface, although occupying a much smaller volume fraction in each voxel (see Discussion).

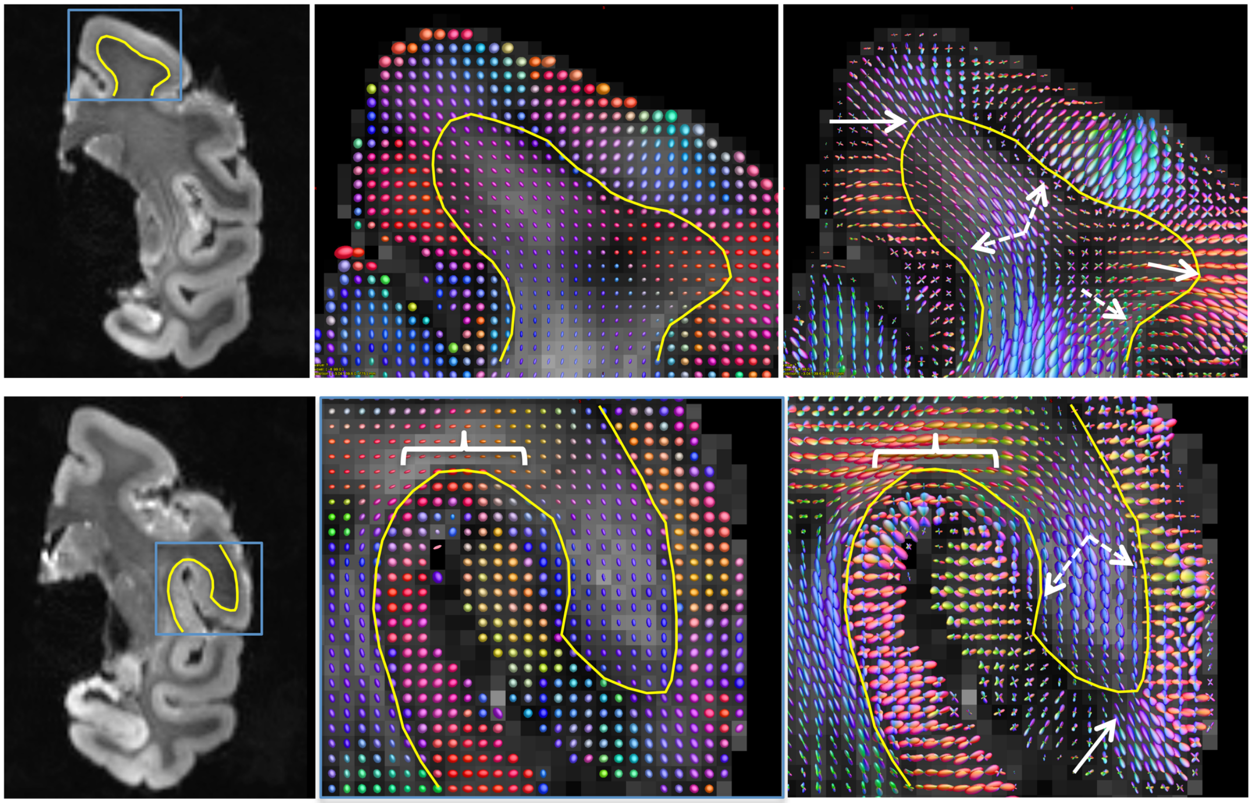

Figure 8.10 CSD shows evidence of multiple fiber populations along the WMGM boundary. DTI ellipsoids (middle column) and CSD fiber orientation glyphs (right column) are shown for SFG (top row) and PRG (bottom row). WMGM boundary is shown as a yellow line. Fibers are largely perpendicular to the WMGM surface at the crowns (solid arrow), while crossing fibers (not detectable using DTI) are prevalent along the walls and in GM (dashed arrow). Dense U-fibers just below the cortical surface are visible between adjacent sulci (white brackets).

Figure 8.11 shows the results of CSD [45, 186, 216] with both deterministic and probabilistic tractography. Comparing these results with Figure 4, CSD has a modest reduction of gyral bias (~1-20% reduction) compared to DTI. In addition, multiple combinations of seeding and scaling strategies are no longer (statistically) significantly biased. However, these results still tend to overestimate the density at the crowns relative to walls. In other words, although the bias is reduced below a statistically detectable level, there is still a numeric difference between the tractography results and the ground truth histology, but we did not have sufficient power to detect a significant difference.

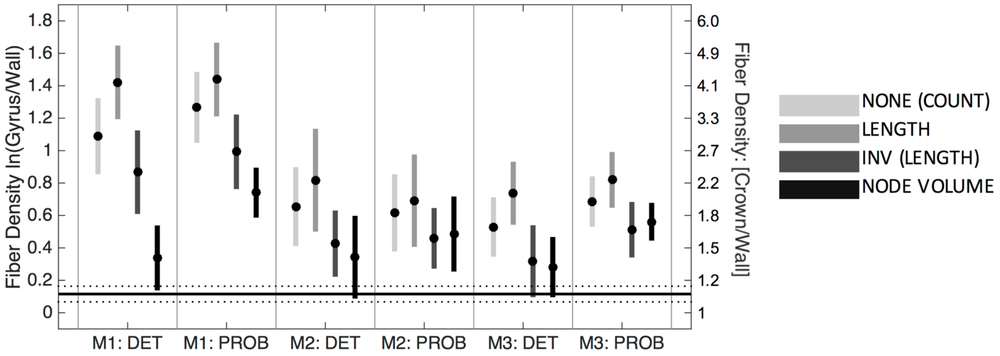

Figure 8.11 CSD streamline bias is reduced compared to DTI (compare to Figure 8.4), but is still greater than histological ground truth. Mean (circle) and 95% confidence intervals (vertical line) are shown over all gyri for each CSD tracking algorithm. Four quantification strategies include (1) no scaling, (2) scaling by length (3) inverse streamline length, (4) and inverse node volume. Histological mean and 95% confidence intervals across all gyri are shown as horizontal solid and dotted lines.

Qualitatively, the tractography results show high levels of similarity with those from DTI (Figure 8.12), however the ability of streamlines to propagate in multiple directions is now apparent in both WM and GM. Similarly, the dominant source of bias from these tractography results comes from the longer fibers (Figure 8.13), where, in all cases, longer fibers are more biased towards the crowns than medium and short fibers. However, this bias is reduced (for all lengths) when compared to DTI tractography (compare to Figure 8.6). Angular agreement in CSD orientation estimates was also assessed. The angular differences along the WMGM boundary were slightly improved compared to DTI, with first, second, and, third quartiles of -8.5°, -0.7°, and 7.3°, respectively, a reduction likely due to the reduced partial volume effects of multiple fiber orientations along the boundary. The median absolute angular difference in WM was 7.9°, again, a slightly better value than for the diffusion tensor.

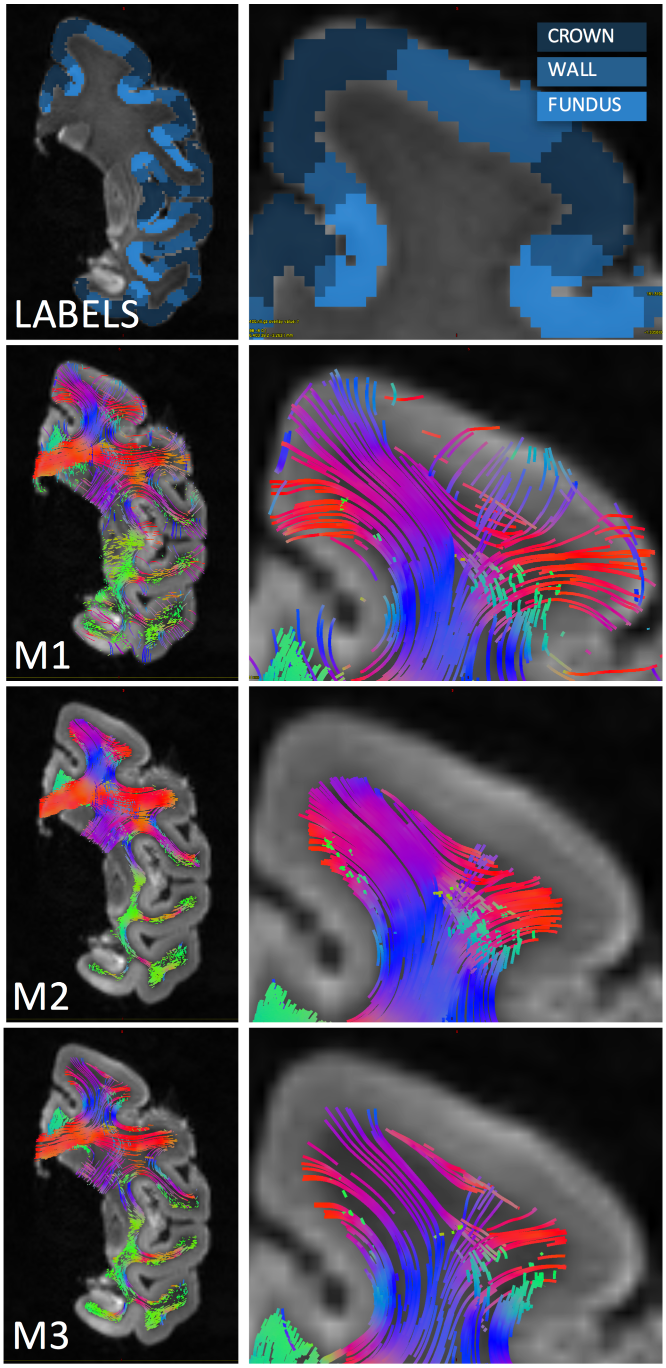

Figure 8.12 Subset of CSD streamlines for each tracking strategy. Labels for crown, wall, and fundi are shown with a zoomed in view of the SFG. CSD streamlines are shown for M1 (whole brain seeding), M2 (WM seeding), and M3 (WMGM boundary seeding), and are colored based on streamline orientation.

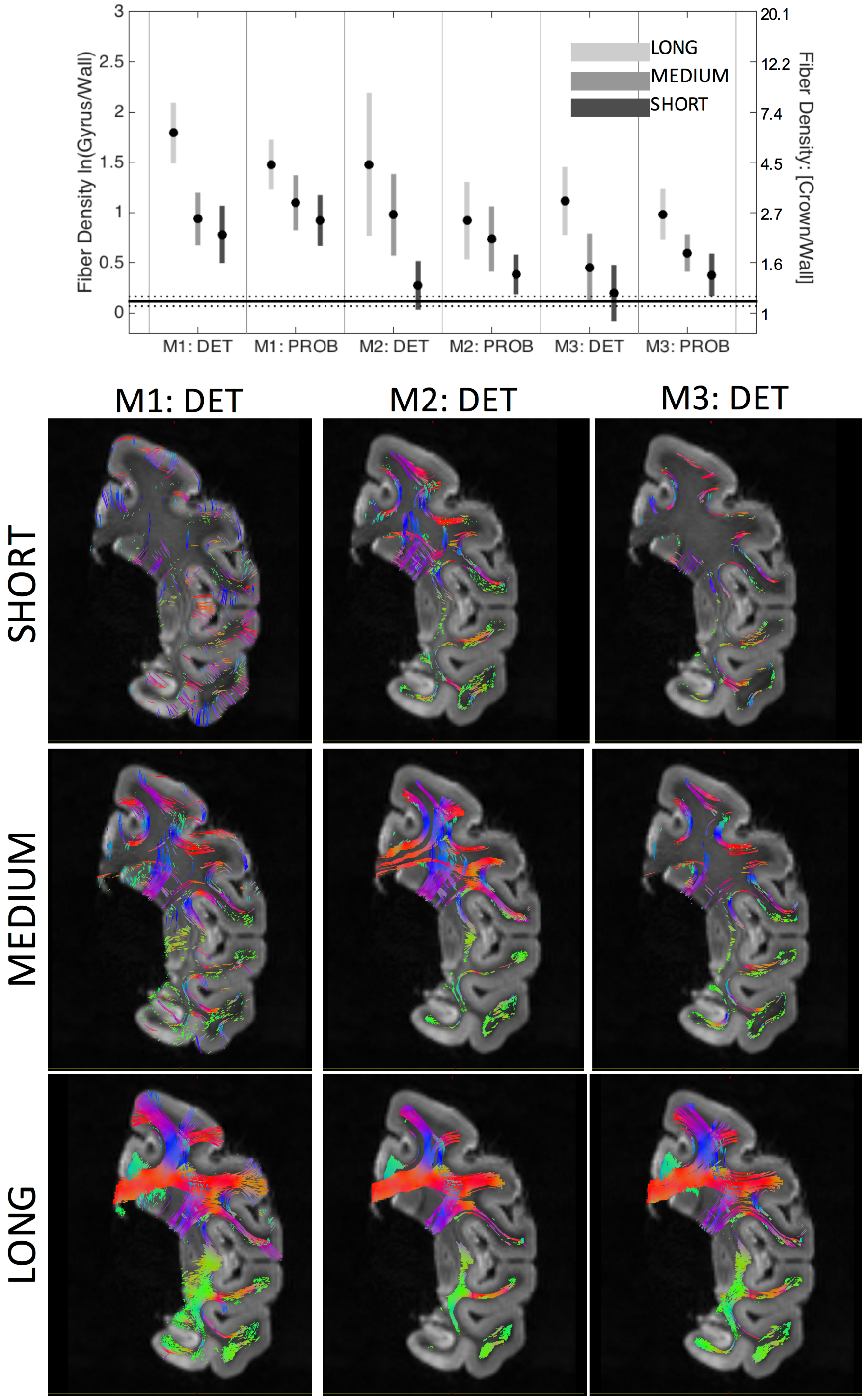

Figure 8.13 The effects of CSD fiber length on gyral bias. The (unscaled) fiber-density profile across all gyral blades is shown for long, medium, and short fibers (top) estimated using CSD tractography. A subset of long, medium, and short fibers is shown for each of the three tracking strategies for a select coronal slice (bottom).

## 8.4 Discussion

Using dMRI tractography to map the neuronal connections of the brain requires accurately estimating connections between large numbers of gray matter regions. In this study, we have shown that there is a significant bias for dMRI tractography streamlines to terminate on gyral crowns, relative to the sulcal banks - an artifact that could significantly affect the results of any quantitative estimates of connectivity using dMRI. It appears that this gyral bias is significant in many gyral blades across the entire brain, and occurs even with exceptionally high-quality ex vivo data. This effect was shown for a range of tracking algorithms, including both deterministic and probabilistic, and varying model complexities, from the simple diffusion tensor (Figure 8.3), to a model capable of describing a complex fiber orientation distribution (Figure 8.11). Additionally, this gyral bias occurred for a range of diffusion weightings, and even for very high spatial resolution datasets (Figure 8.9).

These results have several implications for current tractography practices. As described in [201], the use of the “fiber count” and similar terminology is likely an inaccurate metric to describe the true connection strength between two regions derived from diffusion tractography. However, these measures are widely used in the literature [201], particularly in mapping connectomes [65, 66, 222, 284]. Here, we have shown that a “count” of the streamlines crossing the WMGM boundary does not accurately represent the fiber count in the same regions derived from histological measurements. In fact, no fiber quantification strategy consistently yielded a connectivity measure that was not biased relative to histology. This does not, however, invalidate existing connectivity studies; rather than true measures of connectivity, these graph-theoretical measures and streamline connections reflect some characteristics of the underlying white matter microstructure, with some level of uncertainty and bias. This work focuses on one of several potential sources of fiber tracking bias.

The results from this study should also provide guidance for future generations of tracking algorithms. Specifically, we’ve shown that nearly orthogonal bending over the range of a millimeter, particularly along sulcal walls, is not uncommon. While the average curvature of axons crossing the WMGM border is relatively small (~20°/voxel, see Figure 8.5), there is tremendous variation across the brain, as the gyral blades take a variety of different geometries and sizes (see Figure 8.1). Thus, there is a tradeoff when choosing a curvature threshold parameter. A liberal threshold is necessary to track properly into the cortex, but too high a threshold may result in a loss of tracking specificity [164], and potentially anatomically unrealistic tracks. Even so, very liberal thresholds (including no curvature threshold) still numerically overestimated the connectivity at the gyral crowns. Alternatively, there is a possibility to modify the rules of fiber tracking, possibly at the cortex [108]. Some groundwork has already been laid towards a histology-informed model of diffusion near the cortex by Cottaar et al. [320, 321], but as of yet, no fiber tracking results using modified rules have been reported. However, applying anatomically-informed constraints to fiber tracking algorithms terminations and rejection criteria was proposed in [298], which shows encouraging results, including a more homogenous density of streamlines along the cortical ribbon (see Figure 6 in [298]).

In addition, there is a class of emerging tractography methods in the literature [295, 322, 323] in which whole-brain streamline reconstruction is forced to match the diffusion imaging data, ensuring that the streamline density in each voxel is more reflective of the underlying biological fiber density at that location. If the streamlines approaching any surface of the WMGM boundary have an appropriate spatial density distribution, the gyral bias should disappear [296]. While these methods have been shown to result in more accurate streamline quantification in simulation, phantom, and *in vivo* studies, they have not been validated against histologically defined fiber densities. Results from these techniques, and future tracking strategies, can be compared to our histological results to ensure plausible connectivity measures that are anatomically meaningful.

Finally, although this observed bias causes both false positive (overestimation of fiber termination on gyri) and false negative (underestimation on sulci) connectivity measures, it may not present a significant issue in studies of the human connectome. Because many connectome analyses study regional differences in connectivity at the scale of the entire gyral blade, biases in connection patterns and subsequent graph theoretical measures may be mitigated by coarse parcellation schemes. For example, a parcellation scheme based on gyral-based regions of interest [306], or a relatively low number of regions (~30-70) [307, 308] will probably be less affected by gyral bias than a scheme with ~1000 cortical nodes [66].

### *Sources of Bias – seeding, curvature, partial volume effects, and fiber propagation*

Overall, it appears that the observation that streamlines are denser in gyral crowns than along the sulcal banks may be influenced by a variety of factors. The dominant source of gyral bias is the over-representation of longer fibers due to whole brain and white matter seeding. We show that these long and medium length fibers tend to terminate on gyral crowns, and contribute most to the bias (Figure 8.6). Importantly, scaling the connectivity profile by the inverse fiber length does not eliminate the observed gyral bias.  While this empirical normalization does reduce the gyral bias relative to histology, applying this scaling de-emphasizes almost all neighborhood and long association pathways, as well as all commissural fibers – fibers which form important components of the brains connectome. While seeding from the WMGM boundary partially alleviates this problem (Figure 8.4), there still exists a bias towards the gyral crown in many gyral blades (Figure 8.3), with an average 2x higher connectivity at the crowns that walls. It is important to note that because scaling by inverse fiber length is specifically intended to compensate for homogenous white matter seeding, the application of this metric (although it reduces bias) is not appropriate with WMGM seeding. With DTI tractography, no combination of seeding and subsequent scaling matches the profiles obtained with histological analysis.

Our analysis of myelin-stained sections showed a higher overall curvature of fibers at the sulcal wall compared to the relatively low curvature at the crowns (Figure 8.6). We hypothesized that a higher curvature threshold would allow more streamlines to enter the cortex, resulting in a reduced gyral bias. However, we found that the curvature threshold did not affect the overall bias (Figure 8.7), although it almost certainly does affect anatomical accuracy (which we did not assess). Analysis of individual gyral blades (Figure 8.6, G and H) shows that myelinated axons can curve by as much as 50 degrees per voxel (400um in this dataset) as they enter the gray matter. This means that (assuming perfect orientation estimates), the curvature threshold should be set to at least 50 degrees, and likely even higher with lower resolution datasets.

Partial volume effects due to sub-cortical white matter could cause a bias in orientation estimates along the WMGM boundary to point towards the gyral crown, which would result in a gyral bias in subsequent tractography [108]. Our validation of orientation information on a voxel-by-voxel basis shows that there is a slight propensity for the estimated orientations to be biased towards the gyral crown (by a median value of just 2.2 degrees). This is observed in data acquired at 400um isotropic resolution, and is likely to be even worse in human datasets at 2+mm voxel sizes.

Finally, in the case of a local reconstruction algorithm that is able to reconstruct complex fiber geometries, biases could result due to assumptions inherent in the propagation method of choice. For example, high angular resolution diffusion imaging techniques are able to resolve multiple fiber orientations along the WMGM boundary (see Figure 8.10), in agreement with histology (see [293]). However, most tracking algorithms will choose to follow the path with least angular deviation, rather than make the sharp turns necessary to exit the white matter (even if the curvature threshold allows for it). This explains, at least partially, why a gyral bias is still observed in Figure 8.11, where we have chosen to use CSD for local reconstruction. Similar difficulties of fiber tracks reaching certain cortical areas have been previously documented in the macaque brain [107]. Using dMRI from high resolution ex vivo specimens, Reveley et al. find that a large portion of the cortical surface is inaccessible to fiber tractography. They attribute these results to dense sheets of white matter axons parallel to the WMGM boundary and just beneath the cortex (for example, the U-fibers seen in our Figure 8.10), which inhibit appropriate cortical termination. Even if dMRI is able to detect multiple fiber populations in these superficial white matter bundles (Figure 8.10), the tracking algorithm is unlikely to follow the correct orientation, which may have not only a larger deviation angle, but a smaller volume fraction component in that voxel. The large areas of the cortex inaccessible to tracking are also visible in our data (see Figure 8.5, dashed arrow), and lie predominantly in sulci. Here, we find that the gyral bias is not only caused by inter-voxel (superficial white matter bundles) and intra-voxel (crossing fibers) WM geometries, but is modulated by seeding and stopping strategies, as well as subsequent track weighting and scaling strategies.

*Resolution*

Because the dimensions of the dMRI voxel are orders of magnitude larger than the structures the technique aims to trace (2-3mm vs 1-20um, respectively), image resolution is a clear limitation when it comes to brain connectivity studies [201]. Thus, it is advantageous to increase the spatial resolution (at the expense of SNR) as much as possible in order to minimize the partial volume effects of crossing or bending fibers, and, hopefully, better identify white matter insertion points into the cortex. Results from the Human Connectome Project [282, 324, 325], and other studies pushing the current resolution limits of dMRI [299, 326], including ex vivo imaging [113, 184], show promise in more accurately tracking white matter pathways into the cortex.

The results for M2 in our studies seems contradictory (Figure 8.9), where the gyral bias becomes worse as voxel size decreases. This could have two potential explanations. First, is the over-representation of large white matter tracks (as previously described), which are now seeded more frequently due to smaller voxel volumes. Second, the larger voxel size may cause the fibers within the cortex to have an increased influence on fiber orientations sampled in the WM. This can be due to both partial volume effects between WM and GM, and due to interpolation of orientation information during the tracking process itself. Because the cortical fiber orientations are largely tangential to the WMGM boundary (see Figure 8.7), the estimated fiber orientations in larger voxels may be rotated towards the cortex, causing streamlines entering gyral blades to exit the WM along the sulcal bank before they reach the crowns. It is interesting that M1 does not show share the same trend, even though it will also be affected by homogenous WM seeding. The only difference between M1 and M2 is the inclusion of the GM as a seed region for M1. This suggests that a large source of the bias comes from seeding in the cortex itself. For example, seeds placed in the sulcal wall or fundi may only propagate a few voxels before encountering orthogonal fibers of the underlying WM and terminate propagation due to excessive curvature. Because this propagation is (at most) the length of the cortex, these fibers often do not meet the minimum length threshold. In contrast, fibers seeded from the crown can easily propagate into the deep WM (see Figure 8.5). Both contrasting effects on gyral bias are, in part, partially alleviated with WMGM boundary seeding (Figure 8.9).

### *Histology*

This study is important also from a purely histological perspective. The (non)uniformity of the cortex has implications for evolution, cortical organization, connectional architecture, and cerebral development or morphology. Rather than a structurally uniform cortex [292, 327, 328], it has recently been shown that there is variation of neuronal density both across species [111], and within-species across major cortical areas [111, 329, 330]. Here, we show that the density of axons entering (or leaving) the white matter actually varies even within-gyrus, from gyral crown to sulcal walls. Using a similar parcellation scheme based on convexity, Hilgetag and Barbas [331] found an increase in neuron number in the deep layers (cortical layers V and VI) of the gyrus compared to the same layers of the sulcal and intermediate (sulcal banks) regions, results that are in agreement with our studies. Because the architectural connections of cortical areas are influenced by their location within the gyral blade, the potential exists for future parcellation schemes to further distinguish cortical areas based on structural connectivity.

### *Study Limitations*

There are a number of potential limitations to this study. The most significant is the method for counting histological fibers crossing the WMGM boundary – if the boundary is too deep into white matter, the estimated density would be too high, and too shallow a boundary would make the fiber count too low. To limit errors in fiber counting, we’ve made these measurements across the entire gyral blade in each section, as well as across multiple independent sections (>4) per region of interest. Further, it can be seen (Figure 8.3) that the variability in these histological density measurements is much less than that estimated from dMRI fiber tracking. Another major limitation is the 2D nature of the histological sections. Recent work has extended histological analysis to 3D [115, 136, 199], however, analysis is limited to small fields-of-view, and characterization of multiple whole slices in 3D is a significant technological challenge. In addition, because we are only staining and imaging myelin, our histology is not sensitive to non-myelinated tissue structures (including unmyelinated axons, dendrites, and glial cells) that may contribute to diffusion anisotropy, particularly in the cortex [115]. In addition, our measurements are simply quantifying the agreement (or lack thereof) between the histological "myelinated axon count" and diffusion tractography "fiber count", with the common assumption that streamline density should be in some way related to the number or density (or some measure of connectivity) of axons (in our case, myelinated axons).

Finally, our histological "fiber density" is a simple count of the axons entering the cortex. We do not attempt to determine cortico-cortical connectivity in this study, meaning we have no knowledge of the specific fiber pathway followed other than the fact that the fiber left the white matter and entered the gray matter. The myelinated axons in our study cannot be related or attributed to a specific tract system. A full characterization of gyral-gyral, gyral-sulcal, and sulcal-sulcal connectivity would lend significant support (or opposition) to the various morphogenesis and morphological theories of cortical structure [106, 331]. Similarly, it would be of interest to be able to determine where in the gyral blade those fibers entering the cortex came from. For example, do fibers that form the center of the gyral "stalk" tend to enter the crowns, while those near the periphery "peel-off" from the stalk as they enter the cortex [108]? Visual inspection of myelin-stained or neuron-stained histological slices suggests this is the case in at least some regions. However, a full characterization of this organization would require tracing individual fibers throughout the entire gyral blade, and could enable the development of future tracking algorithms that use anatomical priors to enhance the accuracy of these techniques. We not aware of any studies quantifying the distribution of labeled fibers which could determine whether long- or short-range fibers are expected to terminate preferentially on the crown or walls, nor that determine specific fiber systems that are affected by this bias.

## 8.5 Conclusion

In this study, using histology as a tool for validation, we have shown that there is a bias of fiber tracking algorithms to terminate on gyral crowns. We first show that many gyral regions in the brain have denser histological fiber connectivity than do neighboring sulcal walls. Next, we find that DTI fiber tracking algorithms are significantly biased towards the gyral crowns in many gyral blades. The source of this gyral bias is most heavily dependent on seeding strategy and subsequent connectivity quantification (i.e., scaling). We also find that myelinated fibers curve more at sulcal walls than they do at crowns. However, the curvature threshold of DTI tracking algorithms does not have a significant effect on the bias. A comparison with histological fiber trajectories shows that the underlying dMRI estimated fiber orientations are also biased towards gyral crowns. We then show that this tractography gyral bias still persists with more advanced diffusion models and tracking algorithms, and over a wide range of MRI acquisition resolutions. It is important to keep these limitations in mind when interpreting dMRI connectivity studies. Tracking algorithms may be able to incorporate this anatomical information when constructing streamline trajectories and determining appropriate seeding and stopping criteria. Future dMRI studies may need to incorporate anatomical priors and constraints, or non-dMRI information, to accurately determine the structural connectivity of the brain.

# CHAPTER 9: DISCUSSION, CONCLUSIONS, AND FUTURE WORK

## Summary

The validation of quantitative diffusion MRI and diffusion fiber tractography is fundamental to the implementation of these techniques as useful biomedical tools. This dissertation focuses on validating tractography by comparing diffusion MRI results directly to histological data on multiple spatial scales – the microstructural scale of tissues, the scale of MRI voxels, and the macrostructural scale describing brain connectivity. In Chapter 4, we present a web-based digital atlas of the squirrel monkey brain, which serves as a valuable resource of validation data and methods, both of which are utilized extensively throughout the thesis. Chapter 5 then motivates subsequent chapters by showing that the most commonly utilized diffusion model, diffusion tensor imaging, is inadequate in a large percentage of the brain, which suggests that the use of alternative, more sophisticated, reconstruction methods are necessary for anatomical fidelity. Chapters 6 and 7 then aim to fully validate a large number of experimental methods developed to assess intra-voxel fiber orientation information. Finally, chapter 8 investigates the anatomical accuracy of fiber tractography, and confirms biases associated with both brain anatomy and tractography methodological choices. In this chapter, we summarize the main results of each contribution and potential for future research directions.

## 9.1 Squirrel Monkey Brain Atlas

### 9.1.1 Summary

Neuroscience investigations into the organization of nerve pathways in the brain frequently make use of non-human primates, which allow access to a “gold standard” upon which many of the in vivo experiments for humans are designed and evaluated against. The work in this thesis utilizes the squirrel monkey brain as a tool for validation. In the neuroimaging community, atlases serve as valuable resources for anatomical, physiological, and functional studies of the brain, however, no digital atlas currently exists for the squirrel monkey brain. Because of this, one of our aims was to create a web based squirrel monkey brain atlas and database, both to serve as a foundation for our own validation studies, and for dissemination of validation data to others in the neuroimaging community.

### 9.1.2 Main Contributions/Results

1. The first combined MRI and histology maps of the squirrel monkey brain are made available to the neuroimaging community. The atlas data acquisition includes both in vivo and ex vivo MRI scans, tracer injections, and a variety of histological stains. In addition, a variety of post-processing results are included.
2. A difficulty facing many validation studies is that experts in image analysis rarely have access to histological and MRI data of the same animal. We remove this impediment by providing both light microscopy and diffusion data, as well as an interface to our MRI and histology image archive, and tools for navigating, viewing, analyzing, and downloading the data.
3. All imaging data are aligned using a multi-step registration framework, facilitating comparisons of multiple imaging modalities. This framework is utilized throughout this work to make voxel-wise comparisons between light microscopy and quantitative diffusion metrics.

### 9.1.2 Future Work

The Vanderbilt University Institute of Imaging Science is continually scanning and employing the squirrel monkey in research on the central nervous system. As additional data are acquired, it will frequently be added to the current image archive. This could include more comprehensive diffusion MRI protocols, expanding our current histology or MRI contrasts (BOLD, susceptibility, myelin volume fraction imaging, etc.), or imaging modalities (i.e., confocal data).

The atlas system could be leveraged by external investigators to answer questions beyond the current work. First are quantitative tests of the accuracy of novel dMRI analysis and tractography algorithms. However, other possibilities include quantitative validation of fMRI connectivity, validation methods for parcellating the thalamus based on dMRI connectivity, and comparison of connectivity patterns between primate species (squirrel monkey, macaque, human).

In addition, our diffusion data in combination with our tracer injections are currently being used for a diffusion MRI community challenge for the 2018 IEEE International Symposium of Biomedical Engineering. These publicly organized challenges provide unique opportunities for research communities to fairly compare algorithms in an unbiased format, resulting in quantitative measures of the reliability and limitations of competing approaches. For the first time, the diffusion challenge will use histological data (from our squirrel monkey atlas), with the aim being to most accurately replicate the anatomical connections identified by the histological tracer. These challenges should lead us to conclusions regarding tracking sensitivity and specificity, as well as potential reasons for tractography failures or misalignments.

## 9.2 Crossing Fibers

### 9.2.1 Summary

It has long been recognized that the diffusion tensor model is inappropriate to characterize complex fiber architecture, for example voxels with two crossing fiber populations, causing misleading and erroneous tensor measures. There is much debate about the impact of this problem, and the best approaches to solve and/or mitigate these issues. In this study, we ask if we can mitigate this problem by increasing spatial resolution, or whether future neuroscientists and researchers should focus on more advanced acquisitions or modeling techniques. We approach the problem using ex vivo MRI of the macaque brain, followed by histological analysis of the same specimen to validate the measurements, as well as extend the analysis to resolutions currently not achievable even on pre-clinical systems.

### 9.2.2 Main Contributions/Results

1. Using both diffusion MRI and subsequent histology, we find that crossing fibers are prevalent throughout the macaque brain. In addition, we find that the fraction of voxels with crossing fibers varies with resolution in an unintuitive way – the percentage of crossing fibers increases as the resolution increases.
2. Crossing fibers are still prevalent even at scales of 10’s of microns, a distance smaller than bundles of white matter fiber tracts. Thus, technological advances that may lead to increased spatial resolution still will not “solve” this crossing fiber problem. Rather, because complex fiber

configurations will always exist in real datasets, it is critical to focus on appropriate tissue models for describing fiber geometry.

### 9.3.3 Future Work

This work has several results that should help to prioritize future endeavors to improve fiber tractography. First and foremost, the diffusion tensor, and all derived quantitative indices, will likely result in un-interpretable results in a large portion of the brain, even with high quality datasets. Because of this, higher order models of diffusion become crucial to the successful implementation of tractography, and future tractography studies should focus on implementing these high angular resolution models developed to resolve crossing fibers. This motivates the need to assess, understand, and validate these models, an endeavor undertaken in subsequent chapters.

## 9.3 Validating Fiber Orientation Distributions

### 9.3.1 Summary

The ability of diffusion imaging to accurately assess fiber orientation within each voxel is of paramount importance for valid reconstruction of fiber pathways. As such, it is important to check and quantify the match between the diffusion estimates of fiber orientation information and the true structural orientation of fibers. In this work, we validate the first step of the tracking process: the voxel-wise inference of fiber orientation from diffusion data.

### 9.3.2 Main Contributions/Results

1. We present the first 3D histological validation of fiber orientation distributions, as well as the first histological validation to compare a variety of the most common and cutting-edge algorithms. We do this using high-resolution microscopy data, collected from the same specimen on which diffusion data were acquired. Histological validation has the advantage of containing both the structural complexity and the true diffusion processes (and thus signal generation) of the central nervous system.
2. All high angular resolution diffusion reconstruction methods describe the overall continuous angular structure of the fiber orientation distribution well, however, no method is consistently successful at extracting discrete measures of number of fibers and orientations of fiber

orientation distribution peaks. Thus, care must be taken when interpreting diffusion results, particularly with respect to estimates of number of fibers and fiber orientation based on local maxima of the FOD.

3. No model outperformed others in every quality criteria or experimental condition, and there usually involves some tradeoff in measures of accuracy, sensitivity, and specificity. In addition, the models are particularly robust to the number of diffusion directions, with acquisitions commonly implemented for DTI (containing as few as 20-30 directions) retaining overall moderate to high correlations with the histological fiber orientations.

4. Information extracted from the diffusion signal contains more information than just the number and directions of peaks of the fiber distribution. Specifically, the width of the distribution for many methods is correlated with the histological dispersion of fibers (i.e., the orientation dispersion), a metric that may prove useful for increasing fiber tracking accuracy or specificity for pathologies.

### 9.3.3 Future Work

The combination of high resolution confocal data and multi-shell high angular resolution ex vivo diffusion data is rich with information. A large number of both diffusion validation and tissue microstructure/modeling studies can be performed. For example, incorporating this data into future releases of the brain atlas will allow other researchers to try their own reconstruction algorithms and compare their results to the current state of modeling. In addition, approaches such as machine learning can be studied to attempt to “learn” the relationship between the diffusion signal and resulting fiber distribution. For example, given the diffusion MRI signal and the ground truth histologically defined FOD, if deep networks can learn a better relationship between the signal and distribution than the best current models, it would suggest there is unutilized information remaining in the diffusion signal that could be exploited by clever modeling or interpretation. We expect that these confocal data will be utilized heavily in the future to inform diffusion reconstruction models.

## 9.4 Validating Tractography

### 9.4.1 Summary

While accurate reconstruction of the fiber orientation distribution is an essential step in the tractography process, it is not sufficient in itself to guarantee anatomically accurate fiber pathways. Here, we investigate whether the fiber tractography count, or streamline density, across different locations in the brain accurately reflects that seen in corresponding histological sections. Specifically, this work focuses on one aspect of diffusion tractography, a propensity for streamlines to end at gyral crowns, rather than sulcal walls or fundi. A bias, that if present, could significantly influence our interpretation of fiber tractography streamline counts.

### 9.4.2 Main Contributions/Results

1. This is the first study to confirm the presence of a gyral bias in diffusion tractography compared to histological measures of fiber density. We find that there is a statistically significant bias for streamlines to terminate on gyral crowns, relative to sulcal banks. This gyral bias occurs in many gyral blades across the brain, for a range of tracking algorithms and reconstruction methods, and in very high quality, high resolution datasets.
2. A simple "count" of streamlines connecting two regions is an inaccurate measure of "connection strength", and does not represent the histological fiber densities in these regions. No subsequent quantification strategy common in the literature (normalizing by track length, region volume, etc.) yielded a connectivity measure that was not biased relative to histology.
3. From a histological perspective, this is the first work to characterize both fiber curvature at the cortex and fiber density along the cortex. We find that fibers curve when entering sulcal regions more than they do in gyral crowns. In addition, rather than a structurally uniform cortex, we show that the density of axons entering (or leaving) the white matter actually varies across and within gyri.
4. Sources of this anatomical bias include seeding strategy, fiber curvatures, partial volume effects, and fiber propagation logic. Seeding from the white matter/ gray matter boundary partially alleviates the anatomical bias, relative to other seeding strategies. Curvature thresholds of at least 50 degrees per voxel are recommended to correctly branch into the sulcal

cortical regions. Partial volume effects cause a small bias in orientation estimates towards the crown, an effect which will be strengthened on human in vivo datasets. Finally, even if fiber reconstruction algorithms adequately capture fiber curvatures and crossings, many tractography streamlines will incorrectly choose the next propagation step based on assumptions and simplifications in the tracking algorithms itself.

### 9.4.3 Future Work

There is tremendous potential for future work with data in this atlas, both regarding the gyral bias, and tractography validation in general. There is a class of emerging tractography techniques which force the reconstructed streamlines to match the diffusion data, ensuring streamline density along the gyrus is more reflective of the underlying biology. This, and future generations of tractography algorithms, including those that may be anatomically-informed, should be implemented on our data, and validated using our histological techniques.

There is still much left to do for validating tractography algorithms. Every step in the tracking process – including seeding, track propagation, and stopping criteria - influences the final results of estimated pathways. For example, varying tracking parameters such as curvature limits and path step length, in addition to potential integration of neighboring information, will likely result in differing estimates of white matter pathways. The effects of each of these components on the anatomical accuracy of tractography needs to be studied in order to allow the limitations, in terms of track specificity, sensitivity, and precision, to be understood. Because the incidence of erroneous connections in tractography is largely unknown, future work should probe whether fiber tractography can correctly reflect the anatomical connections in the brain. To do this, one could utilize the diffusion MRI and histological chemical tracer data from the same specimens – all data currently available in our atlas - in order to quantify the anatomical accuracy of diffusion fiber tractography, as well as investigate the systematic effects of existing tracking algorithms and acquisition parameters on tracking specificity and sensitivity. The use of histology is the only tool which offers both high sensitivity to be able to delineate tracks of interest, and the high complexity seen in the tissue of interest – the brain.

## 9.5 Concluding Remarks

Diffusion MRI fiber tractography has the potential to expand our knowledge and understanding of the fiber pathways in both healthy and diseased brains, aid diagnosis of patients with brain injury and disease, and provide insight into basic neuroscience. However, the application of these methods is racing ahead of our ability to understand the data, their limitations and untapped potential. For these techniques to be used in a safe, accurate, and effective manner, we must be sure of their efficacy. To improve the accuracy of diffusion MRI studies, and our ability to understand these techniques, this thesis compares diffusion data directly to histological data. This work highlights some of the leading causes of error of these techniques, on both the tissue microstructure scale to that of brain-scale networks. In addition, we hope that the research described in this dissertation, and methodology and dissemination of validation data, will increase the understanding of the relationship between the diffusion MRI signal and the neuronal organization, tissue properties, and structural connectivity of the brain.

# REFERENCES

1. JC R. Das Balken-System oder die Hirnschenkel-Organisation im groBen Gehirn. Archiv Fur die Physiologie. 1809;(9):172-95.

2. K B. Vom Baue und Leben des Gehirns. Leipzig: In der Dyk'schen Buchhandlung1819.

3. Le Bihan D, Breton E, Lallemand D, Grenier P, Cabanis E, Laval-Jeantet M. MR imaging of intravoxel incoherent motions: application to diffusion and perfusion in neurologic disorders. Radiology. 1986;161(2):401-7. doi: 10.1148/radiology.161.2.3763909. PubMed PMID: 3763909.

4. Mori S, Zhang J. Principles of diffusion tensor imaging and its applications to basic neuroscience research. Neuron. 2006;51(5):527-39. doi: 10.1016/j.neuron.2006.08.012. PubMed PMID: 16950152.

5. Miller KL. Diffusion Acquisition: Pushing the Boundaries. In: Johansen-Berg H, Behrens TEJ, editors. Diffusion MRI : from quantitative measurement to in-vivo neuroanatomy. 2nd ed. London, UK ; Waltham, MA: Elsevier/Academic Press; 2014. p. 35-61.

6. Alexander DC. Multiple-Fiber Reconstruction Algorithms for Diffusion MRI. Annals of the New York Academy of Sciences. 2005;1064(1):113-33. doi: 10.1196/annals.1340.018.

7. Behrens TS, S.N.; Jbabdi, S.;. MR Diffusion Tractography. In: Johansen-Berg H, Behrens TEJ, editors. Diffusion MRI : from quantitative measurement to in-vivo neuroanatomy. 2nd ed. London, UK ; Waltham, MA: Elsevier/Academic Press; 2014. p. 429-52.

8. Mori S, van Zijl PCM. Fiber tracking: principles and strategies – a technical review. NMR in biomedicine. 2002;15(7-8):468-80. doi: 10.1002/nbm.781.

9. Warach S, Boska M, Welch KM. Pitfalls and potential of clinical diffusion-weighted MR imaging in acute stroke. Stroke; a journal of cerebral circulation. 1997;28(3):481-2. PubMed PMID: 9056599.

10. Warach S, Dashe JF, Edelman RR. Clinical outcome in ischemic stroke predicted by early diffusion-weighted and perfusion magnetic resonance imaging: a preliminary analysis. J Cereb Blood Flow Metab. 1996;16(1):53-9. doi: 10.1097/00004647-199601000-00006. PubMed PMID: 8530555.

11. Gonzalez RG, Schaefer PW, Buonanno FS, Schwamm LH, Budzik RF, Rordorf G, et al. Diffusion-weighted MR imaging: diagnostic accuracy in patients imaged within 6 hours of stroke symptom onset. Radiology. 1999;210(1):155-62. doi: 10.1148/radiology.210.1.r99ja02155. PubMed PMID: 9885601.

12. Guo Y, Cai YQ, Cai ZL, Gao YG, An NY, Ma L, et al. Differentiation of clinically benign and malignant breast lesions using diffusion-weighted imaging. Journal of magnetic resonance imaging : JMRI. 2002;16(2):172-8. doi: 10.1002/jmri.10140. PubMed PMID: 12203765.

13. Turkbey B, Shah VP, Pang Y, Bernardo M, Xu S, Kruecker J, et al. Is apparent diffusion coefficient associated with clinical risk scores for prostate cancers that are visible on 3-T MR images? Radiology. 2011;258(2):488-95. doi: 10.1148/radiol.10100667. PubMed PMID: 21177390; PubMed Central PMCID: PMCPMC3029887.

14. Cui Y, Zhang XP, Sun YS, Tang L, Shen L. Apparent diffusion coefficient: potential imaging biomarker for prediction and early detection of response to chemotherapy in hepatic metastases. Radiology. 2008;248(3):894-900. doi: 10.1148/radiol.2483071407. PubMed PMID: 18710982.

15. Le Bihan D, Johansen-Berg H. Diffusion MRI at 25: exploring brain tissue structure and function. NeuroImage. 2012;61(2):324-41. doi: 10.1016/j.neuroimage.2011.11.006. PubMed PMID: 22120012; PubMed Central PMCID: PMCPMC3683822.

16. Fick A. On Liquid Diffusion (Reprinted from the London, Edinburgh, and Dublin Philosophical Magazine and Journal of Science, Vol 10, Pg 30, 1855). J Membrane Sci. 1995;100(1):33-8. doi: Doi 10.1016/0376-7388(94)00230-V. PubMed PMID: WOS:A1995QR54400009.

17. Einstein A. On the motion required by the molecular kinetic theory of heat of small particles suspended in a stationary liquid. Annalen der Physik. 1905;17(549).

18. Beaulieu C. The basis of anisotropic water diffusion in the nervous system - a technical review. NMR in biomedicine. 2002;15(7-8):435-55. Epub 2002/12/19. doi: 10.1002/nbm.782. PubMed PMID: 12489094.

19. Hahn EL. Spin Echoes. Phys Rev. 1950;80(4):580-94. doi: DOI 10.1103/PhysRev.80.580. PubMed PMID: WOS:A1950UB34300017.

20. Carr HY, Purcell EM. Effects of Diffusion on Free Precession in Nuclear Magnetic Resonance Experiments. Phys Rev. 1954;94(3):630-8. doi: DOI 10.1103/PhysRev.94.630. PubMed PMID: WOS:A1954UB48000018.

21. Torrey HC. Bloch Equations with Diffusion Terms. Phys Rev. 1956;104(3):563-5. doi: DOI 10.1103/PhysRev.104.563. PubMed PMID: WOS:A1956WK97700002.

22. Stejskal EO, Tanner JE. Spin Diffusion Measurements: Spin Echoes in the Presence of a Time-Dependent Field Gradient. Journal of Chemical Physics. 1965;42(1):288-+. doi: Doi 10.1063/1.1695690. PubMed PMID: WOS:A19656099500051.

23. Callaghan PT. Physics of Diffusion. In: Jones DK, editor. Diffusion MRI : Theory, Methods, and Applications. 2nd ed. New York, New York: Oxford University Press; 2012. p. 45-56.

24. Wedeen VJ, Hagmann P, Tseng WY, Reese TG, Weisskoff RM. Mapping complex tissue architecture with diffusion spectrum magnetic resonance imaging. Magnetic resonance in medicine : official journal of the Society of Magnetic Resonance in Medicine / Society of Magnetic Resonance in Medicine. 2005;54(6):1377-86. Epub 2005/10/26. doi: 10.1002/mrm.20642. PubMed PMID: 16247738.

25. Johansen-Berg H, Behrens TEJ. Diffusion MRI : from quantitative measurement to in-vivo neuroanatomy. 2nd ed. London, UK ; Waltham, MA: Elsevier/Academic Press; 2014. xii, 614 p. p.

26. Sykova E, Nicholson C. Diffusion in brain extracellular space. Physiol Rev. 2008;88(4):1277-340. doi: 10.1152/physrev.00027.2007. PubMed PMID: 18923183; PubMed Central PMCID: PMCPMC2785730.

27. Shepherd TM, Thelwall PE, Stanisz GJ, Blackband SJ. Aldehyde fixative solutions alter the water relaxation and diffusion properties of nervous tissue. Magnetic resonance in medicine : official journal of the Society of Magnetic Resonance in Medicine / Society of Magnetic Resonance in Medicine. 2009;62(1):26-34. Epub 2009/04/09. doi: 10.1002/mrm.21977. PubMed PMID: 19353660; PubMed Central PMCID: PMC3188415.

28. Moseley ME, Kucharczyk J, Mintorovitch J, Cohen Y, Kurhanewicz J, Derugin N, et al. Diffusion-weighted MR imaging of acute stroke: correlation with T2-weighted and magnetic susceptibility-enhanced MR imaging in cats. AJNR American journal of neuroradiology. 1990;11(3):423-9. PubMed PMID: 2161612.

29. Wedeen VJ, Wang RP, Schmahmann JD, Benner T, Tseng WYI, Dai G, et al. Diffusion spectrum magnetic resonance imaging (DSI) tractography of crossing fibers. NeuroImage. 2008;41(4):1267-77. doi: http://dx.doi.org/10.1016/j.neuroimage.2008.03.036.

30. Basser PJ, Mattiello J, LeBihan D. Estimation of the effective self-diffusion tensor from the NMR spin echo. Journal of magnetic resonance Series B. 1994;103(3):247-54. PubMed PMID: 8019776.

31. Basser PJ, Mattiello J, LeBihan D. MR diffusion tensor spectroscopy and imaging. Biophys J. 1994;66(1):259-67. doi: 10.1016/S0006-3495(94)80775-1. PubMed PMID: 8130344; PubMed Central PMCID: PMCPMC1275686.

32. Jones DK, Cercignani M. Twenty-five pitfalls in the analysis of diffusion MRI data. NMR in biomedicine. 2010;23(7):803-20. doi: 10.1002/nbm.1543. PubMed PMID: 20886566.

33. Alexander DC, Barker GJ, Arridge SR. Detection and modeling of non-Gaussian apparent diffusion coefficient profiles in human brain data. Magnetic resonance in medicine : official journal of the Society of Magnetic Resonance in Medicine / Society of Magnetic Resonance in Medicine. 2002;48(2):331-40. Epub 2002/09/05. doi: 10.1002/mrm.10209. PubMed PMID: 12210942.

34. Behrens TE, Berg HJ, Jbabdi S, Rushworth MF, Woolrich MW. Probabilistic diffusion tractography with multiple fibre orientations: What can we gain? NeuroImage. 2007;34(1):144-55. doi: 10.1016/j.neuroimage.2006.09.018. PubMed PMID: 17070705.

35. Tuch DS. Q-ball imaging. Magnetic resonance in medicine : official journal of the Society of Magnetic Resonance in Medicine / Society of Magnetic Resonance in Medicine. 2004;52(6):1358-72. Epub 2004/11/25. doi: 10.1002/mrm.20279. PubMed PMID: 15562495.

36. Descoteaux M, Angelino E, Fitzgibbons S, Deriche R. Regularized, fast, and robust analytical Q-ball imaging. Magnetic resonance in medicine : official journal of the Society of Magnetic Resonance in Medicine / Society of Magnetic Resonance in Medicine. 2007;58(3):497-510. Epub 2007/09/01. doi: 10.1002/mrm.21277. PubMed PMID: 17763358.

37. Aganj I, Lenglet C, Sapiro G, Yacoub E, Ugurbil K, Harel N. Reconstruction of the orientation distribution function in single- and multiple-shell q-ball imaging within constant solid angle. Magnetic resonance in medicine : official journal of the Society of Magnetic Resonance in Medicine / Society of Magnetic Resonance in Medicine. 2010;64(2):554-66. doi: 10.1002/mrm.22365. PubMed PMID: 20535807; PubMed Central PMCID: PMCPMC2911516.

38. Ozarslan E, Shepherd TM, Vemuri BC, Blackband SJ, Mareci TH. Resolution of complex tissue microarchitecture using the diffusion orientation transform (DOT). NeuroImage. 2006;31(3):1086-103. doi: 10.1016/j.neuroimage.2006.01.024. PubMed PMID: 16546404.

39. Canales-Rodriguez EJ, Lin CP, Iturria-Medina Y, Yeh CH, Cho KH, Melie-Garcia L. Diffusion orientation transform revisited. NeuroImage. 2010;49(2):1326-39. doi: 10.1016/j.neuroimage.2009.09.067. PubMed PMID: 19815083.

40. Jansons KM, Alexander DC. Persistent Angular Structure: new insights from diffusion MRI data. Inf Process Med Imaging. 2003;18:672-83. PubMed PMID: 15344497.

41. Anderson AW. Measurement of fiber orientation distributions using high angular resolution diffusion imaging. Magnetic resonance in medicine : official journal of the Society of Magnetic Resonance in Medicine / Society of Magnetic Resonance in Medicine. 2005;54(5):1194-206. Epub 2005/09/15. doi: 10.1002/mrm.20667. PubMed PMID: 16161109.

42. Anderson AW, Ding Z, editors. Sub-voxel measurement of fiber orientation using high angular resolution diffusion tensor imaging. Tenth Scientific Meeting of the International Society for Magnetic Resonance in Medicine; 2002.

43. Tournier JD, Calamante F, Gadian DG, Connelly A. Direct estimation of the fiber orientation density function from diffusion-weighted MRI data using spherical deconvolution. NeuroImage. 2004;23(3):1176-85. doi: 10.1016/j.neuroimage.2004.07.037. PubMed PMID: 15528117.

44. Dell'acqua F, Scifo P, Rizzo G, Catani M, Simmons A, Scotti G, et al. A modified damped Richardson-Lucy algorithm to reduce isotropic background effects in spherical deconvolution. NeuroImage. 2010;49(2):1446-58. doi: 10.1016/j.neuroimage.2009.09.033. PubMed PMID: 19781650.

45. Tournier JD, Calamante F, Connelly A. Robust determination of the fibre orientation distribution in diffusion MRI: non-negativity constrained super-resolved spherical deconvolution. NeuroImage. 2007;35(4):1459-72. doi: 10.1016/j.neuroimage.2007.02.016. PubMed PMID: 17379540.

46. Szafer A, Zhong J, Anderson AW, Gore JC. Diffusion-weighted imaging in tissues: theoretical models. NMR in biomedicine. 1995;8(7-8):289-96. PubMed PMID: 8739267.

47. Szafer A, Zhong J, Gore JC. Theoretical model for water diffusion in tissues. Magnetic resonance in medicine : official journal of the Society of Magnetic Resonance in Medicine / Society of Magnetic Resonance in Medicine. 1995;33(5):697-712. PubMed PMID: 7596275.

48. Assaf Y, Blumenfeld-Katzir T, Yovel Y, Basser PJ. AxCaliber: a method for measuring axon diameter distribution from diffusion MRI. Magnetic resonance in medicine : official journal of the Society of Magnetic Resonance in Medicine / Society of Magnetic Resonance in Medicine. 2008;59(6):1347-54. doi: 10.1002/mrm.21577. PubMed PMID: 18506799; PubMed Central PMCID: PMCPMC4667732.

49. Assaf Y, Basser PJ. Composite hindered and restricted model of diffusion (CHARMED) MR imaging of the human brain. NeuroImage. 2005;27(1):48-58. doi: 10.1016/j.neuroimage.2005.03.042. PubMed PMID: 15979342.

50. Sotiropoulos SN, Behrens TE, Jbabdi S. Ball and rackets: Inferring fiber fanning from diffusion-weighted MRI. NeuroImage. 2012;60(2):1412-25. Epub 2012/01/25. doi: 10.1016/j.neuroimage.2012.01.056. PubMed PMID: 22270351; PubMed Central PMCID: PMC3304013.

51. Stanisz GJ, Szafer A, Wright GA, Henkelman RM. An analytical model of restricted diffusion in bovine optic nerve. Magnetic resonance in medicine : official journal of the Society of Magnetic Resonance in Medicine / Society of Magnetic Resonance in Medicine. 1997;37(1):103-11. PubMed PMID: 8978638.

52. Xu J, Li H, Harkins KD, Jiang X, Xie J, Kang H, et al. Mapping mean axon diameter and axonal volume fraction by MRI using temporal diffusion spectroscopy. NeuroImage. 2014;103:10-9. doi: 10.1016/j.neuroimage.2014.09.006. PubMed PMID: 25225002; PubMed Central PMCID: PMCPMC4312203.

53. Alexander DC, Hubbard PL, Hall MG, Moore EA, Ptito M, Parker GJ, et al. Orientationally invariant indices of axon diameter and density from diffusion MRI. NeuroImage. 2010;52(4):1374-89. doi: 10.1016/j.neuroimage.2010.05.043. PubMed PMID: 20580932.

54. Zhang H, Schneider T, Wheeler-Kingshott CA, Alexander DC. NODDI: practical in vivo neurite orientation dispersion and density imaging of the human brain. NeuroImage. 2012;61(4):1000-16. Epub 2012/04/10. doi: 10.1016/j.neuroimage.2012.03.072. PubMed PMID: 22484410.

55. Mori S, Crain BJ, Chacko VP, van Zijl PC. Three-dimensional tracking of axonal projections in the brain by magnetic resonance imaging. Annals of neurology. 1999;45(2):265-9. Epub 1999/02/16. PubMed PMID: 9989633.

56. Basser PJ, Pajevic S, Pierpaoli C, Duda J, Aldroubi A. In vivo fiber tractography using DT-MRI data. Magnetic resonance in medicine : official journal of the Society of Magnetic Resonance in Medicine / Society of Magnetic Resonance in Medicine. 2000;44(4):625-32. PubMed PMID: 11025519.

57. Lazar M, Alexander AL. An error analysis of white matter tractography methods: synthetic diffusion tensor field simulations. NeuroImage. 2003;20(2):1140-53. doi: 10.1016/S1053-8119(03)00277-5. PubMed PMID: 14568483.

58. Tuch DS, Reese TG, Wiegell MR, Wedeen VJ. Diffusion MRI of complex neural architecture. Neuron. 2003;40(5):885-95. PubMed PMID: 14659088.

59. Jeurissen B, Leemans A, Jones DK, Tournier JD, Sijbers J. Probabilistic fiber tracking using the residual bootstrap with constrained spherical deconvolution. Human brain mapping. 2011;32(3):461-79. doi: 10.1002/hbm.21032. PubMed PMID: 21319270.

60. Jones DK. Determining and visualizing uncertainty in estimates of fiber orientation from diffusion tensor MRI. Magnetic resonance in medicine : official journal of the Society of Magnetic Resonance in Medicine / Society of Magnetic Resonance in Medicine. 2003;49(1):7-12. doi: 10.1002/mrm.10331. PubMed PMID: 12509814.

61. Behrens TE, Woolrich MW, Jenkinson M, Johansen-Berg H, Nunes RG, Clare S, et al. Characterization and propagation of uncertainty in diffusion-weighted MR imaging. Magnetic resonance in medicine : official journal of the Society of Magnetic Resonance in Medicine / Society of Magnetic Resonance in Medicine. 2003;50(5):1077-88. doi: 10.1002/mrm.10609. PubMed PMID: 14587019.

62. Kaden E, Knosche TR, Anwander A. Parametric spherical deconvolution: inferring anatomical connectivity using diffusion MR imaging. NeuroImage. 2007;37(2):474-88. doi: 10.1016/j.neuroimage.2007.05.012. PubMed PMID: 17596967.

63. Catani M, Jones DK, ffytche DH. Perisylvian language networks of the human brain. Annals of neurology. 2005;57(1):8-16. doi: 10.1002/ana.20319. PubMed PMID: 15597383.

64. Friederici AD, Bahlmann J, Heim S, Schubotz RI, Anwander A. The brain differentiates human and non-human grammars: functional localization and structural connectivity. Proceedings of the National Academy of Sciences of the United States of America. 2006;103(7):2458-63. doi: 10.1073/pnas.0509389103. PubMed PMID: 16461904; PubMed Central PMCID: PMCPMC1413709.

65. Hagmann P, Cammoun L, Gigandet X, Gerhard S, Grant PE, Wedeen V, et al. MR connectomics: Principles and challenges. J Neurosci Methods. 2010;194(1):34-45. doi: 10.1016/j.jneumeth.2010.01.014. PubMed PMID: 20096730.

66. Hagmann P, Cammoun L, Gigandet X, Meuli R, Honey CJ, Wedeen VJ, et al. Mapping the structural core of human cerebral cortex. PLoS Biol. 2008;6(7):e159. doi: 10.1371/journal.pbio.0060159. PubMed PMID: 18597554; PubMed Central PMCID: PMCPMC2443193.

67. Behrens TE, Johansen-Berg H, Woolrich MW, Smith SM, Wheeler-Kingshott CA, Boulby PA, et al. Non-invasive mapping of connections between human thalamus and cortex using diffusion imaging. Nat Neurosci. 2003;6(7):750-7. doi: 10.1038/nn1075. PubMed PMID: 12808459.

68. Johansen-Berg H, Behrens TE, Sillery E, Ciccarelli O, Thompson AJ, Smith SM, et al. Functional-anatomical validation and individual variation of diffusion tractography-based segmentation of the human thalamus. Cereb Cortex. 2005;15(1):31-9. doi: 10.1093/cercor/bhh105. PubMed PMID: 15238447.

69. Johansen-Berg H, Behrens TE, Robson MD, Drobnjak I, Rushworth MF, Brady JM, et al. Changes in connectivity profiles define functionally distinct regions in human medial frontal cortex. Proceedings of the National Academy of Sciences of the United States of America. 2004;101(36):13335-40. doi: 10.1073/pnas.0403743101. PubMed PMID: 15340158; PubMed Central PMCID: PMCPMC516567.

70. Rollins N, Reyes T, Chia J. Diffusion tensor imaging in lissencephaly. AJNR American journal of neuroradiology. 2005;26(6):1583-6. PubMed PMID: 15956534.

71. Albayram S, Melhem ER, Mori S, Zinreich SJ, Barkovich AJ, Kinsman SL. Holoprosencephaly in children: diffusion tensor MR imaging of white matter tracts of the

brainstem--initial experience. Radiology. 2002;223(3):645-51. doi: 10.1148/radiol.2233011197. PubMed PMID: 12034930.

72. Rollins N. Semilobar holoprosencephaly seen with diffusion tensor imaging and fiber tracking. AJNR American journal of neuroradiology. 2005;26(8):2148-52. PubMed PMID: 16155174.

73. Dudink J, Pieterman K, Leemans A, Kleinnijenhuis M, van Cappellen van Walsum AM, Hoebeek FE. Recent advancements in diffusion MRI for investigating cortical development after preterm birth-potential and pitfalls. Front Hum Neurosci. 2014;8:1066. doi: 10.3389/fnhum.2014.01066. PubMed PMID: 25653607; PubMed Central PMCID: PMCPMC4301014.

74. Estep ME, Smyser CD, Anderson PJ, Ortinau CM, Wallendorf M, Katzman CS, et al. Diffusion tractography and neuromotor outcome in very preterm children with white matter abnormalities. Pediatr Res. 2014;76(1):86-92. doi: 10.1038/pr.2014.45. PubMed PMID: 24713814; PubMed Central PMCID: PMCPMC4062577.

75. Yoshikawa K, Nakata Y, Yamada K, Nakagawa M. Early pathological changes in the parkinsonian brain demonstrated by diffusion tensor MRI. J Neurol Neurosurg Psychiatry. 2004;75(3):481-4. PubMed PMID: 14966170; PubMed Central PMCID: PMCPMC1738942.

76. Reading SA, Yassa MA, Bakker A, Dziorny AC, Gourley LM, Yallapragada V, et al. Regional white matter change in pre-symptomatic Huntington's disease: a diffusion tensor imaging study. Psychiatry research. 2005;140(1):55-62. doi: 10.1016/j.pscychresns.2005.05.011. PubMed PMID: 16199141.

77. Frings L, Yew B, Flanagan E, Lam BY, Hull M, Huppertz HJ, et al. Longitudinal grey and white matter changes in frontotemporal dementia and Alzheimer's disease. PloS one. 2014;9(3):e90814. doi: 10.1371/journal.pone.0090814. PubMed PMID: 24595028; PubMed Central PMCID: PMCPMC3940927.

78. Kitamura S, Kiuchi K, Taoka T, Hashimoto K, Ueda S, Yasuno F, et al. Longitudinal white matter changes in Alzheimer's disease: a tractography-based analysis study. Brain Res. 2013;1515:12-8. doi: 10.1016/j.brainres.2013.03.052. PubMed PMID: 23583480.

79. Jacob S, Finsterbusch J, Weishaupt JH, Khorram-Sefat D, Frahm J, Ehrenreich H. Diffusion tensor imaging for long-term follow-up of corticospinal tract degeneration in amyotrophic lateral sclerosis. Neuroradiology. 2003;45(9):598-600. doi: 10.1007/s00234-003-1014-0. PubMed PMID: 12904924.

80. Abe O, Yamada H, Masutani Y, Aoki S, Kunimatsu A, Yamasue H, et al. Amyotrophic lateral sclerosis: diffusion tensor tractography and voxel-based analysis. NMR in biomedicine. 2004;17(6):411-6. doi: 10.1002/nbm.907. PubMed PMID: 15386625.

81. Adler CM, Holland SK, Schmithorst V, Wilke M, Weiss KL, Pan H, et al. Abnormal frontal white matter tracts in bipolar disorder: a diffusion tensor imaging study. Bipolar Disord. 2004;6(3):197-203. doi: 10.1111/j.1399-5618.2004.00108.x. PubMed PMID: 15117398.

82. Taylor WD, MacFall JR, Payne ME, McQuoid DR, Provenzale JM, Steffens DC, et al. Late-life depression and microstructural abnormalities in dorsolateral prefrontal cortex white matter. Am J Psychiatry. 2004;161(7):1293-6. doi: 10.1176/appi.ajp.161.7.1293. PubMed PMID: 15229065.

83. Aoki Y, Abe O, Nippashi Y, Yamasue H. Comparison of white matter integrity between autism spectrum disorder subjects and typically developing individuals: a meta-analysis of diffusion tensor imaging tractography studies. Mol Autism. 2013;4(1):25. doi: 10.1186/2040-2392-4-25. PubMed PMID: 23876131; PubMed Central PMCID: PMCPMC3726469.

84. Cannistraro PA, Makris N, Howard JD, Wedig MM, Hodge SM, Wilhelm S, et al. A diffusion tensor imaging study of white matter in obsessive-compulsive disorder. Depress Anxiety. 2007;24(6):440-6. doi: 10.1002/da.20246. PubMed PMID: 17096398.

85. Jayarajan RN, Venkatasubramanian G, Viswanath B, Janardhan Reddy YC, Srinath S, Vasudev MK, et al. White matter abnormalities in children and adolescents with obsessive-compulsive disorder: a diffusion tensor imaging study. Depress Anxiety. 2012;29(9):780-8. doi: 10.1002/da.21890. PubMed PMID: 22323419.

86. Hong SB, Zalesky A, Fornito A, Park S, Yang YH, Park MH, et al. Connectomic disturbances in attention-deficit/hyperactivity disorder: a whole-brain tractography analysis. Biol Psychiatry. 2014;76(8):656-63. doi: 10.1016/j.biopsych.2013.12.013. PubMed PMID: 24503470.

87. Lin HY, Gau SS, Huang-Gu SL, Shang CY, Wu YH, Tseng WY. Neural substrates of behavioral variability in attention deficit hyperactivity disorder: based on ex-Gaussian reaction time distribution and diffusion spectrum imaging tractography. Psychol Med. 2014;44(8):1751-64. doi: 10.1017/S0033291713001955. PubMed PMID: 23931705.

88. Wheeler AL, Voineskos AN. A review of structural neuroimaging in schizophrenia: from connectivity to connectomics. Front Hum Neurosci. 2014;8:653. doi: 10.3389/fnhum.2014.00653. PubMed PMID: 25202257; PubMed Central PMCID: PMCPMC4142355.

89. Ashtari M, Cottone J, Ardekani BA, Cervellione K, Szeszko PR, Wu J, et al. Disruption of white matter integrity in the inferior longitudinal fasciculus in adolescents with schizophrenia as revealed by fiber tractography. Arch Gen Psychiatry. 2007;64(11):1270-80. doi: 10.1001/archpsyc.64.11.1270. PubMed PMID: 17984396.

90. Phillips OR, Nuechterlein KH, Clark KA, Hamilton LS, Asarnow RF, Hageman NS, et al. Fiber tractography reveals disruption of temporal lobe white matter tracts in schizophrenia. Schizophr Res. 2009;107(1):30-8. doi: 10.1016/j.schres.2008.10.019. PubMed PMID: 19028423; PubMed Central PMCID: PMCPMC2655322.

91. Seitz J, Zuo JX, Lyall AE, Makris N, Kikinis Z, Bouix S, et al. Tractography Analysis of 5 White Matter Bundles and Their Clinical and Cognitive Correlates in Early-Course Schizophrenia. Schizophr Bull. 2016;42(3):762-71. doi: 10.1093/schbul/sbv171. PubMed PMID: 27009248; PubMed Central PMCID: PMCPMC4838095.

92. Audoin B, Guye M, Reuter F, Au Duong MV, Confort-Gouny S, Malikova I, et al. Structure of WM bundles constituting the working memory system in early multiple sclerosis: a quantitative DTI tractography study. NeuroImage. 2007;36(4):1324-30. doi: 10.1016/j.neuroimage.2007.04.038. PubMed PMID: 17513134.

93. Koenig KA, Sakaie KE, Lowe MJ, Lin J, Stone L, Bermel RA, et al. The relationship between cognitive function and high-resolution diffusion tensor MRI of the cingulum bundle in multiple sclerosis. Multiple Sclerosis Journal. 2015:1-8. doi: 10.1177/1352458515576983.

94. Mesaros S, Rocca MA, Kacar K, Kostic J, Copetti M, Stosic-Opincal T, et al. Diffusion tensor MRI tractography and cognitive impairment in multiple sclerosis. Neurology. 2012;78(13):969-75. doi: 10.1212/WNL.0b013e31824d5859. PubMed PMID: 22377806.

95. Shu N, Liu Y, Li K, Duan Y, Wang J, Yu C, et al. Diffusion tensor tractography reveals disrupted topological efficiency in white matter structural networks in multiple sclerosis. Cereb Cortex. 2011;21(11):2565-77. doi: 10.1093/cercor/bhr039. PubMed PMID: 21467209.

96. Chen Z, Tie Y, Olubiyi O, Zhang F, Mehrtash A, Rigolo L, et al. Corticospinal tract modeling for neurosurgical planning by tracking through regions of peritumoral edema and crossing fibers using two-tensor unscented Kalman filter tractography. Int J Comput Assist Radiol Surg. 2016;11(8):1475-86. doi: 10.1007/s11548-015-1344-5. PubMed PMID: 26762104; PubMed Central PMCID: PMCPMC4942409.

97. Schonberg T, Pianka P, Hendler T, Pasternak O, Assaf Y. Characterization of displaced white matter by brain tumors using combined DTI and fMRI. NeuroImage. 2006;30(4):1100-11. doi: 10.1016/j.neuroimage.2005.11.015. PubMed PMID: 16427322.

98. Yu CS, Li KC, Xuan Y, Ji XM, Qin W. Diffusion tensor tractography in patients with cerebral tumors: a helpful technique for neurosurgical planning and postoperative assessment. Eur J Radiol. 2005;56(2):197-204. doi: 10.1016/j.ejrad.2005.04.010. PubMed PMID: 15916876.

99. Golby AJ, Kindlmann G, Norton I, Yarmarkovich A, Pieper S, Kikinis R. Interactive diffusion tensor tractography visualization for neurosurgical planning. Neurosurgery.

2011;68(2):496-505. doi: 10.1227/NEU.0b013e3182061ebb. PubMed PMID: 21135713; PubMed Central PMCID: PMCPMC3112275.

100. Fernandez-Miranda JC, Pathak S, Engh J, Jarbo K, Verstynen T, Yeh FC, et al. High-definition fiber tractography of the human brain: neuroanatomical validation and neurosurgical applications. Neurosurgery. 2012;71(2):430-53. doi: 10.1227/NEU.0b013e3182592faa. PubMed PMID: 22513841.

101. Powell HW, Parker GJ, Alexander DC, Symms MR, Boulby PA, Wheeler-Kingshott CA, et al. MR tractography predicts visual field defects following temporal lobe resection. Neurology. 2005;65(4):596-9. doi: 10.1212/01.wnl.0000172858.20354.73. PubMed PMID: 16116123.

102. Jeong JW, Asano E, Juhasz C, Chugani HT. Localization of specific language pathways using diffusion-weighted imaging tractography for presurgical planning of children with intractable epilepsy. Epilepsia. 2015;56(1):49-57. doi: 10.1111/epi.12863. PubMed PMID: 25489639; PubMed Central PMCID: PMCPMC4354866.

103. Winston GP, Mancini L, Stretton J, Ashmore J, Symms MR, Duncan JS, et al. Diffusion tensor imaging tractography of the optic radiation for epilepsy surgical planning: a comparison of two methods. Epilepsy Res. 2011;97(1-2):124-32. doi: 10.1016/j.eplepsyres.2011.07.019. PubMed PMID: 21885257; PubMed Central PMCID: PMCPMC3223565.

104. Aboitiz F, Scheibel AB, Fisher RS, Zaidel E. Fiber composition of the human corpus callosum. Brain Res. 1992;598(1-2):143-53. PubMed PMID: 1486477.

105. Chen H, Zhang T, Guo L, Li K, Yu X, Li L, et al. Coevolution of gyral folding and structural connection patterns in primate brains. Cereb Cortex. 2013;23(5):1208-17. doi: 10.1093/cercor/bhs113. PubMed PMID: 22586139; PubMed Central PMCID: PMCPMC3615352.

106. Nie J, Guo L, Li K, Wang Y, Chen G, Li L, et al. Axonal fiber terminations concentrate on gyri. Cereb Cortex. 2012;22(12):2831-9. doi: 10.1093/cercor/bhr361. PubMed PMID: 22190432; PubMed Central PMCID: PMCPMC3491768.

107. Reveley C, Seth AK, Pierpaoli C, Silva AC, Yu D, Saunders RC, et al. Superficial white matter fiber systems impede detection of long-range cortical connections in diffusion MR tractography. Proceedings of the National Academy of Sciences of the United States of America. 2015;112(21):E2820-8. doi: 10.1073/pnas.1418198112. PubMed PMID: 25964365; PubMed Central PMCID: PMCPMC4450402.

108. Van Essen DCJ, S.; Sotiropoulos, N.; Chen, C.; Dikranian, E.; Coalson, T.; Harwell, J.; Behrens, T.; Glasser, M;. Mapping Connections in Humans and Non-Human Primates: Aspirations and Challenges for Diffusion Imaging. In: Johansen-Berg H, Behrens TEJ, editors. Diffusion MRI : from quantitative measurement to in-vivo neuroanatomy. 2nd ed. London, UK ; Waltham, MA: Elsevier/Academic Press; 2014. p. 337-58.

109. Markov NT, Ercsey-Ravasz MM, Ribeiro Gomes AR, Lamy C, Magrou L, Vezoli J, et al. A weighted and directed interareal connectivity matrix for macaque cerebral cortex. Cereb Cortex. 2014;24(1):17-36. doi: 10.1093/cercor/bhs270. PubMed PMID: 23010748; PubMed Central PMCID: PMCPMC3862262.

110. Schmahmann JD, Pandya D. Fiber pathways of the brain: OUP USA; 2009.

111. Herculano-Houzel S, Collins CE, Wong P, Kaas JH, Lent R. The basic nonuniformity of the cerebral cortex. Proceedings of the National Academy of Sciences of the United States of America. 2008;105(34):12593-8. doi: 10.1073/pnas.0805417105. PubMed PMID: 18689685; PubMed Central PMCID: PMCPMC2527956.

112. Goldman-Rakic PS, Schwartz ML. Interdigitation of contralateral and ipsilateral columnar projections to frontal association cortex in primates. Science. 1982;216(4547):755-7. PubMed PMID: 6177037.

113. McNab JA, Jbabdi S, Deoni SC, Douaud G, Behrens TE, Miller KL. High resolution diffusion-weighted imaging in fixed human brain using diffusion-weighted steady state free precession. NeuroImage. 2009;46(3):775-85. Epub 2009/04/07. doi: 10.1016/j.neuroimage.2009.01.008. PubMed PMID: 19344686.

114. Miller KL, Stagg CJ, Douaud G, Jbabdi S, Smith SM, Behrens TE, et al. Diffusion imaging of whole, post-mortem human brains on a clinical MRI scanner. NeuroImage. 2011;57(1):167-81. Epub 2011/04/09. doi: 10.1016/j.neuroimage.2011.03.070. PubMed PMID: 21473920; PubMed Central PMCID: PMCPmc3115068.

115. Jespersen SN, Leigland LA, Cornea A, Kroenke CD. Determination of axonal and dendritic orientation distributions within the developing cerebral cortex by diffusion tensor imaging. IEEE transactions on medical imaging. 2012;31(1):16-32. doi: 10.1109/TMI.2011.2162099. PubMed PMID: 21768045; PubMed Central PMCID: PMCPMC3271123.

116. Leuze CW, Anwander A, Bazin PL, Dhital B, Stuber C, Reimann K, et al. Layer-specific intracortical connectivity revealed with diffusion MRI. Cereb Cortex. 2014;24(2):328-39. doi: 10.1093/cercor/bhs311. PubMed PMID: 23099298; PubMed Central PMCID: PMCPMC3888365.

117. Fieremans E, De Deene Y, Delputte S, Ozdemir MS, Achten E, Lemahieu I. The design of anisotropic diffusion phantoms for the validation of diffusion weighted magnetic resonance imaging. Phys Med Biol. 2008;53(19):5405-19. doi: 10.1088/0031-9155/53/19/009. PubMed PMID: 18765890.

118. Alexander AL, Hasan KM, Lazar M, Tsuruda JS, Parker DL. Analysis of partial volume effects in diffusion-tensor MRI. Magnetic resonance in medicine : official journal of the Society

of Magnetic Resonance in Medicine / Society of Magnetic Resonance in Medicine. 2001;45(5):770-80. PubMed PMID: 11323803.

119. Frank LR. Characterization of anisotropy in high angular resolution diffusion-weighted MRI. Magnetic resonance in medicine : official journal of the Society of Magnetic Resonance in Medicine / Society of Magnetic Resonance in Medicine. 2002;47(6):1083-99. doi: 10.1002/mrm.10156. PubMed PMID: 12111955.

120. Tuch DS, Reese TG, Wiegell MR, Makris N, Belliveau JW, Wedeen VJ. High angular resolution diffusion imaging reveals intravoxel white matter fiber heterogeneity. Magnetic resonance in medicine : official journal of the Society of Magnetic Resonance in Medicine / Society of Magnetic Resonance in Medicine. 2002;48(4):577-82. doi: 10.1002/mrm.10268. PubMed PMID: 12353272.

121. Yeh FC, Wedeen VJ, Tseng WY. Generalized q-sampling imaging. IEEE transactions on medical imaging. 2010;29(9):1626-35. doi: 10.1109/TMI.2010.2045126. PubMed PMID: 20304721.

122. Alexander DC, Barker GJ. Optimal imaging parameters for fiber-orientation estimation in diffusion MRI. NeuroImage. 2005;27(2):357-67. doi: 10.1016/j.neuroimage.2005.04.008. PubMed PMID: 15921931.

123. Daducci A, Canales-Rodriguez EJ, Descoteaux M, Garyfallidis E, Gur Y, Lin YC, et al. Quantitative comparison of reconstruction methods for intra-voxel fiber recovery from diffusion MRI. IEEE transactions on medical imaging. 2014;33(2):384-99. doi: 10.1109/TMI.2013.2285500. PubMed PMID: 24132007.

124. von dem Hagen EA, Henkelman RM. Orientational diffusion reflects fiber structure within a voxel. Magnetic resonance in medicine : official journal of the Society of Magnetic Resonance in Medicine / Society of Magnetic Resonance in Medicine. 2002;48(3):454-9. doi: 10.1002/mrm.10250. PubMed PMID: 12210909.

125. Lin C-P, Wedeen VJ, Chen J-H, Yao C, Tseng W-YI. Validation of diffusion spectrum magnetic resonance imaging with manganese-enhanced rat optic tracts and ex vivo phantoms. NeuroImage. 2003;19(3):482-95. doi: http://dx.doi.org/10.1016/S1053-8119(03)00154-X.

126. Perrin M, Poupon C, Rieul B, Leroux P, Constantinesco A, Mangin JF, et al. Validation of q-ball imaging with a diffusion fibre-crossing phantom on a clinical scanner. Philos Trans R Soc Lond B Biol Sci. 2005;360(1457):881-91. doi: 10.1098/rstb.2005.1650. PubMed PMID: 16087433; PubMed Central PMCID: PMCPMC1854933.

127. Poupon C, Rieul B, Kezele I, Perrin M, Poupon F, Mangin JF. New diffusion phantoms dedicated to the study and validation of high-angular-resolution diffusion imaging (HARDI) models. Magnetic resonance in medicine : official journal of the Society of Magnetic Resonance

in Medicine / Society of Magnetic Resonance in Medicine. 2008;60(6):1276-83. doi: 10.1002/mrm.21789. PubMed PMID: 19030160.

128. Pullens P, Roebroeck A, Goebel R. Ground truth hardware phantoms for validation of diffusion-weighted MRI applications. Journal of magnetic resonance imaging : JMRI. 2010;32(2):482-8. doi: 10.1002/jmri.22243. PubMed PMID: 20677281.

129. Farrher E, Kaffanke J, Celik AA, Stöcker T, Grinberg F, Shah NJ. Novel multisection design of anisotropic diffusion phantoms. Magnetic resonance imaging. 2012;30(4):518-26. doi: http://dx.doi.org/10.1016/j.mri.2011.12.012.

130. Zhou H, Touny AH, Bhaduri SB. Fabrication of novel PLA/CDHA bionanocomposite fibers for tissue engineering applications via electrospinning. J Mater Sci Mater Med. 2011;22(5):1183-93. doi: 10.1007/s10856-011-4295-6. PubMed PMID: 21431905.

131. Hubbard PL, Zhou FL, Eichhorn SJ, Parker GJ. Biomimetic phantom for the validation of diffusion magnetic resonance imaging. Magnetic resonance in medicine : official journal of the Society of Magnetic Resonance in Medicine / Society of Magnetic Resonance in Medicine. 2014. doi: 10.1002/mrm.25107. PubMed PMID: 24469863.

132. Leergaard TB, White NS, de Crespigny A, Bolstad I, D'Arceuil H, Bjaalie JG, et al. Quantitative Histological Validation of Diffusion MRI Fiber Orientation Distributions in the Rat Brain. PloS one. 2010;5(1):e8595. doi: 10.1371/journal.pone.0008595.

133. Choe AS, Stepniewska I, Colvin DC, Ding Z, Anderson AW. Validation of diffusion tensor MRI in the central nervous system using light microscopy: quantitative comparison of fiber properties. NMR in biomedicine. 2012;25(7):900-8. doi: 10.1002/nbm.1810. PubMed PMID: 22246940.

134. Budde MD, Frank JA. Examining brain microstructure using structure tensor analysis of histological sections. NeuroImage. 2012;63(1):1-10. Epub 2012/07/05. doi: 10.1016/j.neuroimage.2012.06.042. PubMed PMID: 22759994.

135. Seehaus A, Roebroeck A, Bastiani M, Fonseca L, Bratzke H, Lori N, et al. Histological validation of high-resolution DTI in human post mortem tissue. Front Neuroanat. 2015;9:98. doi: 10.3389/fnana.2015.00098. PubMed PMID: 26257612; PubMed Central PMCID: PMCPMC4511840.

136. Khan AR, Cornea A, Leigland LA, Kohama SG, Jespersen SN, Kroenke CD. 3D structure tensor analysis of light microscopy data for validating diffusion MRI. NeuroImage. 2015;111:192-203. Epub 2015/02/11. doi: 10.1016/j.neuroimage.2015.01.061. PubMed PMID: 25665963; PubMed Central PMCID: PMC4387076.

137. Wang H, Lenglet C, Akkin T. Structure tensor analysis of serial optical coherence scanner images for mapping fiber orientations and tractography in the brain. J Biomed Opt. 2015;20(3):036003. doi: 10.1117/1.JBO.20.3.036003. PubMed PMID: 25741662; PubMed Central PMCID: PMCPMC4350401.

138. Axer M, Strohmer S, Grassel D, Bucker O, Dohmen M, Reckfort J, et al. Estimating Fiber Orientation Distribution Functions in 3D-Polarized Light Imaging. Front Neuroanat. 2016;10:40. doi: 10.3389/fnana.2016.00040. PubMed PMID: 27147981; PubMed Central PMCID: PMCPMC4835454.

139. Lori NF, Akbudak E, Shimony JS, Cull TS, Snyder AZ, Guillory RK, et al. Diffusion tensor fiber tracking of human brain connectivity: aquisition methods, reliability analysis and biological results. NMR in biomedicine. 2002;15(7-8):494-515. doi: 10.1002/nbm.779. PubMed PMID: 12489098.

140. Tournier JD, Calamante F, King MD, Gadian DG, Connelly A. Limitations and requirements of diffusion tensor fiber tracking: an assessment using simulations. Magnetic resonance in medicine : official journal of the Society of Magnetic Resonance in Medicine / Society of Magnetic Resonance in Medicine. 2002;47(4):701-8. PubMed PMID: 11948731.

141. Anderson AW. Theoretical analysis of the effects of noise on diffusion tensor imaging. Magnetic resonance in medicine : official journal of the Society of Magnetic Resonance in Medicine / Society of Magnetic Resonance in Medicine. 2001;46(6):1174-88. Epub 2001/12/18. PubMed PMID: 11746585.

142. Gossl C, Fahrmeir L, Putz B, Auer LM, Auer DP. Fiber tracking from DTI using linear state space models: detectability of the pyramidal tract. NeuroImage. 2002;16(2):378-88. doi: 10.1006/nimg.2002.1055. PubMed PMID: 12030823.

143. Chen B, Song AW. Diffusion tensor imaging fiber tracking with local tissue property sensitivity: phantom and in vivo validation. Magnetic resonance imaging. 2008;26(1):103-8. doi: 10.1016/j.mri.2007.05.003. PubMed PMID: 17587528; PubMed Central PMCID: PMCPMC2830069.

144. Iturria-Medina Y, Canales-Rodriguez EJ, Melie-Garcia L, Valdes-Hernandez PA, Martinez-Montes E, Aleman-Gomez Y, et al. Characterizing brain anatomical connections using diffusion weighted MRI and graph theory. NeuroImage. 2007;36(3):645-60. doi: 10.1016/j.neuroimage.2007.02.012. PubMed PMID: 17466539.

145. Close TG, Tournier JD, Calamante F, Johnston LA, Mareels I, Connelly A. A software tool to generate simulated white matter structures for the assessment of fibre-tracking algorithms. NeuroImage. 2009;47(4):1288-300. doi: 10.1016/j.neuroimage.2009.03.077. PubMed PMID: 19361565.

146. Neher PF, Laun FB, Stieltjes B, Maier-Hein KH. Fiberfox: facilitating the creation of realistic white matter software phantoms. Magnetic resonance in medicine : official journal of the Society of Magnetic Resonance in Medicine / Society of Magnetic Resonance in Medicine. 2014;72(5):1460-70. doi: 10.1002/mrm.25045. PubMed PMID: 24323973.

147. Fillard P, Descoteaux M, Goh A, Gouttard S, Jeurissen B, Malcolm J, et al. Quantitative evaluation of 10 tractography algorithms on a realistic diffusion MR phantom. NeuroImage. 2011;56(1):220-34. doi: 10.1016/j.neuroimage.2011.01.032. PubMed PMID: 21256221.

148. Watanabe M, Aoki S, Masutani Y, Abe O, Hayashi N, Masumoto T, et al. Flexible ex vivo phantoms for validation of diffusion tensor tractography on a clinical scanner. Radiat Med. 2006;24(9):605-9. doi: 10.1007/s11604-006-0076-4. PubMed PMID: 17111268.

149. Cote MA, Girard G, Bore A, Garyfallidis E, Houde JC, Descoteaux M. Tractometer: towards validation of tractography pipelines. Med Image Anal. 2013;17(7):844-57. doi: 10.1016/j.media.2013.03.009. PubMed PMID: 23706753.

150. Morecraft RU, G.; Lanciego, J.; Wouterlood, F.; Pandya, D. Classic and Contemporary Neural Tract-Tracing Techniques. In: Johansen-Berg H, Behrens TEJ, editors. Diffusion MRI : from quantitative measurement to in-vivo neuroanatomy. 2nd ed. London, UK ; Waltham, MA: Elsevier/Academic Press; 2014. p. 359-400.

151. Stephan KE, Kamper L, Bozkurt A, Burns GA, Young MP, Kotter R. Advanced database methodology for the Collation of Connectivity data on the Macaque brain (CoCoMac). Philos Trans R Soc Lond B Biol Sci. 2001;356(1412):1159-86. doi: 10.1098/rstb.2001.0908. PubMed PMID: 11545697; PubMed Central PMCID: PMCPMC1088509.

152. Markov NT, Ercsey-Ravasz M, Lamy C, Ribeiro Gomes AR, Magrou L, Misery P, et al. The role of long-range connections on the specificity of the macaque interareal cortical network. Proceedings of the National Academy of Sciences of the United States of America. 2013;110(13):5187-92. doi: 10.1073/pnas.1218972110. PubMed PMID: 23479610; PubMed Central PMCID: PMCPMC3612613.

153. Oh SW, Harris JA, Ng L, Winslow B, Cain N, Mihalas S, et al. A mesoscale connectome of the mouse brain. Nature. 2014;508(7495):207-14. doi: 10.1038/nature13186. PubMed PMID: 24695228; PubMed Central PMCID: PMCPMC5102064.

154. Azadbakht H, Parkes LM, Haroon HA, Augath M, Logothetis NK, de Crespigny A, et al. Validation of High-Resolution Tractography Against In Vivo Tracing in the Macaque Visual Cortex. Cereb Cortex. 2015;25(11):4299-309. doi: 10.1093/cercor/bhu326. PubMed PMID: 25787833.

155. van den Heuvel MP, de Reus MA, Feldman Barrett L, Scholtens LH, Coopmans FM, Schmidt R, et al. Comparison of diffusion tractography and tract-tracing measures of

connectivity strength in rhesus macaque connectome. Human brain mapping. 2015;36(8):3064-75. doi: 10.1002/hbm.22828. PubMed PMID: 26058702.

156. Donahue CJ, Sotiropoulos SN, Jbabdi S, Hernandez-Fernandez M, Behrens TE, Dyrby TB, et al. Using Diffusion Tractography to Predict Cortical Connection Strength and Distance: A Quantitative Comparison with Tracers in the Monkey. J Neurosci. 2016;36(25):6758-70. doi: 10.1523/JNEUROSCI.0493-16.2016. PubMed PMID: 27335406; PubMed Central PMCID: PMCPMC4916250.

157. Calabrese E, Badea A, Coe CL, Lubach GR, Shi Y, Styner MA, et al. A diffusion tensor MRI atlas of the postmortem rhesus macaque brain. NeuroImage. 2015;117:408-16. doi: 10.1016/j.neuroimage.2015.05.072. PubMed PMID: 26037056; PubMed Central PMCID: PMCPMC4512905.

158. Markov NT, Misery P, Falchier A, Lamy C, Vezoli J, Quilodran R, et al. Weight consistency specifies regularities of macaque cortical networks. Cereb Cortex. 2011;21(6):1254-72. doi: 10.1093/cercor/bhq201. PubMed PMID: 21045004; PubMed Central PMCID: PMCPMC3097985.

159. Gao Y, Anderson AW, editors. Validation of DTI-tractography-based measures of white matter pathways originating from the primary motor area. Internaitional Society for Magnetic Resonance in Medicine; 2012 5-11 May; Melbourne, Australia.

160. Gao Y, Choe AS, Stepniewska I, Li X, Avison MJ, Anderson AW. Validation of DTI tractography-based measures of primary motor area connectivity in the squirrel monkey brain. PloS one. 2013;8(10):e75065. Epub 2013/10/08. doi: 10.1371/journal.pone.0075065. PubMed PMID: 24098365; PubMed Central PMCID: PMC3788067.

161. Schmahmann JD, Pandya DN, Wang R, Dai G, D'Arceuil HE, de Crespigny AJ, et al. Association fibre pathways of the brain: parallel observations from diffusion spectrum imaging and autoradiography. Brain. 2007;130(Pt 3):630-53. doi: 10.1093/brain/awl359. PubMed PMID: 17293361.

162. Dauguet J, Peled S, Berezovskii V, Delzescaux T, Warfield SK, Born R, et al. Comparison of fiber tracts derived from in-vivo DTI tractography with 3D histological neural tract tracer reconstruction on a macaque brain. NeuroImage. 2007;37(2):530-8. doi: 10.1016/j.neuroimage.2007.04.067. PubMed PMID: 17604650.

163. Dauguet J, Peled S, Berezovskii V, Delzescaux T, Warfield SK, Born R, et al. 3D histological reconstruction of fiber tracts and direct comparison with diffusion tensor MRI tractography. Med Image Comput Comput Assist Interv. 2006;9(Pt 1):109-16. PubMed PMID: 17354880.

164. Thomas C, Ye FQ, Irfanoglu MO, Modi P, Saleem KS, Leopold DA, et al. Anatomical accuracy of brain connections derived from diffusion MRI tractography is inherently limited. Proceedings of the National Academy of Sciences of the United States of America.

2014;111(46):16574-9. Epub 2014/11/05. doi: 10.1073/pnas.1405672111. PubMed PMID: 25368179.

165. Lin CP, Tseng WY, Cheng HC, Chen JH. Validation of diffusion tensor magnetic resonance axonal fiber imaging with registered manganese-enhanced optic tracts. NeuroImage. 2001;14(5):1035-47. doi: 10.1006/nimg.2001.0882. PubMed PMID: 11697935.

166. Dyrby TB, Sogaard LV, Parker GJ, Alexander DC, Lind NM, Baare WF, et al. Validation of in vitro probabilistic tractography. NeuroImage. 2007;37(4):1267-77. doi: 10.1016/j.neuroimage.2007.06.022. PubMed PMID: 17706434.

167. Knosche TR, Anwander A, Liptrot M, Dyrby TB. Validation of tractography: Comparison with manganese tracing. Human brain mapping. 2015;36(10):4116-34. doi: 10.1002/hbm.22902. PubMed PMID: 26178765.

168. Hendrickx AG, Binkerd PE. Nonhuman primates and teratological research. J Med Primatol. 1990;19(2):81-108. PubMed PMID: 2187096.

169. Merzenich MM, Kaas JH, Wall J, Nelson RJ, Sur M, Felleman D. Topographic reorganization of somatosensory cortical areas 3b and 1 in adult monkeys following restricted deafferentation. Neuroscience. 1983;8(1):33-55. PubMed PMID: 6835522.

170. Roe AW, Winberry JE, Friedman RM. Study of single and multidigit activation in monkey somatosensory cortex using voltage-sensitive dye imaging. Neurophotonics. 2017;4(3):031219. doi: 10.1117/1.NPh.4.3.031219. PubMed PMID: 28573156; PubMed Central PMCID: PMCPMC5446783.

171. Banks ML, Czoty PW, Negus SS. Utility of Nonhuman Primates in Substance Use Disorders Research. ILAR J. 2017:1-14. doi: 10.1093/ilar/ilx014. PubMed PMID: 28531265.

172. Uno Y, Uehara S, Yamazaki H. Utility of non-human primates in drug development: Comparison of non-human primate and human drug-metabolizing cytochrome P450 enzymes. Biochem Pharmacol. 2016;121:1-7. doi: 10.1016/j.bcp.2016.06.008. PubMed PMID: 27318253.

173. Secci ME, Auber A, Panlilio LV, Redhi GH, Thorndike EB, Schindler CW, et al. Attenuating Nicotine Reinforcement and Relapse by Enhancing Endogenous Brain Levels of Kynurenic Acid in Rats and Squirrel Monkeys. Neuropsychopharmacology. 2017;42(8):1619-29. doi: 10.1038/npp.2017.21. PubMed PMID: 28139681; PubMed Central PMCID: PMCPMC5518900.

174. Murakami T, Ibi K, Kuraishi T, Hattori S, Kai C, Ishiguro N, et al. Failure of heterogeneous amyloid-enhancing factor in geriatric squirrel monkeys (Saimiri boliviensis). J Med Primatol. 2014;43(6):488-91. doi: 10.1111/jmp.12136. PubMed PMID: 25041324.

175. Myers RM, Greiner SM, Harvey ME, Griesmann G, Kuffel MJ, Buhrow SA, et al. Preclinical pharmacology and toxicology of intravenous MV-NIS, an oncolytic measles virus administered with or without cyclophosphamide. Clin Pharmacol Ther. 2007;82(6):700-10. doi: 10.1038/sj.clpt.6100409. PubMed PMID: 17971816; PubMed Central PMCID: PMCPMC2769566.

176. Wang Z, Chen LM, Negyessy L, Friedman RM, Mishra A, Gore JC, et al. The relationship of anatomical and functional connectivity to resting-state connectivity in primate somatosensory cortex. Neuron. 2013;78(6):1116-26. doi: 10.1016/j.neuron.2013.04.023. PubMed PMID: 23791200; PubMed Central PMCID: PMCPMC3723346.

177. Wu TL, Wang F, Anderson AW, Chen LM, Ding Z, Gore JC. Effects of anesthesia on resting state BOLD signals in white matter of non-human primates. Magnetic resonance imaging. 2016;34(9):1235-41. doi: 10.1016/j.mri.2016.07.001. PubMed PMID: 27451405; PubMed Central PMCID: PMCPMC5055423.

178. Chen LM, Mishra A, Yang PF, Wang F, Gore JC. Injury alters intrinsic functional connectivity within the primate spinal cord. Proceedings of the National Academy of Sciences of the United States of America. 2015;112(19):5991-6. doi: 10.1073/pnas.1424106112. PubMed PMID: 25902510; PubMed Central PMCID: PMCPMC4434735.

179. Chen LM, Friedman RM, Roe AW. Optical imaging of a tactile illusion in area 3b of the primary somatosensory cortex. Science. 2003;302(5646):881-5. doi: 10.1126/science.1087846. PubMed PMID: 14500850.

180. Chen LM, Yang PF, Wang F, Mishra A, Shi Z, Wu R, et al. Biophysical and neural basis of resting state functional connectivity: Evidence from non-human primates. Magnetic resonance imaging. 2017;39:71-81. doi: 10.1016/j.mri.2017.01.020. PubMed PMID: 28161319; PubMed Central PMCID: PMCPMC5410395.

181. Akert REK. Stereotaxic Atlas of the Brain of the Squirrel Monkey: University of Wisconsin Press; 1963.

182. MacLean JAGPD. A Stereotaxic Atlas of the Squirrel Monkey's Brain (Saimiri sciureus) U.S. Department of Health, Education, and Welfare; 1962.

183. Schilling KG, Gao Y, Stepniewska I, Wu TL, Wang F, Landman BA, et al. The VALiDATe29 MRI Based Multi-Channel Atlas of the Squirrel Monkey Brain. Neuroinformatics. 2017. doi: 10.1007/s12021-017-9334-0. PubMed PMID: 28748393.

184. D'Arceuil HE, Westmoreland S, de Crespigny AJ. An approach to high resolution diffusion tensor imaging in fixed primate brain. NeuroImage. 2007;35(2):553-65. Epub 2007/02/13. doi: 10.1016/j.neuroimage.2006.12.028. PubMed PMID: 17292630.

185. Andersson JL, Skare S, Ashburner J. How to correct susceptibility distortions in spin-echo echo-planar images: application to diffusion tensor imaging. NeuroImage. 2003;20(2):870-88. doi: 10.1016/S1053-8119(03)00336-7. PubMed PMID: 14568458.

186. Tournier JD, Calamante F, Connelly A. MRtrix: Diffusion tractography in crossing fiber regions. International Journal of Imaging Systems and Technology. 2012;22(1):53-66. doi: 10.1002/ima.22005.

187. Gao Y, Parvathaneni P, Schilling K, Zu Z, Choe A, Stepniewska I, et al. A 3D high resolution ex vivo white matter atlas of the common squirrel monkey (Saimiri sciureus) based on diffusion tensor imaging. In Proceedings of the SPIE Medical Imaging Conference; February; San Diego, California2016.

188. Yeh FC, Verstynen TD, Wang Y, Fernandez-Miranda JC, Tseng WY. Deterministic diffusion fiber tracking improved by quantitative anisotropy. PloS one. 2013;8(11):e80713. doi: 10.1371/journal.pone.0080713. PubMed PMID: 24348913; PubMed Central PMCID: PMCPMC3858183.

189. Reiner A, Veenman CL, Medina L, Jiao Y, Del Mar N, Honig MG. Pathway tracing using biotinylated dextran amines. J Neurosci Methods. 2000;103(1):23-37. PubMed PMID: 11074093.

190. Stepniewska I, Preuss TM, Kaas JH. Architectonics, somatotopic organization, and ipsilateral cortical connections of the primary motor area (M1) of owl monkeys. J Comp Neurol. 1993;330(2):238-71. doi: 10.1002/cne.903300207. PubMed PMID: 7684050.

191. Toga AW, Ambach KL, Schluender S. High-resolution anatomy from in situ human brain. NeuroImage. 1994;1(4):334-44. Epub 1994/11/01. doi: 10.1006/nimg.1994.1018. PubMed PMID: 9343583.

192. Paul CA, Beltz B, Berger-Sweeney J. The nissl stain: a stain for cell bodies in brain sections. CSH Protoc. 2008;2008:pdb prot4805. doi: 10.1101/pdb.prot4805. PubMed PMID: 21356903.

193. Gallyas F. Silver staining of Alzheimer's neurofibrillary changes by means of physical development. Acta Morphol Acad Sci Hung. 1971;19(1):1-8. PubMed PMID: 4107507.

194. Choe AS, Gao Y, Li X, Compton KB, Stepniewska I, Anderson AW. Accuracy of image registration between MRI and light microscopy in the ex vivo brain. Magnetic resonance imaging. 2011;29(5):683-92. Epub 2011/05/07. doi: 10.1016/j.mri.2011.02.022. PubMed PMID: 21546191; PubMed Central PMCID: PMC3100355.

195. Bookstein FL. Principal Warps - Thin-Plate Splines and the Decomposition of Deformations. Ieee T Pattern Anal. 1989;11(6):567-85. doi: Doi 10.1109/34.24792. PubMed PMID: WOS:A1989U674900003.

196. Rohde GK, Aldroubi A, Dawant BM. The adaptive bases algorithm for intensity-based nonrigid image registration. IEEE transactions on medical imaging. 2003;22(11):1470-9. Epub 2003/11/11. doi: 10.1109/tmi.2003.819299. PubMed PMID: 14606680.

197. Goode A, Gilbert B, Harkes J, Jukic D, Satyanarayanan M. OpenSlide: A vendor-neutral software foundation for digital pathology. J Pathol Inform. 2013;4:27. doi: 10.4103/2153-3539.119005. PubMed PMID: 24244884; PubMed Central PMCID: PMCPMC3815078.

198. Dyrby TB, Baare WF, Alexander DC, Jelsing J, Garde E, Sogaard LV. An ex vivo imaging pipeline for producing high-quality and high-resolution diffusion-weighted imaging datasets. Human brain mapping. 2011;32(4):544-63. Epub 2010/10/15. doi: 10.1002/hbm.21043. PubMed PMID: 20945352.

199. Schilling K, Janve V, Gao Y, Stepniewska I, Landman BA, Anderson AW. Comparison of 3D orientation distribution functions measured with confocal microscopy and diffusion MRI. NeuroImage. 2016;129:185-97. doi: 10.1016/j.neuroimage.2016.01.022. PubMed PMID: 26804781; PubMed Central PMCID: PMCPMC4803575.

200. Budde MD, Annese J. Quantification of anisotropy and fiber orientation in human brain histological sections. Front Integr Neurosci. 2013;7:3. doi: 10.3389/fnint.2013.00003. PubMed PMID: 23378830; PubMed Central PMCID: PMCPMC3561729.

201. Jones DK, Knosche TR, Turner R. White matter integrity, fiber count, and other fallacies: the do's and don'ts of diffusion MRI. NeuroImage. 2013;73:239-54. Epub 2012/08/01. doi: 10.1016/j.neuroimage.2012.06.081. PubMed PMID: 22846632.

202. Alexander DC, Seunarine KK. Mathematics of crossing fibers. In: Jones DK, editor. Diffusion MRI: theory, methods, and application. Oxford ; New York: Oxford University Press; 2010. p. 451-64.

203. Tournier JD. The Biophysics of Crossing Fibers. In: Jones DK, editor. Diffusion MRI : theory, methods, and application. Oxford ; New York: Oxford University Press; 2010. p. 465-81.

204. Wiegell MR, Larsson HB, Wedeen VJ. Fiber crossing in human brain depicted with diffusion tensor MR imaging. Radiology. 2000;217(3):897-903. doi: 10.1148/radiology.217.3.r00nv43897. PubMed PMID: 11110960.

205. Parker GJ, Alexander DC. Probabilistic Monte Carlo based mapping of cerebral connections utilising whole-brain crossing fibre information. Inf Process Med Imaging. 2003;18:684-95. PubMed PMID: 15344498.

206. Tariq M, Schneider T, Alexander D, Wheeler-Kingshott CM, Zhang H. In vivo Estimation of Dispersion Anisotropy of Neurites Using Diffusion MRI. In: Golland P, Hata N, Barillot C, Hornegger J, Howe R, editors. Medical Image Computing and Computer-Assisted Intervention – MICCAI 2014. Lecture Notes in Computer Science. 8675: Springer International Publishing; 2014. p. 241-8.

207. Zhang H, Hubbard PL, Parker GJ, Alexander DC. Axon diameter mapping in the presence of orientation dispersion with diffusion MRI. NeuroImage. 2011;56(3):1301-15. doi: 10.1016/j.neuroimage.2011.01.084. PubMed PMID: 21316474.

208. Xu J, Li H, Li K, Harkins KD, Jiang X, Xie J, et al. Fast and simplified mapping of mean axon diameter using temporal diffusion spectroscopy. NMR in biomedicine. 2016;29(4):400-10. PubMed PMID: 27077155; PubMed Central PMCID: PMCPMC4832578.

209. Waxman SG, Kocsis JD, Stys PK. The axon : structure, function, and pathophysiology. New York: Oxford University Press; 1995. xv, 692 p., 2 p. of plates p.

210. Jeurissen B, Leemans A, Tournier JD, Jones DK, Sijbers J. Investigating the prevalence of complex fiber configurations in white matter tissue with diffusion magnetic resonance imaging. Human brain mapping. 2013;34(11):2747-66. doi: 10.1002/hbm.22099. PubMed PMID: 22611035.

211. Caruyer E, Lenglet C, Sapiro G, Deriche R. Design of multishell sampling schemes with uniform coverage in diffusion MRI. Magnetic resonance in medicine : official journal of the Society of Magnetic Resonance in Medicine / Society of Magnetic Resonance in Medicine. 2013;69(6):1534-40. doi: 10.1002/mrm.24736. PubMed PMID: 23625329.

212. Bigun J, Granlund GH, editors. Optimal Orientation Detection of Linear Symmetry. Proceedings of the IEEE First International Conference on Computer Vision; 1987 June.

213. Ronen I, Budde M, Ercan E, Annese J, Techawiboonwong A, Webb A. Microstructural organization of axons in the human corpus callosum quantified by diffusion-weighted magnetic resonance spectroscopy of N-acetylaspartate and post-mortem histology. Brain structure & function. 2014;219(5):1773-85. Epub 2013/06/25. doi: 10.1007/s00429-013-0600-0. PubMed PMID: 23794120.

214. Evans M, Hastings NAJ, Peacock JB. Statistical distributions. 3rd ed. New York: Wiley; 2000. xvi, 221 p. p.

215. Akaike H. A new look at the statistical model identification. Automatic Control, IEEE Transactions on. 1974;19(6):716-23.

216. Tournier JD, Yeh CH, Calamante F, Cho KH, Connelly A, Lin CP. Resolving crossing fibres using constrained spherical deconvolution: validation using diffusion-weighted imaging phantom data. NeuroImage. 2008;42(2):617-25. doi: 10.1016/j.neuroimage.2008.05.002. PubMed PMID: 18583153.

217. Assemlal HE, Campbell J, Pike B, Siddiqi K. Apparent intravoxel fibre population dispersion (FPD) using spherical harmonics. Med Image Comput Comput Assist Interv. 2011;14(Pt 2):157-65. PubMed PMID: 21995025.

218. Savadjiev P, Kindlmann GL, Bouix S, Shenton ME, Westin CF. Local white matter geometry from diffusion tensor gradients. NeuroImage. 2010;49(4):3175-86. doi: 10.1016/j.neuroimage.2009.10.073. PubMed PMID: 19896542; PubMed Central PMCID: PMCPMC2818447.

219. Wedeen VJ, Rosene DL, Wang R, Dai G, Mortazavi F, Hagmann P, et al. The geometric structure of the brain fiber pathways. Science. 2012;335(6076):1628-34. doi: 10.1126/science.1215280. PubMed PMID: 22461612; PubMed Central PMCID: PMCPMC3773464.

220. Frey S, Pandya DN, Chakravarty MM, Bailey L, Petrides M, Collins DL. An MRI based average macaque monkey stereotaxic atlas and space (MNI monkey space). NeuroImage. 2011;55(4):1435-42. Epub 2011/01/25. doi: 10.1016/j.neuroimage.2011.01.040. PubMed PMID: 21256229.

221. Zakszewski E, Adluru N, Tromp do PM, Kalin N, Alexander AL. A diffusion-tensor-based white matter atlas for rhesus macaques. PloS one. 2014;9(9):e107398. doi: 10.1371/journal.pone.0107398. PubMed PMID: 25203614; PubMed Central PMCID: PMCPMC4159318.

222. Hagmann P, Kurant M, Gigandet X, Thiran P, Wedeen VJ, Meuli R, et al. Mapping Human Whole-Brain Structural Networks with Diffusion MRI. PloS one. 2007;2(7):e597. doi: 10.1371/journal.pone.0000597.

223. White T, Nelson M, Lim KO. Diffusion tensor imaging in psychiatric disorders. Top Magn Reson Imaging. 2008;19(2):97-109. doi: 10.1097/RMR.0b013e3181809f1e. PubMed PMID: 19363432.

224. Shenton ME, Hamoda HM, Schneiderman JS, Bouix S, Pasternak O, Rathi Y, et al. A Review of Magnetic Resonance Imaging and Diffusion Tensor Imaging Findings in Mild Traumatic Brain Injury. Brain imaging and behavior. 2012;6(2):137-92. doi: 10.1007/s11682-012-9156-5. PubMed PMID: PMC3803157.

225. Basser PJ, Mattiello J, LeBihan D. MR diffusion tensor spectroscopy and imaging. Biophysical Journal. 1994;66(1):259-67. PubMed PMID: PMC1275686.

226. Sakaie KE, Lowe MJ. An objective method for regularization of fiber orientation distributions derived from diffusion-weighted MRI. NeuroImage. 2007;34(1):169-76. doi: http://dx.doi.org/10.1016/j.neuroimage.2006.08.034.

227. Yanasak N, Allison J. Use of capillaries in the construction of an MRI phantom for the assessment of diffusion tensor imaging: demonstration of performance. Magnetic resonance imaging. 2006;24(10):1349-61. doi: http://dx.doi.org/10.1016/j.mri.2006.08.001.

228. Seehaus AK, Roebroeck A, Chiry O, Kim DS, Ronen I, Bratzke H, et al. Histological validation of DW-MRI tractography in human postmortem tissue. Cereb Cortex. 2013;23(2):442-50. doi: 10.1093/cercor/bhs036. PubMed PMID: 22345356; PubMed Central PMCID: PMCPMC3584953.

229. Jones DK, Horsfield MA, Simmons A. Optimal Strategies for Measuring Diffusion in Anisotropic Systems by Magnetic Resonance Imaging. Magnetic Resonance in Medicine. 1999;42:515-25.

230. Pawley JB, Masters RBR. Handbook of Biological Confocal Microscopy, Second Edition. OPTICE. 1996;35(9):2765-6. doi: 10.1117/1.600871.

231. Biggs DSC, Andrews M. Acceleration of iterative image restoration algorithms. Appl Opt. 1997;36(8):1766-75. doi: 10.1364/AO.36.001766.

232. Biggs DS. 3D deconvolution microscopy. Curr Protoc Cytom. 2010;Chapter 12:Unit 12 9 1-20. doi: 10.1002/0471142956.cy1219s52. PubMed PMID: 20373494.

233. Harris C, Stephens M. A Combined Corner and Edge Detector. Proc Alvey Vision Conf. 1988:147-51. doi: 10.5244/c.2.23.

234. Krause M, Hausherr JM, Burgeth B, Herrmann C, Krenkel W. Determination of the fibre orientation in composites using the structure tensor and local X-ray transform. J Mater Sci. 2010;45(4):888-96. doi: 10.1007/s10853-009-4016-4.

235. Axelsson M. Estimating 3D fibre orientation in volume images. Pattern Recognition, 2008 ICPR 2008 19th International Conference on; 8-11 Dec. 20082008. p. 1-4.

236. Köthe U. Edge and Junction Detection with an Improved Structure Tensor. In: Michaelis B, Krell G, editors. Pattern Recognition. Lecture Notes in Computer Science. 2781: Springer Berlin Heidelberg; 2003. p. 25-32.

237. Structure Tensor - Introduction and Tutorial [Internet]. 2006.

238. Westin CF, Maier SE, Mamata H, Nabavi A, Jolesz FA, Kikinis R. Processing and visualization for diffusion tensor MRI. Medical Image Analysis. 2002;6(2):93-108. doi: http://dx.doi.org/10.1016/S1361-8415(02)00053-1.

239. Woods AE ER. Laboratory histopathology. New York: Churchill Livingstone; 1994.

240. Eltoum I, Fredenburgh J, Myers RB, Grizzle WE. Introduction to the Theory and Practice of Fixation of Tissues. Journal of Histotechnology. 2001;24(3):173-90. doi: doi:10.1179/his.2001.24.3.173.

241. Wehrl HF, Bezrukov I, Wiehr S, Lehnhoff M, Fuchs K, Mannheim JG, et al. Assessment of murine brain tissue shrinkage caused by different histological fixatives using magnetic resonance and computed tomography imaging. Histol Histopathol. 2015;30(5):601-13. PubMed PMID: 25504583.

242. Williams JH, Mepham BL, Wright DH. Tissue preparation for immunocytochemistry. J Clin Pathol. 1997;50(5):422-8. PubMed PMID: 9215127; PubMed Central PMCID: PMCPMC499946.

243. Alexander DC, Pierpaoli C, Basser PJ, Gee JC. Spatial transformations of diffusion tensor magnetic resonance images. Medical Imaging, IEEE Transactions on. 2001;20(11):1131-9. doi: 10.1109/42.963816.

244. Hong X, Arlinghaus LR, Anderson AW. Spatial normalization of the fiber orientation distribution based on high angular resolution diffusion imaging data. Magnetic resonance in medicine : official journal of the Society of Magnetic Resonance in Medicine / Society of Magnetic Resonance in Medicine. 2009;61(6):1520-7. Epub 2009/04/09. doi: 10.1002/mrm.21916. PubMed PMID: 19353649; PubMed Central PMCID: PMC2774933.

245. Cai T, Fan J, Jiang T. Distributions of Angles in Random Packing on Spheres. Journal of machine learning research : JMLR. 2013;14(1):1837-64. PubMed PMID: PMC4196685.

246. Singh M, Rajagopalan A, Kim TS, Hwang D, Chui H, Zhang XL, et al. Co-registration of In-Vivo Human MRI Brain Images to Postmortem Histological Microscopic Images. International journal of imaging systems and technology. 2008;18(5-6):325-35. doi: 10.1002/ima.v18:5/6. PubMed PMID: PMC2630121.

247. Dauguet J, Delzescaux T, Conde F, Mangin JF, Ayache N, Hantraye P, et al. Three-dimensional reconstruction of stained histological slices and 3D non-linear registration with in-vivo MRI for whole baboon brain. J Neurosci Methods. 2007;164(1):191-204. doi: 10.1016/j.jneumeth.2007.04.017. PubMed PMID: 17560659.

248. Ferizi U, Schneider T, Tariq M, Wheeler-Kingshott CM, Zhang H, Alexander D. The Importance of Being Dispersed: A Ranking of Diffusion MRI Models for Fibre Dispersion Using In

Vivo Human Brain Data. In: Mori K, Sakuma I, Sato Y, Barillot C, Navab N, editors. Medical Image Computing and Computer-Assisted Intervention – MICCAI 2013. Lecture Notes in Computer Science. 8149: Springer Berlin Heidelberg; 2013. p. 74-81.

249. Bingham C. An Antipodally Symmetric Distribution on the Sphere. 1974:1201-25. doi: 10.1214/aos/1176342874.

250. Jones DK. The effect of gradient sampling schemes on measures derived from diffusion tensor MRI: a Monte Carlo study. Magnetic resonance in medicine : official journal of the Society of Magnetic Resonance in Medicine / Society of Magnetic Resonance in Medicine. 2004;51(4):807-15. Epub 2004/04/06. doi: 10.1002/mrm.20033. PubMed PMID: 15065255.

251. Nilsson M, Latt J, Stahlberg F, van Westen D, Hagslatt H. The importance of axonal undulation in diffusion MR measurements: a Monte Carlo simulation study. NMR in biomedicine. 2012;25(5):795-805. doi: 10.1002/nbm.1795. PubMed PMID: 22020832.

252. Descoteaux M, Deriche R, Knosche TR, Anwander A. Deterministic and probabilistic tractography based on complex fibre orientation distributions. IEEE transactions on medical imaging. 2009;28(2):269-86. doi: 10.1109/TMI.2008.2004424. PubMed PMID: 19188114.

253. Strasters KC, van der Voort HTM, Geusebroek JM, Smeulders AWM. Fast attenuation correction in fluorescence confocal imaging: A recursive approach. Bioimaging. 1994;2(2):78-92. doi: 10.1002/1361-6374(199406)2:2<78::AID-BIO2>3.0.CO;2-D.

254. Basser PJ, Pierpaoli C. Microstructural and physiological features of tissues elucidated by quantitative-diffusion-tensor MRI. Journal of magnetic resonance Series B. 1996;111(3):209-19. Epub 1996/06/01. PubMed PMID: 8661285.

255. Jbabdi S, Sotiropoulos SN, Haber SN, Van Essen DC, Behrens TE. Measuring macroscopic brain connections in vivo. Nat Neurosci. 2015;18(11):1546-55. doi: 10.1038/nn.4134. PubMed PMID: 26505566.

256. Van Essen DC, Ugurbil K. The future of the human connectome. NeuroImage. 2012;62(2):1299-310. doi: 10.1016/j.neuroimage.2012.01.032. PubMed PMID: 22245355; PubMed Central PMCID: PMCPMC3350760.

257. Riffert TW, Schreiber J, Anwander A, Knosche TR. Beyond fractional anisotropy: extraction of bundle-specific structural metrics from crossing fiber models. NeuroImage. 2014;100:176-91. doi: 10.1016/j.neuroimage.2014.06.015. PubMed PMID: 24936681.

258. Dell'Acqua F, Simmons A, Williams SC, Catani M. Can spherical deconvolution provide more information than fiber orientations? Hindrance modulated orientational anisotropy, a true-tract specific index to characterize white matter diffusion. Human brain mapping. 2013;34(10):2464-83. doi: 10.1002/hbm.22080. PubMed PMID: 22488973.

259. Raffelt D, Tournier JD, Rose S, Ridgway GR, Henderson R, Crozier S, et al. Apparent Fibre Density: a novel measure for the analysis of diffusion-weighted magnetic resonance images. NeuroImage. 2012;59(4):3976-94. doi: 10.1016/j.neuroimage.2011.10.045. PubMed PMID: 22036682.

260. Canales-Rodriguez EJ, Melie-Garcia L, Iturria-Medina Y. Mathematical description of q-space in spherical coordinates: exact q-ball imaging. Magnetic resonance in medicine : official journal of the Society of Magnetic Resonance in Medicine / Society of Magnetic Resonance in Medicine. 2009;61(6):1350-67. doi: 10.1002/mrm.21917. PubMed PMID: 19319889.

261. Gangolli M, Holleran L, Hee Kim J, Stein TD, Alvarez V, McKee AC, et al. Quantitative validation of a nonlinear histology-MRI coregistration method using generalized Q-sampling imaging in complex human cortical white matter. NeuroImage. 2017;153:152-67. doi: 10.1016/j.neuroimage.2017.03.059. PubMed PMID: 28365421; PubMed Central PMCID: PMCPMC5497585.

262. Mollink J, Kleinnijenhuis M, Cappellen van Walsum AV, Sotiropoulos SN, Cottaar M, Mirfin C, et al. Evaluating fibre orientation dispersion in white matter: Comparison of diffusion MRI, histology and polarized light imaging. NeuroImage. 2017;157:561-74. doi: 10.1016/j.neuroimage.2017.06.001. PubMed PMID: 28602815.

263. Tournier JD, Calamante F, Connelly A. Determination of the appropriate b value and number of gradient directions for high-angular-resolution diffusion-weighted imaging. NMR in biomedicine. 2013;26(12):1775-86. doi: 10.1002/nbm.3017. PubMed PMID: 24038308.

264. P. A. Cook YB, S. Nedjati-Gilani, K. K. Seunarine, M. G. Hall, G. J. Parker, D. C. Alexander,, editor Camino: Open-Source Diffusion-MRI Reconstruction and Processing. 14th Scientific Meeting of the International Society for Magnetic Resonance in Medicine; May 2006; Seattle, WA, USA.

265. Chiang MC, Barysheva M, Lee AD, Madsen S, Klunder AD, Toga AW, et al. Brain fiber architecture, genetics, and intelligence: a high angular resolution diffusion imaging (HARDI) study. Med Image Comput Comput Assist Interv. 2008;11(Pt 1):1060-7. PubMed PMID: 18979850; PubMed Central PMCID: PMCPMC3073165.

266. Cohen-Adad J, Descoteaux M, Wald LL. Quality assessment of high angular resolution diffusion imaging data using bootstrap on Q-ball reconstruction. Journal of magnetic resonance imaging : JMRI. 2011;33(5):1194-208. doi: 10.1002/jmri.22535. PubMed PMID: 21509879; PubMed Central PMCID: PMCPMC3087444.

267. Schilling KG, Nath V, Blaber JA, Parvathaneni P, Anderson AW, Landman BA. Empirical consideration of the effects of acquisition parameters and analysis model on clinically feasible

q-ball imaging. Magnetic resonance imaging. 2017;40:62-74. doi: 10.1016/j.mri.2017.04.007. PubMed PMID: 28438712.

268. Cook PA, Symms M, Boulby PA, Alexander DC. Optimal acquisition orders of diffusion-weighted MRI measurements. Journal of magnetic resonance imaging : JMRI. 2007;25(5):1051-8. doi: 10.1002/jmri.20905. PubMed PMID: 17457801.

269. Prckovska V, Achterberg HC, Bastiani M, Pullens P, Balmashnova E, Ter Haar Romeny BM, et al. Optimal short-time acquisition schemes in high angular resolution diffusion-weighted imaging. Int J Biomed Imaging. 2013;2013:658583. doi: 10.1155/2013/658583. PubMed PMID: 23554808; PubMed Central PMCID: PMCPMC3608261.

270. Wilkins B, Lee N, Gajawelli N, Law M, Lepore N. Fiber estimation and tractography in diffusion MRI: development of simulated brain images and comparison of multi-fiber analysis methods at clinical b-values. NeuroImage. 2015;109:341-56. doi: 10.1016/j.neuroimage.2014.12.060. PubMed PMID: 25555998; PubMed Central PMCID: PMCPMC4600612.

271. Schneider T, Brownlee W, Zhang H, Ciccarelli O, Miller DH, Wheeler-Kingshott CG. Sensitivity of multi-shell NODDI to multiple sclerosis white matter changes: a pilot study. Funct Neurol. 2017;32(2):97-101. PubMed PMID: 28676143.

272. By S, Xu J, Box BA, Bagnato FR, Smith SA. Application and evaluation of NODDI in the cervical spinal cord of multiple sclerosis patients. Neuroimage Clin. 2017;15:333-42. doi: 10.1016/j.nicl.2017.05.010. PubMed PMID: 28560158; PubMed Central PMCID: PMCPMC5443965.

273. Wen Q, Kelley DA, Banerjee S, Lupo JM, Chang SM, Xu D, et al. Clinically feasible NODDI characterization of glioma using multiband EPI at 7 T. Neuroimage Clin. 2015;9:291-9. doi: 10.1016/j.nicl.2015.08.017. PubMed PMID: 26509116; PubMed Central PMCID: PMCPMC4579286.

274. Billiet T, Madler B, D'Arco F, Peeters R, Deprez S, Plasschaert E, et al. Characterizing the microstructural basis of "unidentified bright objects" in neurofibromatosis type 1: A combined in vivo multicomponent T2 relaxation and multi-shell diffusion MRI analysis. Neuroimage Clin. 2014;4:649-58. doi: 10.1016/j.nicl.2014.04.005. PubMed PMID: 24936416; PubMed Central PMCID: PMCPMC4053637.

275. Grussu F, Schneider T, Tur C, Yates RL, Tachrount M, Ianus A, et al. Neurite dispersion: a new marker of multiple sclerosis spinal cord pathology? Ann Clin Transl Neurol. 2017;4(9):663-79. doi: 10.1002/acn3.445. PubMed PMID: 28904988; PubMed Central PMCID: PMCPMC5590517.

276. Catani M, Bodi I, Dell'Acqua F. Comment on "The geometric structure of the brain fiber pathways". Science. 2012;337(6102):1605. doi: 10.1126/science.1223425. PubMed PMID: 23019632.

277. Schilling K, Gao Y, Janve V, Stepniewska I, Landman BA, Anderson AW. Can increased spatial resolution solve the crossing fiber problem for diffusion MRI? NMR in biomedicine. 2017. doi: 10.1002/nbm.3787. PubMed PMID: 28915311.

278. Jones DK. Precision and accuracy in diffusion tensor magnetic resonance imaging. Top Magn Reson Imaging. 2010;21(2):87-99. doi: 10.1097/RMR.0b013e31821e56ac. PubMed PMID: 21613874.

279. Landman BA, Farrell JA, Jones CK, Smith SA, Prince JL, Mori S. Effects of diffusion weighting schemes on the reproducibility of DTI-derived fractional anisotropy, mean diffusivity, and principal eigenvector measurements at 1.5T. NeuroImage. 2007;36(4):1123-38. Epub 2007/05/29. doi: 10.1016/j.neuroimage.2007.02.056. PubMed PMID: 17532649.

280. Schilling K, Gao Y, Stepniewska I, Choe AS, Landman BA, Anderson AW. Reproducibility and variation of diffusion measures in the squirrel monkey brain, in vivo and ex vivo. Magnetic resonance imaging. 2017;35:29-38. doi: 10.1016/j.mri.2016.08.015. PubMed PMID: 27587226; PubMed Central PMCID: PMCPMC5125845.

281. Schmahmann JD, Pandya DN. Cerebral white matter--historical evolution of facts and notions concerning the organization of the fiber pathways of the brain. J Hist Neurosci. 2007;16(3):237-67. doi: 10.1080/09647040500495896. PubMed PMID: 17620190.

282. Sporns O. The human connectome: origins and challenges. NeuroImage. 2013;80:53-61. doi: 10.1016/j.neuroimage.2013.03.023. PubMed PMID: 23528922.

283. Sporns O, Tononi G, Kotter R. The human connectome: A structural description of the human brain. PLoS Comput Biol. 2005;1(4):e42. doi: 10.1371/journal.pcbi.0010042. PubMed PMID: 16201007; PubMed Central PMCID: PMCPMC1239902.

284. Honey CJ, Sporns O, Cammoun L, Gigandet X, Thiran JP, Meuli R, et al. Predicting human resting-state functional connectivity from structural connectivity. Proceedings of the National Academy of Sciences of the United States of America. 2009;106(6):2035-40. Epub 2009/02/04. doi: 10.1073/pnas.0811168106. PubMed PMID: 19188601; PubMed Central PMCID: PMC2634800.

285. Mars RB, Jbabdi S, Sallet J, O'Reilly JX, Croxson PL, Olivier E, et al. Diffusion-weighted imaging tractography-based parcellation of the human parietal cortex and comparison with human and macaque resting-state functional connectivity. J Neurosci. 2011;31(11):4087-100. doi: 10.1523/JNEUROSCI.5102-10.2011. PubMed PMID: 21411650; PubMed Central PMCID: PMCPMC3091022.

286. Behrens TE, Johansen-Berg H. Relating connectional architecture to grey matter function using diffusion imaging. Philos Trans R Soc Lond B Biol Sci. 2005;360(1457):903-11. doi: 10.1098/rstb.2005.1640. PubMed PMID: 16087435; PubMed Central PMCID: PMCPMC1854924.

287. Gong G, Jiang T, Zhu C, Zang Y, Wang F, Xie S, et al. Asymmetry analysis of cingulum based on scale-invariant parameterization by diffusion tensor imaging. Human brain mapping. 2005;24(2):92-8. doi: 10.1002/hbm.20072. PubMed PMID: 15455461.

288. Dyrby TB, Sogaard LV, Hall MG, Ptito M, Alexander DC. Contrast and stability of the axon diameter index from microstructure imaging with diffusion MRI. Magnetic resonance in medicine : official journal of the Society of Magnetic Resonance in Medicine / Society of Magnetic Resonance in Medicine. 2013;70(3):711-21. doi: 10.1002/mrm.24501. PubMed PMID: 23023798; PubMed Central PMCID: PMCPMC4199276.

289. Kleinnijenhuis M, van Mourik T, Norris DG, Ruiter DJ, van Cappellen van Walsum AM, Barth M. Diffusion tensor characteristics of gyrencephaly using high resolution diffusion MRI in vivo at 7T. NeuroImage. 2015;109:378-87. doi: 10.1016/j.neuroimage.2015.01.001. PubMed PMID: 25585019.

290. Van Essen DC, Maunsell JH. Two-dimensional maps of the cerebral cortex. J Comp Neurol. 1980;191(2):255-81. doi: 10.1002/cne.901910208. PubMed PMID: 7410593.

291. Peters A, Jones EG. Cerebral cortex. New York: Plenum Press; 1984.

292. Rockel AJ, Hiorns RW, Powell TP. The basic uniformity in structure of the neocortex. Brain. 1980;103(2):221-44. PubMed PMID: 6772266.

293. Sotiropoulos SN, Chen C, Dikranian K, Jbabdi S, Behrens TE, Van Essen DC, et al., editors. Comparison of diffusion MRI predictions and histology in the Macaque brain. ISMRM; 2013; Salt Lake City, Utah.

294. McNab JA, Polimeni JR, Wang R, Augustinack JC, Fujimoto K, Stevens A, et al. Surface based analysis of diffusion orientation for identifying architectonic domains in the in vivo human cortex. NeuroImage. 2013;69:87-100. doi: 10.1016/j.neuroimage.2012.11.065. PubMed PMID: 23247190; PubMed Central PMCID: PMCPMC3557597.

295. Smith RE, Tournier JD, Calamante F, Connelly A. SIFT: Spherical-deconvolution informed filtering of tractograms. NeuroImage. 2013;67:298-312. doi: 10.1016/j.neuroimage.2012.11.049. PubMed PMID: 23238430.

296. Yeh CH, Smith RE, Liang X, Calamante F, Connelly A. Correction for diffusion MRI fibre tracking biases: The consequences for structural connectomic metrics. NeuroImage. 2016. doi: 10.1016/j.neuroimage.2016.05.047. PubMed PMID: 27211472.

297. Girard G, Whittingstall K, Deriche R, Descoteaux M. Towards quantitative connectivity analysis: reducing tractography biases. NeuroImage. 2014;98:266-78. doi: 10.1016/j.neuroimage.2014.04.074. PubMed PMID: 24816531.

298. Smith RE, Tournier JD, Calamante F, Connelly A. Anatomically-constrained tractography: improved diffusion MRI streamlines tractography through effective use of anatomical information. NeuroImage. 2012;62(3):1924-38. doi: 10.1016/j.neuroimage.2012.06.005. PubMed PMID: 22705374.

299. Heidemann RM, Anwander A, Feiweier T, Knosche TR, Turner R. k-space and q-space: combining ultra-high spatial and angular resolution in diffusion imaging using ZOOPPA at 7 T. NeuroImage. 2012;60(2):967-78. doi: 10.1016/j.neuroimage.2011.12.081. PubMed PMID: 22245337.

300. Allen JS, Damasio H, Grabowski TJ. Normal neuroanatomical variation in the human brain: an MRI-volumetric study. Am J Phys Anthropol. 2002;118(4):341-58. doi: 10.1002/ajpa.10092. PubMed PMID: 12124914.

301. C. Alexander CP, P. J. Basser, J. C. Gee. Spatial Transformations of Diffusion Tensor Magnetic Resonance Images. IEEE transactions on medical imaging. 2001;20(11):1131-9.

302. Bakker R, Tiesinga P, Kotter R. The Scalable Brain Atlas: Instant Web-Based Access to Public Brain Atlases and Related Content. Neuroinformatics. 2015;13(3):353-66. doi: 10.1007/s12021-014-9258-x. PubMed PMID: 25682754; PubMed Central PMCID: PMCPMC4469098.

303. Paxinos G, Huang XF, Toga AW. The rhesus monkey brain in stereotaxic coordinates. San Diego, CA: Academic Press; 2000. 163 p. p.

304. Fischl B, Sereno MI, Dale AM. Cortical surface-based analysis. II: Inflation, flattening, and a surface-based coordinate system. NeuroImage. 1999;9(2):195-207. doi: 10.1006/nimg.1998.0396. PubMed PMID: 9931269.

305. Dale AM, Fischl B, Sereno MI. Cortical surface-based analysis. I. Segmentation and surface reconstruction. NeuroImage. 1999;9(2):179-94. doi: 10.1006/nimg.1998.0395. PubMed PMID: 9931268.

306. Desikan RS, Segonne F, Fischl B, Quinn BT, Dickerson BC, Blacker D, et al. An automated labeling system for subdividing the human cerebral cortex on MRI scans into gyral based regions of interest. NeuroImage. 2006;31(3):968-80. doi: 10.1016/j.neuroimage.2006.01.021. PubMed PMID: 16530430.

307. Destrieux C, Fischl B, Dale A, Halgren E. Automatic parcellation of human cortical gyri and sulci using standard anatomical nomenclature. NeuroImage. 2010;53(1):1-15. doi: 10.1016/j.neuroimage.2010.06.010. PubMed PMID: 20547229; PubMed Central PMCID: PMCPMC2937159.

308. Fischl B, van der Kouwe A, Destrieux C, Halgren E, Segonne F, Salat DH, et al. Automatically parcellating the human cerebral cortex. Cereb Cortex. 2004;14(1):11-22. PubMed PMID: 14654453.

309. Li G, Guo L, Nie J, Liu T. Automatic cortical sulcal parcellation based on surface principal direction flow field tracking. NeuroImage. 2009;46(4):923-37. doi: 10.1016/j.neuroimage.2009.03.039. PubMed PMID: 19328234; PubMed Central PMCID: PMCPMC2756525.

310. Li K, Guo L, Li G, Nie J, Faraco C, Cui G, et al. Gyral folding pattern analysis via surface profiling. NeuroImage. 2010;52(4):1202-14. doi: 10.1016/j.neuroimage.2010.04.263. PubMed PMID: 20472071; PubMed Central PMCID: PMCPMC2910197.

311. Li C, Huang R, Ding Z, Gatenby C, Metaxas D, Gore J. A variational level set approach to segmentation and bias correction of images with intensity inhomogeneity. Med Image Comput Comput Assist Interv. 2008;11(Pt 2):1083-91. PubMed PMID: 18982712; PubMed Central PMCID: PMCPMC2782702.

312. Jones DK, Basser PJ. "Squashing peanuts and smashing pumpkins": how noise distorts diffusion-weighted MR data. Magnetic resonance in medicine : official journal of the Society of Magnetic Resonance in Medicine / Society of Magnetic Resonance in Medicine. 2004;52(5):979-93. doi: 10.1002/mrm.20283. PubMed PMID: 15508154.

313. Aitchison J. The statistical analysis of compositional data. London ; New York: Chapman and Hall; 1986. xv, 416 p. p.

314. Calamante F, Tournier JD, Jackson GD, Connelly A. Track-density imaging (TDI): super-resolution white matter imaging using whole-brain track-density mapping. NeuroImage. 2010;53(4):1233-43. doi: 10.1016/j.neuroimage.2010.07.024. PubMed PMID: 20643215.

315. Yeatman JD, Dougherty RF, Myall NJ, Wandell BA, Feldman HM. Tract profiles of white matter properties: automating fiber-tract quantification. PloS one. 2012;7(11):e49790. doi: 10.1371/journal.pone.0049790. PubMed PMID: 23166771; PubMed Central PMCID: PMCPMC3498174.

316. Parker CS, Deligianni F, Cardoso MJ, Daga P, Modat M, Dayan M, et al. Consensus between pipelines in structural brain networks. PloS one. 2014;9(10):e111262. doi: 10.1371/journal.pone.0111262. PubMed PMID: 25356977; PubMed Central PMCID: PMCPMC4214749.

317. Clayden JD. Imaging connectivity: MRI and the structural networks of the brain. Funct Neurol. 2013;28(3):197-203. doi: 10.11138/FNeur/2013.28.3.197. PubMed PMID: 24139656; PubMed Central PMCID: PMCPMC3812744.

318. Chang L-C, Koay CG, Pierpaoli C, Basser PJ. Variance of estimated DTI-derived parameters via first-order perturbation methods. Magnetic Resonance in Medicine. 2007;57(1):141-9. doi: 10.1002/mrm.21111.

319. Liptrot MG, Sidaros K, Dyrby TB. Addressing the path-length-dependency confound in white matter tract segmentation. PloS one. 2014;9(5):e96247. doi: 10.1371/journal.pone.0096247. PubMed PMID: 24797510; PubMed Central PMCID: PMCPMC4010423.

320. Cottaar M, Bastiani M, Chen C, Dikranian K, Van Essen DC, Behrens TE, et al., editors. Fibers crossing the white/gray matter boundary: a semi-global, histology-informed dMRI model. ISMRM Proceedings; 2016; Singapore.

321. Cottaar M, Jbabdi S, Glasser MF, Dikranian K, Van Essen DC, Behrens TE, et al., editors. A Generative Model of White Matter Axonal Orientations Near the Cortex. ISMRM Proceedings; 2015; Toronto, Canada.

322. Daducci A, Dal Palu A, Lemkaddem A, Thiran JP. COMMIT: Convex optimization modeling for microstructure informed tractography. IEEE transactions on medical imaging. 2015;34(1):246-57. doi: 10.1109/TMI.2014.2352414. PubMed PMID: 25167548.

323. Qi S, Meesters S, Nicolay K, Ter Haar Romeny BM, Ossenblok P. Structural Brain Network: What is the Effect of LiFE Optimization of Whole Brain Tractography? Front Comput Neurosci. 2016;10:12. doi: 10.3389/fncom.2016.00012. PubMed PMID: 26909034; PubMed Central PMCID: PMCPMC4754446.

324. Sotiropoulos SN, Jbabdi S, Xu J, Andersson JL, Moeller S, Auerbach EJ, et al. Advances in diffusion MRI acquisition and processing in the Human Connectome Project. NeuroImage. 2013;80:125-43. doi: 10.1016/j.neuroimage.2013.05.057. PubMed PMID: 23702418; PubMed Central PMCID: PMCPMC3720790.

325. Ugurbil K, Xu J, Auerbach EJ, Moeller S, Vu AT, Duarte-Carvajalino JM, et al. Pushing spatial and temporal resolution for functional and diffusion MRI in the Human Connectome Project. NeuroImage. 2013;80:80-104. doi: 10.1016/j.neuroimage.2013.05.012. PubMed PMID: 23702417; PubMed Central PMCID: PMCPMC3740184.

326. Jeong HK, Gore JC, Anderson AW. High-resolution human diffusion tensor imaging using 2-D navigated multishot SENSE EPI at 7 T. Magnetic resonance in medicine : official journal of the Society of Magnetic Resonance in Medicine / Society of Magnetic Resonance in Medicine.

2013;69(3):793-802. doi: 10.1002/mrm.24320. PubMed PMID: 22592941; PubMed Central PMCID: PMCPMC3424313.

327. Carlo CN, Stevens CF. Structural uniformity of neocortex, revisited. Proceedings of the National Academy of Sciences of the United States of America. 2013;110(4):1488-93. doi: 10.1073/pnas.1221398110. PubMed PMID: 23297199; PubMed Central PMCID: PMCPMC3557031.

328. Braitenberg V, Schüz A, Braitenberg V. Cortex : statistics and geometry of neuronal connectivity. 2nd thoroughly rev. ed. Berlin ; New York: Springer; 1998. xiii, 249 p. p.

329. Charvet CJ, Cahalane DJ, Finlay BL. Systematic, cross-cortex variation in neuron numbers in rodents and primates. Cereb Cortex. 2015;25(1):147-60. doi: 10.1093/cercor/bht214. PubMed PMID: 23960207; PubMed Central PMCID: PMCPMC4259279.

330. Collins CE. Variability in neuron densities across the cortical sheet in primates. Brain Behav Evol. 2011;78(1):37-50. doi: 10.1159/000327319. PubMed PMID: 21691046.

331. Hilgetag CC, Barbas H. Role of mechanical factors in the morphology of the primate cerebral cortex. PLoS Comput Biol. 2006;2(3):e22. doi: 10.1371/journal.pcbi.0020022. PubMed PMID: 16557292; PubMed Central PMCID: PMCPMC1409812.